

POLITECNICO DI TORINO

Collegio di Ingegneria Chimica e dei Materiali

**Corso di Laurea Magistrale
in Ingegneria Chimica e dei Processi Sostenibili**

Tesi di Laurea Magistrale

**Influence of Impeller Type and Geometry
on Particle Stress in a Stirred Fermenter
by Means of Particle Image Velocimetry**



Relatori

prof. Daniele Marchisio

prof. Bernardo Ruggeri

Candidato

Giulia Moretti

Luglio 2019

Abstract

In molteplici processi chimici e biotecnologici, la miscelazione rappresenta una delle operazioni unitarie fondamentali ed è spesso esercitata nei serbatoi agitati. L'efficienza del mixing è un parametro importante per quei processi in cui questa operazione è coinvolta e dipende dal design e dalle condizioni operative scelte. L'indagine sul flusso risulta essere uno strumento utile per affrontare e comprendere i meccanismi che avvengono nel fluido all'interno del serbatoio agitato, nonché per effettuare una caratterizzazione delle proprietà del flusso, le quali possono essere misurate attraverso l'impiego di diverse tecniche di analisi. In particolar modo nelle biotecnologie, dove i microrganismi rivestono un ruolo fondamentale per la realizzazione e lo sviluppo dei processi, i fenomeni idromeccanici generati dalla miscelazione meccanica possono influenzare negativamente la produttività del processo, in quanto potenzialmente dannosi per gli agglomerati di cellule che fluiscono all'interno del brodo; per questo motivo risulta fondamentale procedere con un'analisi mirata a conoscere meglio l'influenza dei vari elementi in gioco, quali ad esempio la geometria dell'agitatore utilizzato nella miscelazione.

In un contesto così ampio, questo lavoro sperimentale è centrato sull'analisi del flusso in un serbatoio agitato, mediante l'utilizzo di una tecnica di analisi fotografica, la particle image velocimetry (PIV). L'attenzione è particolarmente rivolta ai fenomeni di stress che si verificano all'interno del fluido.

Il setup sperimentale consiste in un serbatoio agitato, dove una sola fase viene messa in agitazione. Gli esperimenti vengono condotti con tre fluidi, ovvero acqua, una soluzione acquosa di glicerina e una di xantano; questi sono dei fluidi modello non biologici, intenzionalmente definiti per facilitare l'indagine sperimentale e pensati per simulare le proprietà reologiche di un brodo di coltura.

Nell'indagine, l'avviamento preliminare della tecnica di misurazione rende possibile il confronto dei diversi approcci alla PIV, qui utilizzata per misurazioni in due e in tre dimensioni. Successivamente, l'indagine sistematica implica l'utilizzo di nove agitatori di diverse geometrie, tra cui due propeller, due turbine pitched-blade, un anello "bionico" e tre agitatori a nastro ondulato (Möbius). Con le misurazioni effettuate tramite PIV, il gradiente di sforzo di taglio e l'energia cinetica turbolenta sono calcolati direttamente dai gradienti di velocità, con l'obiettivo di osservare e determinare l'influenza della geometria dell'agitatore sulla dinamica del flusso.

Introduzione

La tesi sperimentale qui presentata si colloca nell'ampio campo dei processi chimici e biotecnologici che fanno uso della miscelazione ed ha lo scopo di caratterizzare alcune diverse geometrie di agitatori in termini di stress sulle particelle. Il raggiungimento di tale scopo prevede l'impiego di una tecnica di analisi fotografica, la quale è in grado di produrre una rappresentazione della dinamica del fluido.

Lo stress sulle particelle che fluttuano nel fluido studiato è di grande interesse in questo campo di ricerca, in quanto parametro che può influenzare in modo molto negativo la produttività dell'intero processo (Daub et al., 2014).

Contestualizzazione del Tema

Questo lavoro sperimentale è stato realizzato durante un progetto Erasmus+ svolto presso il dipartimento di ingegneria chimica della Technische Universität di Berlino e prende parte a due progetti di dottorato, condotti da Dipl.-Ing. Chrysoula Bliatsiou e Robert Panckow.

Il primo progetto, SPP1943, intende caratterizzare lo stress meccanico locale in un fermentatore aerato agitato e determinare l'interazione con la produttività degli agglomerati biologici. Gli esperimenti sono modellati sulla coltivazione dell'*Aspergillus niger* e i risultati sono pensati per il design e lo sviluppo di agitatori che producono un basso sforzo di taglio. L'indagine sperimentale sulla fluidodinamica è resa possibile dall'impiego di fluidi modello che simulano le proprietà reologiche del brodo di coltura. Lo stress meccanico è determinato in termini di distribuzione delle dimensioni delle particelle che costituiscono la fase dispersa. Gli strumenti di supporto nell'indagine sono le simulazioni CFD (Computational Fluid Dynamics) e le equazioni di bilancio di popolazione (PBE). Le tecniche di misurazione principalmente utilizzate sono la PIV e la tecnologia endoscopica in situ.

Il secondo progetto, Smart Process Inspection (SPI), finanziato dal "Federal Ministry for Economic Affairs and Energy" si compone di sette project partners, tra cui quattro aziende e tre università tedesche. In questo progetto le tecniche di misurazione di tipo foto ed elettro-ottico sono studiate per un'analisi multiparametrica in sistemi biologici. Gli obiettivi di tale progetto includono la caratterizzazione della distribuzione locale della dimensione delle particelle in reattori multifase e la determinazione dell'influenza dell'aggiunta di una fase dispersa nei sistemi contenenti microrganismi. L'indagine sulle proprietà macroscopiche del fluido di un sistema, caratterizzate dal movimento e dalla miscelazione del fluido stesso, ha lo scopo di comprendere e quantificare i fenomeni microscopici, quali lo stress cellulare, che influenzano la coltura cellulare, prendendo in considerazione l'influenza delle bolle e delle goccioline del campo mesoscopico. I setup sperimentali consistono in un serbatoio aerato agitato e in un bioreattore wave-mixed monouso. Le tecniche di misurazione includono CFD e PIV per l'analisi del flusso, mentre per le misurazioni in situ delle fasi disperse vengono usati dei dispositivi endoscopici foto-ottici in entrambi i tipi di bioreattore.

Approssimazione del Sistema Studiato

In un fermentatore, la progressiva crescita di microrganismi porta spesso a cambiamenti significativi nelle proprietà reologiche del brodo. Le colture altamente viscosi possono risentire di scarsa miscelazione e conseguentemente di trasporto di materia limitato e

manca di ossigeno. L'ossigeno va rifornito e inserito nel sistema nel caso in cui i microrganismi utilizzati abbiano un metabolismo aerobico. In ogni caso, le attività vitali dei microrganismi producono di per sé una fase gassosa, ad esempio sotto forma di anidride carbonica.

La realizzazione dello studio sperimentale presenta la necessità di introdurre un'approssimazione significativa nel sistema considerato. Questa consiste nell'utilizzare un sistema con una sola fase che esclude la coltura biologica e la fase gassosa. Il modello del sistema a singola fase prevede l'uso di un fluido modello non biologico, in grado di approssimare le proprietà del brodo reologico, quindi intenzionalmente definito per facilitare la ricerca sperimentale. Inoltre, tale approssimazione risulta essere essenziale per un'applicazione appropriata e corretta della tecnica di analisi scelta, la PIV.

Questo metodo di analisi fotografica è stato selezionato per la sua potenzialità di produrre risultati validi circa il campo di flusso in un serbatoio agitato. Tuttavia, la presenza di una fase gassosa aggiunta nel fluido comporta delle notevoli complicazioni per l'acquisizione e l'elaborazione dei dati. Per questa ragione, l'applicazione della PIV in sistemi gas-liquidi in serbatoi agitati è scarsamente riportata in lavori presenti nella letteratura scientifica. L'ostacolo al corretto funzionamento di questa tecnica è introdotto dalla presenza delle bolle di gas, le quali producono un campo di flusso meno sistematico rispetto al caso con una fase singola. Di conseguenza, il campo vettoriale di velocità della fase continua risulta più difficile da misurare, poiché le bolle e le ombre che queste creano occupano gran parte dell'area in cui le particelle traccianti dovrebbero essere rilevate per misurare il loro spostamento; inoltre la presenza delle bolle di gas produce una riflessione della luce che disturba la misurazione. Pertanto, la distribuzione disomogenea delle bolle all'interno del serbatoio agitato causa un rilevamento irregolare delle particelle traccianti e la concentrazione di queste ultime nell'area esaminata può avere delle fluttuazioni troppo grandi per poter elaborare dei risultati accurati. (Aubin et al., 2004; Deen et al., 2002)

I microrganismi del brodo crescono e cambiano in dimensione e forma, determinando così una reologia che risulta discontinua nel tempo. I brodi di coltura possono essere descritti da modelli reologici che, a seconda della morfologia della fase dispersa, possono essere Newtoniani o non Newtoniani, e nello specifico pseudoplastici (shear thinning). Nell'approccio sperimentale di questo lavoro, i fluidi modello che rappresentano la singola fase del sistema sono scelti per approssimare il brodo di coltura di interesse, ovvero l'*Aspergillus niger*, un fungo con morfologia filamentosa.

A questo riguardo risulta vantaggioso prendere in considerazione il lavoro di Henzler e Schäfer (1987), i quali hanno condotto uno studio su un brodo contenente un microrganismo miceliare, con l'intento di capire come la reologia di tale brodo cambi nel tempo. È stato osservato che, considerando una concentrazione iniziale del microrganismo tale per cui il fluido sia Newtoniano, quando i miceli iniziano a crescere in dimensione e in numero, la viscosità del brodo non presenta più un valore costante. La pseudoplasticità del brodo è stata e può essere descritta con il modello di Ostwald-de Waele.

Tenendo presente questi risultati, ai fini del primo progetto SPP1943 si è proceduto con la valutazione e il confronto della reologia di brodi di coltura e di alcuni fluidi non biologici, quali soluzioni non Newtoniane di xantano, carbossimetilcellulosa e glicole polietilenico. Il modello reologico che descrive il brodo di coltura pseudoplastico è caratterizzato da un fattore

di consistenza K , che aumenta al crescere della biomassa, e di un indice di comportamento n , che al contrario risulta essere indipendente dalla crescita della biomassa. L'esito di questi esperimenti mostrano che il fluido modello più adatto a simulare la coltura di *A. niger* è la soluzione di xantano. Coerentemente con queste conclusioni, considerando che il medium di coltura è un fluido Newtoniano, i fluidi modello scelti per questo lavoro sperimentale sono l'acqua e due soluzioni acquose di glicerina e di xantano (Bliatsiou et al., 2018°).

Struttura dell'Elaborato di Tesi

Il lavoro si estende toccando gli aspetti fondamentali delle colture microbiche e dei serbatoi agitati, includendo i fenomeni fluidodinamici che si verificano in tali sistemi. Segue una trattazione che descrive la tecnica di analisi, suggerendo come approcciarsi nella pratica al sistema sperimentale.

Nel **Capitolo 2** si propone una revisione letteraria sui concetti fondamentali su cui si basa il lavoro sperimentale, passando per la descrizione della struttura della cellula e la definizione delle quantità fisiche della fluidodinamica, ponendo particolare attenzione sui meccanismi della miscelazione che avvengono nei serbatoi agitati. Nella **Sezione 2.1**, la definizione e la classificazione dei microrganismi è seguita dalla descrizione delle caratteristiche strutturali della cellula che differenziano i due gruppi principali che includono tutti gli esseri viventi. Una breve introduzione al vasto campo delle biotecnologie introduce il concetto di coltura di microrganismi; le principali tecniche usate sono definite, includendo il caso dei terreni di coltura solidi, quali la piastra di Petri, e del brodo liquido. Questa sezione termina con una panoramica sulle tipologie di bioreattori; qui l'attenzione sui microrganismi termina e verrà ripresa alla fine del capitolo. L'obiettivo della **Sezione 2.2** è definire le proprietà reologiche dei fluidi, in quanto permettono di individuare i diversi comportamenti dei fluidi, i quali sono così classificati utilizzando dei modelli reologici. Segue una discussione sulla reologia dei brodi di coltura e viene mostrato come questi, a causa della presenza di materiale biologico, cambiano la loro morfologia, e conseguentemente le loro proprietà reologiche, nel tempo. In questa discussione si introducono quelli che sono i problemi di tipo biologico, individuabili nello specifico con lo stress particellare che si verifica ogni qualvolta si ha un'agitazione meccanica del brodo di coltura. L'attenzione si sposta sulla fluidodinamica nella **Sezione 2.3**, dove la definizione del vettore velocità viene usato per la formalizzazione matematica di diverse quantità fluidodinamiche, quali la vorticità e il tensore degli sforzi, riguardando un maggiore interesse allo sforzo di taglio (shear). Queste quantità si dimostrano utili a capire e quantificare i meccanismi che si verificano nei fluidi. L'introduzione e la comprensione di queste proprietà permettono inoltre la caratterizzazione e l'interpretazione dei risultati ottenuti nel lavoro sperimentale. Viene introdotto il concetto di turbolenza, mostrando quali sono i possibili regimi di flusso. In questa discussione si inizia a familiarizzare con i concetti di energia cinetica turbolenta e di dissipazione dell'energia cinetica, spesso menzionati e considerati per tutto il lavoro presentato, a causa della loro rilevanza nello studio dei fluidi agitati nei serbatoi. Questo anticipa il contenuto della **Sezione 2.4**, dove viene descritta la miscelazione del fluido in un serbatoio agitato che costituisce una parte fondamentale del lavoro sperimentale. La descrizione del meccanismo di miscelazione è qui supportata dalla teoria di Kolmogorov sulla turbolenza isotropica, teoria usata nell'ultima sezione del capitolo, **Sezione 2.5**, per descrivere le interazioni solido-fluido che generano lo sforzo di taglio sui microrganismi.

Nel **Capitolo 3** si intende presentare la tecnica di misurazione scelta e spiegare il metodo sperimentale usato per l'indagine. I principi generali della PIV sono illustrati, quindi l'attrezzatura specifica che costituisce l'hardware e il generale workflow del software usato per i calcoli sono brevemente illustrati. L'attenzione si focalizza sul setup sperimentale usato, considerando l'apparato principale del serbatoio agitato, che include i diversi agitatori e fluidi. La spiegazione della tecnica di misurazione e il suo sviluppo fino all'avviamento finale e definitivo sono seguiti dalla descrizione della creazione della matrice parametrica, fondamentale per l'organizzazione dei data points dell'indagine sistematica.

Il **Capitolo 4** presenta i risultati del lavoro sperimentale in modo organizzato. In primo luogo, gli approcci usati per l'avvio della tecnica di misurazione sono comparati in termini di campo di flusso ottenuto. Secondariamente, alcuni data points della matrice parametrica sono scelti per l'analisi dell'influenza della potenza immessa (power input), della reologia del fluido e della geometria dell'agitatore sulla dinamica sviluppata nel fluido all'interno del serbatoio agitato. Alla fine del capitolo, l'attenzione si sposta sul tema dello stress particellare e come la geometria dell'agitatore influenza questo elemento. Tale discussione è supportata dai risultati dello studio di Bliatsiou, dove gli stessi agitatori di questo lavoro sono impiegati per valutare lo stress particellare in termini di dimensione stazionaria delle particelle sospese nel fluido agitato.

Il lavoro si chiude con il **Capitolo 5**, dove sono formulate le osservazioni conclusive. Quest'ultimo capitolo propone alcuni aspetti che sono considerati validi per il miglioramento della misurazione mediante PIV e presenta alcuni risultati di una simulazione in CFD del sistema analogo investigato nel lavoro sperimentale.

Metodo Sperimentale

Obiettivi

Questa tesi sperimentale pone diversi obiettivi da raggiungere, classificabili in tre tipologie.

Il primo step, fondamentale per procedere successivamente con il resto dell'indagine, prevede la definizione delle condizioni operative di un metodo di misurazione che consente di raggiungere dei risultati validi. L'avvio della tecnica di misurazione, pertanto, rappresenta il primo obiettivo della tesi: complessivamente si usano tre approcci diversi alla PIV, che comprendono sia la misurazione bidimensionale (planar-PIV) che quella tridimensionale (stereo-PIV).

Il secondo obiettivo è quello di effettuare un'indagine sistematica di data points organizzati per fluido e agitatore. I risultati, una volta elaborati, sono interpretati in modo da capire l'influenza della potenza immessa, della reologia del fluido e della geometria degli agitatori sul campo vettoriale di velocità e conseguentemente sulle quantità calcolate a partire da questo.

L'ultimo obiettivo riguarda l'interpretazione e la valutazione dello stress idromeccanico nel serbatoio agitato per mezzo delle misurazioni ottenute con la PIV.

Particle Image Velocimetry

La particle image velocimetry è una tecnica di analisi ottica ampiamente utilizzata per la determinazione del campo di flusso dei fluidi contenuti nei serbatoi agitati. Questa tecnica di visualizzazione del flusso è di tipo non invasivo, dal momento che si basa sulla registrazione di fotografie scattate dall'esterno del sistema studiato. Per poter effettuare le misurazioni, risulta necessario introdurre nel fluido da analizzare delle particelle traccianti. Queste particelle, sospese in modo omogeneo nella fase continua, vengono illuminate da un piano di luce pulsata, determinando così la sezione trasversale che viene registrata con una fotocamera digitale, **Fig. 3-1** (A). Le particelle traccianti devono essere in grado di riflettere la luce e, a seconda del fluido in esame, si sceglie la tipologia più adatta. Nel caso di liquidi, le più usate sono particelle di poliammide, sferette vuote di vetro e particelle fluorescenti. Inoltre, devono essere presenti in una concentrazione tale da non modificare le proprietà del fluido, quali la densità, in quanto devono seguire il flusso nella maniera più precisa, in quanto rappresentano i vettori delle informazioni sulla velocità del fluido. Da queste caratteristiche viene definito un requisito fondamentale: la PIV può essere applicata soltanto a recipienti e fluidi contenuti in essi che sono otticamente trasparenti. Risulta pertanto alquanto difficoltosa l'analisi di fluidi slurry e torbidi, come i brodi di coltura. (Hadad et al., 2011; La Fontaine, 1996; Raffel et al., 2007)

Il primo fondamentale risultato ottenuto con la PIV è il campo vettoriale della velocità, ovvero le velocità locali del fluido, approssimate alle velocità delle particelle traccianti, in ogni punto della sezione trasversale illuminata e fotografata. Per ottenere questo risultato, è indispensabile illuminare le particelle in due istanti diversi a distanza di un tempo infinitesimo e scattare due fotografie consecutive (double frame) con una o più fotocamere. La velocità è calcolata determinando lo spostamento delle particelle e dividendo questo per l'intervallo tra le due esposizioni. Si procede con una discretizzazione spaziale della sezione trasversale

illuminata e la si divide in tante “interrogation windows” (IW o “interrogation area”, IA): ogni IW della prima immagine viene confrontata con la corrispondente IW dell’immagine successiva. La correlazione incrociata, realizzata con la trasformata di Fourier veloce, permette di trovare un picco distinto nella cella, il quale corrisponde allo spostamento medio delle particelle nella cella stessa, come illustrato in **Fig. 3-1** (B), (Deen and Hjertager, 2002). Il campo vettoriale della velocità si ottiene quindi considerando il vettore risultante in ogni cella dell’area di interesse e può essere rappresentato anche come funzione della distribuzione cumulativa (CDF), **Fig. 3-1** (C).

Setup Sperimentale

Gli esperimenti condotti con la tecnica PIV prevedono l’organizzazione del setup in una camera di laboratorio oscura provvista di pareti nere, in modo da prevenire la riflessione del laser e quindi per operare in condizioni di sicurezza. Gli elementi principali di cui si compone il setup sono:

- Serbatoio agitato in analisi, incluso il vessel, un acquario esterno, i baffles, il motore del mixer, l’albero dell’agitatore, nove agitatori e i fluidi con le particelle traccianti
- Sorgente laser
- Fotocamera digitale ad alta risoluzione, due in caso di stereo-PIV
- Software

Setup del Vessel

Il vessel utilizzato negli esperimenti è in vetro e dal fondo torosferico (forma *Klöpferboden*, norma DIN 28011), con un diametro interno $D = 160$ mm; viene riempito con 2,99 L di fluido, che corrisponde a un livello di riempimento pari a $H = 160$ mm. Il vessel viene posto all’interno di un acquario di base quadrata $22,5 \times 22,5$ cm², riempito con acqua. Quattro baffles equidistanziati sono posizionati alle pareti interne del vessel, con le dimensioni e distanze riportate in **Fig. 3-6**. Il motore del mixer è IKA ® *EUROSTAR 60 control* e con esso è possibile scegliere la frequenza rotazionale nell’intervallo 20–2000 rpm.

I nove agitatori scelti per gli esperimenti includono due propeller, tre turbine pitched-blade, un bionic-loop e tre agitatori a nastro ondulato (Möbius). Questi agitatori, aventi le caratteristiche geometriche riportate in dettaglio in **Tab. 3-1**, sono posizionati nel vessel rispettando una clearance pari al diametro interno del vessel moltiplicato per un fattore di 0,33.

I fluidi utilizzati, scelti considerando le motivazioni espresse nell’introduzione, sono tre:

- *Acqua ultrapura*. Le proprietà rilevate dal purificatore *ELGA* ® *PURELAB flex* sono: temperatura 21,6 °C, Total Organic Carbon (TOC) pari a 3 ppb e conduttività elettrica pari a 0,055 µS. La densità è quantificata mediante *Anton Paar Density and Sound Velocity Meter DSA 5000 M* e la viscosità dinamica tramite *Anton Paar Modular Compact Rheometer MCR 302*. Entrambe le quantità sono misurate a temperatura ambiente e sono 997.66 kg m³ e 955.4 µPa s, rispettivamente.
- *Soluzione di glicerina*. Consiste in una soluzione di acqua ultrapura e glicerina pura, quest’ultima presente con una frazione massica del 60%. I valori di densità e di viscosità misurati sono rispettivamente 1150 kg m³ e 11 mPa s. la soluzione, prima di essere utilizzata, viene agitata a poche decine di rpm per almeno trenta minuti.

- *Soluzione di xantano.* Consiste in una soluzione formata da 0,5 g di xantano per ogni kg di acqua ultrapura. La densità misurata è pari a 998,37 kg m³. Dopo un'agitazione di almeno un paio di ore, la soluzione può essere utilizzata per due giorni massimo, dopo i quali la soluzione inizia a presentare dei cambiamenti progressivi nella sua reologia.

Conducendo delle misurazioni con un reometro si è verificato che mentre l'acqua e la soluzione di glicerina sono dei fluidi Newtoniani con un valore costante di viscosità dinamica, la soluzione di xantano è un fluido pseudoplastico. Aumentando la velocità di deformazione (shear rate) si osserva una diminuzione della viscosità per questo terzo fluido, **Fig. 3-8**. Pertanto, la soluzione di xantano può essere descritta con il modello Ostwald–de Waele, con un indice di comportamento n e un fattore di consistenza K rispettivamente pari a 0,3845 e 0,17185.

Le particelle traccianti il fluido usate per tutti gli esperimenti effettuati sono un prodotto *LaVision*. Sono particelle di dimensione 20–50 µm, fatte di polimetilmetacrilato (PMMA) e ricoperte da un colorante fluorescente costituito da rodamina B. La concentrazione ottimale di particelle da utilizzare è da determinare sperimentalmente per ogni applicazione, come indicato da La Fontaine (1996). Il valore ottimale per questo lavoro è pari a 1 mL per 2,99 L di fluido, ovvero 0,33 L di particelle per litro di fluido. Questo valore permette di avere 5–10 particelle nella IW più piccola (24×24 pixel), valore minimo suggerito da Deen e Solberg (2000).

Sorgente laser, Fotocamera e Software

La chiave per la realizzazione della tecnica è la luce pulsata, ottenuta dall'amplificazione della luce mediante emissione stimolata di radiazione (laser). Il piano di luce pulsata monocromatica è formato da un fascio laser, le cui intensità e direzioni vanno manipolate a seconda dell'area di interesse da indagare. L'hardware usato in questo lavoro è prodotto da *LaVision GmbH*. L'intensità emessa impiegata per le misurazioni è ridotta al 10–15% del totale mediante un attenuatore, con l'obiettivo di evitare danni alla lente della fotocamera.

La fotocamera impiegata per l'acquisizione delle immagini è la *Imager Pro SX*, prodotta da *LaVision*.

La sorgente di luce pulsata e la fotocamera sono degli elementi sincronizzati e connessi al software che viene impiegato per la misurazione e per il calcolo del campo vettoriale di velocità. Tale software è *DaVis 8.4*, prodotto da *LaVision*. Tra gli step principali da compiere nell'utilizzo del software c'è la calibrazione, effettuata grazie a un piatto di calibrazione posto all'interno del vessel: i puntini vengono rilevati dal software attraverso la fotocamera e, inserendo le caratteristiche geometriche del piatto, viene determinato un piano di riferimento che servirà successivamente per l'acquisizione e per l'elaborazione dei dati. Per ogni esperimento dell'indagine vengono catturate 300 immagini double frame, come effettuato nel lavoro di Liu et al. (2008). Prima dell'elaborazione dei dati (processing) risulta conveniente eliminare alcune regioni dell'area fotografata: il piano di luce pulsata, passando per il centro del vessel dove è situato l'agitatore, non illumina le particelle dell'intera sezione trasversale e quindi le zone non illuminate vanno eliminate per i calcoli. La correlazione incrociata può essere fatta a single-pass, come illustrato nella **Fig. 3-1 (B)**, o a multi-pass. Con quest'ultimo metodo le immagini vengono divise in IW e i calcoli vengono effettuati per la prima IW di entrambi i frame delle immagini nel primo passo; il calcolo successivo viene

fatto nel secondo passo con una nuova IW, che non corrisponde spazialmente alla prima IW, ma ha le sue dimensioni. I risultati del primo calcolo determinano lo shift del passo, in termini di numero di pixel. Il calcolo continua fino a quando tutti i passi dell'area interessata sono calcolati. In questo modo è possibile produrre risultati più accurati e con risoluzione più alta. Per questo lavoro sperimentale si è scelto di utilizzare la correlazione incrociata con passo decrescente: i calcoli vengono ripetuti per tre volte con passi di 48×48 pixel e altre tre volte 24×24 pixel.

Metodo Sperimentale: i Diversi Approcci

I data points da indagare con la tecnica di analisi vengono dapprima organizzati in una matrice. Gli esperimenti vengono svolti con tre fluidi diversi e nove agitatori e conseguentemente le diverse combinazioni producono un alto numero di data points. Inoltre, una ragionevole interpretazione dei risultati richiede di operare con dei parametri fissi, in modo da poter successivamente formulare delle conclusioni sull'influenza del fluido o della geometria dell'agitatore. Tali parametri scelti mostrano tutti una dipendenza diretta dalla frequenza rotazionale N dell'agitatore e sono legati a questa da semplici relazioni matematiche: la tip speed u_{tip} , il numero di Reynolds Re e la potenza immessa PV^{-1} , rispettivamente definiti in **Eq. 2.50**, **2.51**, **2.52**. Le proprietà reologiche del fluido influenzano entrambi Re e PV^{-1} mentre non riguardano la u_{tip} , la quale dipende unicamente dal diametro dell'agitatore e, come anche per gli altri due parametri, da N . Per il calcolo di PV^{-1} si sono innanzitutto determinati sperimentalmente con un reometro i valori del numero di Newton Ne , definito in **Eq. 2-53**, per ogni agitatore. Tali valori sono riportati in **Tab. 3-5**.

I data points scelti e indagati per ogni agitatore riguardano circa 15 valori tra u_{tip} , Re e PV^{-1} per i diversi fluidi, come mostrato in **Tab. 3-2**, **Tab. 3-3** e **Tab. 3-4**. Essendo il numero di Reynolds dipendente dalla viscosità, i data points relativi a questo numero non sono stati indagati per lo xantano.

I diversi approcci al metodo sperimentale rappresentano l'esecuzione del primo obiettivo, ovvero riuscire a determinare le condizioni operative ottimali che consentono una tecnica di misurazione in grado di fornire dei risultati attendibili.

Il primo approccio consiste nell'uso di una sola fotocamera posta frontalmente rispetto al vessel e quindi produce dei risultati bidimensionali. Con questo approccio si sono riscontrati dei problemi causati dalla riflessione della luce sul fondo torosferico, con la conseguente necessità di coprire tale area e perdere quindi le relative informazioni.

Col secondo approccio si vuole risolvere i problemi trovati al primo step e lo si fa ponendo la fotocamera in modo inclinato, così da poter vedere il fondo del vessel e al contempo evitare la riflessione della luce.

Il terzo e ultimo approccio prevede l'attuazione della PIV tridimensionale e lo si fa con due fotocamere poste lateralmente e inclinate come nello step precedente.

Per semplicità i tre approcci vengono nominati rispettivamente 2DF, 2DA, 3DA e la disposizione dei diversi elementi vengono mostrati in **Fig. 3-11**, **Fig. 3-13** e **Fig. 3-14**.

Risultati

Una volta che il campo vettoriale di velocità viene calcolato da *Davis* 8.4, il software può calcolare le quantità di interesse che derivano dalla velocità e che sono ottenute dalla definizione del gradiente di velocità E_{ij} , come in **Eq. 2-18**.

Con la PIV planare si hanno le informazioni di velocità per due coordinate x e y ; con la stereo-PIV invece, utilizzando due fotocamere, il software è in grado di calcolare le componenti di velocità x , y e z relative al piano di interesse illuminato. Essendo la sezione trasversale un dominio bidimensionale, non è possibile calcolare i gradienti di velocità rispetto alla terza coordinata z . Pertanto, la matrice del gradiente di velocità \underline{V} ha la prima sottomatrice 2×2 disponibile per PIV in 2D e in 3D; gli elementi E_{zx} e E_{zy} sono disponibili solo per la PIV in 3D e la terza colonna risulta nulla per le analisi condotte con un solo piano z illuminato, come mostrato in **Eq. 2-28**.

Dal software è possibile esportare i calcoli ottenuti e plottarli con l'ausilio di MATLAB®. Dal campo vettoriale di velocità è possibile calcolare l'energia cinetica turbolenta (TKE) partendo dal calcolo della velocità turbolenta contenuta nella velocità istantanea, come definito nelle **Eq. 2-37** e **2-38**.

Per la presentazione dei risultati, si sono selezionati i data points riassunti in **Tab. 3-7**, **Tab. 3-8** e **Tab. 3-9**: per ogni data point vengono calcolate le condizioni operative calcolate e relative alla frequenza rotazionale N utilizzata nei diversi data points.

Obiettivo 1 – Avvio della tecnica di misurazione per il serbatoio agitato

In primo luogo, i campi di flusso ottenuti con le stesse condizioni operative ma con i tre approcci 2DF, 2DA e 3DA vengono messi a confronto. I campi di flusso illustrati in **Fig. 4-1**, relativi alle misurazioni effettuate per il propeller con l'anello esterno (PROPRing- $h/d=0.33$) sono relativi alla metà della sezione trasversale illuminata, ipotizzando una simmetria dei risultati rispetto all'albero dell'agitatore. Con il primo approccio 2DF, il campo di flusso è privo della parte del fondo del vessel, per i motivi espliciti precedentemente. Posizionando la camera in modo inclinato per investigare il fondo (2DA e 3DA) si nota una buona coerenza con il primo approccio: l'area relativa ai valori di alta velocità risulta qualitativamente la stessa. Pertanto, si conclude che l'angolo di osservazione utilizzato non influenza la qualità dei risultati. Inoltre, dalla rappresentazione del campo di flusso si può vedere come l'area di alta velocità per 2DF è a tratti e non continua come negli approcci dall'alto: ciò dipende dalla finitura e dallo spessore non uniforme del vetro del vessel nella parte inferiore.

Il confronto tra i tre approcci prosegue in termini di profili di velocità in sette linee all'interno del vessel, tre verticali e quattro orizzontali, con l'intento di indagare le zone di maggiore interesse nel vessel e capire il comportamento dell'agitatore nel fluido. L'effetto della conformazione del vessel sulla velocità è di facile visualizzazione se si considerano i profili di velocità lungo le linee verticali, come mostrato in **Fig. 4-4**: nei tratti in cui i profili relativi a 2DA e 3DA risultano omogenei e continui, quelli relativi al primo approccio è invece a tratti. Facendo un confronto tra i risultati bidimensionali e quelli tridimensionale, è possibile constatare che 3DA produce dei valori tendenzialmente superiori a 2DA.

Il risultato precedente viene confermato dal campo vettoriale di velocità, normalizzata con la u_{tip} , che viene rappresentato come funzione di distribuzione cumulativa (CDF) in **Fig. 4-6 (A)**. La curva è il risultato del campo vettoriale di velocità medio, calcolato facendo la media dei campi vettoriali ottenuti da tutte le immagini double-frame. Da questo confronto è possibile vedere che il 2DF produce i valori più bassi, a causa della rimozione della parte bassa del vessel, dove tendenzialmente si hanno delle velocità intermedie. Il 2DA può rilevare l'intera area di interesse, tuttavia i risultati risultano inferiori al 3DA, poiché con una sola fotocamera non si è in grado di vedere le componenti tangenziali della velocità, cioè quelle che passano attraverso la sezione trasversale.

Per quando riguarda la CDF dell'energia cinetica turbolenta, dato che questa viene calcolata a partire dalla velocità, il trend risulta analogo, **Fig. 4-6 (B)**. Inoltre, si può notare che intorno all'80% della CDF si ha una diminuzione della derivata, il che significa che il gradiente dell'ampiezza delle barre dell'istogramma equivalente decresce. Questo fatto può essere spiegato con l'ausilio della rappresentazione della TKE con le isolinee in **Fig. 4-7**: nel caso di stereo-PIV, il baffle non coincide più spazialmente con l'albero dell'agitatore, ma viene visto dalle due fotocamere e conseguentemente risulta necessario l'inserimento di una maschera geometrica. Mentre per il calcolo del campo vettoriale di velocità *DaVis* riesce a fare un'interpolazione in questa regione, per la determinazione della TKE si rivela conveniente eliminare quest'area prima del calcolo, a causa degli errori che qui si verificano. Pertanto, si ipotizza che i punti dove la TKE è intorno a $0,015-0,3 \text{ m}^2 \text{ s}^{-2}$ siano quelli nascosti dalla parte inferiore del baffle.

Infine, viene fatto un confronto in termini di CDF della velocità normalizzata e della TKE per i tre approcci usati con quattro agitatori e ciò che è stato detto finora viene confermato.

In conclusione, si può affermare che i risultati ottenuti con la 2DA sono validi e veritieri. Con 3DA, grazie all'uso di una seconda fotocamera, i risultati sono comunque più accurati mediante il calcolo della terza componente di velocità, grazie alla distorsione prospettica del vettore di spostamento che viene osservato da due direzioni diverse (Raffel et al., 2007). Tuttavia, dato il maggiore spazio di memoria richiesto dall'approccio tridimensionale, il quale prevede l'acquisizione del doppio delle immagini double-frame, il resto dell'investigazione viene fatto con 2DA. In questo modo si eliminano anche i tempi decisamente più lunghi necessari al salvataggio delle immagini, tempi che allungano la durata complessiva di una singola misurazione. Per queste ragioni, il resto dell'indagine sistematica viene condotta con l'approccio 2DA. Di seguito sono presentati i risultati degli altri obiettivi: i risultati in 3D vengono scelti qualora questi siano disponibili e coerenti con l'interpretazione da effettuare.

Obiettivo 2 – Indagine sistematica

Influenza della Potenza Immessa sulla Fluidodinamica del Serbatoio Agitato

Per lo studio dell'influenza della potenza immessa sulla fluidodinamica sviluppata nel serbatoio agitato vengono scelti cinque data points relativi al propeller con l'anello esterno; il fluido usato è l'acqua e gli esperimenti sono relativi a 3DA. I campi di flusso sviluppati nel serbatoio in **Fig. 4-9** mostrano che, aumentando la potenza immessa, il flusso mantiene il suo

comportamento assiale, ma il vortice creato in prossimità dell'agitatore aumenta. Ciò significa che la circolazione è più ampia e che i tempi di miscelazione diminuiscono, quindi la miscelazione migliora all'aumentare della potenza immessa.

Le curve CDF della velocità normalizzata collassano su una curva unica: il rapporto della velocità con la tip speed quindi mantiene un fattore di scala per i diversi valori di potenza immessa, mostrando così un'autosimilarità del sistema, **Fig. 4-10 (A)**.

Aumentando la potenza immessa, le velocità sviluppate nel fluido sono maggiori e la turbolenza aumenta. Questo si dimostra visualizzando le curve TKE in **Fig. 4-10 (B)**, le quali sono traslate sull'asse x .

La velocità locale di dissipazione dell'energia cinetica (local EDR), **Eq. (2-41)**, è una quantità difficoltosa da calcolare, soprattutto nella zona dell'agitatore, dove i valori sono più alti. Solitamente questa viene determinata ipotizzando l'isotropia, che tuttavia è lontana dal descrivere un reale serbatoio agitato. Inoltre, il calcolo della EDR locale dai gradienti di velocità ottenuti con la PIV dipende profondamente dalla risoluzione spaziale dell'analisi (Delafosse et al., 2011). Questa dovrebbe essere inferiore o uguale alla microscala di Kolmogorov, dove la dissipazione di energia cinetica turbolenta avviene con gli eddies più piccoli. La dimensione finita della griglia usata nella tecnica per calcolare i gradienti di velocità è spesso maggiore della scala degli eddies più piccoli, generando così una distribuzione irrealistica della EDR nello spazio del vessel. Facendo un semplice calcolo della EDR media $\overline{\varepsilon_T}$ della microscala di Kolmogorov η , rispettivamente tramite **Eq. (2-48)** ed **Eq. (2-47)**, è possibile vedere che un aumento della potenza immessa produce una turbolenza maggiore nel fluido, nel quale la TKE è dissipata a velocità maggiori da eddies di scala inferiore, **Tab. 4-4**. Considerando l'intervallo di potenza immessa $19\text{--}488\text{ W m}^{-3}$, la microscala di Kolmogorov relativa si definisce nell'intervallo $85\text{--}38\text{ }\mu\text{m}$. Quest'ultimo intervallo è coerente con i valori tipici della microscala di Kolmogorov di un bioreattore agitato si aggirano intorno ai $50\text{--}200\text{ }\mu\text{m}$ (Delafosse et al., 2011). È possibile affermare quindi che, dato che la dimensione della IW più piccola è di $1,4\text{ mm} = 1,4 \times 10^3\text{ }\mu\text{m}$, la risoluzione spaziale dell'analisi PIV non è in grado di rilevare gli eddies turbolenti più piccoli.

Un altro interessante risultato ottenuto con la PIV è rappresentato dai gradienti delle forze che agiscono sulle particelle. Il gradiente di taglio e il gradiente normale vengono calcolati a partire dalla velocità con le formule fornite da Wollny (2010), riportate in **Eq. (2-33)** e **(2-34)**. La regione di alto shear rate, intorno a 150 s^{-1} , si trova sotto l'agitatore, ovvero dove il fluido presenta un alto gradiente di velocità in uno spazio infinitesimo, **Fig. 4-11 (A)**. I gradienti normali e di taglio rappresentati con le CDF in **Fig. 4-12**, dimostrano che con una potenza immessa maggiore, la turbolenza è maggiore e il fluido esercita uno sforzo maggiore. Il gradiente di taglio risulta maggiore di quello normale, per cui i valori massimi di gradiente normale non eccedono 10^2 s^{-1} .

Influenza della Reologia sulla Fluidodinamica del Serbatoio Agitato

Nella presentazione di questi risultati si sceglie di proseguire con il propeller con l'anello esterno. Considerando l'influenza della reologia, tutti e tre i fluidi vengono investigati con l'approccio 2DA a un valore di potenza immessa pari a 100 W m^{-3} .

Il campo di flusso sviluppato nell'acqua ha una caratteristica più assiale rispetto alla glicerina e allo xantano, dove è presente anche una natura radiale, **Fig. 4-13**. Per l'acqua $Re = 35849$ e per la glicerina 3136 . Avendo lo xantano una viscosità non costante, si calcola,

tramite il modello di Ostwald-de Waele e tramite i valori sperimentali presi dalla rappresentazione dello shear gradient, i valori massimo e minimo di viscosità, a cui corrispondono i valori massimo e minimo di Re , rispettivamente 5624 e 1276: la regione dell'agitatore è caratterizzata da un Re che è 4 volte quello nel resto del vessel. Il flusso sviluppato nella glicerina e nello xantan è nello stato di transizione, mentre nell'acqua il regime è completamente turbolento, il quale causa un flusso più assiale.

Le curve CDF della velocità normalizzata in **Fig. 4-15 (A)** mostrano dei valori maggiori per l'acqua, mentre tra la glicerina e lo xantano non si notano delle differenze significative. Nell'acqua le velocità sono più alte perché, a parità di potenza immessa, la frequenza rotazionale dell'agitatore è più alta rispetto agli altri due fluidi. Questo perché la viscosità più bassa dell'acqua permette alle forze inerziali di prevalere su quelle viscosive a una potenza immessa inferiore.

Per quanto riguarda la TKE, l'agitatore genera valori più alti quando mette in movimento un fluido meno viscoso, come illustrato in **Fig. 4-15 (B)**. Le CDF della TKE sono distinte e quelle relative alla glicerina e allo xantano qui non si confondono come nel caso precedente della velocità normalizzata. Ciò suggerisce che anche se la distribuzione delle velocità normalizzate risulta simile per questi due fluidi, le velocità fluttuanti non lo sono. La curva dello xantano si colloca tra i valori più bassi a causa della sua alta viscosità che contrasta la turbolenza.

In ultimo, le CDF dei gradienti di taglio e normale in **Fig. 4-16** non mettono in risalto nessuna differenza consistente. Calcolando le EDR medie locali, anche queste risultano simili per i tre fluidi.

Influenza della *Geometria dell'Agitatore* sulla Fluidodinamica del Serbatoio Agitato

In quest'ultima fase del secondo obiettivo, tutti i nove agitatori vengono messi a confronto, per ognuno dei tre fluidi, considerando l'approccio 2DA e una potenza immessa pari a 100 W m^{-3} . Per ragioni di sintesi, in questo elaborato riassuntivo vengono riportati soltanto i risultati relativi all'acqua.

Il primo set di agitatori analizzato riguarda i due propeller, di cui vengono rappresentati i campi di flusso in **Fig. 4-17**. Il normale propeller (PROP- $h/d=0.33$) pompa il fluido verso il basso e sviluppa un flusso perfettamente assiale, caratterizzato da un unico anello di circolazione. L'aggiunta dell'anello esterno nel PROPRing- $h/d=0.33$ riduce il comportamento assiale, pompando il fluido più diagonalmente e producendo due anelli di circolazione. I numeri di Newton del normale propeller e del propeller con l'anello sono rispettivamente 0,33 e 0,39 e questi due agitatori, per immettere una potenza pari a 100 W m^{-3} ruotano con una frequenza pari rispettivamente a 780 e 706 rpm. La differenza tra le CDF della velocità normalizzata è trascurabile, mentre è più significativa per la TKE, **Fig. 4-20**. Quello che cambia quindi sono sostanzialmente le velocità fluttuanti, che producono dei valori più alti di energia cinetica turbolenta nel caso del normale propeller.

Si passa quindi alle turbine pitched blade, con angoli di inclinazione pari a $22,5^\circ$, 45° e 90° . Il primo risultato facilmente osservabile dai campi di flusso in **Fig. 4-18** è la riduzione del comportamento assiale con l'aumento dell'angolo delle pale: la regione di alta velocità si muove verso l'alto e la dimensione del vortice in prossimità dell'agitatore decresce. È possibile definire una dipendenza tra il numero di Newton Ne e l'angolo di inclinazione delle pale: uno studio condotto da C. Y. Ge et al. (2014) sul campo di flusso generato dalle turbine

pitched blade, mediante simulazioni CFD e misurazioni PIV, sostiene che un aumento dell'angolo di inclinazione delle pale corrisponde a un aumento di Ne . Ciò viene confermato dai risultati di questo lavoro, per il quale i valori di Ne valutati sperimentalmente per PBT-6x22.5°, PBT-6x45° e PBT-6x90° sono rispettivamente 0,55, 1,79 e 4,00; questa tendenza viene ottenuta anche per il caso della glicerina e i valori sono riportati in **Tab. 4-7**. Le curve CDF della velocità normalizzata in **Fig. 4-21** (A) si sovrappongono per PBT-6x45° e PBT-6x90°, mentre per PBT-6x22.5° i valori sono nettamente inferiori. Riguardo la TKE in **Fig. 4-21** (B), il trend non è univoco: bassi valori di TKE sono più presenti per PBT-6x90° e meno per PBT-6x45°. Alti valori di TKE, sebbene molto pochi, sono presenti per PBT-6x90°. In generale PBT-6x45° presenta i valori più alti tra le tre turbine analizzate. Con il supporto del campo della TKE in **Fig. 4-22**, la comprensione dei commenti appena fatti viene facilitata. Infatti per PBT-6x90° c'è una piccola zona sotto l'agitatore in cui i valori raggiungono $0,4 \text{ m}^2 \text{ s}^{-2}$, circa 4 volte maggiori dei valori massimi raggiunti per le altre due turbine.

Il terzo e ultimo set di agitatori riguarda il bionic-loop (BiLoop) e i tre agitatori a nastro di Möbius (WRI- $d/D=0.4-41.4^\circ$, WRI- $d/D=0.4-28.8^\circ$, WRI- $d/D=0.33-51.2^\circ$). I campi di flusso in **Fig. 4-19** mostrano un comportamento particolare per BiLoop, il quale pompa il fluido verso l'alto, generando un vortice al lato e un altro nella parte alta del vessel. Tra gli agitatori WRI, i due che producono un flusso assiale sono WRI- $d/D=0.4-41.4^\circ$ e WRI- $d/D=0.33-51.2^\circ$, mentre WRI- $d/D=0.4-28.8^\circ$ ha chiaramente una natura più radiale. Gli agitatori con $d/D=0.4$ mostrano un aumento del carattere assiale con l'aumento dell'angolo, che corrisponde con l'aumento di h/D . Il carattere assiale risulta maggiore per WRI- $d/D=0.33-51.2^\circ$ e a seguire WRI- $d/D=0.4-41.4^\circ$ e WRI- $d/D=0.4-28.8^\circ$. Come per le turbine, viene riscontrato che un aumento dell'angolo corrisponde a un aumento di Ne , che è sempre inferiore a 1 per questa tipologia, sia per l'acqua che per la glicerina, come riassunto in **Tab. 4-8**. BiLoop genera valori più alti di velocità e di TKE, come mostrato in **Fig. 4-23**; la TKE cresce molto velocemente, a causa dei due grandi vortici nella prima metà del vessel. Un aumento del carattere assiale degli agitatori WRI corrisponde a un aumento dei valori di velocità e di TKE.

In generale, vedendo le curve dei nove agitatori nello stesso grafico in **Fig. 4-23**, BiLoop genera i valori più alti di TKE, insieme al normale propeller e alla turbina PBT-6x45°. I valori più bassi sono generati dai WRI, mentre il propeller con l'anello e le altre due turbine si collocano a metà.

Obiettivo 3 – Interpretazione dello stress idromeccanico nel serbatoio agitato

Avvio della tecnica di misurazione per il serbatoio agitato

Nei processi chimici che fanno uso di serbatoi agitati con sospensione di particelle, come solidi, cellule o agglomerati di cellule, l'agitazione meccanica assume un ruolo importante nello stress particellare, soprattutto quando si opera in regime turbolento. L'energia fornita alle pale dell'agitatore produce la generazione di eddies grandi, i quali si trasformano progressivamente in eddies più piccoli trasferendo l'energia cinetica turbolenta, fino a quando le forze viscosive diventano dominanti e l'energia rimanente viene dissipata sotto forma di calore. Le velocità fluttuanti del fluido generano uno stress meccanico sul materiale sospeso.

La velocità di dissipazione dell'energia è un parametro cruciale per il micromixing, poiché determina la dimensione finale degli eddies più piccoli, che coincide con la microscala

di Kolmogorov. Come discusso nella **Sezione 2.5**, la relazione tra la dimensione degli eddies e delle particelle è determinante per lo stress particellare, in particolar modo per gli sforzi di taglio.

In un flusso turbolento le proprietà sono locali, come la EDR, di cui il calcolo o la diretta misurazione risulta però difficoltosa e complessa. Tuttavia, è possibile utilizzare altri parametri per studiare e correlare lo stress sulle particelle. Tra questi c'è l'EDR media $\bar{\epsilon}$, che può essere calcolata con l'**Eq. (2-48)**, e l'EDR massima ϵ_{\max} , che può essere stimata considerando la maggior parte della dissipazione che avviene nella regione dell'agitatore. Questo approccio viene usato da Bliatsiou (2018b) per studiare l'effetto della geometria dell'agitatore sullo stress particellare.

Lo studio di Bliatsiou mira anche a trovare delle nuove geometrie valide che possono produrre dei valori minori di sforzo di taglio. Gli esperimenti vengono condotti con gli stessi agitatori utilizzati in questo lavoro e consistono nella misurazione tramite endoscopia della dimensione delle particelle di olio silconico disperse in acqua allo stato stazionario, con i diversi agitatori. In generale, un grande sforzo di taglio (shear stress) causa la rottura delle particelle, determinando particelle di dimensioni minori. Lo studio di Bliatsiou viene qui usato per fare un confronto e una validazione dei risultati ottenuti in questo lavoro sperimentale, in particolare vengono presi in esame gli esperimenti condotti in acqua. L'approccio scelto da Bliatsiou utilizza il diametro medio di Sauter, ovvero il diametro che corrisponde alla particella con lo stesso rapporto volume/area superficiale di quello dell'intero insieme.

Partendo dalle turbine, le curve CDF del gradiente di shear riportate in **Fig. 4-33** mostrano che PBT-6x22.5° produce i valori più alti, seguita da PBT-6x45° e poi da PBT-6x90°. I risultati di Bliatsiou mostrano che a parità di potenza immessa, e quindi di $\bar{\epsilon}$, PBT-6x22.5° produce le particelle più piccole, il che significa che lo stress generato da questa turbina è il più alto; seguono PBT-6x45° e poi PBT-6x90°. Il confronto tra la distribuzione di gradienti normali e di taglio suggerisce che quest'ultimo sia il responsabile principale della rottura delle particelle. In conclusione, un aumento dell'angolo corrisponde a un aumento di Ne e il flusso diventa più radiale; l'agitatore con maggior carattere assiale genera più stress sulle particelle.

Il normale propeller produce uno shear maggiore rispetto al propeller con l'anello esterno e al BiLoop, come mostrato in **Fig. 4-34**: questo risultato è coerente con quanto ottenuto da Bliatsiou. In questa seconda fase però, il confronto non trova pieno successo. Considerando i WRI, questi producono le particelle col più basso diametro di Sauter, ovvero producono lo shear più alto. L'angolo dell'onda sembra essere il parametro che influenza maggiormente l'intensità dello stress: un angolo minore genera particelle di dimensione minore. Ciò non viene riscontrato prendendo in considerazione la distribuzione dei gradienti di taglio, i quali al contrario risultano i più bassi. La ragione che spiega questo fatto non è del tutto chiara: lo stress particellare potrebbe essere dovuto ai valori molto alti di shear che sono localizzati sulla superficie dei WRI. In generale, nella regione delle pale le particelle risentono di valori più alti di shear, perché quando la particella è attaccata all'agitatore la sua velocità relativa rispetto all'agitatore è nulla, ma quando si muove di una distanza infinitesima è soggetta alle velocità più alte, date dalla girante al fluido. Il motivo per cui i risultati sono incoerenti per i WRI quindi, potrebbe essere dovuto al fatto che la tecnica di analisi PIV non è

in grado di rilevare questi valori a causa della risoluzione spaziale e a causa della maschera geometrica che, applicata alla regione dell'agitatore, copre il suo perimetro e scarta i relativi valori dal calcolo. Per accertare queste assunzioni sarebbe bene eseguire delle simulazioni in CFD, strumento in grado di fornire delle informazioni più dettagliate in prossimità dell'onda.

Visti i risultati di Bliatsiou, gli agitatori WRI sono idonei ai processi che hanno a che fare con la dispersione. Uno studio di Moucha et al. (2003) conclude che gli agitatori con Ne maggiore di 1 assicurano un migliore trasporto di materia, mentre quelli con Ne minore di 1 producono intensità maggiori di dispersione; ciò viene confermato con quanto osservato. BiLoop, agitatore up-pumping, produce invece delle particelle di dimensioni maggiori e produce degli sforzi di taglio inferiori. Mandenius (2016) spiega che per ridurre i danni delle cellule mammarie dovuti allo shear, è conveniente usare agitatori up-pumping che producono basso shear, specialmente con delle pale ampie.

Lo stress particellare è un argomento di grande interesse nel mixing è la sua indagine può dare dei risultati validi che possono essere usati per compiere al meglio quei processi che fanno impiego di fasi sospese, come i processi biotecnologici. La scelta delle migliori condizioni operative e di un design appropriato delle apparecchiature, incluso l'agitatore, è determinante per una buona riuscita del processo. In biotecnologia, l'uso di vari microrganismi, cellule ed enzimi creano delle difficoltà per la definizione di regole generali del sistema. La natura delle particelle o degli aggregati, le proprietà reologiche della sospensione, la presenza o meno di una fase gassosa sono parametri che influenzano profondamente il carattere del sistema complessivo. Il particle stress è pertanto un argomento molto ampio e complesso che richiede di essere ulteriormente investigato.

I risultati delle misurazioni PIV mostrano una buona coerenza con i risultati presenti nella letteratura scientifica e che sono stati finora pubblicati. Tuttavia, questo studio sperimentale è stato condotto con delle nuove tipologie di agitatori, pertanto la quantità di materiale con cui fare un confronto è scarsa. Questo rappresenta un'ulteriore motivazione per continuare lo studio di questi agitatori con delle simulazioni in CFD.

Infine, dal campo vettoriale di velocità calcolato con la tecnica PIV, è possibile valutare altre quantità, quali la somma dei gradienti assoluti e la vorticità, come rappresentato in **Fig. 4-35** e **Fig. 4-36**. L'intensità della vorticità indica la direzione rotazionale: una vorticità positiva corrisponde a una rotazione antioraria e viceversa. Questa rappresentazione fornisce un'idea delle zone critiche all'interno del vessel, localizzate nella parte inferiore, dove la vorticità causa un cambio del flusso. Il fluido pertanto esercita degli alti valori di shear in queste zone.

Conclusioni e Outlook

Conclusioni

Obiettivo 1 – Avvio della tecnica di misurazione per il serbatoio agitato

Nonostante lo spazio di memoria e i tempi di salvataggio delle immagini che allungano la durata complessiva della misurazione, l'approccio in 3D è in grado di fornire risultati più dettagliati riguardo il campo vettoriale di velocità. L'approccio 2D fornisce comunque dei risultati validi.

Obiettivo 2 – Indagine sistematica

- *Potenza immessa.* Si riscontra un'auto-similarità del sistema.
- *Reologia.* Diversi regimi di flusso allo stesso valore di potenza immessa.
- *Geometria dell'agitatore.* È possibile fare una caratterizzazione del flusso e dai campi di flusso si possono calcolare i Flow number, definiti nella **Sezione 2**.

Obiettivo 3 – Interpretazione dello stress idromeccanico nel serbatoio agitato

Avvio della tecnica di misurazione per il serbatoio agitato
L'interpretazione dello stress meccanico risulta nel complesso difficoltosa con il solo utilizzo delle curve di distribuzione dei gradienti normali e di taglio, sebbene per alcuni agitatori si sono ritrovati dei riscontri positivi nel confronto fatto con altri risultati sperimentali.

Le *limitazioni* dovute alla tecnica PIV sono principalmente due:

- L'accesso alla zona dell'agitatore, a causa delle maschere geometriche che sono indispensabili da applicare, risulta problematico
- La risoluzione spaziale dell'analisi non consente di rilevare gli eddies turbolenti più piccoli, poiché le IW sono di dimensione maggiore degli eddies.

Outlook

Miglioramento della tecnica di misurazione

La particle image velocimetry consente di ottenere il campo vettoriale di velocità, da cui si possono ricavare, specialmente tramite i gradienti di velocità, altre quantità e rappresentazioni della dinamica del fluido. I gradienti di velocità situati lungo la diagonale del tensore rappresentano i termini di divergenza. Quando la derivata di v_x rispetto a x è positiva, significa che il fluido si "allunga" lungo la direzione x , altrimenti si "comprime" e in questo secondo caso il termine si chiama convergenza. In realtà l'utilizzo di questi termini è improprio, dato che il fluido di studio è incomprimibile. I gradienti di velocità sono considerati come accelerazione e decelerazione del fluido lungo le due direzioni. Un diagramma a colori bidimensionale aiuta la visualizzazione di queste due componenti, come in **Fig. 5-1**.

La stereo-PIV consente di ricostruire il vettore di velocità con le tre componenti, grazie all'uso delle due fotocamere. La componente v_z può essere rappresentata con il surface plot, il quale mostra l'intensità di questa componente attraverso il piano illuminato, come rappresentato in **Fig. 5-2**. Tuttavia, la terza colonna della matrice del gradiente di velocità

risulta impossibile da calcolare, poiché il vettore velocità viene valutato soltanto in un piano, quindi non si può fare la derivata rispetto alla coordinata z .

La PIV multiplanare è una estensione della stereo-PIV: l'aggiunta di un piano illuminato parallelo al primo permette di calcolare l'intera matrice del gradiente di velocità. Il sistema di funzionamento viene illustrato in **Fig. 5-3**.

Uno step successivo viene fatto dalla PIV tomografica (tomo-PIV), che consiste nell'illuminare con una sorgente laser una parte di volume del fluido. L'uso di diverse fotocamere in diverse posizioni permette di ottenere diverse "volume images" che vengono elaborate con una correlazione tridimensionale usando degli elementi volumici, chiamati voxel, **Fig. 5-4**. Questa tecnica permette quindi di catturare campi di flusso tridimensionali localizzati nelle strutture turbolente complesse, come ad esempio nella regione dell'agitatore.

Confronto con CFD

Le limitazioni espresse precedentemente possono essere superate con l'ausilio di CFD. Questo strumento è ampiamente utilizzato per predire i campi di flusso nei serbatoi agitati e la sua applicazione consente di determinare la distribuzione del campo vettoriale medio di velocità, della TKE e della EDR, come in **Fig. 5-5**. La validazione sperimentale delle simulazioni in CFD fanno spesso uso della PIV (Sheng et al., 1988).

Prospettive future

L'uso di attrezzatura metallica all'interno del vessel, come l'agitatore, l'albero e i baffles, introduce l'esclusione dall'analisi di una parte fondamentale del piano illuminato, ovvero la regione dell'agitatore. Una proposta per trattare questo problema può essere l'uso di attrezzatura realizzata in PMMA (Plexiglas®). Questo materiale trasparente consente la visualizzazione delle particelle situate tra le pale dell'agitatore. In **Fig. 5-6** viene rappresentato il setup sperimentale con i baffles e una turbina Rushton realizzata in PMMA.

Infine, un possibile metodo per poter valutare lo stress sulle particelle con la PIV potrebbe essere quello di usare delle particelle contenenti un inchiostro. La misurazione, che deve essere effettuata in condizioni di sicurezza aggiuntive, avviene aumentando la frequenza rotazionale e si valuta a quale valore si rompono le particelle. Il problema di questo metodo è la scelta adeguata dell'uso di colorante, il quale deve essere visibile dal laser ma non deve riflettere troppo la luce, in quanto potrebbe compromettere l'integrità dell'obiettivo della fotocamera.

Influence of Impeller Type and Geometry on Particle Stress in a Stirred Fermenter by Means of Particle Image Velocimetry

MASTER THESIS

Giulia Moretti

Student Number: 398932

Date: 25.09.2018



TECHNISCHE UNIVERSITÄT BERLIN
FACULTY III PROCESS SCIENCES
CHAIR OF CHEMICAL & PROCESS ENGINEERING

SCIENTIFIC ADMINISTRATION:
PROF. DR.-ING. MATTHIAS KRAUME

SCIENTIFIC SUPERVISION:
DIPL.-ING. CHRYSOULA BLIATSIU



Abstract

In many chemical and biotechnological processes, mixing represents one of the fundamental unit operations and it is often performed in stirred vessels. The efficiency of mixing is an important parameter for the processes where this operation is involved and this depends on the design and on the operative conditions that are employed in the process. The investigation on the flow is a tool to approach and understand the fluid mechanisms that occur in the stirred vessel and to make the characterization of the flow properties that can be measured with various analysis techniques. Especially in biotechnologies, where microorganisms are used for the development of the processes, the hydromechanical phenomena generated by the mechanical mixing can severely affect the process productivity, hence there comes the necessity of investigation to comprehend the influence of various elements, such as the geometry of the impeller used for mixing.

In this wide context, this experimental work is centered on the investigation of the flow in a stirred vessel by means of a photographic analysis technique, the particle image velocimetry. The focus is particularly oriented on the stress phenomena exerted in the fluid.

The experimental setup consists of a stirred vessel, where a single phase is agitated. The chosen fluids, water, glycerin and xanthan solutions, are non-biological model fluids, purposely defined to facilitate the experimental investigation and supposed to simulate the rheological properties of a cultivation broth.

In the investigation, a preliminary establishment of the measuring technique makes possible the comparison of different approaches to the PIV analysis, employed for two-dimensional and three-dimensional measurements. The systematic investigation involves nine impellers of different geometries, including two propellers, two pitched blade turbines, a bionic loop impeller and three wave ribbon impellers. With PIV measurements, the shear gradient and the turbulent kinetic energy are calculated from the velocity gradients in order to observe and comprehend the influence of the impeller geometry on the dynamics of the flow.

Acknowledgements

For the realization of this master thesis, I would first like to thank my super work team at Verfahrenstechnik at TU Berlin. A big thanks to my tutor Chrysoula Bliatsiou, for having been always ready to spur me with the time management and to provide me with tons of scientific literature. A thanks from my heart to Robert Panckow, for having been a fundamental support in the organization and development of this work and especially for being a precious moral support. A special thanks to Bastian Krämer, for having been an excellent working partner and for having immensely helped me with the *MATLAB*[®] programming.

I would like to thank the sincere friends that I met in this university, for having comfortably lightened the stress of the everyday work with pleasant conversations in the students room. Thanks to Nikol, Olaya and Gheid.

I would like to thank my family, for always having supported me during my academic journey that brought me away from home for five years, and especially with the decision of spending six months abroad with an ERASMUS program, with which the achievement of this work was possible. Thanks to “mamma”, “babbo” and Silvia for being my certainty.

Moreover, I would like to thank my Professors at Politecnico di Torino, for having helped me to create a solid background that resulted fundamental for the development of this work. A sincere thanks to the university of TU Berlin that, in accepting the collaboration with my home university, allowed me to have a wonderful experience, for my personal growth and for my studies.

Eidesstattliche Erklärung

Hiermit versichere ich, dass ich die vorliegende Arbeit selbstständig verfasst und keine anderen als die angegebenen Quellen und Hilfsmittel benutzt habe. Alle Ausführungen, die anderen veröffentlichten oder nicht veröffentlichten Schriften wörtlich oder sinngemäß entnommen wurden, habe ich kenntlich gemacht.

Die Arbeit hat in gleicher oder ähnlicher Fassung noch keiner anderen Prüfungsbehörde vorgelegen.

Ort, Datum

Unterschrift



Aufgabe für die Masterarbeit

von

Frau Giulia Moretti,
Matr. Nr. 398932

Aufgabe: **Influence of Impeller Type and Geometry on Particle Stress in a Stirred Fermenter by Means of Particle Image Velocimetry**

Erläuterung: Für zahlreiche verfahrenstechnische Prozesse, wie die Kultivierung schერempfindlicher Mikroorganismen, sind die Partikelbeanspruchungen durch das unter hohem Energieeintrag umgewälzte Kultiviermedium von hoher Bedeutung. Da die in gerührten Bioreaktoren auftretenden fluidmechanischen Beanspruchungen nicht direkt bestimmt werden können, lassen sich die Auswirkungen stattdessen durch geeignete Modellstoffsyste m e beobachten.

Im Rahmen dieser Arbeit sollen einphasige Modellsyste m e, welche die repräsentativen Phasen einer Kultivierung abbilden können, als nicht-biologische Testsysteme eingesetzt werden. Neun Rührertypen werden im Rührkessel untersucht. Die durch die unterschiedlichen Rührorgane erzeugte Strömung wird mittels Particle Image Velocimetry vermessen und charakterisiert. Zunächst besteht die Aufgabe in der Etablierung der PIV Messtechnik für einen gerührten Reaktor. Sowohl Planar-PIV als auch Stereo-PIV sollen eingesetzt werden. Durch Variation des Leistungseintrags, der Rheologie des Fluids und den Einsatz unterschiedlicher Rührergeometrien soll eine Aussage bezüglich der Scherintensität getroffen werden.

Neben der experimentellen Arbeit sollen eine Literaturrecherche durchgeführt und die Versuchsergebnisse mit Literaturdaten verglichen und diskutiert werden.

Die Arbeit wird nach einer sicherheitstechnischen Unterweisung in das Arbeiten im Labor und unter Beachtung der sicherheitsrelevanten Vorschriften und Betriebsanweisungen am Fachgebiet Verfahrenstechnik durchgeführt.

Tag der Ausgabe: 01.04.2018

Tag der Abgabe: 25.09.2018

Wissenschaftliche Leitung: Prof. Dr.-Ing. Matthias Kraume
Wissenschaftliche Betreuung: Dipl.-Ing. Chrysoula Bliatsiou

Prof. Dr.-Ing. M. Kraume

Table of Contents

Definition of Task.....	vii
List of Figures.....	xi
List of Tables.....	xvii
Abbreviations	xix
Table of Symbols.....	xxi
Chapter 1 – Introduction	1
1.1 Objectives	1
1.2 Thesis Layout.....	3
Chapter 2 – Literature Review – Basical Fundamentals	5
2.1 Microorganisms and Biotechnology	5
2.1.1 Prokaryotic cells	7
2.1.2 Eukaryotic cells	7
2.1.3 Cultivation Systems.....	8
2.2 Fluid Rheology	11
2.3 Fluid Dynamics.....	14
2.4 Fluid Mixing	21
2.4.1 Mechanism of Mixing	22
2.4.2 Flow Patterns in Stirred Vessels.....	26
2.4.3 Impeller Types.....	28
2.4.4 Flow Field Investigations in Stirred Vessels	31
2.5 Stress on Microorganisms.....	32
2.5.1 Physical and Chemical Stress.....	32
2.5.2 Influence of Hydromechanical Stress on Microorganisms.....	33
Chapter 3 – Experimental Methods	37
3.1 Particle Image Velocimetry	37
3.1.1 Hardware	38
3.1.2 Software.....	40
3.2 Experimental Setup.....	42
3.3 Parameter Matrix	48
Chapter 4 – Results	55
4.1 Pre-experimental Establishment of Measuring Technique.....	55
4.2 Systematic Investigation	62
4.2.1 Influence of Power Input on the Fluid Dynamics in Stirred Vessel.....	62
4.2.2 Influence of Fluid Rheology on the Fluid Dynamics in Stirred Vessel	66
4.2.3 Influence of Impeller Geometry on the Fluid Dynamics in Stirred Vessel	70
4.2.4 Interpretation of the Particle Stress Induced by Various Impeller Geometry	79

Chapter 5 – Conclusions and Outlook	85
5.1 Improvement of Measuring with PIV	85
5.2 Comparison with CFD.....	87
5.3 Future Perspectives.....	88
References.....	89
Appendix.....	I
Appendix A.....	I
Appendix B	IV

List of Figures

Fig. 2-1	Classification of microorganisms.	5
Fig. 2-2	Percentage of biopharmaceuticals produced in different expression systems (Baeshen et al., 2014).	7
Fig. 2-3	Simple representations of cells with their most important functional elements: (A) prokaryotic cell, (B) eukaryotic cell (Bamforth, 2007).	7
Fig. 2-4	The streak-plate technique: (A) Petri dish with agar and a microbial culture. (B) Streaking patterns made with a wire loop showing the corresponding procedural steps (Brooks et al., 2013).	9
Fig. 2-5	Important types of bioreactors: (A) stirred tank reactor, (B) bubble column reactor, (C) airlift column with external loop and with internal loop.	10
Fig. 2-6	Flow curves of Newtonian and non-Newtonian fluids (Brown et al., 2004).	11
Fig. 2-7	Morphological change of <i>Cephalosporium acremonium</i> in a fermenter: (A) after two, (B) four and (C) six days (Lim et al., 2002).	13
Fig. 2-8	Laminar and turbulent flow shown with a dye trace.	15
Fig. 2-9	Timescale of the velocity profile formation of a fluid between two plates from rest until reaching the laminar, steady state (Bird et al., 2002).	16
Fig. 2-10	Stress acting in a fluid element: (A) normal and tangential component, (B) stress components of a fluid around a rotating coaxial cylinder (Paul et al., 2004), (C) cubic volume of fluid with its stress components.	17
Fig. 2-11	Reference frames referred to the flow stream used for the calculation of the velocity gradients: (A) stream lines not parallel to x coordinate, (B) stream lines parallel to \tilde{x} coordinate (Wollny, 2010).	19
Fig. 2-12	(A) Mean and turbulent velocities. (B) Instantaneous velocity and time-averaged velocity (ANSYS, 2009).	20
Fig. 2-13	Conventional mechanically stirred vessel (Hemrajani and Tattersson, 2004)	22
Fig. 2-14	Eddy length scale in Kolmogorov's theory. Subscripts: DI Dissipation-Inertial, EI Energy-Inertial.	23
Fig. 2-15	Sketch of the energy cascade showing large eddies being broken into smaller and smaller eddies (Sagaut, 2006).	24
Fig. 2-16	Measurement of circulation and mixing times (Nienow, 1997).	25
Fig. 2-17	Radial, axial and tangential components of velocity.	26
Fig. 2-18	(A) Secondary flows in a stirred vessel with radial impeller. (B) Secondary flows in a stirred vessel with axial impeller. (C) Vortex formation in a stirred vessel without baffles. (D) Stagnant area due to the presence of baffles.	27
Fig. 2-19	Important characteristic geometrical lengths: (A) vessel, (B) impeller (Bliatsiou et. al, 2018b).	27
Fig. 2-20	Impeller types and use according to the viscosity of the fluid to mix, (Doran, 2012).	29
Fig. 2-21	Characteristic curves of the power number as a function of Reynolds number, relative to different impeller geometries, (Kumaresan and Joshi, 2006).	30
Fig. 2-22	Impeller discharge flow: (A) radial flow impeller, (B) axial flow impeller, (Nienow, 1997).	30
Fig. 2-23	Maximum length of the circulation path characteristic of the impeller type: (A) radial flow impeller, (B) axial flow impeller, (Nere, 2003).	31

Fig. 2-24	Interaction of turbulent eddies with particles (cells on microcarriers): (A) eddies larger than the particles, (B) eddies and particles of the same size, (C) eddies smaller than particles. (Kuzmichew and Tsybulski, 2008).	34
Fig. 3-1	Working principle of PIV: (A) experimental setup with camera perpendicular to laser sheet, (B) cross-correlation to find velocity vectors in every interrogation window, (C) distribution of velocity vectors for all interrogation windows. (Scarano, 2013).	38
Fig. 3-2	Schematic representation of the working principle of a laser: (A) laser material in a mirror system supplied with pump energy, (B) emission of two photons in a laser, (Raffel et al., 2007).	39
Fig. 3-3	Laser source used in the experiments: (A) pump source and mirror arm, (B) focusing of the laser beam into a two-dimensional sheet.	39
Fig. 3-4	Image recording hardware: (A) <i>Imager Pro SX</i> with Nikon lens, (B) Scheimpflug adapter (KamepalQ, 2018).	40
Fig. 3-5	Calibration of the laser sheet for the software: (A) calibration plate, (B) creation of the grid after the calibration process.	41
Fig. 3-6	Vessel setup: (A) vessel placed in the aquarium with the stirring system, (B) four equally spaced baffles used in the experiments.	43
Fig. 3-7	Investigated impeller types: (A) PROP- $h/d=0.33$, (B) PROPRing- $h/d=0.33$, (C) PBT-6x22.5°, (D) PBT-6x45°, (E) PBT-6x90°, (F) BiLoop, (G) WRI- $d/D=0.33-51.2^\circ$, (H) WRI- $d/D=0.4-28.8^\circ$, (I) WRI- $d/D=0.4-41.4^\circ$, (Bliatsiou et al, 2018b).	44
Fig. 3-8	Experimental measurement of viscosity of water, glycerin solution and xanthan solution.	45
Fig. 3-9	Flow seeding particles: (A) PMMA particles covered with Rhodamine B by <i>LaVision</i> , (B) picture of the laser sheet with illuminated particles.	45
Fig. 3-10	Experimental determination of the concentration of the flow seeding particles: (A) pictures obtained with four different quantities, (B) interrogation windows of 24×24 pixels and 48×48 pixels, (Krämer, 2018).	46
Fig. 3-11	First approach of the measuring technique including one camera: (A) positioning of the equipment in the experimental setup, (B) schematic representation viewed from the top and the side.	46
Fig. 3-12	Calibration resulting with the frontal camera: the non-homogeneous glass thickness leads to distortions in the captured images.	47
Fig. 3-13	Second experimental approach with one camera that is directed at the vessel bottom: (A) angular direction of the camera, (B) schematic representation of the experimental setup viewed from the top and the side.	48
Fig. 3-14	Third experimental approach with two cameras directed at the vessel bottom: (A) angular direction of the cameras, (B) schematic representation of the experimental setup.	48
Fig. 3-15	Measurements done in the experimental investigation.	49
Fig. 3-16	Characteristic curves of power number as function of Reynolds number for the nine impellers investigated. Measurements carried out with silicone oil, glycerin solution and water.	51
Fig. 4-1	Flow field observed with PROPRing- $h/d=0.33$ with the three approaches: (A) 2DF, (B) 2DA, (C) 3DA.	56
Fig. 4-2	Lines laying in the examined plane, where velocity profiles are calculated: (A) vertical, (B) horizontal.	57

Fig. 4-3	Vertical profiles of normalized velocity magnitude, PROPRing- $h/d=0.33$: (A) position 1, (B) position 2, (C) position 3.....	58
Fig. 4-4	Vertical profiles of normalized velocity along y direction, PROPRing- $h/d=0.33$: (A) position 1, (B) position 2, (C) position 3.....	58
Fig. 4-5	Horizontal profiles of normalized velocity, PROPRing- $h/d=0.33$: (A) position 4, (B) position 5, (C) position 6, (D) position 7.....	59
Fig. 4-6	CDF of the average vector field and of the turbulence kinetic energy inside the vessel, for the three approaches, PROPRing- $h/d=0.33$: (A) normalized velocity, (B) TKE.	60
Fig. 4-7	TKE field with isolines for the three approaches, PROPRing- $h/d=0.33$: (A) 2DF, (B) 2DA, (C) 3DA.	61
Fig. 4-8	CDFs of velocity and TKE for PROP- $h/d=0.33$, PROPRing- $h/d=0.33$, WRI- $d/D=0.4-28.8^\circ$ and WRI- $d/D=0.33-51.2^\circ$, measured with 2DA and 3DA: (A) velocity, (B) TKE.	61
Fig. 4-9	Flow field observed with PROPRing- $h/d=0.33$ with increasing power input: (A) 19 W m^{-3} , (B) 98 W m^{-3} , (C) 488 W m^{-3}	63
Fig. 4-10	Influence of power input with PROPRing- $h/d=0.33$, measured in water with 3DA: (A) CDF of normalized velocity, (B) CDF of TKE.....	63
Fig. 4-11	Strain tensor calculated for PROPRing- $h/d=0.33$, $PV^{-1} = 98 \text{ W m}^{-3}$: (A) Shear and normal gradient fields, (B) Shear and normal gradients histograms and CDFs, (C) Strain tensor's magnitude field.....	65
Fig. 4-12	Influence of power input, PROPRing- $h/d=0.33$: (A) shear gradients, (B) normal gradients.....	66
Fig. 4-13	Influence of rheology on the flow patterns developed with PROPRing- $h/d=0.33$, for $PV^{-1} = 100 \text{ W m}^{-3}$: (A) water, (B) glycerin, (C) xanthan.....	67
Fig. 4-14	Shear gradient observed in xanthan at $PV^{-1} = 100 \text{ W m}^{-3}$ with PROPRing- $h/d=0.33$	68
Fig. 4-15	Influence of rheology for PROPRing- $h/d=0.33$, with two constant values of power input: (A) CDF of the normalized velocities of the vector field, (B) CDF of the TKE field.	68
Fig. 4-16	Influence of rheology for PROPRing- $h/d=0.33$ at $PV^{-1} = 98 \text{ W m}^{-3}$: (A) shear gradient, (B) normal gradient.....	69
Fig. 4-17	Flow fields in water: (A) PROPRing- $h/d=0.33$, (B) PROP- $h/d=0.33$	71
Fig. 4-18	Flow fields in water: (A) PBT- $6 \times 22.5^\circ$, (B) PBT- $6 \times 45^\circ$, (C) PBT- $6 \times 90^\circ$	71
Fig. 4-19	Flow fields in water: (A) BiLoop, (B) WRI- $d/D=0.4-41.4^\circ$, (C) WRI- $d/D=0.4-28.8^\circ$, (D) WRI- $d/D=0.33-51.2^\circ$	71
Fig. 4-20	CDFs for PROPRing- $h/d=0.33$ and PROP- $h/d=0.33$, water: (A) normalized velocity, (B) TKE.....	72
Fig. 4-21	CDFs for PBT- $6 \times 22.5^\circ$, PBT- $6 \times 45^\circ$ and PBT- $6 \times 90^\circ$, water: (A) normalized velocity, (B) TKE.....	73
Fig. 4-22	TKE fields in water: (A) PBT- $6 \times 22.5^\circ$, (B) PBT- $6 \times 45^\circ$, (C) PBT- $6 \times 90^\circ$	73
Fig. 4-23	CDFs for BiLoop, WRI- $d/D=0.4-41.4^\circ$, WRI- $d/D=0.4-28.8^\circ$ and WRI- $d/D=0.33-51.2^\circ$, water: (A) normalized velocity, (B) TKE.	74
Fig. 4-24	CDFs for all nine impellers, water: (A) normalized velocity, (B) TKE.	74
Fig. 4-25	Flow fields in glycerin: (A) PROPRing- $h/d=0.33$, (B) PROP- $h/d=0.33$	75
Fig. 4-26	Flow fields in glycerin: (A) PBT- $6 \times 22.5^\circ$, (B) PBT- $6 \times 45^\circ$, (C) PBT- $6 \times 90^\circ$	75
Fig. 4-27	Flow fields in glycerin: (A) BiLoop, (B) WRI- $d/D=0.4-41.4^\circ$, (C) WRI- $d/D=0.4-28.8^\circ$, (D) WRI- $d/D=0.33-51.2^\circ$	75

Fig. 4-28	CDFs of TKE for all nine impellers, glycerin: (A) PROPRing- $h/d=0.33$ and PROP- $h/d=0.33$, (B) PBT-6x22.5°, PBT-6x45° and PBT-6x90°, (C) BiLoop, WRI- $d/D=0.4$ -41.4°, WRI- $d/D=0.4$ -28.8° and WRI- $d/D=0.33$ -51.2°	77
Fig. 4-29	Flow fields in xanthan: (A) PROPRing- $h/d=0.33$, (B) PROP- $h/d=0.33$	78
Fig. 4-30	Flow fields in xanthan: (A) PBT-6x22.5°, (B) PBT-6x45°, (C) PBT-6x90°	78
Fig. 4-31	Flow fields in xanthan: (A) BiLoop, (B) WRI- $d/D=0.4$ -41.4°, (C) WRI- $d/D=0.4$ -28.8°, (D) WRI- $d/D=0.33$ -51.2°	78
Fig. 4-32	CDFs of TKE for all nine impellers, xanthan	79
Fig. 4-33	Particle stress with PBT-6x22.5°, PBT-6x45° and PBT-6x90°: (A) shear gradient, (B) normal gradient, (C) power input and corresponding particle size	80
Fig. 4-34	Particle stress with PROPRing- $h/d=0.33$ and PROP- $h/d=0.33$, BiLoop, WRI- $d/D=0.4$ -41.4°, WRI- $d/D=0.4$ -28.8°, WRI- $d/D=0.33$ -51.2°: (A) shear gradient, (B) normal gradient, (C) power input and corresponding particle size	81
Fig. 4-35	Directed velocity gradients for PROP- $h/d=0.33$, water at $PV^{-1} = 100 \text{ W m}^{-3}$, 3DA approach: (A) scalar field and histogram with CDF of G_x , (B) scalar field and histogram with CDF of G_y	83
Fig. 4-36	Vorticity field for PROP- $h/d=0.33$, water at $PV^{-1} = 100 \text{ W m}^{-3}$, 3DA approach. ...	83
Fig. 5-1	Two-dimensional color diagram representing the divergence with the corresponding flow field, both calculated with 3DA in water with PROPRing- $h/d=0.33$ at a constant power input $PV^{-1} = 100 \text{ W m}^{-3}$: (A) divergence, (B) flow field	85
Fig. 5-2	Surface plot of the third component of the velocity vector normalized with the tip speed, PROPRing- $h/d=0.33$ in water at a constant power input $PV^{-1} = 100 \text{ W m}^{-3}$	86
Fig. 5-3	Schematic representation of multiplane stereo-PIV (Raffel et al., 2007)	87
Fig. 5-4	Tomographic PIV: (A) working principle of Tomo-PIV, (B) three-dimensional flow field induced by a propeller (Scarano, 2013).	87
Fig. 5-5	Exemplary output of a CFD simulation for PROP- $h/d=0.33$: (A) streamlines, (B) velocity vector field, (C) turbulence kinetic energy	88
Fig. 5-6	Rushton turbine and baffles made of PMMA	88

Fig. A-1	Horizontal profiles of normalized velocity along y direction, PROPRing- $h/d=0.33$: (A) position 4, (B) position 5, (C) position 6, (D) position 7.	I
Fig. A-2	Vertical profiles of normalized velocity along x direction, PROPRing- $h/d=0.33$: (A) position 1, (B) position 2, (C) position 3.	II
Fig. A-3	Horizontal profiles of normalized velocity along x direction, PROPRing- $h/d=0.33$: (A) position 4, (B) position 5, (C) position 6, (D) position 7.	II
Fig. A-4	Flow fields observed with the approaches 2DA and 3DA: (A) PROP- $h/d=0.33$, 2DA, (B) PROP- $h/d=0.33$, 3DA, (C) WRI- $d/D=0.4-28.8^\circ$, 2DA, (D) WRI- $d/D=0.4-28.8^\circ$, 3DA, (E) WRI- $d/D=0.33-51.2^\circ$, 2DA, (F) WRI- $d/D=0.33-51.2^\circ$, 3DA.	III
Fig. B-1	Flow field observed with PROPRing- $h/d=0.33$ in water with approach 3DA, with increasing power input: (A) $PV^{-1} = 49 \text{ W m}^{-3}$, (B) $PV^{-1} = 195 \text{ W m}^{-3}$	IV
Fig. B-2	Influence of rheology on the flow patterns developed with PROPRing- $h/d=0.33$, for $PV^{-1} = 200 \text{ W m}^{-3}$: (A) water, (B) glycerin, (C) xanthan.	IV
Fig. B-3	Influence of rheology on TKE field developed with PROPRing- $h/d=0.33$, for $PV^{-1} = 100 \text{ W m}^{-3}$: (A) water, (B) glycerin, (C) xanthan.	V
Fig. B-4	TKE fields in water: (A) BiLoop, (B) WRI- $d/D=0.4-41.4^\circ$, (C) WRI- $d/D=0.4-28.8^\circ$, (D) WRI- $d/D=0.33-51.2^\circ$	V
Fig. B-5	TKE fields in water: (A) PROPRing- $h/d=0.33$, (B) PROP- $h/d=0.33$	V

List of Tables

Tab. 2-1	Relative geometries in a stirred vessel.....	28
Tab. 3-1	Geometry of the nine impellers used in the experimental investigation.....	43
Tab. 3-2	Values of Reynolds number investigated for water and glycerin solution.	49
Tab. 3-3	Values of tip speed investigated for the three fluids.....	50
Tab. 3-4	Values of volumetric power input investigated for the three fluids.....	50
Tab. 3-5	Newton numbers measured for the nine impellers in water and glycerin solution..	52
Tab. 3-6	Operating conditions for the comparison of different camera positioning approaches with the same power input for fluid water.	52
Tab. 3-7	Operating conditions for the investigation on the influence of power input for fluid water with 3DA approach.	53
Tab. 3-8	Operating conditions for the investigation on the influence of rheology with constant power input with approach 2DA.	53
Tab. 3-9	Operating conditions for the investigation on the influence of geometry for fluids water, glycerin and xanthan with approach 2DA.....	53
Tab. 4-1	Data points used for the comparison of the three approaches to PIV technique.	55
Tab. 4-2	Position of the vertical and horizontal lines in the investigated laser sheet.....	57
Tab. 4-3	Chosen data points of power input to investigate the influence on the flow field, developed by PROPRing- $h/d=0.33$	62
Tab. 4-4	Average energy dissipation rate and Kolmogorov scale calculated for different values of power input.....	64
Tab. 4-5	Data points used for the study of the rheology influence on the flow field, with PROPRing- $h/d=0.33$	66
Tab. 4-6	Calculation of ε with $V = 2.99$ L, volume of the fluid in the vessel.	69
Tab. 4-7	Power numbers of the PBTs, measured for water and glycerin.....	76
Tab. 4-8	Power numbers of the wave ribbon impellers, measured for water and glycerin....	76

Abbreviations

2D	two-dimensional
2DA	two-dimensional, above position
2DF	two-dimensional, front position
3D	three-dimensional
3DA	three-dimensional, above position
ALR	airlift bioreactor
BCR	bubble column bioreactor
CDF	cumulative distribution function
CFD	computational fluid dynamics
DNA	deoxyribonucleic acid
EDR	energy dissipation rate
FDA	US Food and Drug Administration
FFT	Fast Fourier Transform
IA	interrogation areas
IW	interrogation window
laser	light amplification by stimulated emission of radiation
LB	Luria Broth
LDA	laser Doppler anemometry
LDH	Lactate dehydrogenase
LIF	laser-induced fluorescence
Nd:YAG	neodymium-doped yttrium aluminum garnet
PDE	partial differential equation
pixel	picture element
PBE	population balance equation
PBT	pitched blade turbine
PDA	phase Doppler anemometry
PIV	particle image velocimetry
PMMA	poly(methyl methacrylate)
PSD	particle size distribution
PTV	Particle Tracking Velocimetry
SSF	solid-state fermentation
STR	stirred tank reactor
TOC	Total Organic Carbon
Tomo-PIV	Tomographic particle image velocimetry
TKE	turbulence kinetic energy
voxel	volume element
WRI	wave ribbon impeller

Table of Symbols

Symbol	Description	Unit
a	part of the eigenvalue	—
A	surface	m^2
A	matrix	—
A_B	distance of the baffles from the vessel wall	m
b	part of the eigenvalue	—
C	transformation matrix	—
C	concentration	mol m^{-3}
C	impeller clearance	m
C_∞	stationary concentration	mol m^{-3}
d	impeller diameter	m
D	diameter of stirred vessel	m
e	baffles clearance	m
E_{ij}	velocity gradient	s^{-1}
F	force	N
Fl	flow number	—
G_i^{xyz}	strain in i direction	s^{-1}
h	impeller blade width	m
h	Planck constant	$6.626 \cdot 10^{-34} \text{ J s}$
h_C	off-bottom clearance of the impeller	m
H	level of liquid (filling height)	m
H_B	baffles immersed length	m
H_g	level of aerated liquid	m
i	variable	—
j	variable	—
J_B	baffles width	m
k	turbulence kinetic energy	$\text{m}^2 \text{ s}^{-2}$
K	flow consistency index	$\text{kg m}^{-1} \text{ s}^{n-2}$
k_L	mass transfer coefficient	m s^{-1}
$k_L a$	volumetric mass transfer coefficient	s^{-1}
K_S	Metzner-Otto constant	—
l	impeller blade length	m
l	turbulent eddy size	m
L	distance of the parallel plates	m
L	characteristic dimension	m
l_{EI}	critical eddy length (energy-inertial)	m
l_{DI}	critical eddy length (dissipation-inertial)	m
l_0	larger eddies size	m
m	mass	kg
M	impeller shaft torque	N m

Symbol	Description	Unit
M_R	relative molecular mass	—
n	flow behaviour index	—
N	rotational frequency	s^{-1}
N_B	number of stirrer blades	—
Ne	Newton number	—
N_P	power number	—
N_{Qd}	pumping number	—
N_{QP}	primary flow number	—
P	power	W
Q	volumetric flow rate	$m^3 s^{-1}$
Q_{ax}	volumetric flow rate of an axial flow impeller	$m^3 s^{-1}$
Q_{rad}	volumetric flow rate of a radial flow impeller	$m^3 s^{-1}$
r	radial coordinate	m
Re	Reynolds number	—
Re_a	apparent Reynolds number	—
Re_t	turbulent eddy Reynolds number	—
\underline{S}	symmetric part of the velocity gradient tensor	s^{-1}
t	time	s
t	thickness of the impeller blade	m
T_B	baffles thickness	m
t_R	thickness of the impeller ring	m
u	velocity x component	$m s^{-1}$
u	characteristic velocity of an eddy	$m s^{-1}$
u_{tip}	tip speed	$m s^{-1}$
v	velocity y component	$m s^{-1}$
v'	turbulent fluctuating velocity	$m s^{-1}$
\bar{v}	average velocity	$m s^{-1}$
v_a	axial velocity component	$m s^{-1}$
\bar{v}_C	average circulation velocity	$m s^{-1}$
v_r	radial velocity component	$m s^{-1}$
v_t	tangential velocity component	$m s^{-1}$
V	fluid volume	m^3
\underline{V}	velocity gradient tensor	s^{-1}
V_s	swept volume	m^3
w	velocity z component	$m s^{-1}$
x	Cartesian coordinate	m
\tilde{x}	transformed coordinate, parallel to the flow stream	m
y	Cartesian coordinate	m
\tilde{y}	transformed coordinate, orthogonal to the flow stream	m
z	Cartesian coordinate	m
\tilde{z}	transformed coordinate, orthogonal to the flow stream	m

Symbol	Description	Unit
α	microscale coefficient	—
α	blade angle	°
β	microscale coefficient	—
$\dot{\gamma}$	shear rate	s^{-1}
$\dot{\gamma}_{\text{av}}$	average shear rate	s^{-1}
$\dot{\gamma}_{\text{nn}}$	normal gradient	s^{-1}
$\dot{\gamma}_{\text{nt}}$	shear gradient	s^{-1}
ε	energy dissipation rate	$\text{m}^2 \text{s}^{-3}$
$\overline{\varepsilon}_{\text{T}}$	average energy dissipation rate	$\text{m}^2 \text{s}^{-3}$
η	Kolmogorov microscale	m
θ_{C}	circulation time	s
θ_{M}	mixing time	s
κ	wavenumber	m^{-1}
λ	eigenvalue	—
μ	dynamic viscosity	Pa s
μ_{a}	apparent dynamic viscosity	Pa s
ν	kinematic viscosity	$\text{m}^2 \text{s}^{-1}$
ν	photon's frequency	s^{-1}
ρ	density	kg m^{-3}
$\underline{\sigma}$	stress tensor	s^{-1}
τ	shear stress	Pa
τ	eddy timescale	s^{-1}
$\underline{\tau}$	stress tensor	s^{-1}
τ_{y}	yield shear stress	Pa
Φ_{g}	hold up gaseous phase	—
$\vec{\omega}$	vorticity vector	s^{-1}
$\underline{\Omega}$	antisymmetric part of the velocity gradient tensor	s^{-1}

Chapter 1

Introduction

1.1 Objectives

Placed in the broad field of chemical and biotechnological processes that make use of stirred vessels, this master thesis aims at characterizing different impeller geometries in terms of particle stress.

This experimental work is centered on the investigation of the flow by using a photographic analysis technique, which produces various representations of the flow dynamics.

The attention is particularly focused on the stress that the fluid acts on the particles suspended in the fluid. In case of bioprocesses, these particles are represented by single cells or cellular agglomerates, which flow in the broth inside the fermenter. The topic of particle stress is of major interest in this field of research, since this parameter can negatively affect the productivity of the process. (Daub et al., 2014).

The context of the topic

This work takes part in two PhD projects, conducted by Dipl.-Ing. Chrysoula Bliatsiou and Robert Panckow, M.Sc. at Technische Universität Berlin, Chair of Chemical and Process Engineering.

The aim of the first project, SPP1943, is to characterize the local mechanical stress in an aerated stirred fermenter and to determine its interaction with the productivity of biological agglomerates. The experiments are modeled on the cultivation of *Aspergillus niger*, and the results are intended to be used for the development of impellers that produce low shear stress. The experimental investigation on the fluid dynamics, including the mechanical stress, is possible with the use of model fluids that can simulate the rheological properties of the cultivation broth. The mechanical stress is evaluated in terms of particle size distributions of the dispersed phase and the results need to be used for the description of the break-up processes that occur in the stirred fermenters, using the support of computational fluid dynamics (CFD) simulations and population balance equations (PBE). The measuring techniques primarily used in the investigations of the project include particle image velocimetry (PIV), CFD and in-situ endoscopic technology.

Smart Process Inspection (SPI) is the second project, funded by the Federal Ministry for Economic Affairs and Energy and is composed of seven project partners: four companies and three universities in Germany. In this project, photo- and electro-optical measurement techniques are studied for the investigation of multi-parameter analyses in biological systems. In particular, the objectives of this project partner, TU Berlin, Chair of Chemical and Process Engineering, are the characterization of local particle size distributions in multiphase reactors and the determination of the influence of additional dispersed phases in systems that contain microorganisms. The investigation on the macroscopic flow properties of a system, characterized by the fluid movement and mixing, aims at comprehending and quantifying the microscopic phenomena (cell stress) that affect the cell cultivation, considering the influence

of bubbles and droplets of the mesoscopic field. The experimental setups used for the flow and particle investigation consist of an aerated stirred tank and a wave-mixed single-use bioreactor. The measuring techniques include CFD and PIV for the flow analysis and the in-situ use of photo-optical endoscopic devices for the measurement of the dispersed phases in both bioreactor types.

Approximation to approach the studied system

In a fermenter, the growth of the microorganisms leads to often significant changes of the rheological properties over time. Highly viscous cultivations can suffer poor mixing and consequently low mass transport and lack of oxygen. The supply of oxygen must be inserted as an air stream in the reactor only when the cultivated microorganisms have an aerobic metabolism. However, the life activities of the microorganisms produce themselves a gas phase, for example in the form of CO₂.

The realization of the experimental investigation finds the necessity of introducing a significant approximation in the involved system, developing a single-phase system that does neither include the biological phase nor the gaseous phase. The single-phase-model system consists of non-biological fluid, which can approximate the properties of the cultivation broth, thus are purposely defined to facilitate the experimental research. Moreover, the general approximation is essential for the appropriate application of the chosen analysis technique, PIV.

This image analysis method is chosen for its ability to produce valuable results on the flow field in a stirred vessel. However, the additional presence of a gaseous phase in the fluid brings complications for the acquisition and for the processing of the data. For this reason, the application of PIV in gas-liquid flows in stirred vessels is reported in few published works. The obstacle to the technique is introduced by the presence of the gas bubbles, which produces a less periodic flow field as compared to the single-phase case. The resulting velocity vector field of the continuous phase is more difficult to measure, since the bubbles and their shadows can occupy a great part of the area where the tracing particles should be detected for the measurement of the displacement and moreover result in disturbing reflections. The inhomogeneous distribution of the bubbles inside the stirred vessel produces irregular detection of the flow seeding particles, of which varying concentration in the examined area can fluctuate too strong to develop accurate results. (Aubin et al., 2004; Deen et al., 2002).

The microorganisms of the broth grow and change in size and shape, producing a discontinuous rheology of the broth over time. Broth cultures can be described with rheological models that, depending on the morphology of the dispersed phase, can be both Newtonian and non-Newtonian, in particular pseudoplastic (shear thinning). In the experimental approach of this work, the model fluids that constitute the single-phase system are chosen to approximate the broth culture of interest, that regards particularly the *Aspergillus niger*, a fungus with filamentous morphology.

In this respect, it is advantageous to consider the work of Henzler and Schäfer (1987), who conducted a study on a broth containing a mycel-forming microorganism in order to understand how the rheology changes over time. It was observed that, considering an initial concentration of the microorganisms such that the broth was Newtonian, when the mycel started to grow in size and number, the viscosity of the broth did not have a constant value

anymore. The shear thinning rheology of the broth could be described with the Ostwald-de-Waele model.

Taking into account these results, the evaluation and comparison of the rheology of broth cultures and non-biological fluids, such as the non-Newtonian xanthan, carboxymethyl cellulose and polyethylenglycole, are done. The rheological model that describes the pseudoplastic broth cultures is characteristic of the flow consistency factor K , which increases with the growth of the biomass, and of the flow behaviour index n , which on the other hand is found to be independent of the biomass growth. The outcome of these experiments shows that the most suitable model fluid for the culture of *A. niger* is xanthan. Coherently with these conclusions, considering that the cultivation medium is Newtonian, the model fluids chosen for this experimental work are water and two aqueous solutions of glycerin and xanthan. (Bliatsiou et al., 2018a)

1.2 Thesis Layout

The main parts of this work are connected by a common thread that follows the central aspects of microbial cultures and stirred vessels and the fluid dynamical phenomena that occur in these systems. Additionally, an overlook on the chosen analysis technique describes the practical approach to the investigation of the experimental system.

The resolution of this big topic starts with **Chapter 2**, that offers a wide literature review of the fundamentals on which this experimental work is based. These range from the structure of the cell to the physical quantities of fluid dynamics, including the mechanism of mixing in a stirred vessel.

In the introductory part of the chapter, in **Section 2.1**, the definition and the classification of microorganisms is followed by the explanation of the cellular structure characteristics that differentiate the two main groups that include all the living beings. A brief introduction to the huge field of biotechnologies introduces the concept of culture of microorganisms. Here, the primary techniques used to develop a microbial culture are presented, including the solid-state Petri dish and the liquid broth culture. This section ends with a concise overview of the typologies of bioreactors and closes, for the moment, the focus on microorganisms. The aim of **Section 2.2** is to explain the rheological properties of fluids, properties that help to individualize the various behaviours of fluids. These are classified and their characteristics are described, also with the use of rheological models. This section closes with a discussion on the rheology of broth cultures, showing how these, since they contain biological material, change their morphology and, consequently, their rheological properties over time. This discussion introduces the biological problems, especially identifiable with the cellular stress, that can occur when dealing with the mechanical agitation of the broth culture. In **Section 2.3**, the attention is focused on the fluid dynamics. Here, the definition of the velocity vector is used for the mathematical formalization of several quantities of the fluid dynamics, such as the vorticity and the strain tensor, with a deeper focus on the shear. These quantities are useful to understand and quantify the mechanisms that occur in the fluids. The introduction and comprehension of these properties are particularly advantageous for the characterization and the interpretation of the results obtained in this experimental work. In this section, the concept of turbulence is introduced, pointing out the possibilities of flow regime at which the fluid can

flow. Within this discussion, it is possible to start to familiarize with the concepts of turbulence kinetic energy and the kinetic energy dissipation, which are often mentioned and discussed throughout the entire work, because of their relevance in the study of agitated fluids in stirred vessels. This anticipates the content of **Section 2.4**, where fluid mixing performed in stirred vessels is described. The stirred vessel constitutes the main part of the experimental setup of this work. The description of the mechanism of mixing is here supported by the explanation of the Kolmogorov's theory on the isotropic turbulence, a theory that is used in **Section 2.5** to describe the solid-fluid interactions that generate the shear stress on microorganisms.

In **Chapter 3** it is intended to present the chosen measuring technique and explain the experimental method used for the investigation. Here, the general principles of PIV are explained and thereafter the specific equipment constituting the hardware and the general workflow of the software used for the calculations are briefly illustrated. The attention is then focused on the experimental setup, regarding the global apparatus of the stirred vessel, including the different impellers and the fluids. The explanation of the measuring technique and its development until the final establishment are followed by the description of the creation of the parameter matrix, which is fundamental for the organization of the data points of the systematic investigation.

Chapter 4 presents the results of the experimental work in a schematic way. Firstly, the approaches that are used for the establishment of the measuring technique are compared in terms of flow field. In the second part, some of the data points of the parameter matrix are chosen for the analysis of the influence of power input, fluid rheology and impeller geometry on the fluid dynamics of the stirred vessel. At the end of the chapter, the attention moves to the topic of particle stress and how the impeller geometry influences this parameter. This discussion is supported by the results of the study of Bliatsiou, in which the same impellers of this work are used to evaluate the particle stress.

The work closes with **Chapter 5**, where the conclusive observations on the work are formulated. The chapter suggests some prospects, considered valuable for the improvement of the measuring with PIV, and it presents some results of a CFD simulation of the analogous system that is investigated in the experimental work.

Chapter 2

Literature Review – Basical Fundamentals

2.1 Microorganisms and Biotechnology

Microorganisms are microscopic organisms that exist as single cells or in a colony of cells. The cellular structure of a microorganism can be classified as prokaryotic or eukaryotic. According to the classification proposed by Thomas Cavalier-Smith in 1987, this is the most important distinction for characterizing groups of organisms. As reported in the lately revised classification (Ruggiero et al., 2015), all living organisms can be divided into two superkingdoms, Prokaryota and Eukaryota, and successively into seven Kingdoms: Archaea, Bacteria, Protozoa, Chromista, Fungi, Plantae and Animalia.

Since in this discussion the interest is focused on microorganisms, only their classification will be represented and described more in detail, see **Fig. 2-1**.

Bacteria constitute a really large domain of prokaryotic unicellular microorganisms; they can be classified into different types according to their shape, to their optimal growth temperature and to their connection with one or more other organisms. The most common shapes are spheres (coccus), rods (bacillus) and spirals (spirillus). The reproduction of bacteria is asexual, known as binary fission: a duplication of the genetic material is developed by the cell, which then divides itself into two cells. One of the most studied bacteria is *Escherichia coli* (*E. coli*), which is widely used in Biotechnology (Cooper, 2000; D.L.Nelson and M.MCox, 2010; Idalia and Bernardo, 2017).

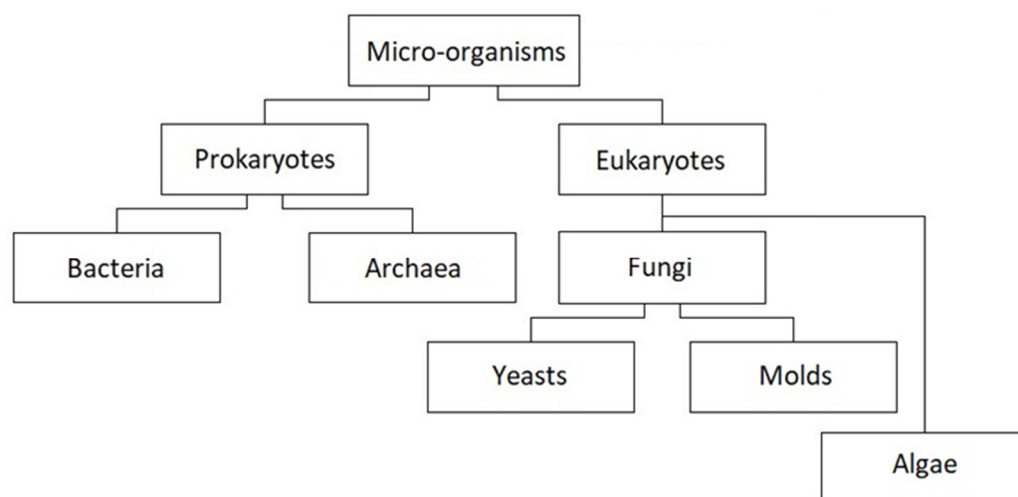


Fig. 2-1 Classification of microorganisms.

Archaea belong to the superkingdom of Prokaryota. They are unicellular microorganisms and they reproduce by means of binary fission, like bacteria do. Archaea have been found in every habitat, but originally they were considered extremophiles, because of their ability to live in extreme environments, such as high and low temperatures, high concentrations of salt, high pressures and extreme values of pH (Brooks et al., 2013).

Among eukaryotic microorganisms there are fungi, which include yeasts and molds. Yeasts are single-celled microorganisms, while molds are multicellular, characterized by filament structures called hyphae. Reproduction in the kingdom of Fungi can be asexual, by means of spores or through budding, or sexual, through meiosis. *Saccharomyces cerevisiae* (*S. cerevisiae*) is the most studied yeast and it has several applications in food processes, such as brewing, distilling, vinification and bread production (Karathia et al., 2011; Stewart, 2016).

Algae belong to the superkingdom of Eukaryota and they can be both unicellular and pluricellular organisms. Generally they are photosynthetic, that means they use sunlight as a source of energy: in the photosynthetic reaction carbon dioxide and water are converted into glucose and oxygen. Photosynthesis is conducted in special cellular organelles called chloroplasts, which contain chlorophyll, a pigment capable of storing light energy. Successively the energy is transferred to protein complexes, the photosystems, that are responsible of carrying out the photosynthetic reaction (Yang et al., 2015). In addition there is a minority of algae that are mixotrophic, that means that their nutrient source consists of external organic materials as well as inorganic nutrients and light. Finally there are also some algae that lost their ability to perform photosynthesis, hence they are heterotrophic and use only external organic materials for their growth (Raven and Giordano, 2014).

Microorganisms play an indispensable role in biotechnology, a discipline based on the combined use of microbiology, biochemistry, chemical and genetic engineering, aimed at producing substances with a commercial interest by means of industrial processes that use biological systems. In general, biotechnology uses either living material, such as bacteria, yeasts, molds and mammalian cells, or biological products, like components or enzymes produced and/or extracted by the just mentioned biological systems. The goal of this discipline is the creation of new products for their use in pharmaceutical, medical, agricultural and environmental applications (Verma et al., 2011; Arevalo-Villena et al., 2017; Cairns et al., 2018).

Modern biotechnology differs from the traditional one in the fact that microorganisms and cells can be genetically modified in order to achieve the products of interest. The beginning of genetic engineering goes along with the invention of the deoxyribonucleic acid (DNA) cloning technique: their first application allowed the production of recombinant proteins for therapeutic purposes, like insuline and growth hormone. The achievement of recombinant proteins is the result of cloning and expressing the genetic material of interest in different cells, which work as expression systems. In the history of biotechnology, human insulin is the first licensed drug obtained with the use of recombinant DNA technology, cloned and expressed in *Escherichia coli* in 1982. This bacterium, together with the yeast *Saccharomyces cerevisiae*, is the main expression system used for human insulin (Baeshen et al., 2014). The production of biopharmaceuticals takes advantage of expression systems of various nature, including yeast, insect cells and mammalian cells, see **Fig. 2-2**. In 2013, the biopharmaceutical products on the market accepted by the US Food and Drug Administration (FDA) were more than 300, with sales exceeding US\$100 billion (Nielsen, 2013; Roche, 2013).

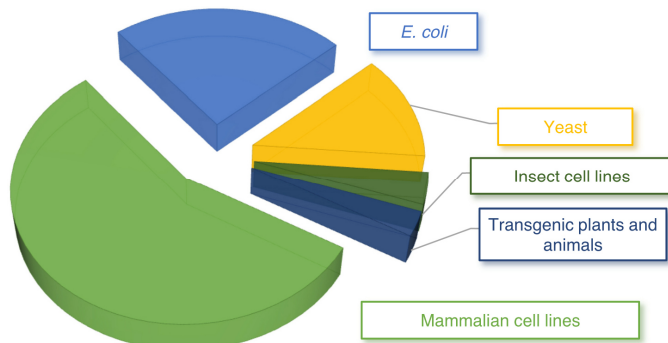


Fig. 2-2 Percentage of biopharmaceuticals produced in different expression systems (Baeshen et al., 2014).

2.1.1 Prokaryotic cells

Between the two main categories of microorganisms, the prokaryotic cell has the simplest and smallest structure. Indeed the dimensions of a prokaryotic cell are in the range of 1–10 μm , while a eukaryotic cell can reach 100 μm .

In a prokaryotic cell, see **Fig. 2-3 (A)**, the nuclear material consists of a single chromosome (circular DNA molecule), not surrounded by a membrane, and restricted to an area of the cytoplasm called nucleoid. The cytoplasm, the part of the cell where all the enzymes aimed at carrying out the metabolic reactions are located, is surrounded by the protective cell wall and by a plasma membrane, which regulates the movements of ions and organic molecules in and out of the cell. In the cytoplasm, there are also ribosomes, a molecular machine where the protein synthesis takes place.

Furthermore, some prokaryotic cells have particular protein structures on the outer surface called flagella and pili, which are mainly employed for movement (Bamforth, 2007).

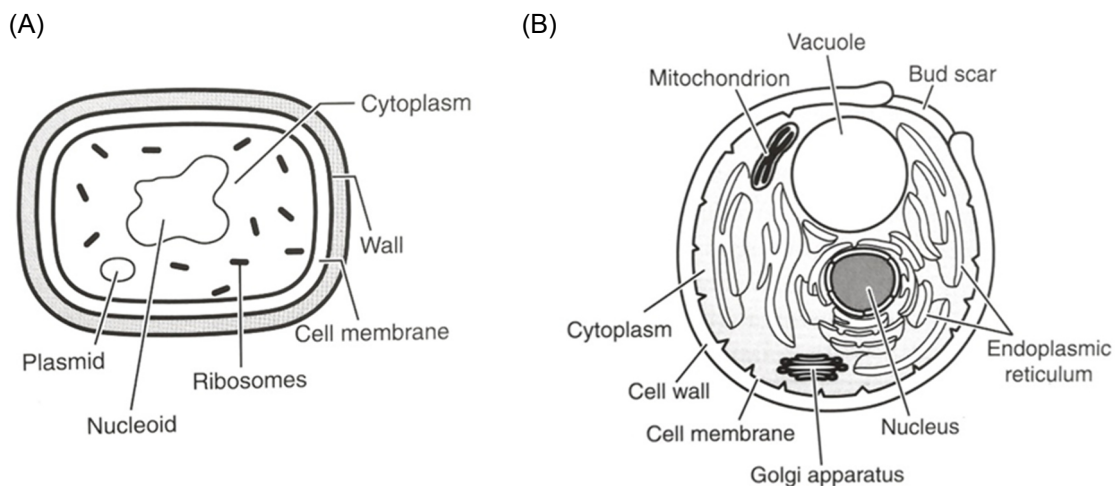


Fig. 2-3 Simple representations of cells with their most important functional elements: (A) prokaryotic cell, (B) eukaryotic cell (Bamforth, 2007).

2.1.2 Eukaryotic cells

The eukaryotic cell, on the other hand, is typically constructed of cellular compartments or organelles, as shown in **Fig. 2-3 (B)**. Organelles are parts of the cell that are separated from the cytoplasm by a membrane; each of them has its own function.

One of the main differences between these two types of cells is that the eukaryotic cell has a nucleus, an organelle that contains the genetic material organized into multiple linear

chromosomes. The eukaryotic cell is delimited by a cellular membrane and, in some cases, also by a cell wall.

In the cytoplasm there are proteins, ribosomes and several organelles, such as endoplasmic reticulum, Golgi apparatus and mitochondria. The endoplasmic reticulum is responsible for the folding of protein molecules and for the transport of these in vesicles to Golgi apparatus, where proteins and other cellular products are collected and dispatched to the cell. Mitochondria are present in most eukaryotic cells and their main function is the regulation of metabolism. Finally, organisms like plants and algae have chloroplasts, organelles where photosynthesis takes place; here, light energy is converted to chemical energy that can be used by the organism for its different activities (Bamforth, 2007).

2.1.3 Cultivation Systems

A microbiological culture is a laboratory method that allows the multiplication of microorganisms, both prokaryotic and eukaryotic, in a growth environment called medium. Cultivation of microorganisms represents one of the main diagnostic methods in microbiology, thanks to its capability of determining the type and amount of microorganism present in the analyzed sample. In Biotechnology, the cultivation of microorganisms plays a fundamental role for the final success of the bioprocess, which aims at obtaining specific products.

The subject of microbial cultivation may appear simple on the surface, but there are various factors that make this topic considerably complex (Prakash et al., 2013). As a matter of fact, microorganisms require proper environmental conditions and precise nutrients to grow and to make replicas of themselves. In particular, the chemical composition of microorganisms reveals which are the elements that must be provided with nutrients and that, additionally, should be in a metabolically accessible form. The nutrients present in the growth media can be divided in different categories, according to the elements that they supply: carbon, nitrogen, sulfur, phosphorus and mineral sources are essential for living organisms. Another requirement for microbial growth is the metabolic energy, fundamental for the synthesis of macromolecules and for the maintaining of essential chemical gradients across microorganisms' membranes. Metabolic energy can be generated by three main mechanisms: fermentation, respiration and photosynthesis. It is clear that every microorganism has its specific demand of nutrients and metabolic pathway to grow. To satisfy all these necessities, the accurate control of the following environmental factors during the growth is determining: nutrients, pH, temperature, aeration, salt concentration and ionic strength of the medium (Brooks et al., 2013).

The *cultivation method* and the choice of the medium depend on the investigation type, which may aim at obtaining one among the following objectives: growing cells of a given species, isolation of a microorganism species from a natural source, microbiological analysis of the sample. Moreover, microbiological cultures can be categorized by the physical state of the medium culture, that can be solid or liquid, such as agar and broth, respectively.

Agar is a gel used for plating, a technique that consists in growing a pure culture of microorganisms in the so-called *Petri dish*, see **Fig. 2-4 (A)**. This device, thanks to its transparent lid, allows to observe the colonies and to limit contamination from other species. The physical properties of agar, which is an acidic polysaccharide extracted from certain red

algae, allow to immobilize the cells in this solid medium and to let them grow in different colonies, originated by single cells. The streak-plate technique is made up of few steps, starting with the preparation of the Petri dish: agar, once dissolved in water at 100 °C, is enriched with nutrients and stored at 50 °C, then it is poured in the plate and its gel formation occurs at 45 °C. With a sterile wire loop some cells are caught from the inoculum and they are streaked on a limited area of the gel. Afterwards the wire loop is sterilised again, rubbed on the previous area to catch some cells and then streaked on another area, see **Fig. 2-4** (B). By repeating this procedure, the cells deposited on the gel by the wire loop are more and more isolated, so that it is possible to identify the different colonies after the incubation time that for most routine laboratories is 5 days circa, although most of the pathogens grow after 24–28 hours (Brooks et al., 2013; Lagier et al., 2015).

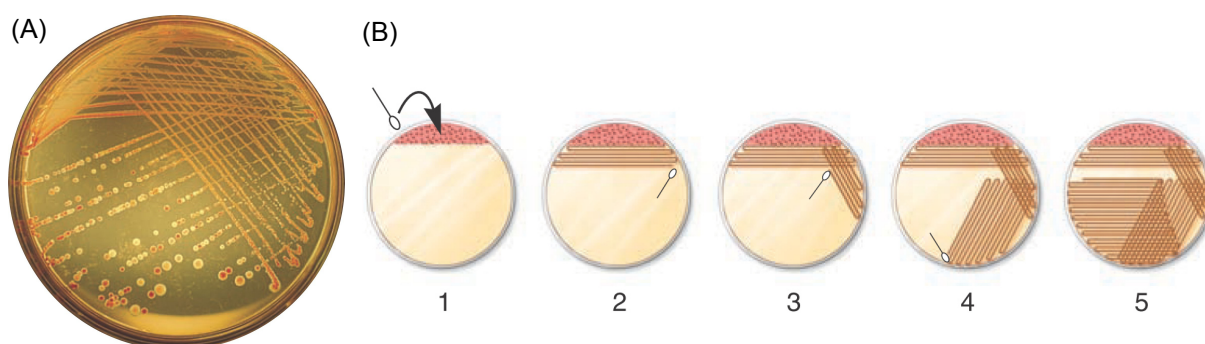


Fig. 2-4 The streak-plate technique: (A) Petri dish with agar and a microbial culture. (B) Streaking patterns made with a wire loop showing the corresponding procedural steps (Brooks et al., 2013).

A *broth* culture consists of liquid growth medium and microorganisms: the sterile growth medium must contain all the necessary nutrients for the microorganisms that will be here inoculated.

An example of liquid growth medium is Luria Broth (LB), which is widely used for bacterial culture. It is a very rich medium that contains tryptone, yeast extract and NaCl (MacWilliams and Laio, 2006). The potential of a broth culture is revealed by the chance of growing a large number of microorganisms in a quite small amount of time; additionally it is chosen as a method of storage in sealed *shaking flasks*.

Broth culture is generally used in bioreactors to grow and use microorganisms; in this case it is called submerged fermentation. However, there is also a fermentation process called solid-state fermentation (SSF) that works with a solid matrix in absence, or nearly absence, of water, hence it is more appropriate when dealing with filamentous fungi, because they are microorganisms that are naturally adapted to this condition (Spier et al., 2012).

Bioreactors are the main unit operations for industrial biochemical transformation, in which the treated materials promote the biotransformation by the action of the living cells or by the cellular components, such as enzymes (Pandey et al., 2008). The purposes that can be achieved through these reactors are various: biomass production, metabolite formation such as organic acids and antibiotics, transformation of substrates, and production of enzymes. In general, bioreactors are cylindrical vessels or tanks, with a volume that goes from a liter to some cubic meters, depending on the design and on the operation mode (Spier et al., 2012). Due to their great potentials and to the various operations that can be carried out, there exists a very wide variety of bioreactors, that can be considered the heart of the bioprocesses (Cinar et al., 2003).

The operation mode of a bioreactor can be classified in batch, fed-batch and continuous processes, although batch systems are definitely prevalent and extensively used (Spier et al., 2012). Generally, in a batch bioprocess the system (fermenter) is partially closed and the required materials are supplied before the starting of the operation in sterile conditions, and removed together with the products at the end.

In fed-batch processes, instead, sterile substrate and nutrients are continuously added inside the bioreactor, in which the volume increases due to the lack of an outflow. Hereafter, the main types of submerged bioreactors, that are the ones dealing with broth culture, are briefly presented, according to Spier et al. (2012).

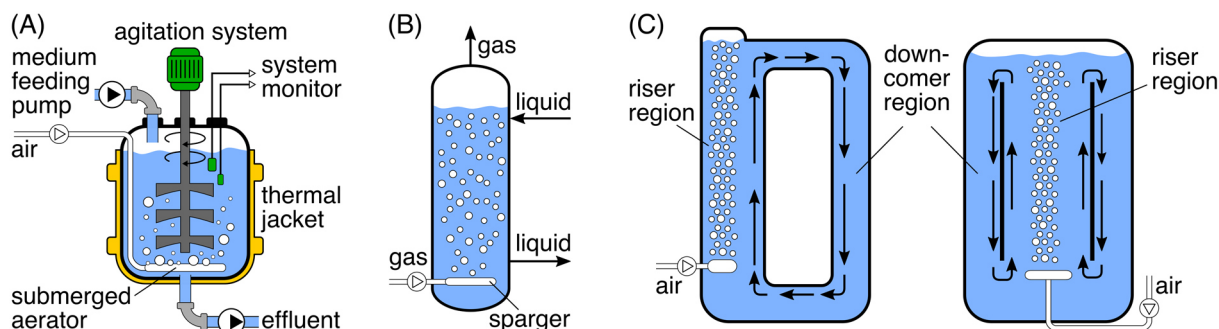


Fig. 2-5 Important types of bioreactors: (A) stirred tank reactor, (B) bubble column reactor, (C) airlift column with external loop and with internal loop.

The mainly used bioreactor is the *stirred tank reactor* (STR), see **Fig. 2-5** (A), where one or more impellers, according to the design specifications, promote the mechanical agitation of the broth, improving mass and heat transfer. There are aerated and non-aerated STRs; when aeration is required, its rate must be over-stoichiometric to promote higher contact between the broth and the air bubbles (Doran, 1995). The broth generally occupies 70–80% of the total volume of the fermenter, in order to have a headspace used for gas exhaust and foam formation.

Pneumatic mixing is instead performed in a *bubble column bioreactor* (BCR), where a sparger is equipped at the bottom of the cylindrical tank for the formation of air bubbles, see **Fig. 2-5** (B). For this type of reactor, the choice of the sparger is determinant on the size and on the number of the bubbles, hence on the mass transfer.

A variation of the BCR is the *airlift bioreactor* (ALR), where the pneumatic mixing is promoted by the presence of components that help to circulate the fluid, see **Fig. 2-5** (C). The different configurations of ALRs can be classified in two main types: external loop and internal loop.

Bioreactors own an additional complexity as compared to other reactors, due to the presence of the biological phase, which requires the establishment of favorable environmental conditions and the supply of proper nutrients for the growth of the living organisms. Hence, it is fundamental, for a good performance of the bioreactor, to pay attention and to control all the factors that can threaten the health of the microorganisms, i.e. in terms of cell stress. To achieve this, it is indispensable to translate the necessities of the biotic phase in physical quantities that can be measured and controlled in the reactor.

In the **Sections 2.2–2.4**, some important quantities of fluid dynamics are defined, with the intention of enhancing the clearness of the topic discussed in **Section 2.5**, concerning the stress on microorganisms.

2.2 Fluid Rheology

Fluid rheology is etymologically the study of the flow of matter. Rheological models can be used to describe fluids and to analyze their deformation resulting from applied forces. The rheology of the fluids is determinant for the fluid dynamics of a stirred vessel. The aim of this section is to explain the physical quantities that determine and characterize the flow of matter as well as introduce some of the important aspects of this experimental work.

The main physical quantities that characterize a fluid are density and viscosity. The *density*, i.e. volumetric mass density, see **Eq. (2-1)**, is generally indicated with ρ and it is the mass m per unit volume V of the fluid:

$$\rho = \frac{m}{V} \quad (2-1)$$

The *dynamic viscosity* μ can be seen as the resistance of the fluid to the shearing flow, generated by the relative motion of adjacent layers of the fluid. The dynamic viscosity is related to the *kinematic viscosity* ν through the fluid density ρ according to

$$\nu = \frac{\mu}{\rho} \quad (2-2)$$

The SI units of μ are both, $\text{Pa}\cdot\text{s}$ and $\text{kg}\cdot\text{m}^{-1}\cdot\text{s}^{-1}$, as a consequence, the dimension of the kinematic viscosity is $\text{m}^2\cdot\text{s}^{-1}$. The Newton's law of viscosity, explained more in detail in **Section 2.3**, shows the dependency of the shear stress τ on the shear rate $\dot{\gamma}$ and on the dynamic viscosity μ :

$$\tau = \mu \cdot \dot{\gamma} \quad (2-3)$$

This law also provides a definition of viscosity, as the ratio of shear stress to shear rate. It is possible to use this law as a criterion of distinction between fluids: Newtonian fluids obey to **Eq. (2-3)**, non-Newtonian fluids do not. Therefore, for Newtonian fluids, the viscosity is the constant proportionality factor of the Newton's law, and depends only on temperature and pressure. Usually fluids with a relative molecular mass M_R less than 5000 (all gases and some liquids, such as water, oil, sugar solution) are Newtonian, while other fluids, as polymeric fluids, suspensions, pastes and slurries are non-Newtonian (Bird et al., 2002).

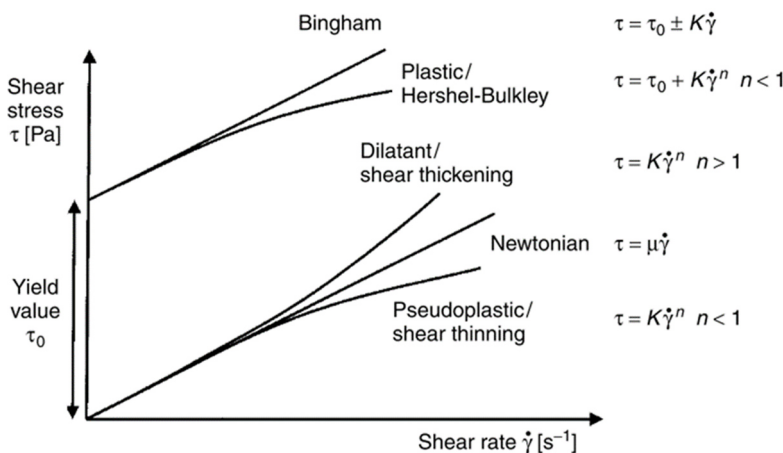


Fig. 2-6 Flow curves of Newtonian and non-Newtonian fluids (Brown et al., 2004).

Non-Newtonian flow differs from the Newtonian, since viscosity is a function of the shear rate, and for this reason it was named as apparent viscosity μ_a , see **Eq. (2-4)**.

$$\mu_a = \frac{\tau}{\dot{\gamma}} \quad (2-4)$$

Non-Newtonian fluids can be divided in three classes (Skelland, 1967): time-independent fluids, time-dependent fluids and viscoelastic fluids. The first class is summarized in **Fig. 2-6**, being the one of interest for this discussion.

Time-Independent Fluids

They are mainly *pseudoplastic*, of which viscosity decreases with the increase of the shear rate, at a large range of shear rate. The behaviour of this fluid is described by the power-law model of *Ostwald-de-Waele*

$$\tau = K \cdot \dot{\gamma}^n \quad (2-5)$$

where n is the flow behaviour index (–) and K is the consistency index ($\text{kg} \cdot \text{m}^{-1} \cdot \text{s}^{n-2}$), as per

$$\mu_a = K \cdot \dot{\gamma}^{n-1} \quad (2-6)$$

For pseudoplastic fluids $0 < n < 1$ applies. For *dilatant* fluids it is $n > 1$, and their viscosity increases with the increase of the shear rate. According to this power law model, it is easy to demonstrate that for Newtonian fluids $n = 1$.

Pseudoplastic and dilatant fluids start showing a deformation as a force is applied. This is not valid for plastic fluids, which start to flow after a yield value of shear stress τ_y is exceeded. This behaviour is characteristic, as shown in **Fig. 2-6**, for *Bingham* and *viscoplastic fluids* and it is described by the *Herschel-Bulkley* model

$$\tau = \tau_y + K \cdot \dot{\gamma}^n \quad (2-7)$$

$$\mu_a = (\tau_y + K \cdot \dot{\gamma}^n) / \dot{\gamma} \quad (2-8)$$

Hereby, **Eqs. (2-7) and (2-8)** describe Bingham fluids when $n = 1$.

Non-Newtonian fluids exhibit difficulties in obtaining homogeneity in a stirred vessel. This problem was discussed by Metzner and Otto (1957), whose work is the best known about non-Newtonian fluids in mixing systems (Ramírez-Muñoz et al., 2017).

The suggested method is aimed at matching the power requirements of a non-Newtonian fluid with Newtonian data, considering the same operating conditions, such as agitation system and impeller rotational frequency. In doing this it is necessary to firstly define an apparent Reynolds number Re_a (definition of Reynolds number Re in **Section 2.3**), which is given by

$$Re_a = \frac{\rho N d^2}{\mu_a} \quad (2-9)$$

where ρ is the density of the fluid ($\text{kg}\cdot\text{m}^{-3}$), N the rotational frequency of the impeller (s^{-1}), d the diameter of the impeller (m) and μ_a is the apparent viscosity ($\text{Pa}\cdot\text{s}$), which is related to the impeller average shear rate $\dot{\gamma}_{av}$ by the power-law in **Eq. (2-6)**, resulting in

$$\dot{\gamma}_{av} = (\mu_a/K)^{1/(n-1)} \quad (2-10)$$

Metzner and Otto suggested that a linear correlation can describe the proportionality of the average shear rate $\dot{\gamma}_{av}$ around the impeller, with the impeller rotational frequency N , by introducing the *Metzner-Otto* constant K_s , described by

$$\dot{\gamma}_{av} = K_s \cdot N \quad (2-11)$$

The constant K_s decreases rapidly with the distance from the impeller blade tip. The linear correlation in **Eq. (2-11)** was found valid for laminar and transitional flow and only for a part of turbulent regime. It is not valid for fluids in which the shear rates are highly located around the impeller, while the remaining regions of the vessel are stagnant, e.g. Bingham and dilatant fluids (Hemrajani and Tatterson, 2004).

Rheology of Broth Cultures

Understanding the rheology of a fluid represents a fundamental step to proceed with the design and the actuation of an industrial process. When a process deals with biological materials, things get more complex to describe and to manage. A *broth culture* is a suspension of particles and macromolecules. Moreover, fermentation broths contain living organisms that grow, change in size and shape, and produce a gaseous phase. Therefore, the characteristics of a broth culture change in time and a further control of the mixing is necessary. **Fig. 2-7** shows the typical morphological change of *Cephalosporium acremonium* over time in a fermenter (Lim et al., 2002).

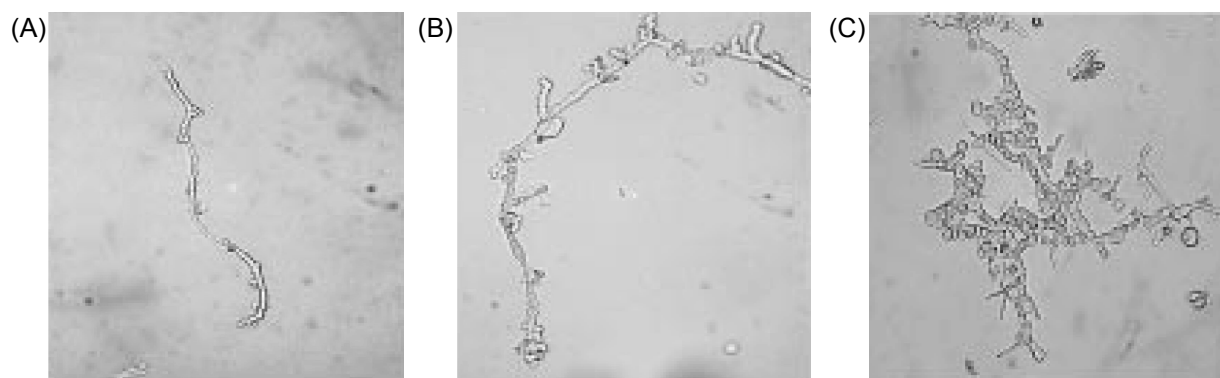


Fig. 2-7 Morphological change of *Cephalosporium acremonium* in a fermenter: (A) after two, (B) four and (C) six days (Lim et al., 2002).

The rheology of a fermentation broth depends on the concentration and on the morphology of the biotic phase. Generally with low concentrations, especially with spherical particles, the behaviour of the broth can be described as Newtonian. However, as the concentration of the biological phase increases, the deviation from the Newtonian model increases.

If the biotic phase consists of mycelial cells, the broth shows a pseudoplastic non-Newtonian rheological behavior, that can be described by the power-law model in **Eq. (2-5)** (Spier et al., 2012). The rheology of this type of broth has significant effect on the

performance of the bioreactor, since it influences the mixing flow, hence it affects the power requirement and the processes of mass and heat transfer (Gavrilescu et al., 1993).

When, during an aerobic fermentation, the biotic phase changes and its concentration increases, also the apparent viscosity μ_a of the broth increases. To overcome this, it is possible to increment the rotational frequency N of the impeller, so that the mass transfer of the gaseous phase into the liquid phase can be accomplished by maintaining a proper value of volumetric mass transfer coefficient k_{La} . The increase of N , however is generally followed by the generation of regions around the impeller, where shear is so high that it can physically damage the cells, compromising the success of the bioprocess (Smith et al., 1990).

2.3 Fluid Dynamics

In this section, the aim is to define those physical quantities and dimensionless numbers, characteristic in fluid dynamics, which are important to explain and comprehend the mechanisms of stress, that occur on the cells located in a stirred vessel. The perspective is also to make a review of the physical quantities that are used for the interpretation of the results of this work.

Velocity

A fundamental physical quantity, used for the calculations of mostly all the other quantities, is the velocity \vec{v} . Considering the Cartesian space xyz , the velocity vector can be defined as

$$\vec{v} = \begin{bmatrix} dx/dt \\ dy/dt \\ dz/dt \end{bmatrix} = \begin{bmatrix} v_x \\ v_y \\ v_z \end{bmatrix} = \begin{bmatrix} u \\ v \\ w \end{bmatrix} \quad (2-12)$$

Reynolds Number

Introduced in **Section 2.2**, the Reynolds number Re is a basic dimensionless number in fluid dynamics. The use of this number helps in the determination of the fluid flow under certain conditions, in particular it is used to evaluate the transition from laminar to turbulent flow. The reason of its large use in this field is due to the fact that, like other dimensionless numbers do, it allows to appreciate the similarity of systems that belong to a wide class. The Reynolds number is defined as

$$Re = \frac{\rho v L}{\mu} \quad (2-13)$$

where ρ is the fluid density, v is the fluid average velocity (scalar quantity), L is a characteristic dimension and μ is the dynamic viscosity of the fluid.

From a physical point of view, Re is interpreted as the ratio of inertial forces and viscous forces. Viscous forces are predominant in the laminar regime, in which the fluid is “laminated” and it flows in parallel layers. Inertial forces become predominant on the viscous forces in the turbulent regime, characterized by chaotic and unsteady motion. In **Fig. 2-8** the flow is represented with parallel flow lines: a trace of dye is added to the fluid and follows the

stream lines, showing the motion of the fluid and its behaviour from laminar to turbulent conditions.

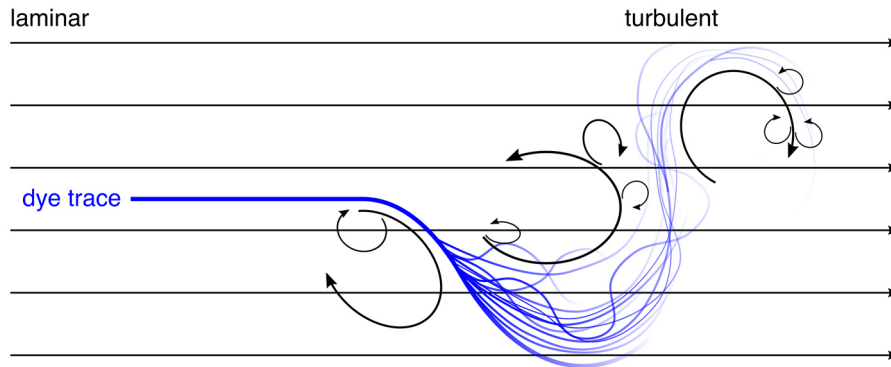


Fig. 2-8 Laminar and turbulent flow shown with a dye trace.

In a mixer, the mechanical agitation can be carried out both, in laminar and in turbulent regimes. The value of Re tells in which condition the system is working (Hemrajani and Tatterson, 2004), whereby

$$\begin{array}{ll} Re < 10 & \text{laminar} \\ 10 \leq Re < 10^4 & \text{transitional} \\ 10^4 \leq Re & \text{turbulent} \end{array} \quad (2-14)$$

Velocity Gradient

In the development and analysis of the results of this work, velocity plays an essential role. Some complex fluid mechanisms are described by Haimes and Kenwright (1999) through the interpretation of the eigenvalues of the velocity gradient, which is a 3×3 tensor. This matrix tells how the velocity changes in space and is defined by

$$\underline{V} = \begin{bmatrix} \partial u / \partial x & \partial u / \partial y & \partial u / \partial z \\ \partial v / \partial x & \partial v / \partial y & \partial v / \partial z \\ \partial w / \partial x & \partial w / \partial y & \partial w / \partial z \end{bmatrix} \quad (2-15)$$

This vector field has the units of s^{-1} , as most of the data calculated from \underline{V} are in the form of a rate. It is important to point out that for the calculation of the velocity gradient in the three-dimensional (3D) form, it is supposed to have the punctual velocities referred to a small volume, because they must be differentiated with respect to the 3 coordinates x, y, z .

In this work, the use of the PIV technique provides data corresponding to the plane of the stirred vessel that is illuminated by the laser. Hence, due to the lack of information of velocities in the thickness dz , the third column of the velocity gradient cannot be solved. To start to familiarize with some of the quantities derived from the velocity gradient, it is convenient to decompose \underline{V} in its symmetric and antisymmetric units: \underline{S} is a measure of the strain (bulk and shear) and $\underline{\Omega}$ includes the rotational part of the flow, referred to as vorticity and swirling.

$$\underline{S} = (\underline{V} + \underline{V}^T) / 2 \quad (2-16)$$

$$\underline{\Omega} = (\underline{V} - \underline{V}^T)/2 \quad (2-17)$$

For the definition of the quantities of interest derived from velocity, the definitions proposed and used by the Software employed in this work (*DaVis* 8.4) are additionally reported. They are based on the following definition of the velocity gradient E_{ij} .

$$E_{ij} = \frac{\partial v_i}{\partial j}, \text{ with } i \in \{x, y, z\} \text{ and } j \in \{x, y, z\} \quad (2-18)$$

Shear

In order to define and to clearly understand what the shear stress is, two parallel plates at a distance L are considered, with a still fluid, that can be gas or liquid, in between, see **Fig. 2-9**. The higher plate is still, while the lower one starts moving at instant time $t = 0$ with a constant velocity v along the positive x axis. The fluid shows a gradient of velocity along the distance between the two plates and this becomes constant over the y coordinate when the steady state is reached. In order to maintain the lower plate at a constant velocity, a constant force F is required. This force is directly proportional to the velocity and to the area A of each plate, and inversely proportional to the distance L between the plates. F also clearly depends on the nature of the fluid, in particular on the dynamic viscosity μ .

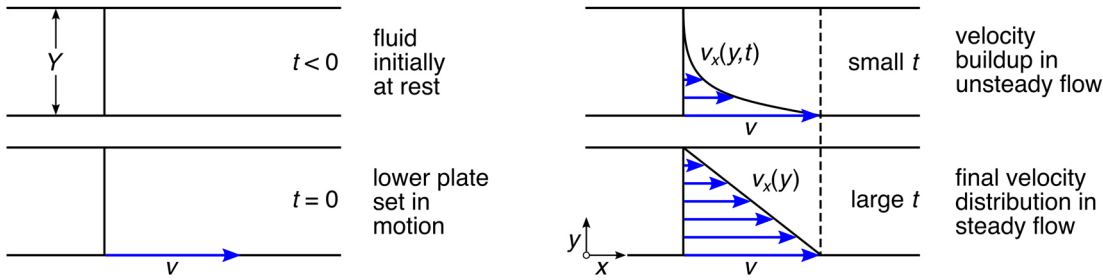


Fig. 2-9 Timescale of the velocity profile formation of a fluid between two plates from rest until reaching the laminar, steady state (Bird et al., 2002).

If the ratio F/A is written as τ_{xy} , where x subscript indicates the direction of the force F and y subscript the direction perpendicular to the area A , the following is easily stated

$$\tau_{xy} = -\mu \frac{\partial v_x}{\partial y} \quad (2-19)$$

This equation is the *Newton's law of viscosity* and shows how the shear force τ_{xy} depends on the velocity gradient and on the viscosity coefficient μ . Since the force is exerted by the fluid at small y to the part of the fluid at high y , the sign minus in the formula is needed. The units of shear force as the unit of a pressure are

$$[\tau_{xy}] = \text{Pa s} \cdot \text{m s}^{-1} \cdot \text{m}^{-1} = \text{Pa} \quad (2-20)$$

The shear stress τ_{xy} can also be interpreted as the flux (flow per unit area) of the x momentum in the positive y direction. Since the lower plate, located at $y = 0$ in the reference system, starts moving, the part of the fluid that touches the plate acquires an x momentum, which is transmitted to the adjacent layer of fluid along the y direction. It follows that momentum is

transported from a region of high velocity to a region of low velocity. Thus, from this perspective, the velocity gradient of the Newton's law can be seen as a driving force for momentum transport.

Next up, the definition of the strain tensor and the introduction of the normal stress is given. In general, a force acting on a surface can be decomposed in two components: the normal component σ along the normal to the surface and the tangential component τ along the tangent to the surface, see **Fig. 2-10** (A). In a cylindrical vessel with a rotating coaxial cylinder, the volume of fluid inside the vessel is subject to stress on the surface, see **Fig. 2-10** (B). The stress tensor $\underline{\tau}$ contains nine components and is defined by

$$\underline{\tau} = \begin{bmatrix} \tau_{xx} & \tau_{xy} & \tau_{xz} \\ \tau_{yx} & \tau_{yy} & \tau_{yz} \\ \tau_{zx} & \tau_{zy} & \tau_{zz} \end{bmatrix} \quad (2-21)$$

where in τ_{ij} the index i indicates the direction of the force F along an area A and j the direction perpendicular to the area A . The stress tensor is a symmetric matrix, so

$$\tau_{ij} = \tau_{ji}, \text{ with } i \neq j \quad (2-22)$$

whereby the components $i \neq j$ are shearing stresses (τ_{xy} , τ_{yx} , τ_{xz} , τ_{zx} , τ_{yz} , τ_{zy}) and the components $i = j$ denote normal stresses (τ_{xx} , τ_{yy} , τ_{zz}) representing the compression or the expansion that occurs in the fluid.

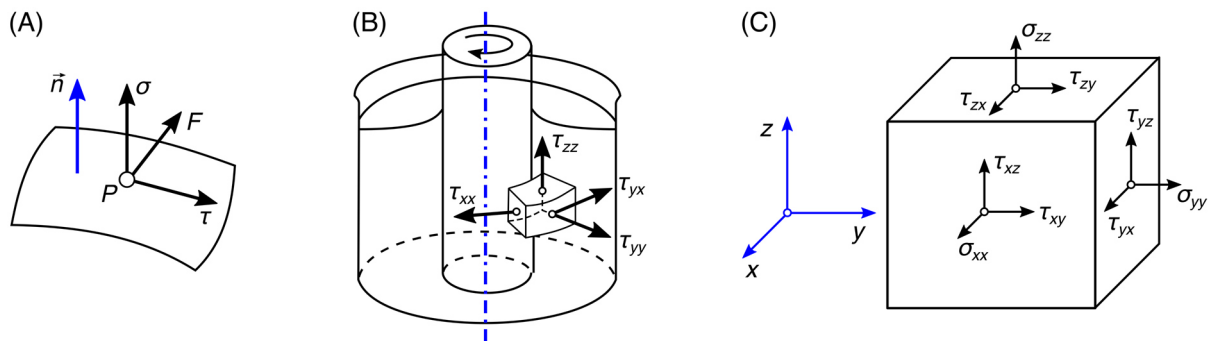


Fig. 2-10 Stress acting in a fluid element: (A) normal and tangential component, (B) stress components of a fluid around a rotating coaxial cylinder (Paul et al., 2004), (C) cubic volume of fluid with its stress components

Another notation for the strain tensor is

$$\underline{\sigma} = \begin{bmatrix} \sigma_x & \tau_{xy} & \tau_{xz} \\ \text{sym} & \sigma_y & \tau_{yz} \\ & & \sigma_z \end{bmatrix} \quad (2-23)$$

Considering the system represented in the **Fig. 2-10** (B), since the rotational flow, and consequently the shear, acts along the x direction, the following simplification can be done: $\tau_{xy} = \tau_{yx} \neq 0$, $\tau_{xz} = \tau_{zx} = 0$, $\tau_{yz} = \tau_{zy} = 0$.

When the fluid is static there are only the normal components, since there is no relative motion between the adjacent layers of the fluid. This is translated with null shear stresses

$$\tau_{ij} = 0, \text{ with } i \neq j \quad (2-24)$$

A normal component can also be elucidated by the *divergence* of the fluid's velocity vector field. When the divergence is positive, it means that the velocity gradient is positive in its flow direction (normal to the flow). So, the fluid element is stretched in that direction, whereas when the divergence is negative the fluid compresses, also referred to as *convergence*.

Wille et al. (2001) suggested to describe the strain as a condensed and directed sum of gradients according to the cartesian directions x, y, z by

$$G_i^{xyz} = \left| \frac{\partial v_x}{\partial i} \right| + \left| \frac{\partial v_y}{\partial i} \right| + \left| \frac{\partial v_z}{\partial i} \right|, \text{ with } i \in \{x, y, z\} \quad (2-25)$$

In *DaVis*, the computation of shear follows the quantity E_{ij} , defined in **Eq. (2-18)**. In 2D, velocity is $\vec{v} = [v_x, v_y]^T$, and the velocity gradient is calculated by

$$\underline{V} = \begin{bmatrix} E_{xx} & E_{xy} \\ E_{yx} & E_{yy} \end{bmatrix} \quad (2-26)$$

Analogously to the approach of Haimes and Kenwright (1999), the software calculates the eigenvalues λ_1, λ_2 of the tensor. These are in the form $a \pm b^{1/2}$, with

$$b = E_{xy}E_{yx} - \frac{E_{xx}E_{yy}}{2} + \frac{E_{xx}^2 E_{yy}^2}{4} \quad (2-27)$$

If b is positive, it is shear, and the software displays the shear strength with the values $\max(0, b)$. If b is negative, it is swirl, and the values displayed for the swirling strength are $\max(0, -b)$.

3D shear is calculated by the software only when it is possible to differentiate the velocity components with respect to a third coordinate z , and this happens when the analysis is carried out with more than one z plane, like with 3D Particle Tracking Velocimetry (PTV) and Tomographic PIV. **Eq. (2-35)** shows the availability of the elements of the velocity gradient tensor \underline{V} dependent on what PIV setup is used.

$$\underline{D} = \underline{V} = \begin{bmatrix} \overbrace{\begin{pmatrix} E_{xx} & E_{xy} \\ E_{yx} & E_{yy} \end{pmatrix}}^{\substack{\text{available for} \\ \text{2D and 3D}}} & \begin{pmatrix} E_{xz} \\ E_{yz} \\ E_{zz} \end{pmatrix} \\ \underbrace{\begin{pmatrix} E_{zx} & E_{zy} \end{pmatrix}}_{\substack{\text{available} \\ \text{only for 3D}}} & \underbrace{\begin{pmatrix} E_{zz} \end{pmatrix}}_{\substack{\vec{0}, \text{ for single } z \text{ plane}}} \end{bmatrix} \quad (2-28)$$

The summing-up of single velocity gradients out of this global tensor into an average velocity gradient $\dot{\gamma}$, also termed *shear strain rate*, is defined by

$$\begin{aligned}\dot{\gamma}^2 &= 1/2 \cdot \text{tr} \left[(\underline{D} + \underline{D}^T)^2 \right] \\ &= 2(E_{xx}^2 + E_{yy}^2 + E_{zz}^2) + (E_{xy} + E_{yx})^2 + (E_{xz} + E_{zx})^2 + (E_{yz} + E_{zy})^2\end{aligned}\quad (2-29)$$

with $\text{tr}(A)$ as the trace, being the sum of the diagonal elements of a matrix A . The transformation of the global velocity gradient tensor \underline{D} to a local tensor $\underline{\tilde{D}}$, which is aligned with the flow, is performed by a transformation matrix C according to

$$\underline{\tilde{D}} = C \cdot \underline{D} \cdot C^T = \begin{bmatrix} \tilde{E}_{xx} & \tilde{E}_{xy} & \tilde{E}_{xz} \\ \tilde{E}_{yx} & \tilde{E}_{yy} & \tilde{E}_{yz} \\ \tilde{E}_{zx} & \tilde{E}_{zy} & \tilde{E}_{zz} \end{bmatrix} \quad (2-30)$$

whereby $\tilde{E}_{ij} = \partial \tilde{v}_i / \partial j$, with $i \in \{x, y, z\}$ and $j \in \{\tilde{x}, \tilde{y}, \tilde{z}\}$. The \tilde{x} component of the resulting coordinate system after transform points in the direction of the flow, see **Fig. 2-11**.

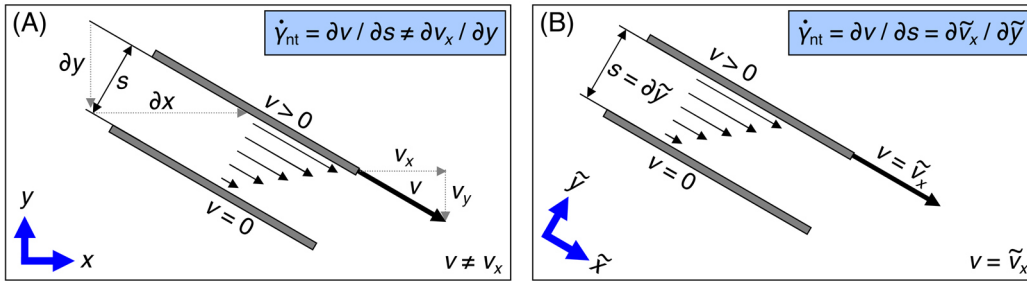


Fig. 2-11 Reference frames referred to the flow stream used for the calculation of the velocity gradients: (A) stream lines not parallel to x coordinate, (B) stream lines parallel to \tilde{x} coordinate (Wollny, 2010).

The transformation matrix C is composed of three orthogonal vectors as per

$$C = \begin{bmatrix} \vec{v}_{C1} \\ \vec{v}_{C2} \\ \vec{v}_{C3} \end{bmatrix} = \begin{bmatrix} (v_x/|\vec{v}|) & (v_y/|\vec{v}|) & (v_z/|\vec{v}|) \\ (v_{ox}/|\vec{v}_0|) & (v_{oy}/|\vec{v}_0|) & (v_{oz}/|\vec{v}_0|) \\ \vec{v}_{C1} \times \vec{v}_{C2} \end{bmatrix}, \text{ with } \vec{v}_0 = \begin{pmatrix} v_y - v_z \\ v_z - v_x \\ v_x - v_y \end{pmatrix} \quad (2-31)$$

and with $|\vec{v}|$ and $|\vec{v}_0|$ being the magnitudes of the respective vectors. The local velocity gradient tensor $\underline{\tilde{D}}$ again allows the calculation of an average velocity gradient $\tilde{\gamma}$, which is invariant and equal to the one defined in **Eq. (2-36)**.

$$\dot{\gamma} = \tilde{\gamma} = 2(\tilde{E}_{xx}^2 + \tilde{E}_{yy}^2 + \tilde{E}_{zz}^2) + (\tilde{E}_{xy} + \tilde{E}_{yx})^2 + (\tilde{E}_{xz} + \tilde{E}_{zx})^2 + (\tilde{E}_{yz} + \tilde{E}_{zy})^2 \quad (2-32)$$

The new direction of the velocity gradients allows the definition of the normal gradient $\dot{\gamma}_{nn}$ and the shear gradient $\dot{\gamma}_{nt}$, see **Eqs. (2-40) and (2-34)**, respectively.

$$\dot{\gamma}_{nn} = \sqrt{2\tilde{E}_{xx}^2} = \sqrt{2} \cdot \frac{\partial \tilde{v}_x}{\partial \tilde{x}} \quad (2-33)$$

$$\dot{\gamma}_{nt} = \sqrt{(\tilde{E}_{xy} + \tilde{E}_{yx})^2 + (\tilde{E}_{xz} + \tilde{E}_{zx})^2} = \sqrt{\left(\frac{\partial \tilde{v}_x}{\partial \tilde{y}} + \frac{\partial \tilde{v}_y}{\partial \tilde{x}}\right)^2 + \left(\frac{\partial \tilde{v}_x}{\partial \tilde{z}} + \frac{\partial \tilde{v}_z}{\partial \tilde{x}}\right)^2} \quad (2-34)$$

Rotational Motion of the Fluid: Vorticity

A simplistic way to define vorticity is describing it as the spiral pattern of the flow. In mathematical terms the vorticity vector $\vec{\omega}$ is the curl of velocity, representing the measure of the solid body rotation

$$\vec{\omega} \stackrel{\text{def}}{=} \nabla \times \vec{v} = \begin{bmatrix} \partial w / \partial y - \partial v / \partial z \\ \partial u / \partial z - \partial w / \partial x \\ \partial v / \partial x - \partial u / \partial y \end{bmatrix} = \begin{bmatrix} \omega_x \\ \omega_y \\ \omega_z \end{bmatrix} \quad (2-35)$$

This vector is defined by the terms contained in the antisymmetric part of the velocity gradient $\underline{\underline{\Omega}}$.

$$\underline{\underline{\Omega}} = \frac{1}{2} (\underline{\underline{V}} - \underline{\underline{V}}^T) = \frac{1}{2} \begin{bmatrix} 0 & -\omega_z & \omega_y \\ \omega_z & 0 & -\omega_x \\ -\omega_y & \omega_x & 0 \end{bmatrix} \quad (2-36)$$

In a turbulent fluid flow, the vorticity is shown in the form of a phenomenon called vortex, a region of fluid that rotates around an axis.

k - ε Model: Turbulence Kinetic Energy and Turbulence Dissipation Rate

The physical behaviour of the flow is described by Navier-Stokes equations, which are partial differential equations (PDE). The mathematical solution of these complicated equations is not feasible for a turbulent flow, because of the presence of fluctuating terms that are not predictable nor calculable. For this reason, a study approach is the flow averaging, which uses the Reynolds-averaged Navier-Stokes equations: The PDEs are averaged in a lapse of time that is large enough to include the turbulence phenomena. This simplification makes the problem indeterminate, hence there comes the necessity of other equations to have the same number of unknown variables and conditions. A solution to this indeterminate problem is introduced by Jones and Launder (1972), proposing the k - ε model, used in CFD to describe the turbulent behaviour of the fluid. This model is based on two transport equations that refer to the turbulence kinetic energy (TKE) k and to the turbulence dissipation rate ε .

In a turbulent flow, $\vec{v}(t)$ does not have a constant value, and it can be described, through the Reynolds decomposition, as the sum of the mean and the turbulent velocities, as represented in **Fig. 2-12 (A)**.

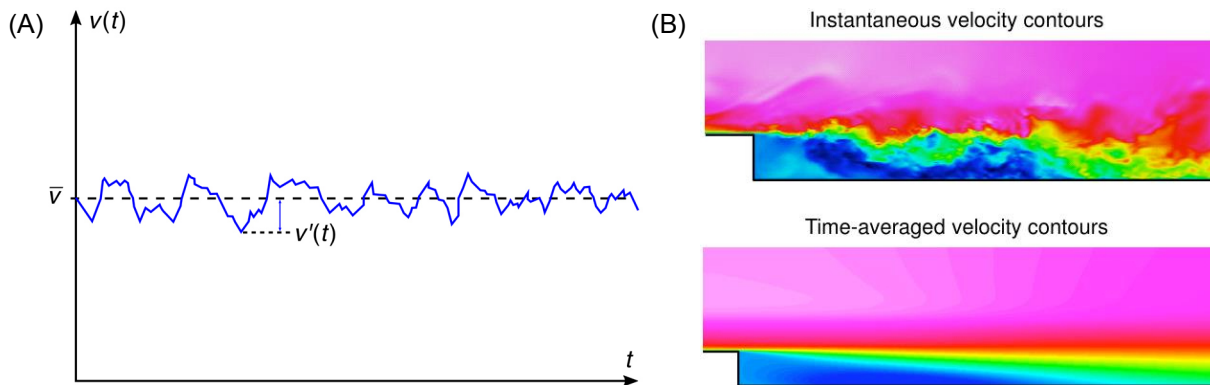


Fig. 2-12 (A) Mean and turbulent velocities. (B) Instantaneous velocity and time-averaged velocity (ANSYS, 2009).

The instantaneous velocity contains both parts, so, supposing to do the average of several instantaneous velocity values, what ideally happens to the fluid is illustrated in **Fig. 2-12 (B)**. For each component v_i , the velocity along $i = x, y, z$ is composed of

$$v_i(t) = \overline{v_i} + v_i'(t) \quad (2-37)$$

TKE k is the specific kinetic energy of the turbulent fluctuations v_i' in a turbulent flow. It is the energy generated by the shear forces exerted in the fluid, and it is transferred from large eddies to smaller eddies through a phenomenon called *turbulent energy cascade*, see **Section 2.4.1**. TKE represents the energy contained in the fluctuations of the turbulent flow according to

$$k = \overline{v_i'v_i'}/2 = (\overline{v_x'^2} + \overline{v_y'^2} + \overline{v_z'^2})/2 \quad (2-38)$$

If the value of the fluctuation velocity is the same for the three coordinates, then

$$k = 3/2 \cdot \overline{v'^2} \quad (2-39)$$

The SI unit of k is that of mass-specific energy as per

$$[k] = \text{J} \cdot \text{kg}^{-1} = \text{N m} \cdot \text{kg}^{-1} = \text{kg m}^2 \text{s}^{-2} \cdot \text{kg}^{-1} = \text{m}^2 \text{s}^{-2} \quad (2-40)$$

Turbulence dissipation rate ε , or energy dissipation rate (EDR), refers to the rate at which the turbulence kinetic energy is converted into thermal internal energy, with SI unit $\text{J kg}^{-1} \text{s}^{-1} = \text{m}^2 \text{s}^{-3}$. This quantity determines the scale (intensity) of the turbulence. The definition of EDR in **Eq. (2-41)**, with ν being the kinematic viscosity of unit $\text{m}^2 \text{s}^{-1}$, is valid for incompressible fluids, that are not affected by the pressure field.

$$\varepsilon = \nu \frac{\overline{\partial u_i'} \partial u_i'}}{\partial x_k \partial x_k} \quad (2-41)$$

2.4 Fluid Mixing

Mixing of fluids represents one of the fundamental unit operations of chemical and industrial processes. It can be performed either mechanically or pneumatically, by using a rotating impeller and an air stream respectively, whereby the former method is the most used as well as the one employed in this experimental work.

Mixing is a physical mechanism that aims at removing, or at least at reducing, the inhomogeneity of the properties in the reactor, such as concentration and temperature gradients. With higher mixing efficiency, the reactor's performance increases. The purposes of mixing are multiple: suspension of solid particles in a liquid, mixing of two or more miscible liquids, emulsion of immiscible liquids, dispersion of a gas in the liquid phase, promoting the mass transfer and the heat exchange (Hemrajani and Tatterson, 2004).

In the case of a bioreactor, the mixing operation aims at promoting the contact between the biotic phase and the nutrients, which include oxygen when the bioreactor is aerobic.

Especially for bioreactors, it is important to investigate the effects of mixing on the biotic phase, because of mechanical stress phenomena that may cause irreversible damages, see **Section 2.5**.

This operation is carried out in mechanically stirred tanks, that are cylindrical vessels, generally vertical, provided with a mixer consisting of an impeller, a shaft, a motor and a gearbox (**Fig. 2-13**). The principal equipment is the impeller, which requires a certain power input to move at the rotational frequency that is indicated in the design specifications. Evidently the required energy for the implementation of mixing represents a considerable contribution for the overall costs of the process.

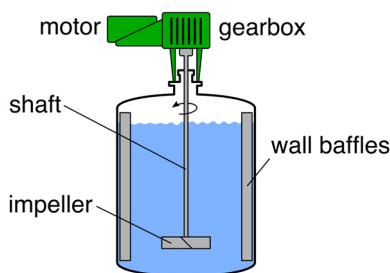


Fig. 2-13 Conventional mechanically stirred vessel (Hemrajani and Tatterson, 2004)

Fluid mechanics and physical phenomena relative to mixing are very complex, so that the resulting efficiency of the operation is profoundly affected by many different parameters:

- design of the impeller: shape, size, number and orientation of the blades
- geometry and dimensional relations of impeller and vessel: location of the impeller and its size relative to the vessel

Stirred vessels, where transitional and turbulent mixing is performed, contain baffles, long flat plates that are generally installed at the vessel's wall. The function of baffles is not only avoiding the vortexing of the fluid and increasing the turbulence. As a matter of fact, helical coils, pipe baffles and plate coil baffles can be placed in the vessel to improve the heat exchange (Hemrajani and Tatterson, 2004). Clearly the presence of baffles modify the overall shape, and it is well-known that any minor change in the vessel geometry has substantial effects on the flow pattern and hence on the mixing characteristics (Nere et al., 2003).

2.4.1 Mechanism of Mixing

The mechanism of mixing is the result of three distinct phenomena: distribution, dispersion and diffusion. These phenomena can be respectively described as motion at three different levels: bulk, eddy and molecular motion (Nere et al., 2003).

The description of these mechanisms needs to be preceded by the introduction of the concept of eddy motion, to understand how this phenomenon occurs and affects the mixing.

Here the explanation of the mixing mechanism takes advantage of the *Kolmogorov's theory on the isotropic turbulence*, briefly presented below (Kolmogorov, 1968; 1991a; 1991b).

In turbulent conditions, the fluid is characterized by the presence of molecular circulating aggregates called eddies, which are able to transport and distribute the kinetic energy k , originally introduced in the vessel by the impeller blades, in different regions of the fluid.

In the Kolmogorov's theory, eddies are assumed to bump into other eddies and to progressively convert into smaller eddies. When eddies reach a certain size, that corresponds to the Kolmogorov length scale η , they are not able to hold the rotational motion anymore, because their energy is not high enough. Hence, they remain in a certain position and they dissipate the remaining energy in the form of heat by means of positional vibrations. Eddies have a size l and a characteristic velocity $u(l)$, producing a timescale $\tau(l) = l/u(l)$. The Reynolds number corresponding to the turbulent flow with these conditions is

$$Re_l = \frac{u(l) \cdot l}{\nu} \quad (2-42)$$

The Kolmogorov's theory makes a division, based on the size of the eddies, in the energy that they contain, considering the larger eddies having size l_0 . It proposes the existence of two macro-fields: the first one referring to primary eddies and the second one indicated as universal equilibrium range. The latter consists of the dissipation range and the inertial subrange, see Fig. 2-14.

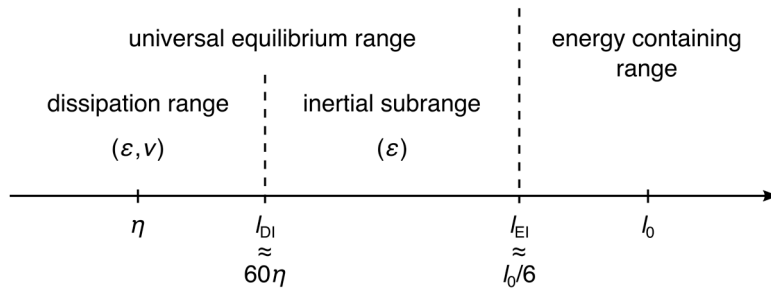


Fig. 2-14 Eddy length scale in Kolmogorov's theory. Subscripts: DI Dissipation-Inertial, EI Energy-Inertial.

Kolmogorov elaborated this theory by making three assumptions, of which the first is the *local isotropy hypothesis*. This hypothesis states that at very large Reynolds numbers, the eddies with size $l \ll l_0$ are statistically isotropic. This means that for these small-scale turbulent motions, TKE is homogeneous because of the same behaviour of eddies in all directions. Hence,

$$\overline{v_x'^2} = \overline{v_y'^2} = \overline{v_z'^2} \quad (2-43)$$

Large eddies instead, are anisotropic: the demarcation line between anisotropic and isotropic eddies is represented by the length scale l_{EI} , which can be estimated as $l_{EI} \approx l_0/6$.

The *energy containing range* ($l > l_{EI}$) includes primary eddies, which are the largest. Their size is determined by the size of the impeller blades in the stirred vessel. Primary eddies, responsible for the macro-mixing, gradually transfer the kinetic energy introduced by the impeller to smaller eddies through the so-called turbulent energy cascade.

The second assumption of Kolmogorov's theory is the *first similarity hypothesis*, that states that the statistics of small eddies, i.e. with size $l < l_{EI}$, depends uniquely on the dissipation rate ϵ and on the kinematic viscosity ν .

The third and last assumption of this theory is the *second similarity hypothesis*. It states that in a turbulent flow, there exists a range that goes from larger eddies to eddies at the Kolmogorov scale, $\eta \ll l \ll l_0$, where Re_l is relatively high, so that the effect of the viscosity is

negligible, hence the phenomena depend only on ε . This is the *inertial range*, that belongs to the universal equilibrium range. The *viscous range* is characterized by the viscous dissipation of the energy of the small eddies into heat. The length scale that divides the inertial and the viscous ranges is l_{DI} , which can be estimated as $l_{DI} \approx 60 \eta$.

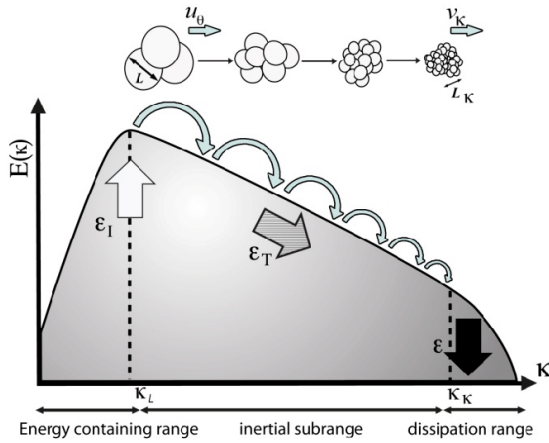


Fig. 2-15 Sketch of the energy cascade showing large eddies being broken into smaller and smaller eddies (Sagaut, 2006).

Additionally, the length scale can be referred to another quantity, the wavenumber κ , being defined by

$$\kappa = \frac{1}{l} \quad (2-44)$$

In **Fig. 2-15**, the energy spectrum $E(\kappa)$ is represented. This is the energy contained in the eddies with wavenumber $\kappa(l)$. The integral of $E(\kappa)$ over wavenumber κ corresponds to the turbulence kinetic energy k with

$$k = \int_0^{\infty} E(\kappa) d\kappa \quad (2-45)$$

It should be reminded that in the turbulent flow regime it is necessary to always consider local properties. The Kolmogorov microscale η indeed has not a unique value, but changes in every point of the reactor. By knowing the dependence of the length η on the kinematic viscosity ν and on the dissipation rate ε , with units $\text{m}^2 \text{s}^{-1}$ and $\text{m}^2 \text{s}^{-3}$ respectively, the definition is made with a dimensional analysis

$$\eta = \nu^\alpha \cdot \varepsilon^\beta \quad (2-46)$$

The solution of the exponents α and β gives the definition of Kolmogorov microscale as

$$\eta = \nu^{3/4} \cdot \varepsilon^{-1/4} = \left(\frac{\nu^3}{\varepsilon} \right)^{1/4} \quad (2-47)$$

For a stirred vessel operating with a single liquid phase, the average turbulent dissipation rate $\overline{\varepsilon_T}$ can be calculated with the formula (Delafosse et al., 2011)

$$\overline{\varepsilon_T} = \frac{P}{\rho V} \quad (2-48)$$

considering P the power input implemented to the fluid by the impeller, and V the volume of the fluid in the stirred vessel.

The turbulent flow motion and the transfer of energy inside the fluid constitute the mechanisms that establish mixing.

Distribution is a mechanism referred to as macro-mixing and it is responsible for the transport of the fluid material in all regions of the vessel, acted by bulk circulation streams. This process is related to macro-circulation and can represent a limiting process for the mixing in the case of big reactors. Indeed circulation paths are here longer, hence the circulation time is bigger.

It should be reminded that the circulation time θ_C is an important parameter for mixing and can be defined as the necessary time for a particle of the fluid to go from a specific point and return to the same spatial point inside the reactor. To more precisely define and to measure the circulation time θ_C , a tracer is added into the fluid that is moving in the stirred vessel. A detector placed in the vessel saves the values of the concentration C of the tracer, that changes in time in the transient state, until the stationary C_∞ is reached. The time lapse between two peaks in the curve $C(t)$ is defined as circulation time, and the time at which the steady state is developed is called mixing time θ_M , see **Fig. 2-16** (Nienow, 1997). The importance of θ_C lays on the fact that it tells how much time the particles of the fluid are spending in different regions of the reactor, which are characterized by quite various properties. The mixing time θ_M is used to indicate the mixing efficiency of the impeller. Concerning the circulation paths, these evidently depend on the type of stirrer, since it effects the flow.

Dispersion is the mixing mechanism that refers to the eddy dispersion.

Diffusion is a process that involves the molecular motion of distinct particles and diminishes the concentration gradients. This mechanism is referred to as micromixing, which is controlled by the turbulence dissipation rate (Liu et al., 2008).

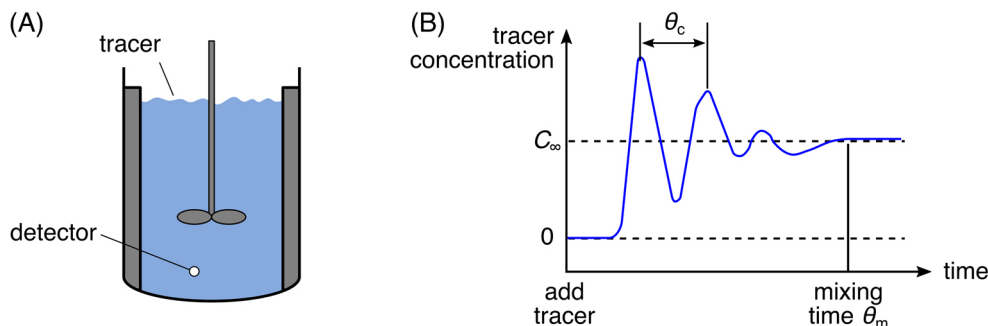


Fig. 2-16 Measurement of circulation and mixing times (Nienow, 1997).

Mixing takes part in the majority of industrial chemical processes. The used equipment can perform mechanical and pneumatical agitation.

Among the different types of reactors in which mixing is performed, the *stirred vessel*, illustrated in **Fig. 2-13**, is the one of interest in this work, and its characteristics will be presented in the next sections.

Pneumatical agitation is performed in the *bubble column*, where a sparger placed in the bottom of the tank releases the gaseous phase. Analogously to the airlift bioreactor shown in **Section 2.1.3**, the gas in the bubble column increases the mass transfer by increasing the gas-liquid interfacial area. An important parameter for the efficiency of mixing is the hold up of the gaseous phase Φ_g (Hemrajani and Tatterson, 2004), defined as

$$\Phi_g = \frac{H_g - H}{H} \quad (2-49)$$

where H_g is the height of the volume including the gaseous phase, and H is the level without aeration (Zhu et al., 2009).

2.4.2 Flow Patterns in Stirred Vessels

The choice of impeller and vessel geometries produces a certain flow pattern. It is important to mention that the velocity in every spatial point of a stirred tank has three components: axial, radial and tangential, see **Fig. 2-17**. The axial and radial components are defined in the direction that is parallel and perpendicular to the stirrer axis, respectively; the tangential component is oriented along or in the direction of a tangent to the stirrer perimeter.

The typical flow patterns of the secondary flow in the stirred vessel are the radial flow and the axial flow, generated by specific impeller types. Beside the impeller, also baffles play an essential role in the development of the flow pattern and on the mixing efficiency. Without baffles, indeed, the tangential component of the velocity is not “balanced” and the resulting flow exhibits the so-called fluid swirl. In other words, the flow can be described as a solid body motion, because of the tangential component that creates a vortex pushing the liquid to the top of the tank along the walls (R. Hemrajani, 2004). Therefore, in order to avoid the vorticing and swirling of the fluid, as well as to promote a proper mixing in the axial direction between the top and the bottom of the vessel (R. Hemrajani, 2004), baffles are installed in the majority of cases, thanks to their ability of deflecting the tangential velocity component. In addition, it is remarkable to mention that the width of the baffle is suggested to not be too big with respect to the diameter of the tank, in favor of small stagnant regions in the tank, which may reduce the mixing efficiency. All of this introductory information about the mixing in a stirred vessel is summarized and illustrated in **Fig. 2-18**.

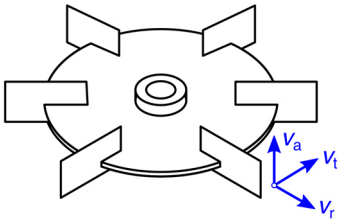


Fig. 2-17 Radial, axial and tangential components of velocity.

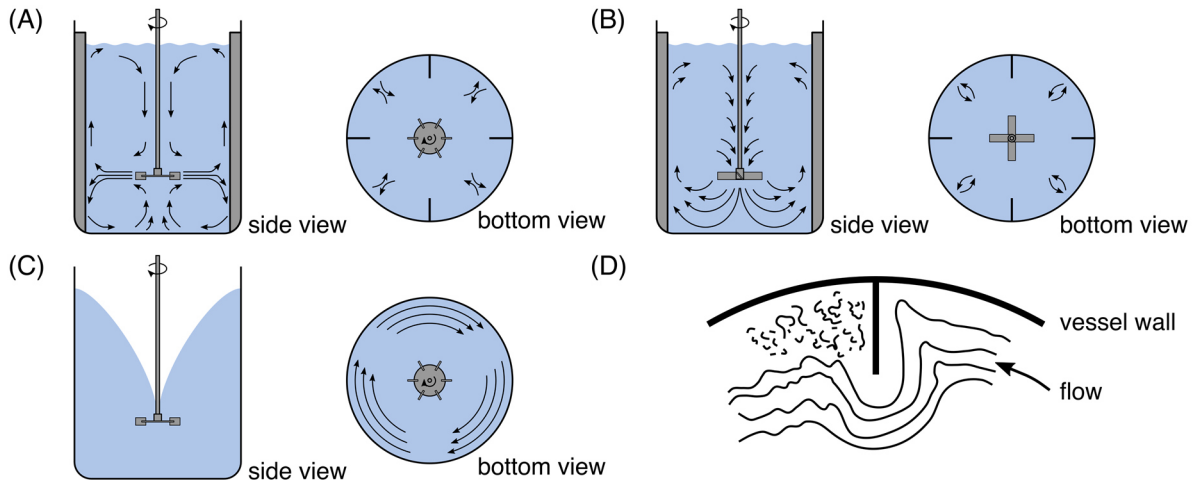


Fig. 2-18 (A) Secondary flows in a stirred vessel with radial impeller. (B) Secondary flows in a stirred vessel with axial impeller. (C) Vortex formation in a stirred vessel without baffles. (D) Stagnant area due to the presence of baffles.

The operating conditions in a stirred vessel depend on the dimensioning of the mixing equipment, which includes vessel, baffles and impeller. The important lengths, see **Fig. 2-19**, that must be taken into account are:

- D diameter of the vessel
- H height of the fluid inside the vessel (filling height)
- J_B width of the baffles
- e clearance of the baffles
- d diameter of the impeller
- C clearance of the impeller, i.e. the distance between the bottom of the vessel and the centre of the impeller
- l length of impeller blade
- h width of impeller blade

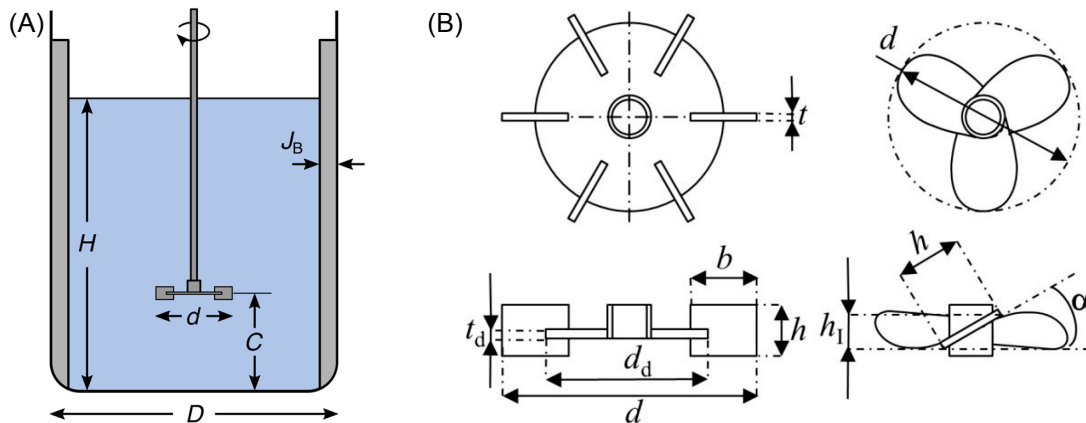


Fig. 2-19 Important characteristic geometrical lengths: (A) vessel, (B) impeller (Bliatsiou et. al, 2018b).

Additionally, also the number of the baffles, generally four, and the number of the impeller blades, six for a Rushton turbine, have a substantial effect on the mixing (R. Hemrajani, 2004).

For the design of the stirred vessel, the singular absolute lengths have no meaning for the characterization of the system. Hence, it is important to consider the relative geometry of the equipment, expressed with the ratios summarized in **Tab. 2-1**.

Tab. 2-1 Relative geometries in a stirred vessel.

Geometrical ratio	Common values	References
J/D	1/12 until 1/10	(Hemrajani and Tatterson, 2004)
d/D	1/3	(Li et al., 2011)
H/D	1, when > 1 another impeller on the same shaft should be added	(Aubin and Xuereb, 2006; Armenante et al., 1999)
C/D	1/3, 0.15	(Li et al., 2011)
h/D	1/5 for standard Rushton turbine	(Hemrajani and Tatterson, 2004)
l/d	1/4 for standard Rushton turbine	(Hemrajani and Tatterson, 2004)

Subsequently, some characteristic quantities of mixing in a stirred vessel are defined. The tip speed u_{tip} is a scalar quantity, that indicates the speed of the point corresponding to the external edge of the impeller blade. Considering N , the impeller frequency (s^{-1}), the tip speed is defined by

$$u_{\text{tip}} = \pi d N \quad (2-50)$$

The Reynolds number, as mentioned in **Section 2.3**, is an important dimensionless number that characterizes the flow regime of a system. For a stirred vessel, Re can be calculated with the formula

$$Re = \frac{\rho N d^2}{\mu} \quad (2-51)$$

The power input is the power supplied to the impeller to rotate, according to

$$P = \rho N^3 d^5 \cdot Ne \quad (2-52)$$

where Ne is the Newton number, often indicated as power number N_P , which depends on impeller geometry, including number of blades and their width and angle, on the configuration of the baffles and on the impeller clearance (Hemrajani and Tatterson, 2004). Usually P is referred to the volume V of fluid contained in the vessel.

2.4.3 Impeller Types

For an industrial process where mixing is performed, it is necessary to understand what is the best equipment to employ. In particular, the choice of the impeller must be adequate to the requirements of the process. Generally, the turbines can be categorized in two main groups, depending on the flow pattern that they produce. Those are the axial and the radial flow impellers. The rheological properties of the fluid, i.e. the viscosity, is determinant on the choice of the most proper impeller for the process, **Fig. 2-20**.

Axial flow impellers are mainly used for solid suspensions, gas inducement and heat transfer. The most common, among this class, are the propellers and the pitched blade turbines (PBT). The propeller consists of three blades, while the PBTs have an even number of blades, which form an angle with the horizontal that can vary from 10° to 90° . (Hemrajani and Tatterson, 2004)

Radial flow impellers are especially recommended for gas-liquid and liquid-liquid dispersion. The typical example of this category is the Rushton turbine, consisting of a disk with six blades. The disk is the element responsible for the generation of the radial flow: the impeller discharge is radial and the fluid is pumped upward and downward, when impinging on the wall of a baffled vessel. (Hemrajani and Tatterson, 2004)

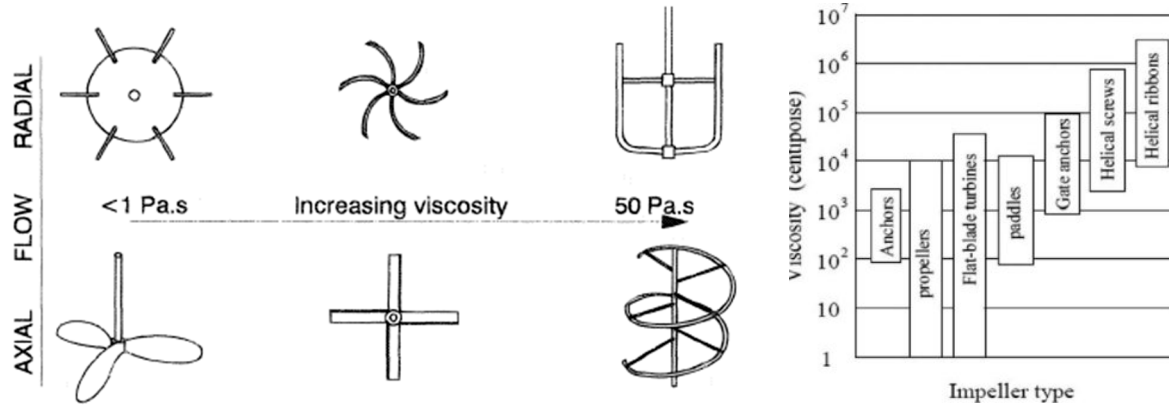


Fig. 2-20 Impeller types and use according to the viscosity of the fluid to mix, (Doran, 2012).

The impeller characteristics and the mixing efficiency that these provide are described with parameters like power number Ne , mixing time θ_M and flow number Fl . The power number is a dimensionless number, defined as

$$Ne = \frac{2\pi NM}{\rho N^3 d^5} = \frac{P}{\rho N^3 d^5} \quad (2-53)$$

where M is the impeller shaft torque (Nm). The power number is a fundamental impeller parameter, of which use is essential for the calculation of the power required by the mixing operation (Chudacek, 1985).

Experimentally, it is possible to measure the torque and see how this changes with the change of rotational frequency of the impeller. By knowing the properties of the fluid and the diameter of the impeller, the impeller Reynolds number can be calculated and be correlated with the power number. Some experimental results by Hemrajani and Tatterson (2004) are shown in **Fig. 2-21**. The curves clearly show a trend that is common for the different impellers: for small values of Re , so in the laminar regime, the power number is proportional to the reciprocal of the Reynolds number. In the transitional region, where $10^2 < Re < 10^4$, the dependency of Ne on Re considerably decreases until the turbulent regime is reached and the power number remains at a constant value.

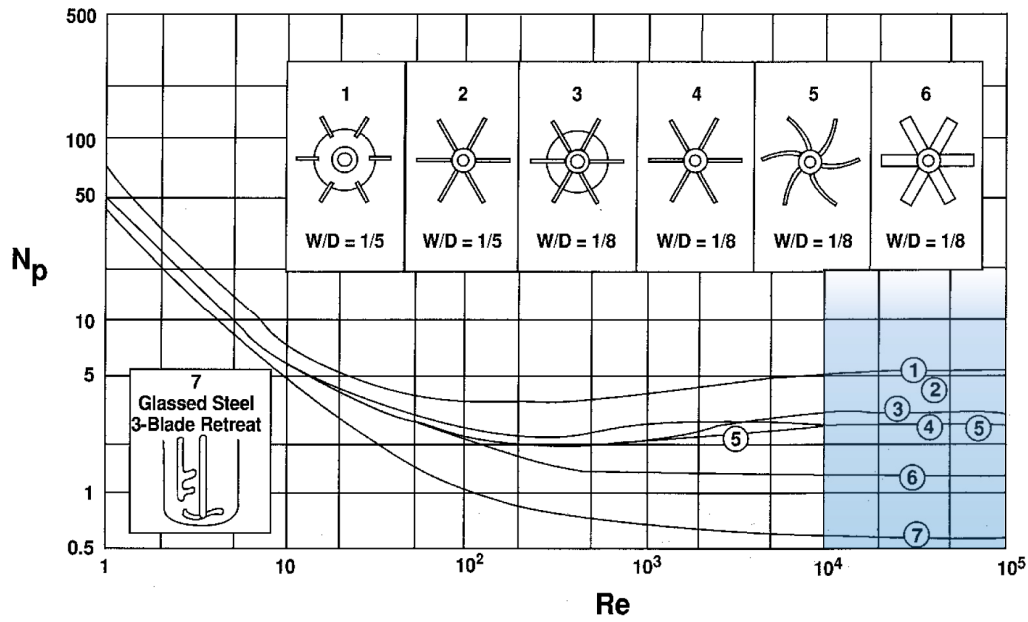


Fig. 2-21 Characteristic curves of the power number as a function of Reynolds number, relative to different impeller geometries, (Kumaresan and Joshi, 2006).

Another dimensionless number is the flow number Fl , also indicated in literature as pumping number N_{Qd} , or primary flow number N_{QP} (Ge et al., 2014; Kumaresan and Joshi, 2006; Nienow, 1997). It represents the capacity of the impeller to pump the fluid in a given geometry, and it is used to describe the impeller efficiency (Chudacek, 1985). The mathematical definition of Fl includes Q , that is the volumetric flow rate ($\text{m}^3 \text{s}^{-1}$) discharged by the impeller, see Eq. (2-54).

$$Fl = \frac{Q}{Nd^3} \quad (2-54)$$

The type of impeller determines the flow, so also the discharge flow. The flow Q corresponds to the flow that crosses the swept volume V_s (Aubin et al., 2001) according to

$$V_s = \frac{\pi}{4} d^2 h \quad (2-55)$$

Nienow (1997) represents the discharge flow of radial and axial impellers with Fig. 2-22.

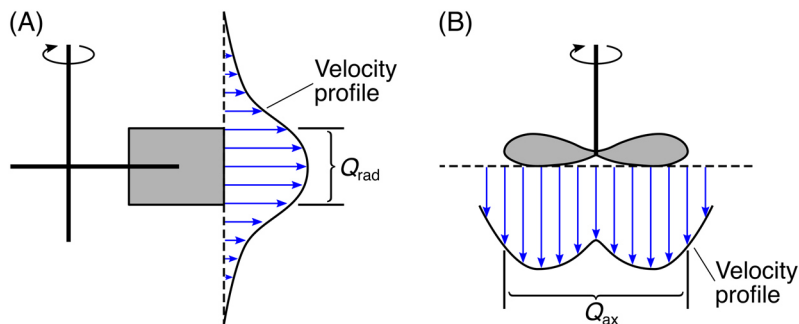


Fig. 2-22 Impeller discharge flow: (A) radial flow impeller, (B) axial flow impeller, (Nienow, 1997).

Considering r and z the radial and the axial coordinates, respectively, with the origin of this reference frame located in the centre of the impeller, it is possible to define Q . For a radial

impeller Q_{rad} is the flow that passes through the outer lateral surface of the swept volume πdh , with radial velocity $v_r(z)$

$$Q_{\text{rad}} = \int_{-h/2}^{h/2} v_r(z) 2\pi r dz \quad (2-56)$$

For an axial impeller, the flow discharge crosses the imaginary disk below the impeller, with area $\pi d^2/4$ with the axial velocity $v_z(r)$. Kumaresan and Joshi (2006), define Q_{ax} with the formula

$$Q_{\text{ax}} = \int_0^{d/2} v_z(r) 2\pi r dr \quad (2-57)$$

Another parameter that describes the quality of mixing performed by the impeller is the mixing time. Holmes et al. (1964) define the mixing time θ_M , after which the concentration in the vessel is stationary, as 5 times the circulation time θ_C . The calculation of θ_C , and so of θ_M as well, proposed by McManamey (1980) and reviewed by Nere et al. (2003), is based on the average circulation velocity \bar{v}_C and the maximum length of the circulation path

$$\theta_C = \frac{\text{maximum circulation path length}}{\text{average circulation velocity}} \quad (2-58)$$

The maximum circulation path is equal to $2D$ ($2T$) for a radial flow and to $3D$ ($3T$) for an axial flow, see Fig. 2-23, and \bar{v}_C is defined by

$$\bar{v}_C = \frac{Fl \cdot Nd^3}{\pi d^2/4} \quad (2-59)$$

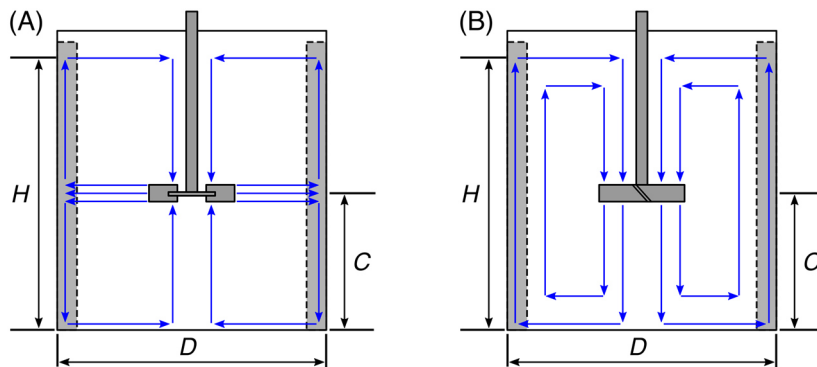


Fig. 2-23 Maximum length of the circulation path characteristic of the impeller type: (A) radial flow impeller, (B) axial flow impeller, (Nere, 2003).

2.4.4 Flow Field Investigations in Stirred Vessels

Mechanically stirred vessels are widely used in various industrial chemical processes for single-phase mixing and for more complex multi-phase processes (Aubin et al., 2001). The flow pattern developed in a stirred vessel is very important for the mixing efficiency (Pan et al., 2008).

In this experimental work the investigation on the flow field is performed by using a photographic analysis technique, PIV, but this is not the only measuring technique available

for the determination of the fluid flow properties. Among these, there are phase Doppler anemometry (PDA), laser Doppler anemometry (LDA) and laser-induced fluorescence (LIF). The choice of the measuring technique for the investigation is usually based on the significant features that are characteristic of the technique itself, such as the possibility of direct determination of a quantity, the spatial dimension of the acquired information (point, field or volume) and if the realization of the measurement is invasive or not (Hohl et al., 2018).

The one-dimensional velocities of a fluid can be measured with LDA and PDA, both non-invasive techniques. They are optical techniques based on the employment of a laser that crosses the investigated fluid. With LDA, the particles that move through the volume defined by two laser beams scatter a light, of which frequency shift is used for the determination of the velocity. The PDA method can additionally measure the particles size, by taking into account the observed phase difference of the scattered light that is related to the particles diameter. (Ofner, 2011; Gouesbet and Gréhan, 2015)

LIF is a spectroscopic technique, based on the use of laser and a fluorescence dye, that allows the measuring of temperature, pH and concentration of a certain substance in the fluid. This non-invasive method provides two-dimensional (2D) results and it requires a transparent flow with a low fraction of dispersed phase $\Phi < 1\%$. (Lemoine et al., 1996; Gouesbet and Gréhan, 2015; Hohl et al., 2018)

Depending on the number of cameras that are used in the measurements, PIV can provide a 2D or a 3D velocity vector field. From this first fundamental result, it is then possible to calculate other fluid dynamical quantities, as described in **Section 2.3**. In general, the major results obtainable with PIV are the velocity, the shear rates and the turbulent kinetic energy and its dissipation rate (Saarenrinne and Piirto, 2000; Xu and Chen, 2013; Sheng et al., 2000). The description of this technique is reported in **Chapter 3**.

2.5 Stress on Microorganisms

The building block of life, the cell, constitutes all living organisms. Some of them are made of a unique cell, others are pluricellular.

To live, a cell must successfully develop all its basic functions, including the metabolism of energy, the reproduction and the transport of molecules through the cellular membrane.

However, the realization of these primary functions can be impeded by improper environmental conditions, characterized by several factors that may represent a stress for the cell. It is clear that the environmental requirements of the cell are not univocal, but they depend on the individual living organism.

2.5.1 Physical and Chemical Stress

In biotechnology, the use of microorganisms in the process must contemplate the study of the proper environmental conditions that have to be provided, in order to ensure the growing of the culture and to possibly prevent, or decrease, the presence of stress factors. Stress factors can be represented by temperature, osmotic pressure, pH, UV rays and mechanical stress.

In the design of a bioreactor, the presence of the biotic phase must be taken into account as well as attention has to be paid to some phenomena that may be dangerous for the bio-phase itself, leading to conditions that contribute to have a bad performance of the reactor.

The biological phase in a bio-reactor can consist of microorganisms, such as fungi, enzymes or cell and plant cultures. In the case of an aerobic reactor the first parameter to control that one can think about is surely the concentration of oxygen. Every microorganism indeed has its characteristic critical concentration of oxygen, below which the life and activity of the microorganism are endangered.

Apart from the loss of oxygen, there is also another significant factor that can seriously cause the death or the damage of the microorganisms: the hydromechanical stress.

2.5.2 Influence of Hydromechanical Stress on Microorganisms

The hydromechanical stress, or turbulence intensity, is considered a crucial parameter for the biotechnological processes, since it performs a direct action on the biological phase (Daub et al., 2014).

In a bioreactor, the hydromechanical stress can be divided in two categories, depending on the nature of the interactions inside the broth. The first type concerns the fluid-solid interactions, which consist in the reciprocal action of the turbulent eddies in the fluid with the suspended cells, generating the shear stress. The second kind of hydromechanical stress regards the solid-solid interactions, occurring because of the collisions between the microcarriers or between the microcarriers and the wall of the reactor (Delafosse et al., 2015; Cherry and Papoutsakis, 1988).

Microcarriers are particles of different size and shape that are used in suspension cultures, especially when these include anchorage-dependent cells that exhibit scarce ability to adapt to this kind of culture (Mandenius, 2016).

As described by Paul et al. (2004), it is crucial to point out the difference between the terms *shear* and *shear stress*, to avoid using these terms in a confusing way. *Shear* itself indicates the relative motion between two layers of the fluid that show a velocity gradient; *shear stress*, as explained in **Section 2.3**, is the force per unit area (with the unit Pa of pressure) that acts in the tangential direction with respect to the surface area. In a biological phase this area is the surface area of the cells suspended in the medium culture. The shear stress in the biotic phase comes from the forces that act on the cells. These surface forces are the consequence of the kinetic energy dissipation to the cell surface area and they can be calculated by using **Eq. (2-19)**, once viscosity and velocity gradient are known. Mixing is generally carried out in turbulent regime, which complicates the evaluation of shear stress as opposed to the laminar regime. In the turbulent regime, the biological phase is exposed to different values of shear stress, because this changes over time and space inside the reactor.

The fluid-mechanical mechanisms that act on the cells of the biotic phase can be explained with the theory of *Kolmogorov*, described in **Section 2.3**. The mechanism of mixing induces the generation of large eddies, which transform in smaller eddies until they reach the Kolmogorov microscale. The particles that are suspended in the fluid are induced by the agitation to approach the Kolmogorov scale. Evidently, the stress that acts on the agglomerates of cells or single cells is opposed to the aggregation forces of the biological phase.

It is hence possible to describe the interaction between the cell and the eddy only in a qualitative way. There are generally three possible situations, see **Fig. 2-24**:

1. The particle size is smaller than the size of the eddy: In this case particles are transported from the eddy in the fluid and the shear stress is smallest. The particles are able to grow and reach the size of the eddy.
2. The particle size is greater than the size of the eddy: the eddy is so small that it simply slips on the surface of the particle, producing a negligible shear stress.
3. The particle and eddy sizes are comparable: this is the case that produces the maximum value of shear stress and the particles can undergo to breakage.

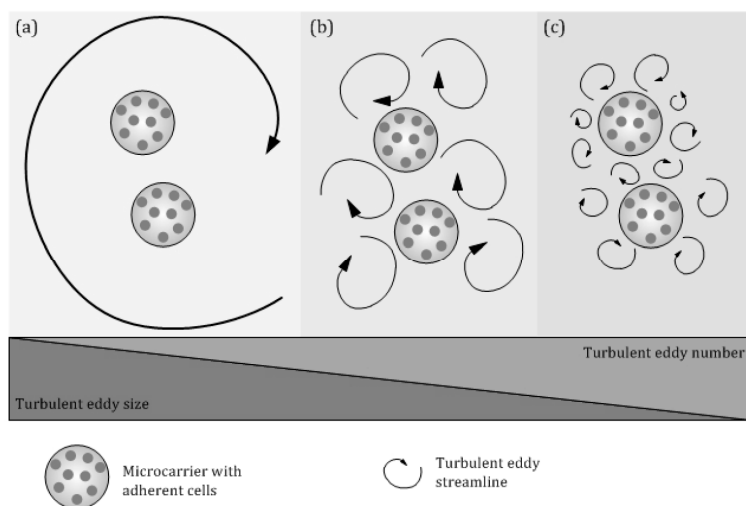


Fig. 2-24 Interaction of turbulent eddies with particles (cells on microcarriers): (A) eddies larger than the particles, (B) eddies and particles of the same size, (C) eddies smaller than particles. (Kuzmichew and Tsybulski, 2008).

It is valuable to remark that the damages resulting from shear stress that can occur to the cells are more plausible if the biological phase consists of animal cells, because these are lacking in cell wall, which represents a further protection for the cell itself, (Mandenius, 2016). Microorganisms and animal cells may undergo damages at different levels, such as the irreversibility of death or slighter damages that are not severe enough to cause the decease.

An indicator for good performance of the bioreactor is the health of the biological phase, which can be investigated by using different techniques. Among these, one of the most used techniques for the evaluation of the cell damage uses the lactate dehydrogenase (LDH) as detector. LDH is a soluble cytoplasmatic enzyme that is released in the extracellular region when a damage in the plasmatic membrane occurs. The advantage of this detector is that the LDH enzyme is present in almost every cell (Burd and Usategui-Gomez, 1973). This type of analysis is largely used to detect the necrosis, that is the death of the cells in the bioreactor. Other useful methods for the inspection of potential cell non-lethal damage consider the control of metabolic parameters, like the growth rate and the enzymatic activity.

Many studies have been made to discover how the hydrodynamics in the bioreactor affect the cell damage due to shear stress. What was found is that the effect of hydromechanical stress becomes even more complex when, for the furnishing of oxygen to the bio-phase, a sparger is employed in the bioreactor (Oh et al., 1992). In this case, the risk of damaging the cell mechanically derives also from the bursting of the bubbles of gas. Inside the bioreactor there are generally four regions where these phenomena can lead to cell damage, and these are connected to the major liquid-air interface. These regions are located close to the sparger where bubbles are formed, at the impeller discharge where bubbles

coalesce and break, throughout the space of the bioreactor where bubbles arise as well as at the air-medium interface where bubble bursting occurs. (Amanullah et al., 2004).

This experimental work is carried out by using a single phase mechanically agitated in a stirred vessel, without taking into account the gaseous phase, because of the measuring problematics related to the presence of this phase. Hence, the above-mentioned questions were not faced in the practice, but only considered and not too much deeply explored in the available literature.

Chapter 3

Experimental Methods

3.1 Particle Image Velocimetry

Particle Image Velocimetry (PIV) is an optical technique that is widely used for the study and determination of the flow field of fluids in stirred vessels. This flow visualisation technique is non-invasive, since it is based on the recording of pictures of flow seeding particles from outside of the reactor. These particles are suspended in the continuous phase that is intended to be examined. A pulsed light sheet is employed to illuminate the particles, determining the flow cross section that is recorded with a digital camera, see **Fig. 3-1**. For this reason the application of PIV is possible only by means of optically transparent vessels and fluids. Hence, it is obviously unfeasible for slurries and blurred fluids, as well as for transparent fluids in metallic vessels.

The tracing particles must be able of reflecting the light that hits them. Depending on the properties of the fluid that is intended to be analysed, it is possible to use the most proper type of flow seeding particles, which differ in shape and chemical composition. For a liquid, the most common tracing particles are polyamide particles, glass hollow spheres and fluorescing particles. They must be present in the transparent fluid in a homogeneous way and in a certain concentration that does not affect the fluid's properties, like the density. Indeed, the particles should follow the direction of the flow in the most exact way without interfering with it, so that the velocity measurement can be reliable and truthful. Flow seeding particles are in a way the carriers of the velocity information of the fluid. (Hadad et al., 2011)

The principles of this technique are illustrated in the book “Particle Image Velocimetry: A Practical Guide” (Raffel et al., 2007). Its application to a stirred vessel is described in several scientific papers, e.g. by La Fontaine (1996). Because of the popularity of this technique, the scientific platform offers an abundant amount of literature concerning the description and the various applications of PIV. The applications of PIV analysis in stirred vessels are summarized in **Subsection 2.4.4**.

The first aim of this method is determining the velocity vector field, hence the local velocities of the fluid, which are approximated with the velocities of the particles. To realize that, the flow seeding particles, illuminated twice by a pulsing light sheet, are captured by one or more digital camera(s), which take(s) two consecutive pictures, see **Fig. 3-1** (A). Thereafter, in order to get the value of the local velocity, it is necessary to determine the displacement of the particles in the light sheet by the time interval between the exposures, defined also as exposure time delay. The pictures, or frames, are first divided in many interrogation areas (IA), or interrogation windows (IW). Each IA of one frame is correlated to the corresponding IA of the following frame. The cross-correlation, realized by Fast Fourier Transform (FFT), allows to find a distinct peak. The position of that peak corresponds to the average displacement of the particles in the considered IA, see **Fig. 3-1** (B), (Deen and Hjertager, 2002). The resulting velocity vector field includes all the vectors calculated for each IW and can be represented also with the cumulative distribution function (CDF), see **Fig. 3-1** (C).

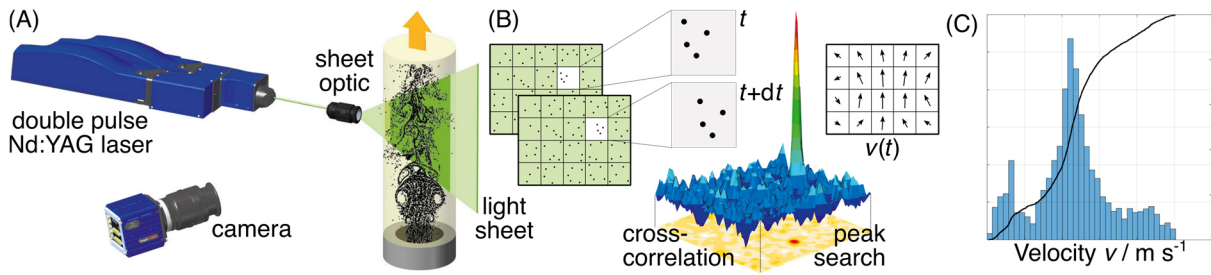


Fig. 3-1 Working principle of PIV: (A) experimental setup with camera perpendicular to laser sheet, (B) cross-correlation to find velocity vectors in every interrogation window, (C) distribution of velocity vectors for all interrogation windows. (Scarano, 2013)

Since PIV is capable of calculating thousands of velocity vectors for the analyzed flow cross section at the same time, it is considered to have a bigger efficiency than other known and used computational and photographic techniques, such as laser Doppler anemometry (LDA) (Liu et al., 2008). Indeed LDA, contrary to PIV, is able to record a singular velocity point at a time. The great potential of PIV can be expressed by the multitude of results that this method can provide. First of all, this technique allows the determination of the velocity vector field and the flow pattern in the stirred tank. PIV data can be used further to evaluate shear stress in the fluid as well as turbulent kinetic energy and its dissipation rate, (Calluad et al., 2011; Liu et al., 2008; Pan et al. 2008). Moreover, particle image velocimetry can be carried out with one camera, giving two-dimensional results and also with two cameras, increasing the potential of the technique by producing three-dimensional results.

3.1.1 Hardware

The PIV analysis makes use of a laser source to illuminate the vessel and expose a camera, which takes several pictures of the light sheet, with a small time interval between one frame and the following one. The camera and the pulsing laser, in order to have pictures of the light sheet with the tracing particles, work together with a synchronizer.

The key for the realization of this technique is the light source, represented by light amplification by stimulated emission of radiation (laser). The pulsing monochromatic light sheet is formed by a laser beam, of which intensity and direction must be manipulated depending on the measurement area of interest.

There are different types of lasers, but they generally consist of three main elements, of which characteristics can change: the laser material, the pump source and the mirror arrangement, represented by M and P in the **Fig. 3-2**. The laser material, which can be either a gas or a solid, is excited by the electromagnetic or chemical energy supplied by the pump source. The electromagnetic wave, with its packet of energy (photon $h\nu$), can excite the atom that is located at an energy level (E_2), which non-spontaneously descends to the energy level (E_1). Then, the electromagnetic wave, carrying a photon, excites again the atom that spontaneously emits two photons. Hence, the wave is amplified. (Raffel et al., 2007)

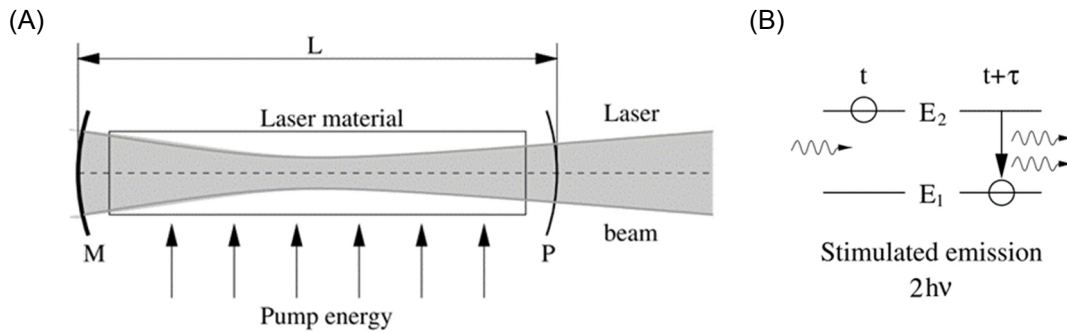


Fig. 3-2 Schematic representation of the working principle of a laser: (A) laser material in a mirror system supplied with pump energy, (B) emission of two photons in a laser, (Raffel et al., 2007).

The neodymium-doped yttrium aluminum garnet (Nd:YAG) laser is the one used in this experimental work as well as the most largely used in PIV analysis, (Raffel et al., 2007). This crystal solid material consists of an yttrium aluminum garnet (YAG) matrix $Y_3Al_5O_{12}$ with neodymium ions Nd^{3+} . The wavelength of the generated monochromatic light is 532 nm and the thickness of the laser sheet is about 1 mm. The hardware of the laser source, see **Fig. 3-3**, is produced by the *LaVision GmbH*.

The laser intensity, during the measurements, must be controlled in order to avoid damages for the sensor of the camera. During the investigation, the laser intensity is used at values around 10–15% of the total produced. The emitted laser intensity is reduced by means of an attenuator.

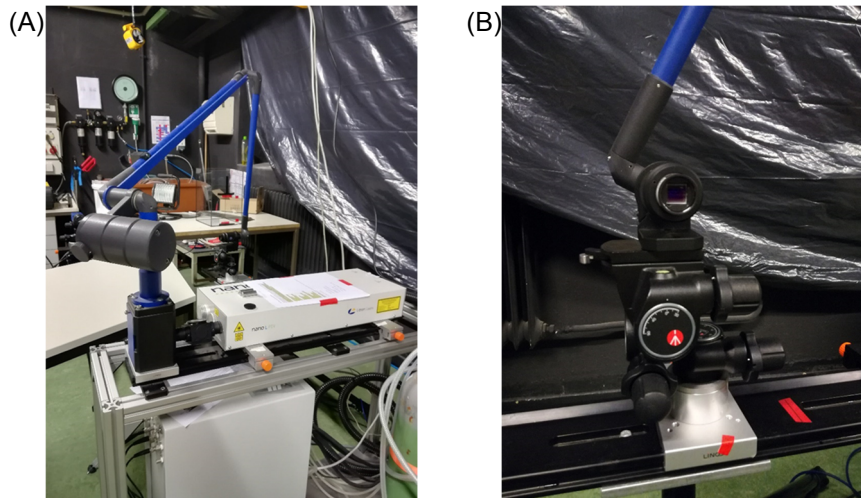


Fig. 3-3 Laser source used in the experiments: (A) pump source and mirror arm, (B) focusing of the laser beam into a two-dimensional sheet.

To see and capture the particles located in the laser sheet in several pictures, it is fundamental to employ high-resolution digital cameras that must be specific for PIV analysis. The PIV technique uses double-frame pictures, i.e. two frames are recorded in a small time interval. The camera used in this experimental work is the *Imager Pro SX*, produced by *LaVision*. For this camera, the smallest time lapse of recording between two double frames is 1 μs . However, due to the building characteristics of this camera, it is not possible to maintain this time lapse between two frames as recording rate for all pictures, but only for the two frames that constitute each single picture. The maximum recording frequency for a series of several double-frame pictures in a row is 15 Hz. (Lenhart, 2012)

The camera is fixed on a horizontal metallic support, where it can be moved to the left and right, see **Fig. 3-4 (A)**. Moreover, at the base of the camera there are two control knobs that can be used to orientate the camera to the target, by rotating the device both horizontally and vertically.

The addition of a *Scheimpflug adapter*, **Fig. 3-4 (B)**, is indicated when the lens of the camera is not parallel to the image plane (the laser sheet), because in this case the image is not equally focused in its entire visible plane. This follows the geometrical principle of Scheimpflug, used to find the plane of focus in an optical system like the one described. Hence, the use of this device is necessary for any case in which the camera looks at the laser sheet from an outer, non frontal, view, such as for 3D-PIV. The technique of 3D-PIV, also called *stereo-PIV*, uses two cameras, which are placed at different observation angles. The Scheimpflug adapter is positioned between the camera and the objective, and it can be rotated around in the horizontal and the vertical axes to find the plane of focus.

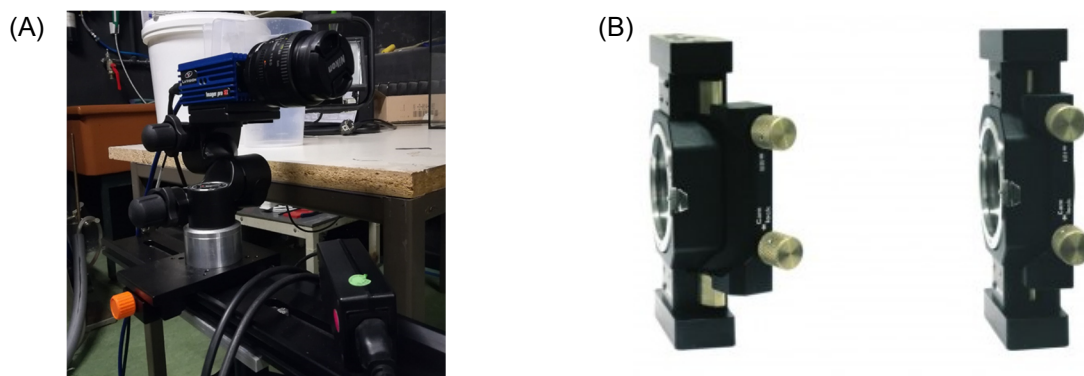


Fig. 3-4 Image recording hardware: (A) *Imager Pro SX* with Nikon lens, (B) Scheimpflug adapter (KamepalQ, 2018).

3.1.2 Software

The camera and the laser source are synchronized and connected to a software, employed to do the measurements and the calculation of the vector field. The software used in this work is *DaVis 8.4*, produced by *LaVision*.

To start a measurement and do the calculations, it is necessary to follow fundamental steps, beginning with the creation of a *new project* and the main settings. For a PIV analysis the requirement of *double-frame* is indispensable: every picture must be recorded with two consecutive frames, labeled by the software as 0 and 1. Furthermore, it is possible to select an area of interest from the total area seen by the camera. In removing unnecessary information, some memory space in the computer can be saved.

Before starting with the recording, the software needs to have spatial information regarding the plane that is intended to record, hence the *calibration* is made. A calibration plate, with a pattern of equally spaced dots on the surface, see **Fig. 3-5 (A)**, is placed inside the vessel without the baffles and the impeller. The positioning and the focus of the camera is done, depending on the live images that can be seen in the software (live mode). When the focus is optimal and it is possible to see all the dots as sharp as possible, one picture is taken. In the calibration procedure, the software asks the user to select three points and to insert the actual distances between these points. The software looks for all the dots (markers) and, at the end of the calibration, it shows the resulting grid overlapped to the picture, see **Fig. 3-5 (B)**.

In case of 3D-PIV, it is necessary to provide the software with the depth spatial information. This can be done with a three-dimensional calibration plate, made of parallel teeth: The software in this case needs also the distance between the two surface levels. However, in this experimental work, this plate is not able to produce a satisfying calibration. Hence, the same 2D calibration plate is used, as in the 2D-PIV measurements, see **Fig. 3-5**. In the case of 3D-PIV calibration with that plate, a picture of the plate in two different z positions (depth coordinate perpendicular to the image plane), distant 1 mm from each other, is taken. One very important aspect is that the calibration plate must lay in the same position where the light sheet is formed, so that the results are reliable.

The effective measurement can start only after the *laser intensity* is adjusted: when the laser is triggered and the live mode is used, the software shows the light sheet and makes a mapping with the intensities detected by the camera (counts), that must not exceed 4×10^3 counts.

At this point it is possible to start the measurement. Based on the work of Liu et al. (2008), in each measurement of the investigation, 300 pictures are taken.

After the double-frame pictures are saved in the project, it is necessary to tell the software which are the regions of the area of interest to investigate and process. Geometrical masks are used for this purpose to remove some areas, like the area outside the vessel and the impeller region

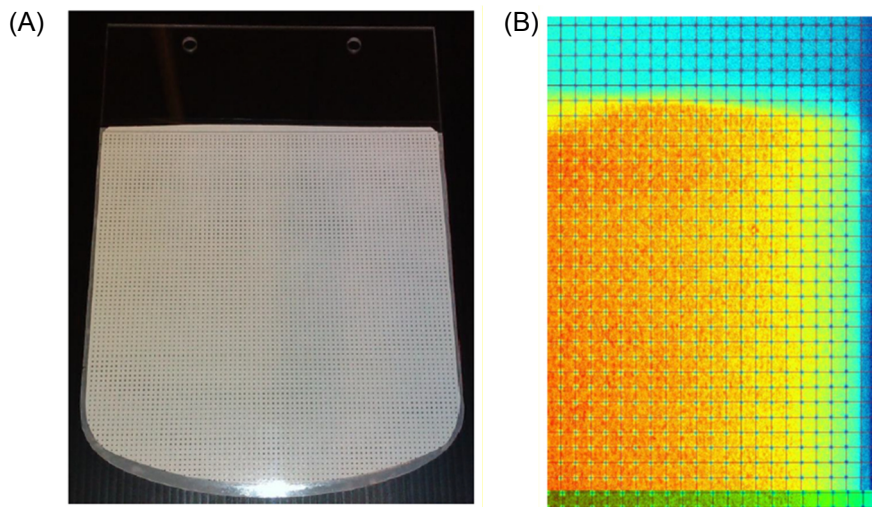


Fig. 3-5 Calibration of the laser sheet for the software: (A) calibration plate, (B) creation of the grid after the calibration process.

The calculation of the vector field follows the cross-correlation, that can be done with single-pass, or multi-pass. Contrarily to single-pass, illustrated in **Fig. 3-1** (B), multi-pass does not compare every single IW of the first frame to the corresponding IW of the second frame. With this method, the frames are first divided in interrogation windows and the calculation is done for the first IW of both frames in the first pass. The next calculation is done in the second pass with a new IW, which does not coincide spatially with the first IW, but has its size. The result of the first calculation determines the shift of the pass, in terms of number of pixels. The calculation continues until all the passes of the area of interest are calculated. With this method, it is possible to produce more accurate values of the vector field and to increase its resolution. In this work the cross-correlation method with decreasing pass is used: the

calculations are done for three times with passes of 48×48 pixels and other three times with 24×24 pixels.

3.2 Experimental Setup

For this PIV analysis, an experimental setup is assembled in a dark laboratory room, with black walls to prevent the reflection of the laser, hence to operate in safe conditions. The main elements that constitute the experimental setup are:

- Stirred vessel under investigation, including vessel, aquarium, stirrer gearbox, impeller shaft, impellers, baffles, fluids with flow seeding particles
- Laser source
- High-resolution digital camera, or two in case of 3D-PIV
- Software

Vessel setup

The glass vessel with torispherical bottom (*Klöpfer* form, following the norm DIN 28011) has an internal diameter $D = 160$ mm and it is filled with 2.99 L of fluid to investigate, a volume that corresponds to a filling height $H = 160$ mm. The vessel is placed inside an aquarium, which is a glass box open on the top and it is kept still in a precise position by means of a metallic support, which also holds the motor of the stirrer, situated on the top, see **Fig. 3-6 (A)**. The aquarium, with square base 22.5×22.5 cm², is filled with pure water until a level of 26–29 cm, considering the vessel inside. The aquarium, with the support that holds the vessel and the stirrer gearbox, is placed on a table, close to the laser source and to the camera(s).

The metallic parts of this vessel setup are covered with black cardboard for the above-mentioned reason. Furthermore, the metallic elements inside the vessel, like impellers, shaft and baffles, are sprayed with a black dye, in order to avoid the laser from reflecting to the camera.

The baffles, see **Fig. 3-6 (B)**, are four equally spaced flat plates holded by a ring that fits on the internal vessel wall. They are made of stainless steel and they have a width $J_B = 12$ mm, immersed length $H_B = 114$ mm, thickness $T_B = 2$ mm and distance of the baffle from the vessel wall $A_B = 5$ mm.

The motor of the stirrer is an *IKA® EUROSTAR 60 control*. It has a control knob for the start/stop of the stirring and for the change of rotational frequency, that can be set from 20 up to 2000 rpm, with *unit steps*.

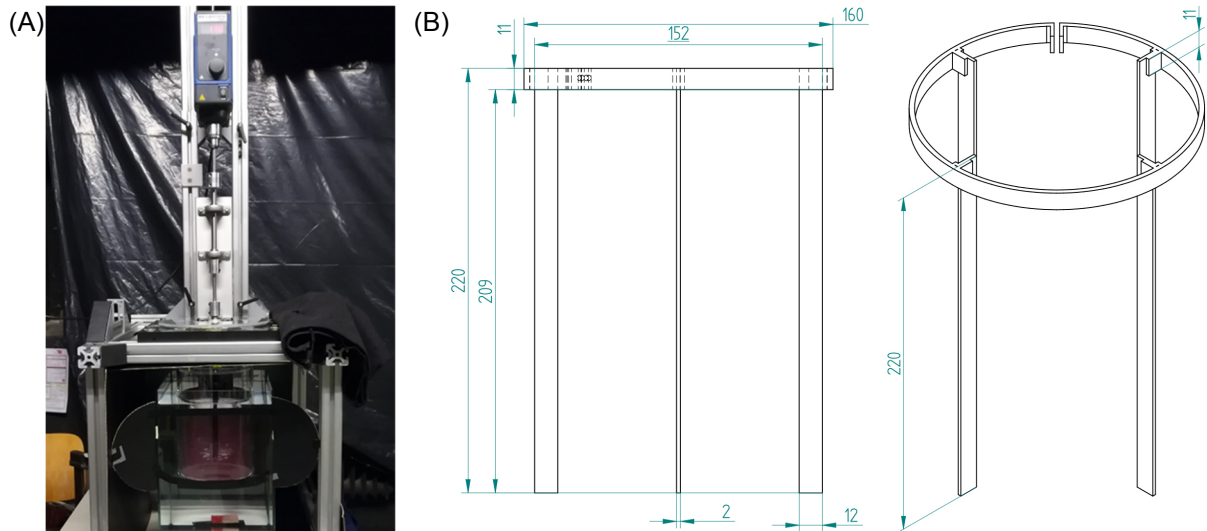


Fig. 3-6 Vessel setup: (A) vessel placed in the aquarium with the stirring system, (B) four equally spaced baffles used in the experiments.

Impellers

Altogether nine different impellers are employed in the investigation, including two propellers, three pitched blade turbines, one bionic-loop impeller and three wave ribbon impellers. All of them are inserted in the vessel with an off-bottom clearance $h_C = 0.33 D$. The geometry of these impellers is defined in detail in **Tab. 3-1**.

Tab. 3-1 Geometry of the nine impellers used in the experimental investigation.

Impeller	Name	d/D (–)	N_B (–)	α (°)	h/d (–)	h_I/d (–)	t/d (–)	Additional dimensions
Propeller	PROP- $h/d=0.33$	0.325	3	25.0	0.33	0.14	0.02	–
Propeller-ring impeller	PROPRing- $h/d=0.33$	0.338	3	25.0	0.33	0.15	0.02	ring geometry: $h_R/d = 0.15$, $t_R/d = 0.04$
Pitched blade turbines	PBT-6x22.5°	0.330	6	22.5	0.24	0.09	0.02	–
	PBT-6x45°	0.330	6	45.0	0.24	0.17	0.02	–
	PBT-6x90°	0.330	6	90.0	0.24	0.24	0.02	–
Bionic-loop impeller	BiLoop	0.330	7	55.0	0.24	0.19	0.02	ring geometry: $h_R/d = 0.05$, $t_R/d = 0.02$
Wave-ribbon impellers	WRI- $d/D=0.33$ -51.2°	0.330	–	51.2	–	0.49	0.01	–
	WRI- $d/D=0.4$ -28.8°	0.400	–	28.8	–	0.25	0.01	–
	WRI- $d/D=0.4$ -41.4°	0.400	–	41.4	–	0.35	0.01	–

Moreover, in **Fig. 3-7** photographs of the impellers are shown. Those were taken, after the impellers have been sprayed with black dye to prevent reflections in the stirrer zone.

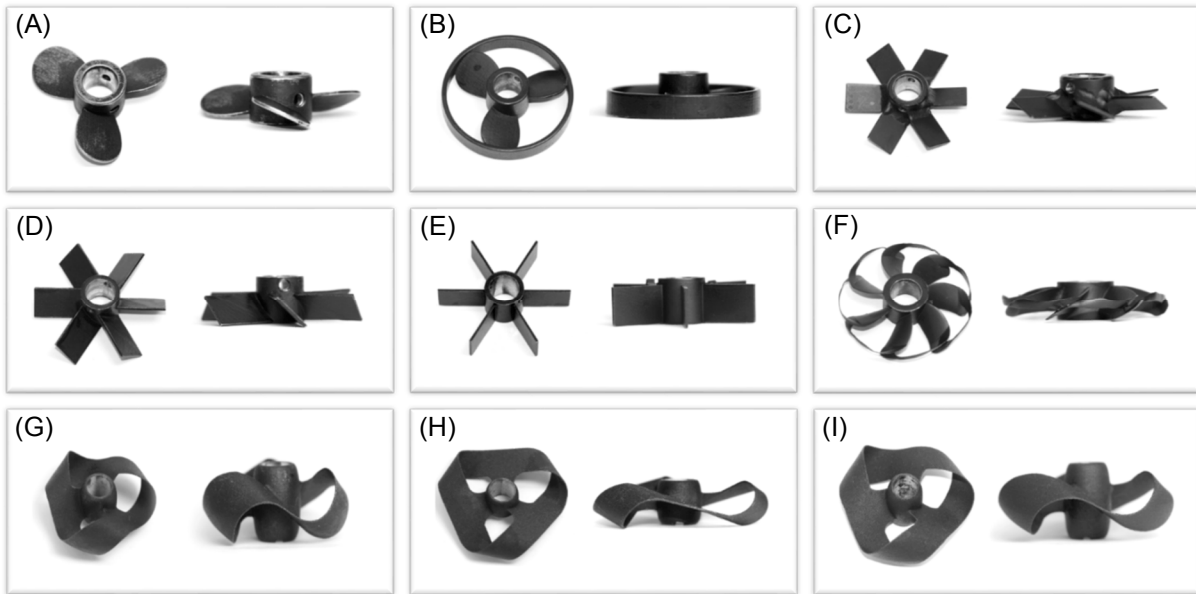


Fig. 3-7 Investigated impeller types: (A) PROP- $h/d=0.33$, (B) PROPRing- $h/d=0.33$, (C) PBT-6x22.5°, (D) PBT-6x45°, (E) PBT-6x90°, (F) BiLoop, (G) WRI- $d/D=0.33-51.2^\circ$, (H) WRI- $d/D=0.4-28.8^\circ$, (I) WRI- $d/D=0.4-41.4^\circ$, (Bliatsiou et. al, 2018b).

Fluids

Three different fluids are employed in the presented PIV experiments.

- *Ultrapure water.* The properties in the purifier machine, *ELGA® PURELAB flex*, are indicated as temperature being 21.6 °C, Total Organic Carbon (TOC) being 3 ppb and electric conductivity being 0.055 μS . The density is quantified by *Anton Paar Density and Sound Velocity Meter DSA 5000 M* and the dynamic viscosity is quantified by the device *Anton Paar Modular Compact Rheometer MCR 302*. Both are measured at room temperature and are 997.66 kg m^{-3} and 955.4 $\mu\text{Pa s}$, respectively.
- *Glycerin solution.* It consists of ultrapure water and pure glycerin, with mass fraction of 60 % glycerin. The measured density is 1150 kg m^{-3} and the dynamic viscosity is 11 mPa s. The solution is agitated at low rotational frequency for at least thirty minutes.
- *Xanthan solution.* It consists of 0.5 g of xanthan (powder) for every kg of ultrapure water. The density is quantified as 998.37 kg m^{-3} . After a minimum stirring time of two hours, this solution can be used for a maximum of two days, because of its progressive changes of rheologic properties over time.

The viscosity of the three fluids is evaluated with the rheometer, which is connected to a software that records the shear rate, the viscosity, the shear stress and torque applied to the shaft that rotates at accelerating frequencies. The viscosity is plotted as function of the shear rate, see **Fig. 3-8**. Water and the glycerin solution show a Newtonian behaviour, since the viscosity has a constant value. The Newtonian law is not followed by the xanthan solution, which exhibits a decreasing viscosity with the increase of shear rate. This pseudoplastic fluid can be described with the Ostwald-de-Waele model, as described with **Eq. (2-5)**. The flow behaviour index and the consistency index of the xanthan solution are found to be $n = 0.3845$ and $K = 0.17185$, respectively.

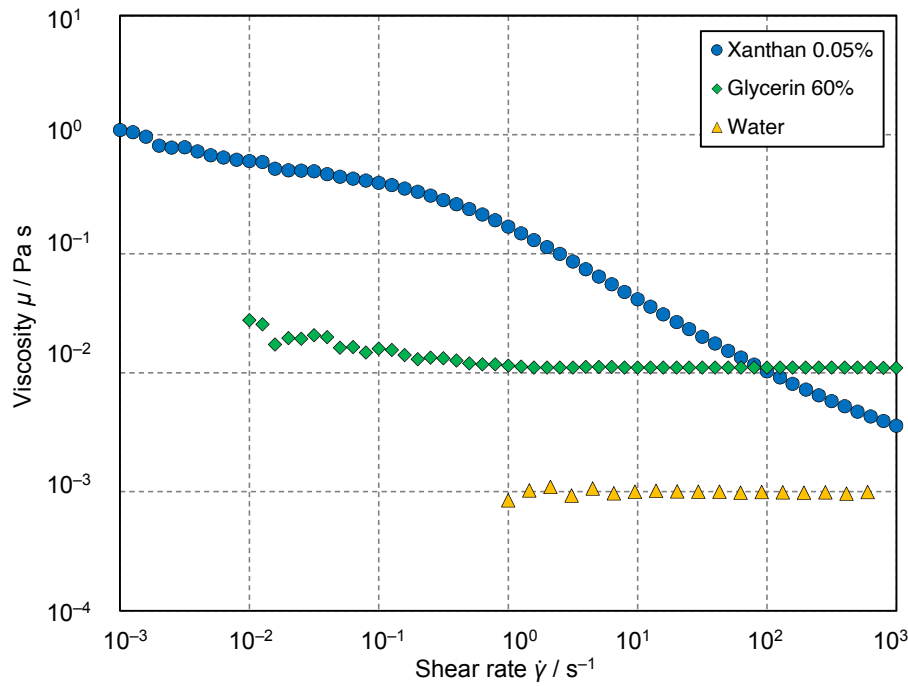


Fig. 3-8 Experimental measurement of viscosity of water, glycerin solution and xanthan solution.

Flow seeding particles

The flow seeding particles used for the whole investigation are from *LaVision*. They are particles of 20–50 μm in size and they are made of Poly(methyl methacrylate) (PMMA). In addition, they are covered with the fluorescence dye *Rhodamine B* and are present in suspension, see **Fig. 3-9** (A).

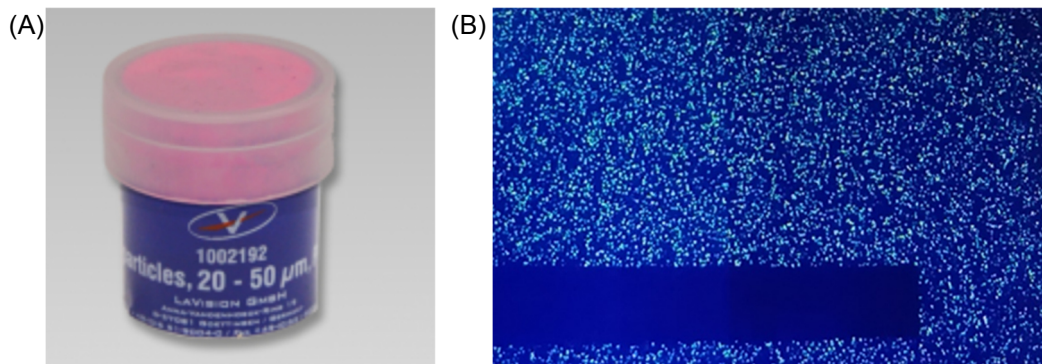


Fig. 3-9 Flow seeding particles: (A) PMMA particles covered with Rhodamine B by *LaVision*, (B) picture of the laser sheet with illuminated particles.

The tracing particles are added to the fluid in a certain amount that, as indicated by La Fontaine (1996), must be determined experimentally for each application. In fact, if the density of the particles in the fluid is too high, the targeting of the particles is challenging; it follows that the calculation of the velocity vector values is not accurate. In the opposite case, if the particles are too few in the fluid, it becomes more probable that the particles do not remain in the measuring area (light sheet) during the time of recording and an insufficient number of particles per IW is recorded.

In these PIV measurements, the optimal concentration of flow seeding particles is found to be 1 mL for the whole fluid volume of 2.99 L, so about 0.33 mL of particles per 1 L of solution.

The experimental determination of that amount of tracing particles to be used is based on different attempts with different quantities of particle suspension: 0.5, 1.0, 1.5, 2.0 mL. The camera takes one picture of the particles illuminated by the laser sheet, see **Fig. 3-9 (B)**, then the pictures corresponding to the different concentrations are compared. The value that is considered valid is evaluated by counting the particles that are present in the IWs, which are 48×48 pixels and 24×24 pixels in size for the used multi-pass method. The concentration corresponding to 5–10 particles in the smallest IW (24×24 pixels) is taken as valid and it is used for the measurements (Deen and Solberg, 2000).

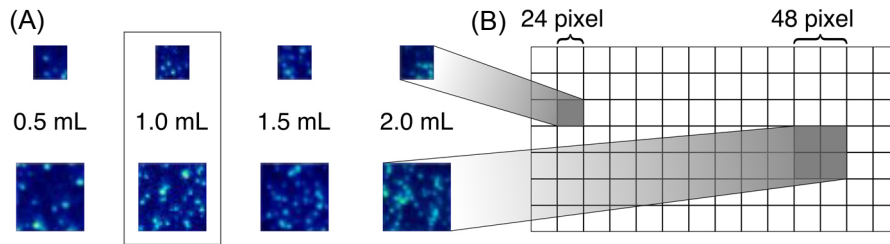


Fig. 3-10 Experimental determination of the concentration of the flow seeding particles: (A) pictures obtained with four different quantities, (B) interrogation windows of 24×24 pixels and 48×48 pixels, (Krämer, 2018).

Experimental Method: Different Approaches

The presented experiments are carried out by testing different approaches, including 2D-PIV and 3D-PIV as well as different angles of observation. The nine stirrers in the three fluids are investigated with measurements that use different values of rotational frequency. The values used are first calculated in a matrix, of which derivation is described in **Section 3.3**.

In each of the three approaches, the baffles are positioned in a way, such that most of the laser sheet can be analyzed. They are rotated of 3° , so the laser, hitting perfectly the center of the vessel, it passes in front of the right baffle and it stops when it meets the shaft and the impeller, see **Fig. 3-11 (B)**.

The first approach to PIV technique consists in the use of only one camera positioned in front of the vessel, with the lens parallel to the laser sheet. The obtainable results are in this case two-dimensional.

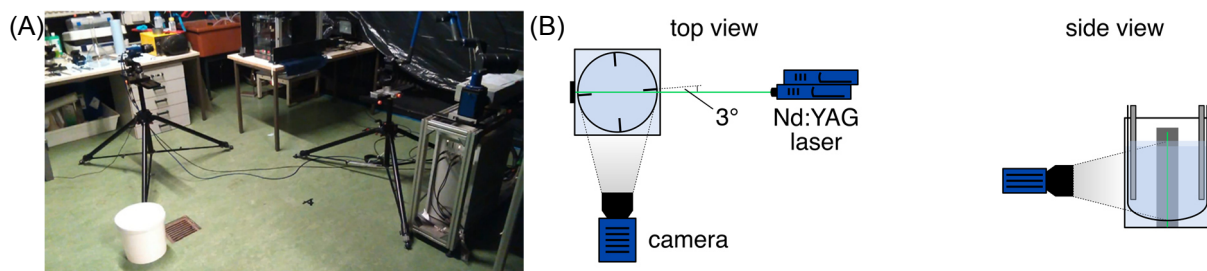


Fig. 3-11 First approach of the measuring technique including one camera: (A) positioning of the equipment in the experimental setup, (B) schematic representation viewed from the top and the side.

The reason why more than one method is used is due to measurement difficulties that can be solved only by changing the approach of the measuring technique. In fact, the first problem observed with this arrangement is the incapability of investigating on the bottom part of the vessel.

It is observed that by positioning the camera in the front of the vessel, the counts (relative to the laser intensities, parameter detected by the camera) get higher in the “critical” areas of

the vessel, such as the fluid surface and the bottom. The explanation of this is that the laser gets reflected in such critical regions. Indeed the fluid, that is mechanically agitated by the stirrer in turbulent regime, shows a surface that is not flat. Concerning the bottom of the vessel, the cause of the reflection is represented by the glass constituting the vessel. In order to have a sufficient laser exposure for the PMMA particles, it is necessary to increase the laser intensity, but this must not reach the safety threshold. The only way is decreasing the highest peaks in the counts: the most reasonable solution to overcome this problem is hiding these critical regions by sticking some black tape on the glass of the aquarium, by following the contour line of the vessel. By doing this, the highest peaks decrease considerably, thus it is possible to increase again the laser intensity until the counts reach the highest possible, still safe values. After this procedure, the resulting area of interest is lacking in the very bottom part of the vessel; as a consequence, all the information concerning this region are lost. Furthermore, the frontal position of the camera introduces a distortion of the image in the lowest visible part of the vessel. In the torispherical part of the vessel's bottom, the Klöpper bottom, the shape and the finish of the glass are not perfectly smooth, so that it is possible to see also by eye a horizontal striping pattern. These characteristics are not able to produce truthful results, because of the deeply distorted images in that region, see **Fig. 3-12**.

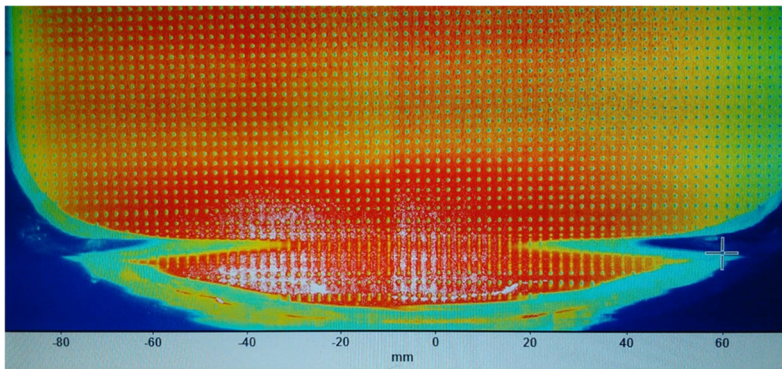


Fig. 3-12 Calibration resulting with the frontal camer: the non-homogeneous glass thickness leads to distortions in the captured images.

The problems observed with this arrangement of the experimental setup lead to the attempt of another technique. The intention of recording the largest possible area of interest suggests to find a suitable alternative. This can be realized by moving the camera in a position that allows to look at the bottom of the vessel, without a significant distortion of the information, see **Fig. 3-13**. By setting the camera from a higher position with a forward leaning and by using the Scheimpflug adapter, it is quite easy to fulfill the previous requirement. The camera is placed in front of the vessel, with an angle of observation of about 45° , with respect to the horizontal plane.

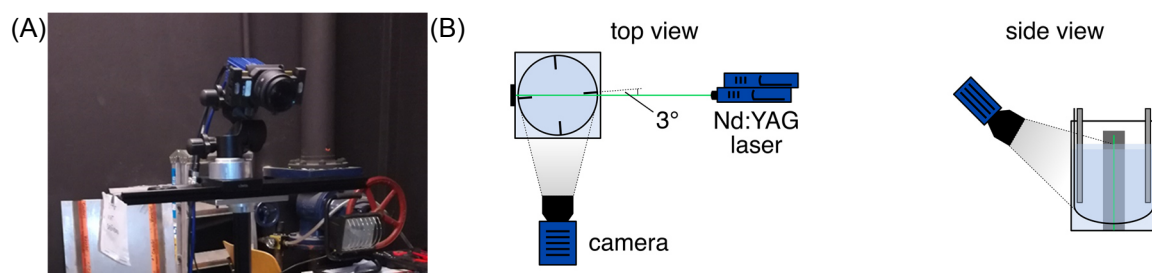


Fig. 3-13 Second experimental approach with one camera that is directed at the vessel bottom: (A) angular direction of the camera, (B) schematic representation of the experimental setup viewed from the top and the side.

Even with this arrangement of the experimental setup, it turns out to be necessary to use some black tape to cover a part of the aquarium, corresponding to the surface of the fluid, which is visible with this angle of observation. This covered part becomes larger as compared to the previous case. Nevertheless, the information regarding the bottom of the vessel are found available and reliable.

Once verified that this position of the camera allows the achievement of better results for the analysis, another variation is attempted: Instead of using only one camera, another one is added to the experimental setup and the stereo-PIV is carried out, see **Fig. 3-14**. Both cameras are placed at the same height of the previous case, by maintaining the same distance from the vessel. With this disposition the direction of the cameras is not frontal to the vessel anymore: they are rotated to one side, pointing downwards. Also in this case the Scheimpflug adapter is used.

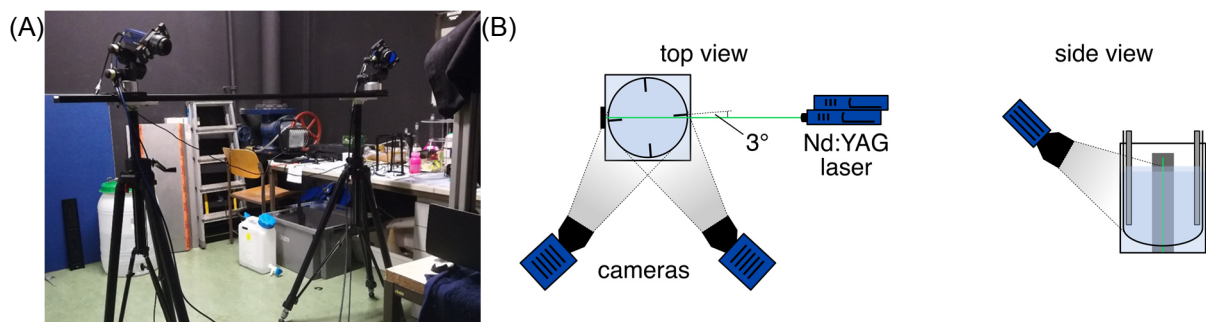


Fig. 3-14 Third experimental approach with two cameras directed at the vessel bottom: (A) angular direction of the cameras, (B) schematic representation of the experimental setup.

For the reference to the approaches in the matrix and in the results, the following nomenclature is used:

- one camera, front position: 2DF
- one camera, pointing at the bottom from above: 2DA
- two cameras, pointing at the bottom from above: 3DA

3.3 Parameter Matrix

A parameter matrix with all the data points is calculated to start the experiments.

The experiments are carried out by employing three different fluids and nine impellers. In order to propose reasonable interpretations of the results and to make valuable comparisons between the impellers' behaviour, it is necessary to keep some fixed parameters throughout the different arrangements of the system.

The experiments are performed for each of the three fluids with one impeller at a time, and during a single measurement the impeller rotates at a constant number of revolutions per minute. Then, the measurement is repeated several times with another constant value of revolutions per minute, by maintaining the same fluid and the same impeller. These operations are repeated for all the impellers. Then the whole procedure is performed also for the other two fluids.

The used values of rotational frequency N are firstly calculated in a parameter matrix, where three independent variables are considered: power input PV^{-1} , Reynolds number Re and

tip speed u_{tip} . These quantities are linked to N through elementary mathematical relationships, see **Chapter 2**.

Thanks to the use of this parameter matrix, each measurement is performed at a fixed and constant value of one of these three parameters, so that a comparison between fluids or impellers is possible at the end. For each impeller three sets of measurements are performed, with each set relating to one independent variable, see **Fig. 3-15**.

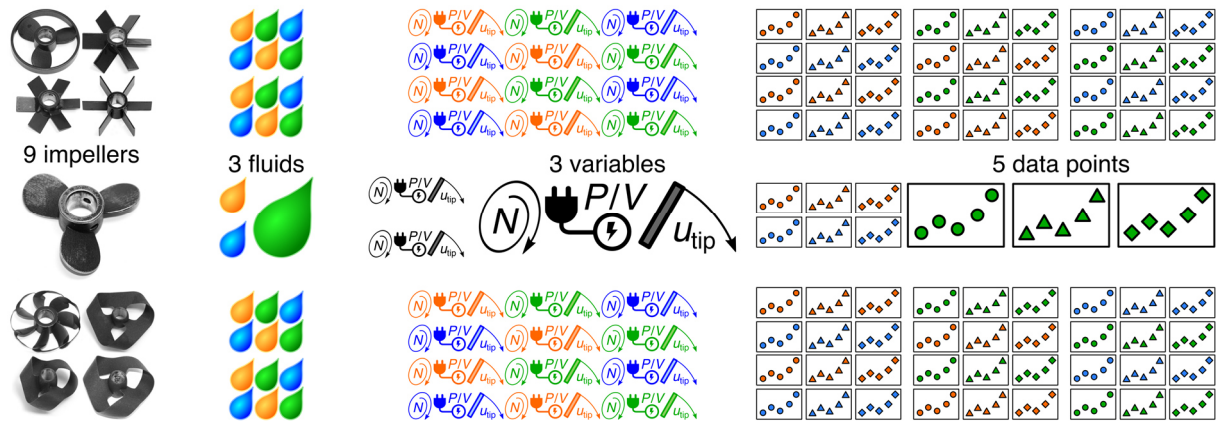


Fig. 3-15 Measurements done in the experimental investigation.

Considering only one impeller, with the dependency of both Reynolds number and power input on the rheological properties of the fluid, different values of operating rotational frequency N for every fluid are calculated. With the tip speed instead, since it depends only on the impeller diameter and on N , the same values of N are found for each fluid.

Reynolds number Re / –

The non-Newtonian behaviour of the xanthan solution makes the calculation of the Reynolds number unfeasible. Hence, this set of measurements is done only for water and for the glycerin solution. For each impeller, the values of Re at which the measurements are done are summarized in **Tab. 3-2**.

Tab. 3-2 Values of Reynolds number investigated for water and glycerin solution.

Fluid	Reynolds number Re / –				
Water	10,000	15,000	20,000	25,000	30,000
Glycerin	1,000	1,500	2,000	2,500	3,000

Tip Speed u_{tip} / m s^{-1}

The values used for this set of measurements are more than five for xanthan, due to the lack of measurements for the Reynolds number set. For each impeller, the measurements are done at the values of tip speed u_{tip} summarized in **Tab. 3-3**. In the full matrix, for each parameter set, also the other two parameters are calculated. If only one fluid is considered, the difference between the Reynolds numbers at a fixed N is due to the diameter of the different impellers. Since four out of the nine impellers have the same diameter ($d = 53$ mm), the values of tip speed are chosen by looking at the set of Reynolds numbers of these impellers.

Tab. 3-3 Values of tip speed investigated for the three fluids.

Fluid	Tip Speed $u_{tip} / \text{m s}^{-1}$							
Water	0.568	0.851	1.135	1.419	1.703	–	–	–
Glycerin	0.568	0.851	1.135	1.419	1.703	–	–	–
Xanthan	0.568	0.851	1.135	1.419	1.703	2.000	2.500	4.000

Power Input $PV^{-1} / \text{W m}^{-3}$

For this set of five data points, the values of power input PV^{-1} are calculated, only for water and glycerin solution, by means of the Newton number Ne . The calculation of this dimensionless number is done with the use of experimental data acquired with a torquemeter, which records the rotational frequency and the corresponding impeller shaft torque. For xanthan, due to its higher viscosity (and its non-Newtonian behavior), it is not possible to define a unique value of Ne at low Re , especially for axial impellers that show a bigger slope in the curve Ne over Re , see **Fig. 3-16**. The solution to this problem is using the data recorded by the software *HAAKE*TM that is connected to the torquemeter, calculating the PV^{-1} values from the torque and plotting the PV^{-1} as a function of the rotational frequency. Hence, for xanthan the PV^{-1} values are interpolated in an experimental curve. For each impeller, the values of power input at which the measurements are done are summarized in **Tab. 3-4**.

Tab. 3-4 Values of volumetric power input investigated for the three fluids.

Fluid	Power Input $PV^{-1} / \text{W m}^{-3}$				
Water	20	50	100	200	500
Glycerin	20	50	100	200	500
Xanthan	–	–	100	200	500

Newton number $Ne / –$

The Newton number is evaluated for each impeller in every different fluid by using a *HAAKE*TM rheometer (torquemeter). In this measurement step, the vessel, baffles, and the positions of baffles and impeller are the same as those used in the PIV experiments. Each impeller is accelerated, starting from a rotational frequency of 50 rpm up to a final value that is found to be different for every impeller. Indeed, the maximum final value must not generate a torque bigger than the safety threshold of the measuring device. For example, lower values are found around 300–500 rpm for the pitched blade turbines, while higher values lay around 600–700 rpm for propellers, wave ribbon impellers and BiLoop. During the measurement, the impeller is rotating at a constant rotational frequency, in every cycle of 15–20 s. The rotational frequency increases for every successive cycle until the final value is reached.. The software records the values of the torque, corresponding to each number of revolutions per minute. The data are then exported and for each of the 20 cycles the Newton number is calculated from the torque M , by using **Eq. (2-53)** from **Subsection 2.4.3** on page 29

$$Ne = \frac{2\pi M}{\rho N^2 d^5} \quad (2-53)$$

For each data point (cycle of measurement) also the Reynolds number is calculated. The final value of the Newton number characteristic of every impeller is determined by averaging the

values of Ne corresponding to values of Re greater than 10^4 for water and greater than 10^3 for the glycerin solution.

The characteristic curves Ne over Re , see **Fig. 3-16**, for each impeller are calculated with the experimental data acquired by the software. For these experiments the three fluids—water, glycerin solution and silicone oil—with their different viscosities are used. The data obtained by the most viscous fluid, the silicone oil, are in the region of low Re , followed by glycerin solution and water.

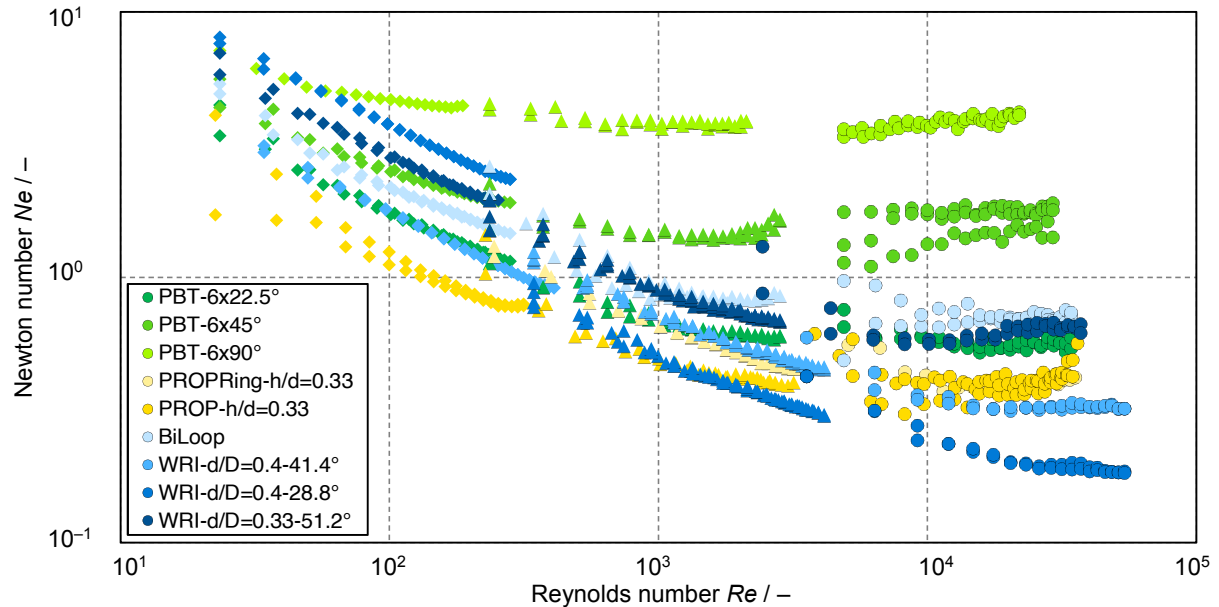


Fig. 3-16 Characteristic curves of power number as function of Reynolds number for the nine impellers investigated. Measurements carried out with silicone oil, glycerin solution and water.

The values of Newton numbers used for the calculation of PV^{-1} in the matrix are summarized in **Tab. 3-5**.


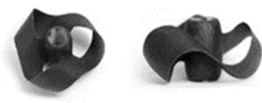


Tab. 3-5 Newton numbers measured for the nine impellers in water and glycerin solution.

Impeller type	Newton number Ne / –	
	Water	Glycerin
PBT-6x22.5°	0.55	0.62
PBT-6x45°	1.79	1.48
PBT-6x90°	4.00	3.80
PROPRing- $h/d=0.33$	0.35	0.43
PROP- $h/d=0.33$	0.39	0.52
BiLoop	0.70	0.84
WRI- $d/D=0.33-51.2^\circ$	0.63	0.66
WRI- $d/D=0.4-28.8^\circ$	0.20	0.25
WRI- $d/D=0.4-41.4^\circ$	0.33	0.39


The matrix, with its big dimension and its huge amount of data points, provides the possibility of making different comparisons between the parameters and the impellers. Moreover, some measurements are repeated with different positions of the camera(s), and also these results are compared. The big matrix is divided in smaller, selected parts for the comparisons presented in **Chapter 4**. A comparison of the different approaches of positioning the camera(s) is

presented in **Tab. 3-6**, with the descriptions and abbreviations of the approaches given in **Section 3.2**. The **Tab. 3-7**, **Tab. 3-8** and **Tab. 3-9** condense the experimental parameters used for the investigations of the influences of power input, rheology and geometry.


Tab. 3-6 Operating conditions for the comparison of different camera positioning approaches with the same power input for fluid water.

Impeller type	Operating condition		Approaches
 WRI- $d/D=0.4-28.8^\circ$	N / min^{-1}	671	2DA, 3DA
	$PV^{-1} / \text{W m}^{-3}$	100	
	$Re / -$	47,798	
	$u_{\text{tip}} / \text{m s}^{-1}$	2.247	
 WRI- $d/D=0.33-51.2^\circ$	N / min^{-1}	626	2DA, 3DA
	$PV^{-1} / \text{W m}^{-3}$	100	
	$Re / -$	30,620	
	$u_{\text{tip}} / \text{m s}^{-1}$	1.738	
 PROPRing- $h/d=0.33$	N / min^{-1}	706	2DF, 2DA, 3DA
	$PV^{-1} / \text{W m}^{-3}$	98	
	$Re / -$	35,849	
	$u_{\text{tip}} / \text{m s}^{-1}$	1.997	
 PROP- $h/d=0.33$	N / min^{-1}	786	2DA, 3DA
	$PV^{-1} / \text{W m}^{-3}$	100	
	$Re / -$	37,012	
	$u_{\text{tip}} / \text{m s}^{-1}$	2.141	



















Tab. 3-7 Operating conditions for the investigation on the influence of power input for fluid water with 3DA approach.

Impeller type	Operating condition					
	N / min^{-1}	413	561	706	890	1208
 PROPRing- $h/d=0.33$	$PV^{-1} / \text{W m}^{-3}$	19	49	98	195	488
	$Re / -$	20,964	28,453	35,849	45,166	61,300
	$u_{\text{tip}} / \text{m s}^{-1}$	1.168	1.585	1.997	2.516	3.415

Tab. 3-8 Operating conditions for the investigation on the influence of rheology with constant power input with approach 2DA.

Impeller type		Fluid		
		Water	Glycerin	Xanthan
 PROPRing- $h/d=0.33$	N / min^{-1}	706	617	715
	$PV^{-1} / \text{W m}^{-3}$	98	100	100
	$Re / -$	35,849	3,136	-
	$u_{\text{tip}} / \text{m s}^{-1}$	1.997	1.745	2,022
	N / min^{-1}	890	778	948
	$PV^{-1} / \text{W m}^{-3}$	195	200	200
	$Re / -$	45,166	3,952	-
	$u_{\text{tip}} / \text{m s}^{-1}$	2.516	2.199	2,680

Tab. 3-9 Operating conditions for the investigation on the influence of geometry for fluids water, glycerin and xanthan with approach 2DA.

Impeller type		Fluid			
		Water	Glycerin	Xanthan	
PBT-6x22.5°	 	N / min^{-1}	655	601	577
		$PV^{-1} / \text{W m}^{-3}$	100	100	100
		$Re / -$	32,038	2,939	–
		$u_{\text{tip}} / \text{m s}^{-1}$	1.819	1.667	1.601
PBT-6x45°	 	N / min^{-1}	442	449	439
		$PV^{-1} / \text{W m}^{-3}$	100	100	100
		$Re / -$	21,619	2,199	–
		$u_{\text{tip}} / \text{m s}^{-1}$	1.227	1.247	1.218
PBT-6x90°	 	N / min^{-1}	338	328	347
		$PV^{-1} / \text{W m}^{-3}$	100	100	100
		$Re / -$	16,536	1,606	–
		$u_{\text{tip}} / \text{m s}^{-1}$	0.939	0.911	0.963
PROP- $h/d=0.33$	 	N / min^{-1}	786	700	697
		$PV^{-1} / \text{W m}^{-3}$	100	100	100
		$Re / -$	37,012	3,300	–
		$u_{\text{tip}} / \text{m s}^{-1}$	2.141	1.907	1.898
PROPRing- $h/d=0.33$	 	N / min^{-1}	706	617	715
		$PV^{-1} / \text{W m}^{-3}$	98	100	100
		$Re / -$	35,849	3,136	–
		$u_{\text{tip}} / \text{m s}^{-1}$	1.997	1.745	2.022
BiLoop	 	N / min^{-1}	605	542	540
		$PV^{-1} / \text{W m}^{-3}$	100	100	100
		$Re / -$	29,563	2,653	–
		$u_{\text{tip}} / \text{m s}^{-1}$	1.678	1.504	1.499
WRI- $d/D=0.33-51.2^\circ$	 	N / min^{-1}	626	588	447
		$PV^{-1} / \text{W m}^{-3}$	100	100	100
		$Re / -$	30,620	2,879	–
		$u_{\text{tip}} / \text{m s}^{-1}$	1.738	1.632	1.240
WRI- $d/D=0.4-28.8^\circ$	 	N / min^{-1}	671	594	416
		$PV^{-1} / \text{W m}^{-3}$	100	100	100
		$Re / -$	47,798	4,237	–
		$u_{\text{tip}} / \text{m s}^{-1}$	2.247	1.989	1.394
WRI- $d/D=0.4-41.4^\circ$	 	N / min^{-1}	553	499	332
		$PV^{-1} / \text{W m}^{-3}$	100	100	100
		$Re / -$	40,659	3,672	–
		$u_{\text{tip}} / \text{m s}^{-1}$	1.882	1.698	1.130

Chapter 4

Results

In this chapter, the results of the experimental work are presented and interpreted.





The first main section concerns the results corresponding to the different approaches to PIV technique, discussed in **Chapter 3**. In the second part, it is intended to compare the influence of factors like power input, fluid rheology and impeller geometry on the fluid dynamics in the stirred vessel.

All the results are based on the values of velocity calculated by the software *DaVis*. The velocity vector field, once processed by the software, is exported and further calculations are done with a *MATLAB*® code, in which the formulas presented in **Chapter 2** are implemented. The obtained data result from a measuring technique, which, as such, can be affected by minimal errors, due to the positioning of the equipment and/or by the calibration, that had to be repeated throughout the whole investigation.

4.1 Pre-experimental Establishment of Measuring Technique

The analysis of the three approaches is based on the available measured data points summarized in **Tab. 4-1**, which reports the values of power input PV^{-1} (W m^{-3}) of each measurement. All these measurements were carried out in water, solely. The full table with all the operating conditions of the measurements is presented in **Section 3.3**

Tab. 4-1 Data points used for the comparison of the three approaches to PIV technique.

Impeller type	$PV^{-1} / \text{W m}^{-3}$	Approach
WRI- $d/D=0.4-28.8^\circ$	100	2DA, 3DA
		
WRI- $d/D=0.33-51.2^\circ$	100	2DA, 3DA
		
PROPRing- $h/d=0.33$	98	2DF 2DA, 3DA
		
PROP- $h/d=0.33$	100	2DA, 3DA
		

For the comparison of the three approaches, only the data of PROPRing- $h/d=0.33$ are used. The comparison of 2DA with 3DA can be examined for all four impellers, after the comparison with the PROPRing- $h/d=0.33$.

The flow patterns developed and observed with PROPRing- $h/d=0.33$ are shown in **Fig. 4-1**. This representation of the velocity field corresponds only to the right vertical half of the vessel, where the laser sheet is complete. The left half of the vessel instead, since the laser hits the shaft in the middle, is lacking information. The flow pattern caused by PROPRing- $h/d=0.33$ meets the expectations based on the literature reviewed in **Section 2.4.3**, confirming the axial behaviour of the propeller. At first sight, an important difference between the two approaches can be remarked. With the frontal camera, **Fig. 4-1 (A)**, the information regarding the bottom of the vessel is missing, because of the exigency of purposely removing this region from the area of interest, as discussed in **Chapter 3**. The geometrical masks relative to the impeller area are different in shape due to the different angle of observation. The investigation in the bottom of the vessel, by positioning the camera from above, shows coherence with the first approach: the high velocity region is qualitatively the same and present in a quite identical position. Hence, this different angle of observation does not affect the quality of the results.

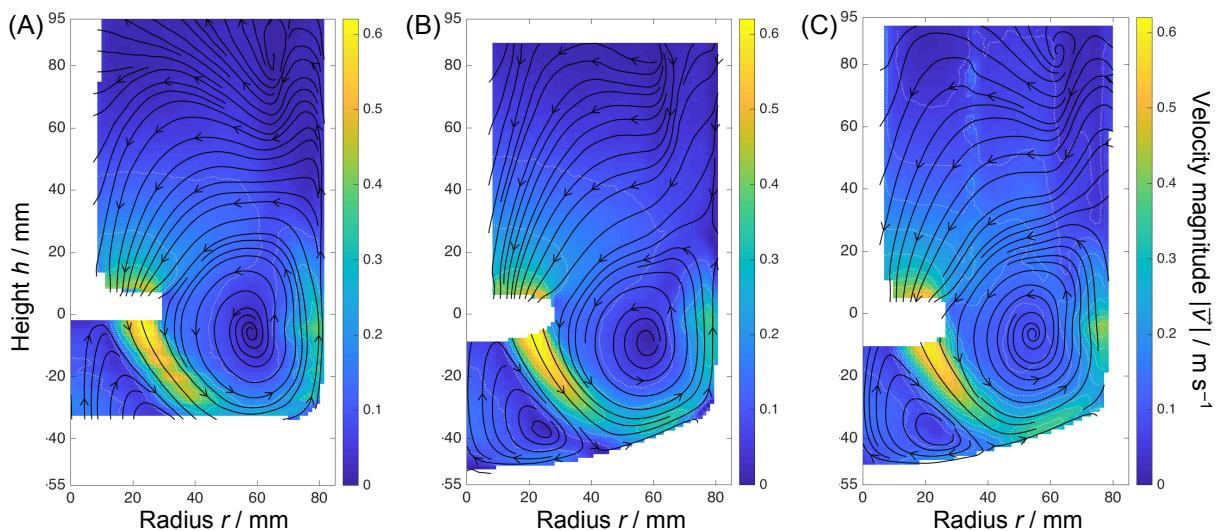


Fig. 4-1 Flow field observed with PROPRing- $h/d=0.33$ with the three approaches: (A) 2DF, (B) 2DA, (C) 3DA.

The main difference between the two angles of observation, except for the mentioned missing area at the bottom, is caused by the shape and the finish of the glass of the vessel. The non-uniform thickness of the glass in the part of the torispherical bottom produces a horizontal striping pattern, visible in **Fig. 3-12**. This characteristic, when the camera is frontal, generates results that are not truthful, because the captured images are deeply distorted in this region. It is possible to observe this feature in the flow pattern, in the region with higher velocities, which looks scattered along the axial direction. However, this characteristic is better visualized with the plots of velocity profiles, that show how velocity changes along some fixed lines of the illuminated plane of the stirred vessel, see **Fig. 4-2**.

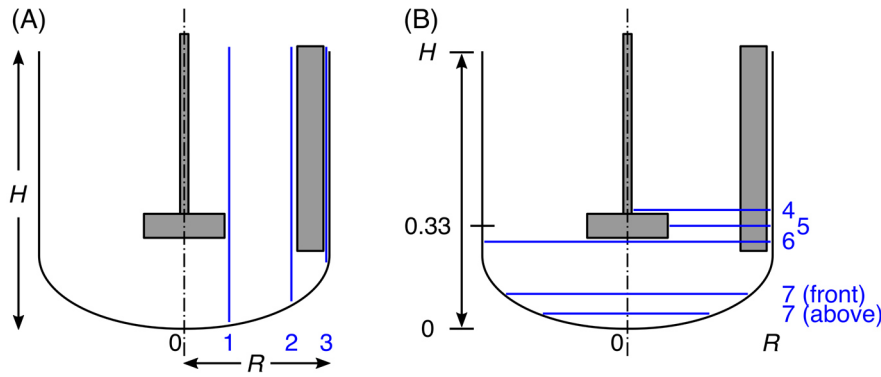


Fig. 4-2 Lines laying in the examined plane, where velocity profiles are calculated: (A) vertical, (B) horizontal.

From the velocity field, the local velocity vectors corresponding to three vertical and four horizontal lines are exported. The choice of these positions is suggested by the intention of investigating the main areas of interest for the understanding of the impeller behaviour in the fluid. The vertical lines pass through the entire height of the vessel in the vicinity of the impeller, near the vessel and near the vessel wall. The horizontal lines are fixed above and below the impeller, on the bottom of the vessel and at the centre of the impeller. The horizontal lines that correspond to the positions above and in the centre of the impeller stop where the shaft is located, because it is not possible to have information in the other half. For 2DF, 2DA and 3DA, the horizontal line laying in the bottom is different, because of the different observation in this region. The coordinates of these vertical and horizontal lines, relative to the reference frame that has the centre of the impeller as origin, are summarized in **Tab. 4-2**. For a better visualisation and comprehension of this type of result, the velocity is normalized with the tip speed u_{tip} , as well as the vertical and horizontal lines are normalized with the vessel height and radius, respectively. The curves are plotted in the Cartesian plane, with the axes that respect the actual orientation of the vessel, see **Fig. 4-3**.

Tab. 4-2 Position of the vertical and horizontal lines in the investigated laser sheet.

line #	x (mm)	y (mm)
1	30	$-53 < y < 107$
2	60	$-53 < y < 107$
3	78	$-53 < y < 107$
4	$0 < x < 80$	+15
5	$0 < x < 80$	0
6	$-80 < x < 80$	-15
7	$-80 < x < 80$	-33 (front) -45 (above)

The angle of observation allows to overcome the defects of the glass and to investigate the bottom with more complete results. In the velocity profiles, it should be noticed how the curve is scattered in the region below the impeller, which, in dimensionless coordinates, corresponds to $h/H = 0.33$.

This characteristic is significant for the position 3, especially. In general, the curves obtained with the frontal camera start at a bigger value of h/H , because of the cropped area at the bottom. On the other hand, the positioning of the camera from above encountered the need

of cutting off the surface area, hence the curves relative to 2DA and 3DA go to 0 before reaching H . The curves of position 1 show higher velocity at $h/H = 0.2$, that corresponds to the yellow region in the flow pattern representation.

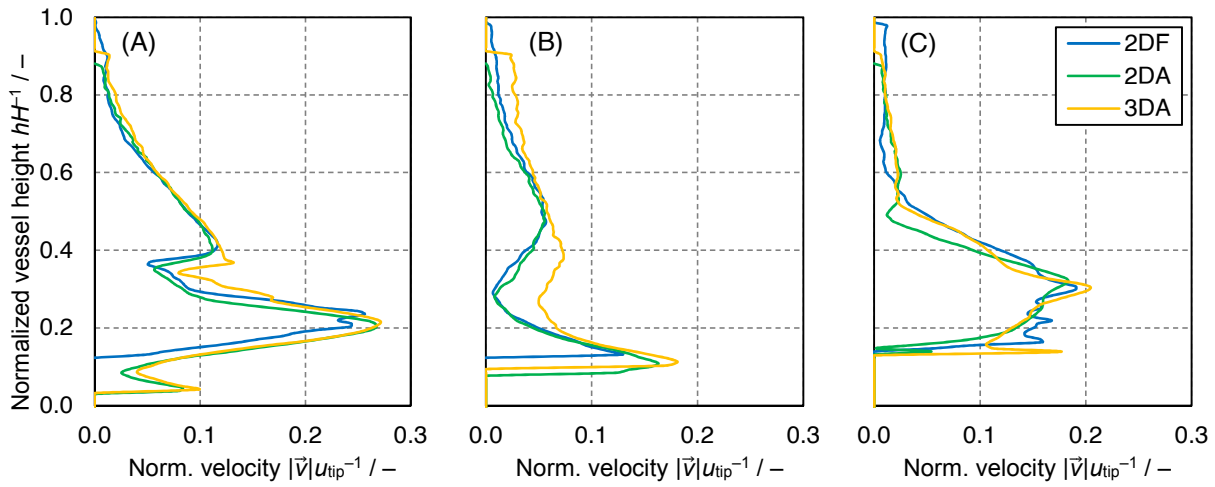


Fig. 4-3 Vertical profiles of normalized velocity magnitude, PROPRing- $h/d=0.33$: (A) position 1, (B) position 2, (C) position 3.

The uncertain scattered velocity along y direction can be better observed with v_y component, by considering only the three vertical lines, see **Fig. 4-4**.

The scattering is more significant in the positions 1 and 3, relative to a higher velocity region in the vessel. The y component of the vector velocity, as well as the x component, can be either positive or negative: in position 1 the negative velocity tells that the flow is directed downwards, like it is shown in the vector field. In the positions 2 and 3 the curves have positive values, which means that the flow is rising near the wall. In position 3 the values are higher as compared to position 2, as confirmed by the velocity field.

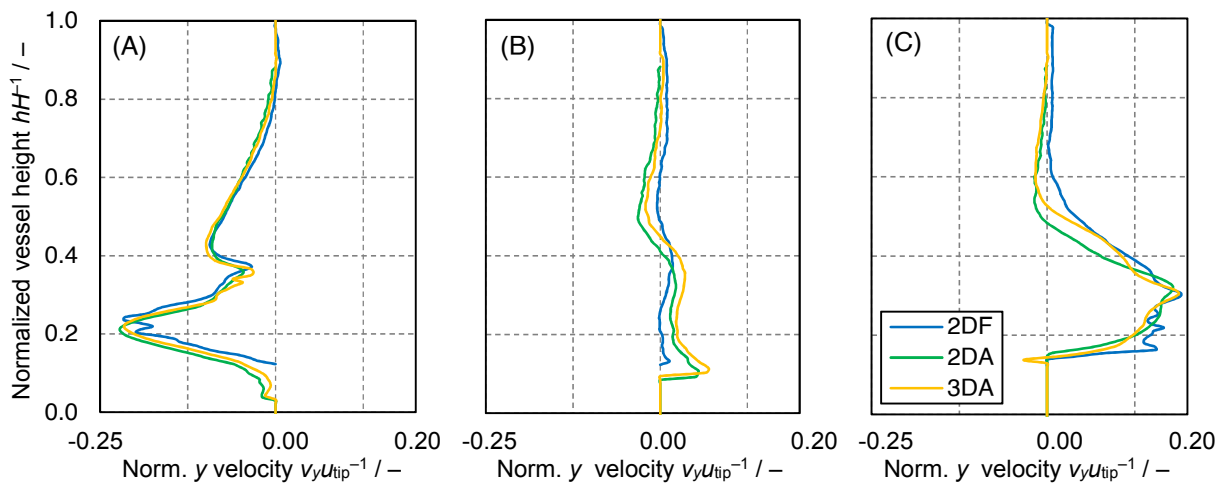


Fig. 4-4 Vertical profiles of normalized velocity along y direction, PROPRing- $h/d=0.33$: (A) position 1, (B) position 2, (C) position 3.

In the **Appendix A**, the horizontal profiles of v_y component and all the seven profiles of v_x component are reported.

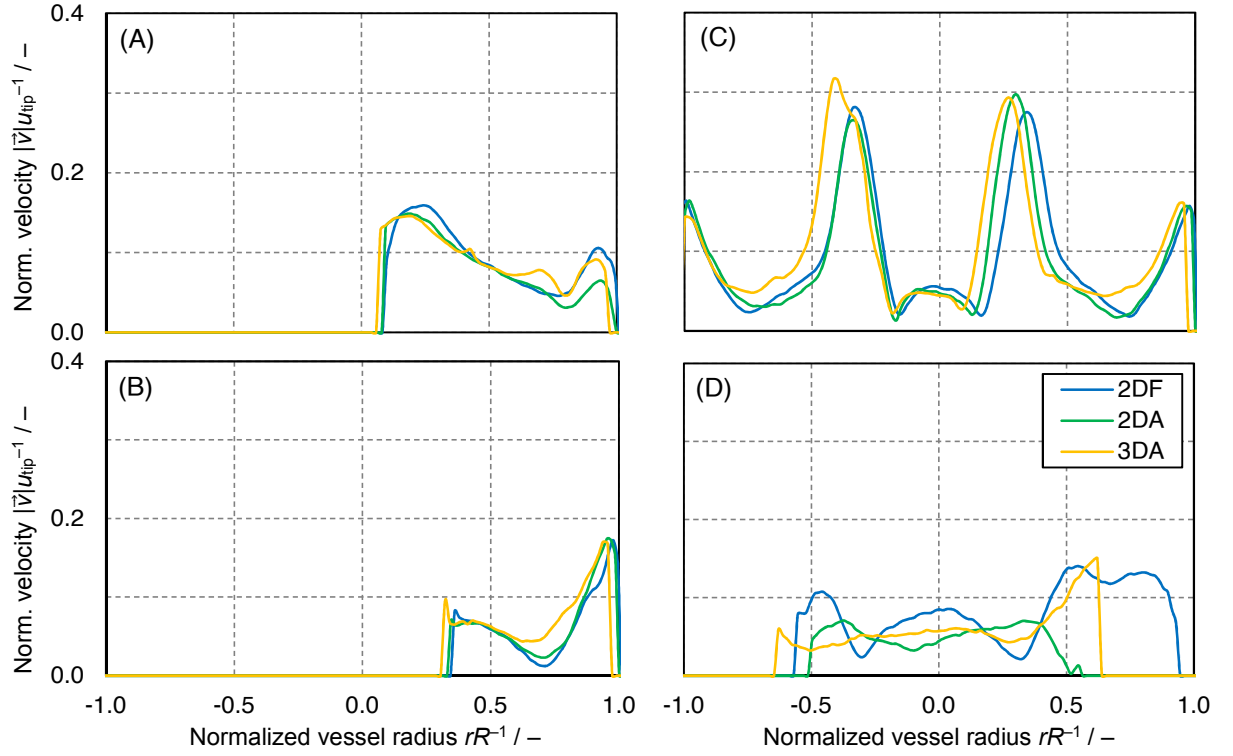


Fig. 4-5 Horizontal profiles of normalized velocity, PROPRing- $h/d=0.33$: (A) position 4, (B) position 5, (C) position 6, (D) position 7.

The velocity profiles along the horizontal lines are now considered with the normalized total velocity, see **Fig. 4-5**. In position 7, the curves are significantly different between the two angles of observation: this is due to the position of line 7, that is not at the same height. Hence, the comparison at this point works as long as only 2DA and 3DA are considered.

In general, the velocities calculated with 3DA are slightly bigger than the ones obtained with 2DA. The 3D analysis can also provide the tangential components of velocity that passes through the plane of investigation. These components, instead, are invisible with the two-dimensional analysis.

This is confirmed by **Fig. 4-6** (A), which shows the CDF of the normalized velocity. This curve is a result of the average vector field, calculated by averaging the vector fields obtained by all the double-frame pictures. The 2DF curve is characteristic of smaller velocities among the three approaches, because this position does not allow to investigate on the bottom part, where velocity is generally higher with respect to the upper part of the vessel. The curve that is relative to 3DA corresponds to higher values of velocities. The 2DA lays in between: since the bottom part can be examined, there are more higher velocities; however the tangential components are out of the investigation.

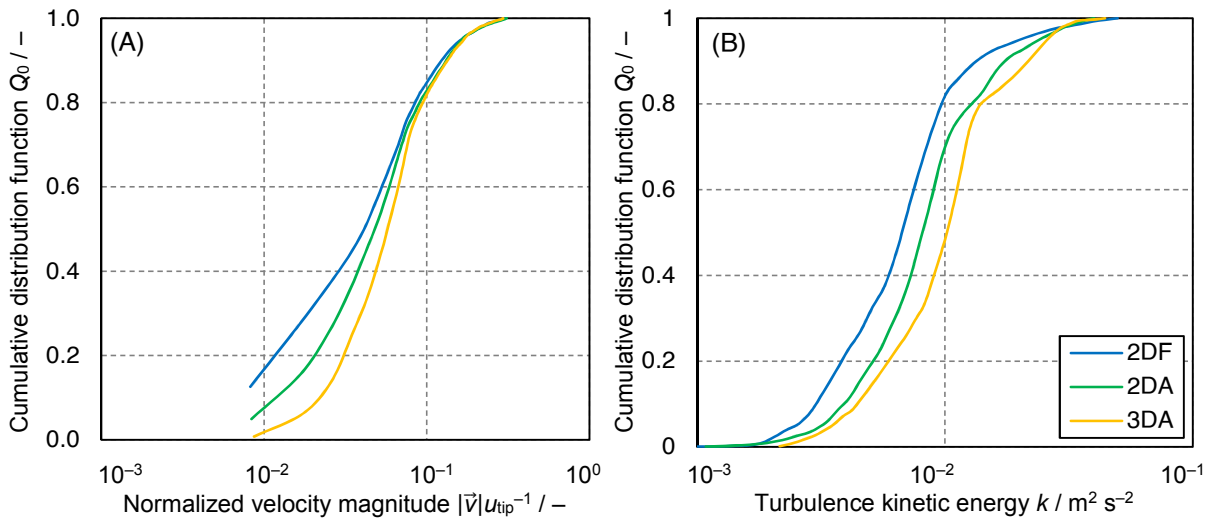


Fig. 4-6 CDF of the average vector field and of the turbulence kinetic energy inside the vessel, for the three approaches, PROP Ring- $h/d=0.33$: (A) normalized velocity, (B) TKE.

Concerning the TKE, see **Fig. 4-6** (B), since this is calculated from the values of velocity, the trend among the three approaches is analogous. With the three-dimensional investigation, the TKE results to be higher as compared to the other two approaches, because here also the tangential velocity is taken into account. The curve relative to 2DF is the smallest, because a part of the region of turbulence is missing in the calculation. The 2DA approach can detect this area entirely, but is not able to see the velocities that pass through the plane, so the curve relative to this approach lays between the other two.

It should be noticed that around the 80% value of the CDF, the curve representing 3DA shows a decrease in the derivative, meaning that the gradient of the bars' amplitude of the equivalent histogram decreases. This may be explained with **Fig. 4-7**, which represents the TKE field with isolines. With the 3DA, since two cameras look at the vessel from a non-frontal position, the observed and captured plane contains the baffles. The baffle is not hidden with a mask in the calculation of the velocity vector field, because *DaVis* can interpolate the values in those points. However, in the determination of TKE, errors relative to the baffle region occur, so these points are removed before the actual calculation is done. Hence, the points where the TKE is around $0.015\text{--}0.3\text{ m}^2\text{ s}^{-2}$, corresponding to the decrease of the curve's derivative, may be the points hidden by the lowest extremity of the baffle, discarded from the TKE calculation.

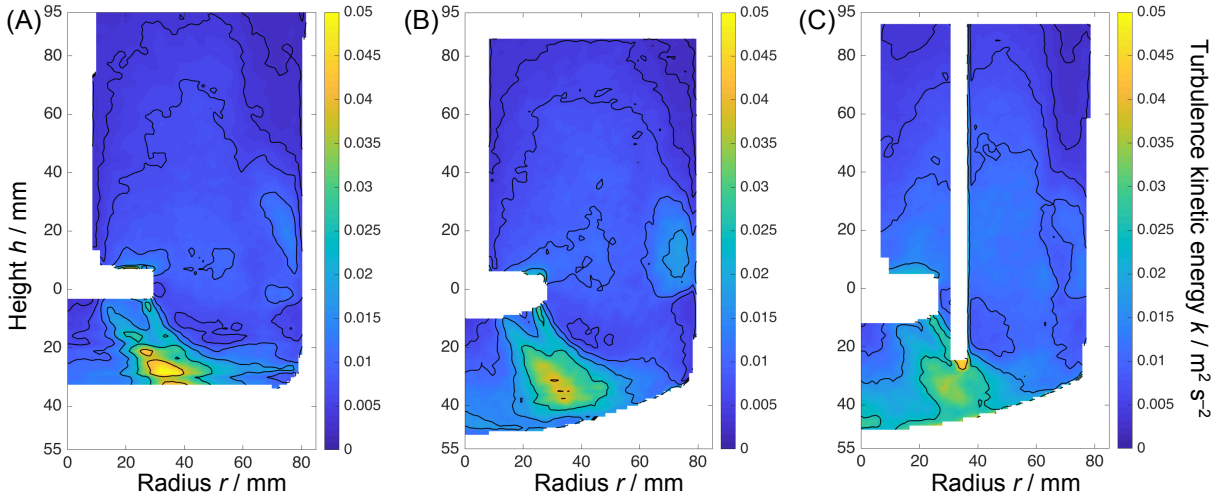


Fig. 4-7 TKE field with isolines for the three approaches, PROPRing- $h/d=0.33$: (A) 2DF, (B) 2DA, (C) 3DA.

Taking into account the other three impellers chosen for this comparison, the observations expressed for PROPRing- $h/d=0.33$, concerning the differences from 2DA and 3DA, are confirmed, see **Fig. 4-8**.

With the three-dimensional approach, indeed, the velocity and the TKE are found to be higher as compared to 2DA for all the impellers.

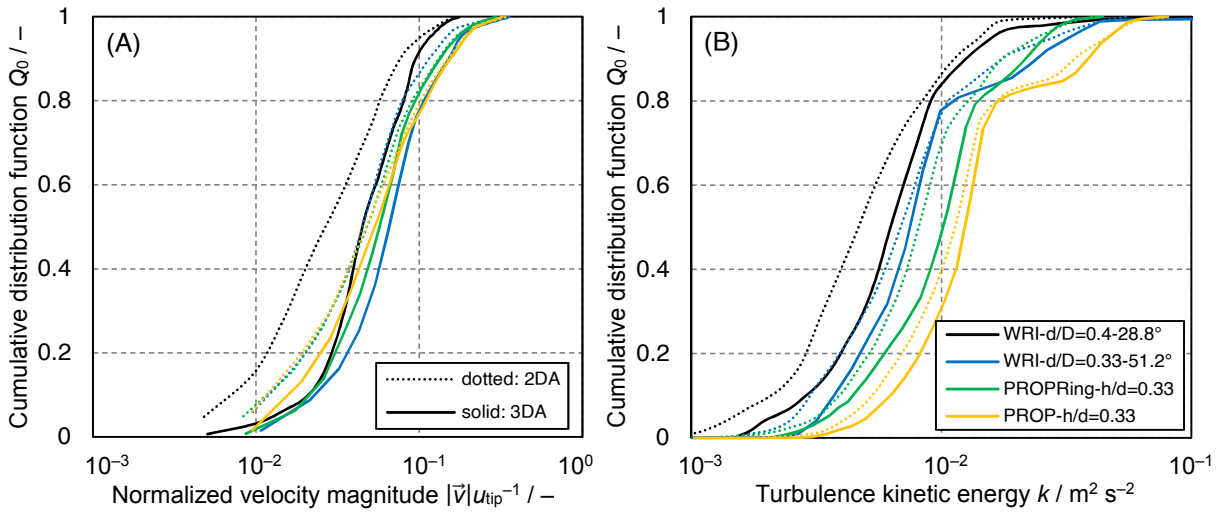


Fig. 4-8 CDFs of velocity and TKE for PROP- $h/d=0.33$, PROPRing- $h/d=0.33$, WRI- $d/D=0.4-28.8^\circ$ and WRI- $d/D=0.33-51.2^\circ$, measured with 2DA and 3DA: (A) velocity, (B) TKE.

The flow fields of PROP- $h/d=0.33$, WRI- $d/D=0.4-28.8^\circ$ and WRI- $d/D=0.33-51.2^\circ$ calculated with the approaches 2DA and 3DA are reported in the **Appendix A**.

In conclusion, considering the flow patterns and the CDFs of both velocity and TKE, obtained with the three approaches to PIV technique, it is quite clear that 2DA can provide valuable and truthful results. However, 3DA, thanks to the use of two cameras, gives more complete results that arise out of the acquiring and calculation of the additional tangential component.

With the three-dimensional approach, since this makes use of two cameras, the acquisition and the saving of the pictures requires much more storage space in the computer. Moreover, the duration of a single experiment becomes longer, due to the longer saving process.

For these reasons, the investigation with 3D-PIV is not done for all the impellers, but only for the four presented. The two-dimensional PIV is used for the whole investigation. However, in the next comparisons the results obtained with the 3D-PIV are presented whenever they are available and coherent within the set of chosen data points.


4.2 Systematic Investigation

In this section the results obtained with the formerly discussed measuring technique are presented and interpreted. The results are organized in three subsections, where the influence of power input, fluid rheology and stirrer geometry is analyzed. Finally the particle stress generated by the different impellers is discussed. Moreover, in the last subsection, further results achievable with the PIV analysis are briefly presented.

4.2.1 Influence of Power Input on the Fluid Dynamics in Stirred Vessel

The comparison between five values of power input is discussed here. The measurements are all carried out in water with the approach 3DA, with one impeller, PROPRing- $h/d=0.33$. The data points, summarized in **Tab. 4-3**, indicate the values of power input PV^{-1} (W m^{-3}). The full table with the operating parameters is reported in **Section 3.3**.

Tab. 4-3 Chosen data points of power input to investigate the influence on the flow field, developed by PROPRing- $h/d=0.33$.

Impeller type	$PV^{-1} / \text{W m}^{-3}$				
PROPRing- $h/d=0.33$	19	49	98	195	488
					

For simplicity, **Fig. 4-9** shows the flow patterns that are developed with PROPRing- $h/d=0.33$ at only three values of power input: 19, 98 and 488 W m^{-3} . The flow patterns relative to 49 and 195 W m^{-3} are reported in the **Appendix B**. In general, the flow maintains the same axial characteristic as shown in the previous section. However, with the increase of power input, the swirl of the fluid in proximity of the impeller becomes wider. This means that the circulation path becomes longer and that the circulation and the mixing times decrease with the increase of power input. The mixing becomes more efficient with a higher power input.

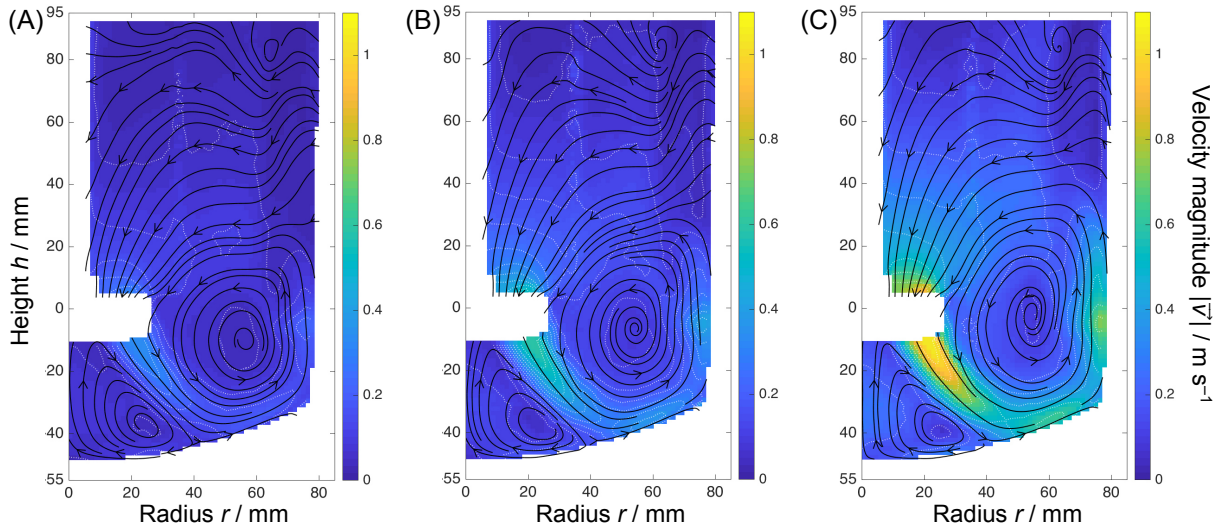


Fig. 4-9 Flow field observed with PROPring- $h/d=0.33$ with increasing power input: (A) 19 W m^{-3} , (B) 98 W m^{-3} , (C) 488 W m^{-3} .

With the increase of power input, also the intensity of the velocity field increases, since the impeller rotational frequency is increased. The CDF for the normalized velocity with the five values of power input shows slight differences, since all the curves are overlapped with each other, see **Fig. 4-10** (A). This outcome of the CDF demonstrate that the ratio of the velocity with the tip speed maintains a scale factor for the different values of power input, exhibiting the self-similarity of the system.

Providing a higher power input to the fluid means operating at a higher impeller frequency, hence generating a higher Re . As a consequence, the fluid flows with a higher turbulence, that is translated to higher values of TKE in the stirred vessel. This is confirmed by the CDF of the TKE, shifted on the x axis for different power input values, see **Fig. 4-10** (B).

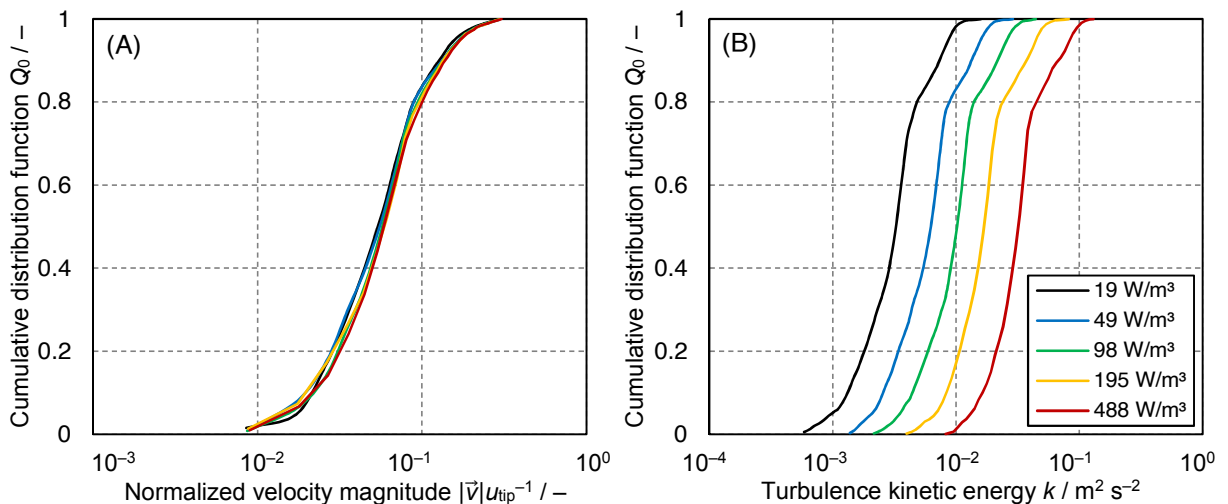


Fig. 4-10 Influence of power input with PROPring- $h/d=0.33$, measured in water with 3DA: (A) CDF of normalized velocity, (B) CDF of TKE.

The local EDR is an important as well as challenging quantity to determine, especially in the impeller region, where highest values are found. The determination of local EDR is usually based on the assumption of isotropy, which is far from describing the reality of a stirred vessel. Furthermore, the calculation of local EDR from the velocity gradients obtained by PIV

deeply depends on the spatial resolution of the analysis (Delafosse et al., 2011). This should be equal or smaller than the Kolmogorov microscale, where the dissipation occurs with the eddies of smallest size. The finite grid sizes used by PIV to calculate the velocity gradients, the IWs, often exceed the smallest size of the eddies, generating an unreal distribution of EDR in the space of the stirred vessel. A suggested way to determine the local EDR is the large eddy method, suggested by Sagaut and Lee (2002).

In this experimental work, with the preliminary tests on the measuring technique and the processing of the great amount of different results, the local EDR is not calculated. However, by calculating the average EDR with **Eq. (2-48)**, it is possible to see the influence of the power input on this quantity according to

$$\overline{\varepsilon_T} = \frac{P}{\rho V} \quad (2-48)$$

with $\rho = 997.66 \text{ kg m}^{-3}$ and $V = 0.00299 \text{ m}^3$, the density and volume of the fluid, respectively. Moreover, the determination of the Kolmogorov microscale with **Eq. (2-47)**, gives an idea on the change of the eddies' size with the change of power input.

$$\eta = (v^3 / \overline{\varepsilon_T})^{1/4} \quad (2-47)$$

with $v = \mu \rho^{-1} = 1.0023 \times 10^{-6} \text{ m}^2 \text{ s}^{-1}$. The values calculated this way, are reported in **Tab. 4-4** with the corresponding values of power input and Reynolds number.

Tab. 4-4 Average energy dissipation rate and Kolmogorov scale calculated for different values of power input.

$PV^{-1} / \text{W m}^{-3}$	$Re / -$	$\varepsilon / \text{m}^2 \text{s}^{-3}$	$\eta / \mu\text{m}$
19	20,964	0,019	85
49	28,453	0,049	67
98	35,849	0,098	57
195	45,166	0,195	48
488	61,300	0,489	38

The increase of power input produces a higher turbulence in the fluid, in which the TKE is dissipated at a higher rate by eddies of smaller size.

Considering that the size of the smallest IW used for the calculation is equal to 24×24 pixels, which corresponds to $1.4 \text{ mm} = 1.4 \times 10^3 \mu\text{m}$, it is possible to say that the spatial resolution of this PIV analysis is not able to detect the smallest turbulent eddies. The typical Kolmogorov scale of a tank bioreactor is around the range of $50\text{--}200 \mu\text{m}$ (Delafosse et al., 2011), as estimated in the calculation of the mean value of η , in **Tab. 4-4**.

Another valuable result from the analysis of the data obtained by PIV is represented by the gradients of the forces that act on the particles. The shear and normal gradients are calculated with the formulas explained and provided by Wollny (2010), see **Section 2.3**. In the derivation of the formulas, a coordinate transformation is operated in the velocity tensor, in order to have the tangential and the normal components of the velocity with respect to the direction of the flow. The values calculated for each IW result in the vector field of shear and normal gradients and the field of the strain tensor's magnitude. From the statistical analysis of

the field it is possible to calculate the distribution of the values in the area of interest, by using the histogram and the CDF. These representations are given in **Fig. 4-11**.

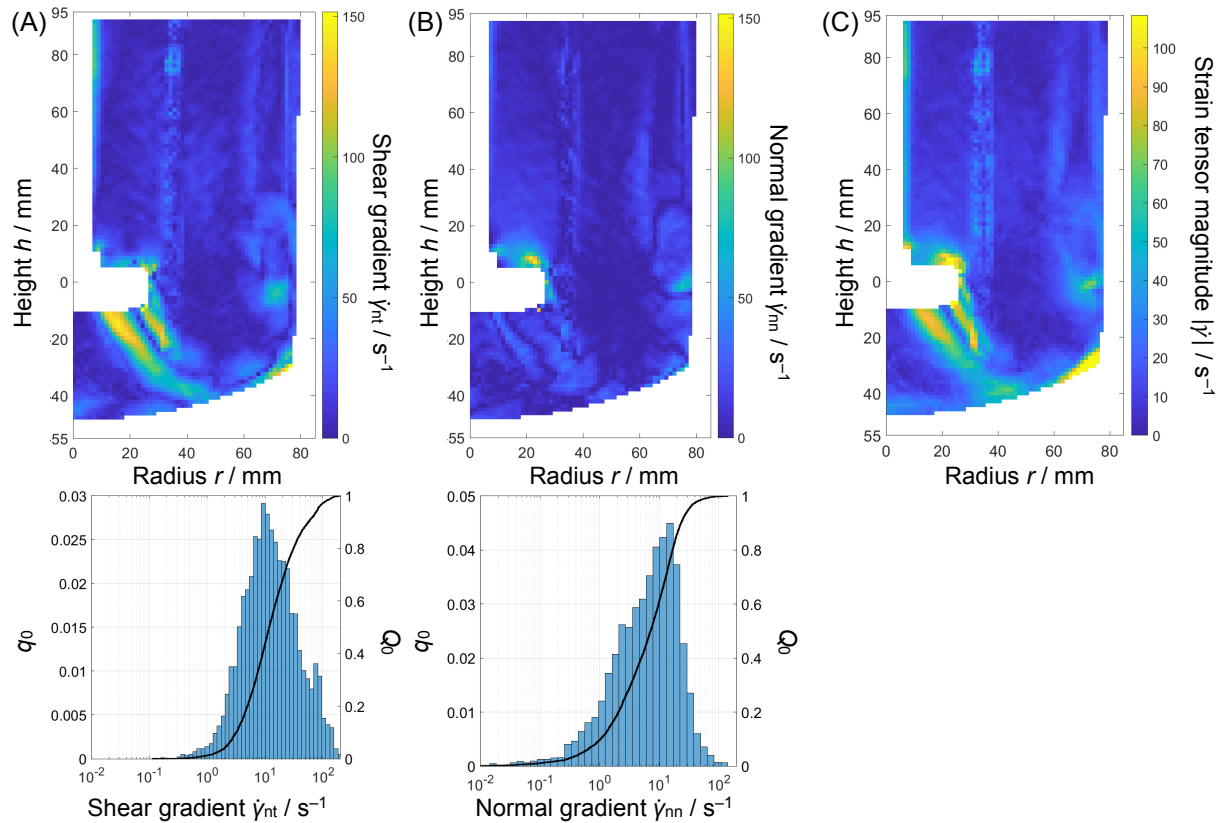


Fig. 4-11 Strain tensor calculated for PROPRing- $h/d=0.33$, $PV^{-1} = 98 \text{ W m}^{-3}$: (A) Shear and normal gradient fields, (B) Shear and normal gradients histograms and CDFs, (C) Strain tensor's magnitude field.

The high shear rate zone corresponds to the region, below the impeller, that delimits the points of high velocity. Here the velocity gradients in the direction that is normal to the flow stream are the highest, since the velocity decreases from the highest to a very low value, and the other way around. In this case, considering the flow field in **Fig. 4-9** (B), the velocity goes from about 0.6 m s^{-1} to 0.2 m s^{-1} in a reduced length of some mm: the shear gradient, in **Fig. 4-11** (A), in this region shows the maximum value of shear rate, which is around 150 s^{-1} .

However, the vector field is not the best option to use when a direct, quantitative comparison is required. The representation of several distribution functions, when easy to interpret, can give a good and intuitive idea of the analysis. The CDFs of the shear and normal gradients, for the five values of power input, are represented in **Fig. 4-12**.

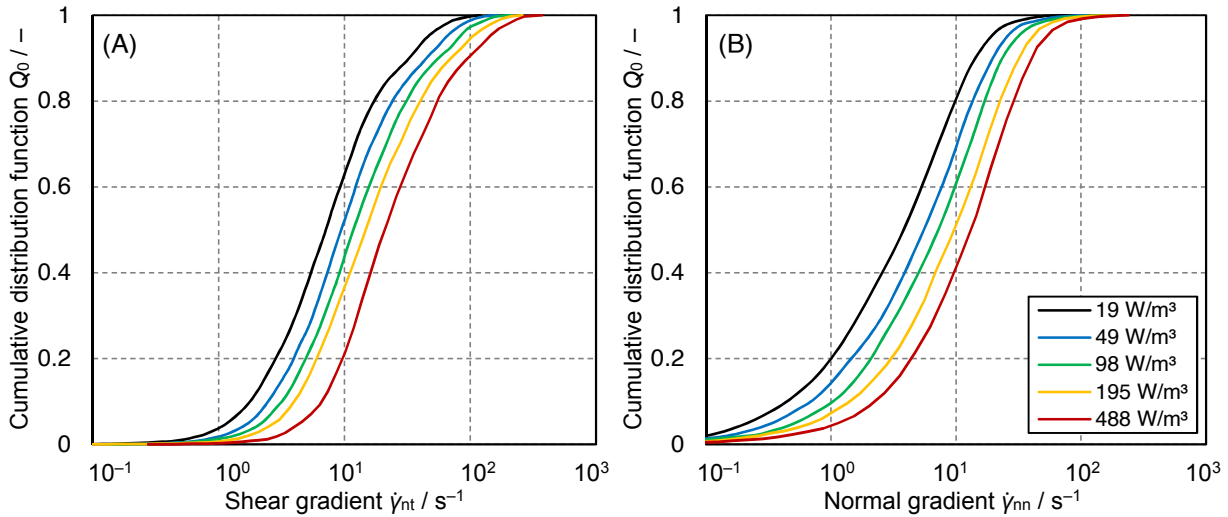



Fig. 4-12 Influence of power input, PROPRing- $h/d=0.33$: (A) shear gradients, (B) normal gradients.

The increase of power input produces a stronger hydomechanical stress on the particles, that results with the increase of both shear and normal gradients. The fluid flows with a higher turbulence and it exerts a higher strain, so the particles in the fluid feel more shear, the tangential component, and more normal, elongational forces. However, from the CDFs plotted in **Fig. 4-12**, it results clear that the shear components are prevalent on the normal ones, which contrarily to the former do not exceed 10^2 s^{-1} .

4.2.2 Influence of Fluid Rheology on the Fluid Dynamics in Stirred Vessel

For the analysis of the influence of the fluid rheology, the choice of the impeller concerns PROPRing- $h/d=0.33$. The measurements are all taken with 2D-PIV, with the camera from above (approach 2DA). Two values of power input are investigated. With one constant value of power input, the results concerning the three fluids, which are characterized by different rheological properties, are compared. An initial error in the estimation of the Newton number is the reason why the power input values for water are not 100 and 200 W m^{-3} , nevertheless, the relative error of 2% can be neglected. The data points of this comparison are reported in **Tab. 4-5**. The operating conditions of these measurements are completely reported in **Section 3.3**

Tab. 4-5 Data points used for the study of the rheology influence on the flow field, with PROPRing- $h/d=0.33$.

Impeller type		Fluid		
		Water	Glycerin	Xanthan
 PROPRing- $h/d=0.33$	$PV^{-1} / \text{W m}^{-3}$	98	100	100
		195	200	200

For simplicity, the flow fields shown in **Fig. 4-13** correspond only to the lowest value of the investigated power input. The flow fields developed at $PV^{-1} = 200 \text{ W m}^{-3}$ are reported in

Appendix B. The flow patterns developed with PROPRing- $h/d=0.33$ show a more axial behaviour in water, with respect to glycerin and xanthan, where the flow presents also a radial feature.

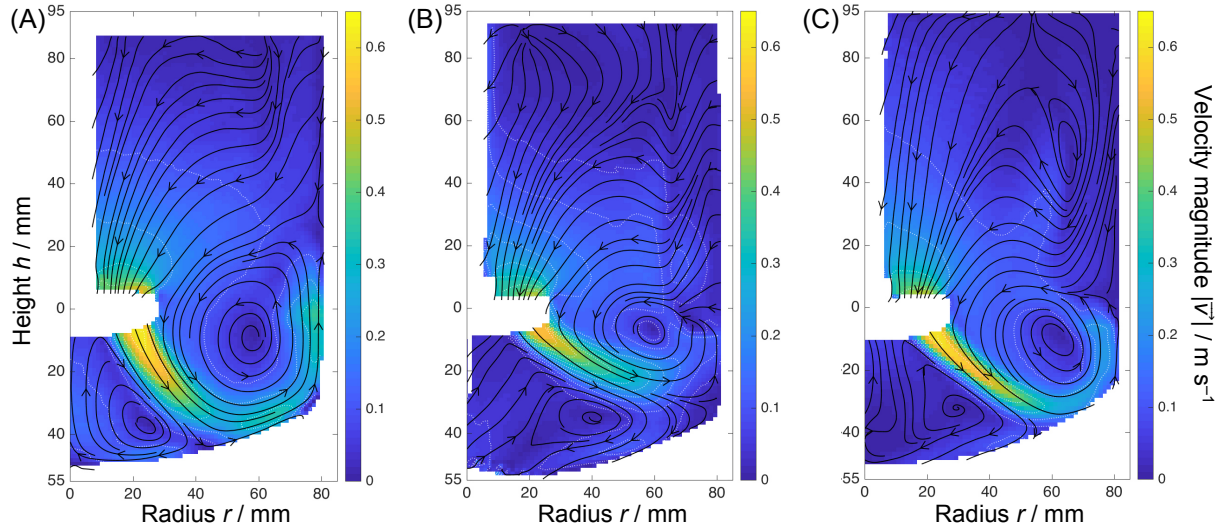


Fig. 4-13 Influence of rheology on the flow patterns developed with PROPRing- $h/d=0.33$, for $PV^{-1} = 100 \text{ W m}^{-3}$: (A) water, (B) glycerin, (C) xanthan.

If the nature of the flow regime is taken into account, this result is reasonable. Water is here characterized by a Reynolds number $Re = 35,849$ and glycerin by $Re = 3,136$. For xanthan, due to its non-Newtonian behaviour, the determination of Re is more difficult, since the viscosity has not a constant value. The Reynolds number for a non-Newtonian fluid can be determined with the apparent viscosity μ_a . Xanthan is described with *Ostwald-de-Waele* model, which uses two characteristic coefficients of the fluid, n and K , see **Section 2.2**. For xanthan, these coefficient are $n = 0.3845$ and $K = 0.17185 \text{ kg m}^{-1} \text{ s}^{-2}$. The apparent viscosity of the fluids that are described with this model can be calculated by

$$\mu_a = K\dot{\gamma}^{n-1} \quad (2-6)$$

and, considering that the shear rate locally changes, μ_a does not have a constant value. A possible solution may consist in taking only those into regions account with the highest and the (quasi) lowest shear. In the shear gradient field, showed in **Fig. 4-14**, it is possible to take 200 s^{-1} and 20 s^{-1} as the maximum and minimum values of shear, respectively. The corresponding maximum and minimum values of apparent viscosity are $\mu_{a,\max} = 0.00659 \text{ Pa s}$ and $\mu_{a,\min} = 0.027187 \text{ Pa s}$. The calculation of Re gives a maximum and a minimum value: $Re_{\max} = 5,624$ and $Re_{\min} = 1,276$. The impeller region is characterized by a Re that is 4 times the Re in the rest of the vessel. The flow is in a transitional flow. The full turbulent regime of water determines a more axial flow, with respect to the transitional flow of glycerin and xanthan.

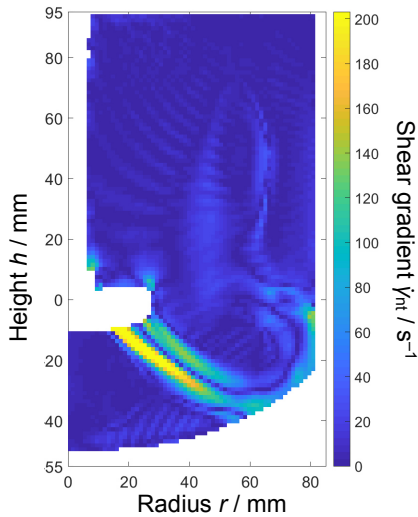


Fig. 4-14 Shear gradient observed in xanthan at $PV^{-1} = 100 \text{ W m}^{-3}$ with $\text{PROPRing-}h/d=0.33$.

The CDF of the normalized velocity does not show big differences between glycerin and xanthan, for both power input values, see **Fig. 4-15 (A)**. In water the velocities are generally higher, because at the same power input, the rotational frequency of the impeller in water is higher as compared to the other two fluids. The lower viscosity of water allows the inertial forces to overcome the viscous forces with lower power input.

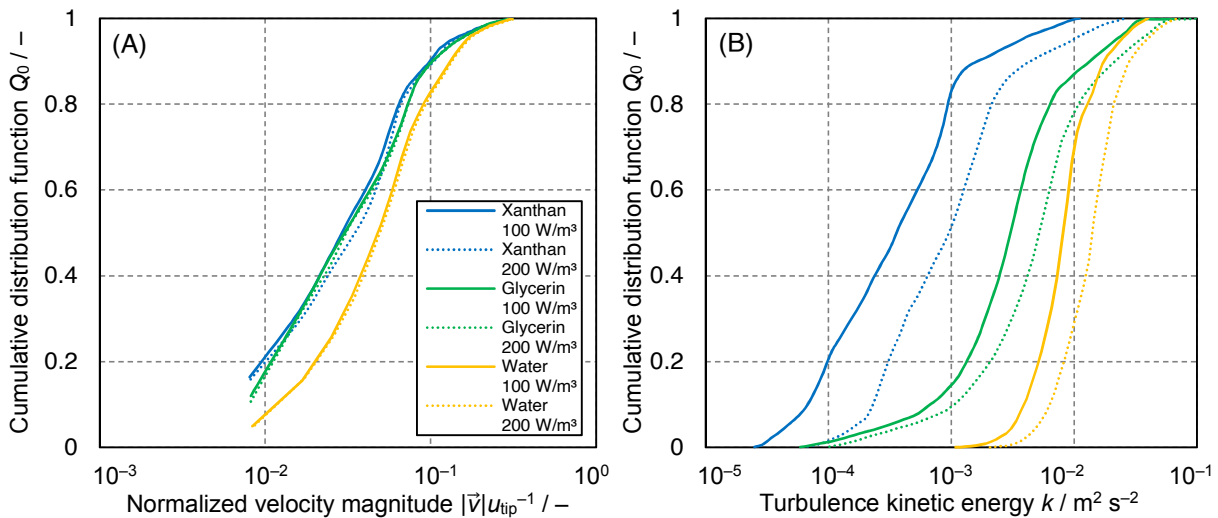


Fig. 4-15 Influence of rheology for $\text{PROPRing-}h/d=0.33$, with two constant values of power input: (A) CDF of the normalized velocities of the vector field, (B) CDF of the TKE field.

The TKE generated by the motion of the impeller is higher when it stirs a less viscous fluid, see **Fig. 4-15 (B)**. In a fluid with low viscosity, like water, the dominance of the inertial forces upon the viscous forces is translated with higher values of Re , hence to a higher turbulence. With the CDFs of TKE, it is possible to appreciate a significant difference between the three fluids. Here, xanthan and glycerin curves do not overlap, but they are distinct and different. This means that, even if the distribution of the normalized velocities is comparable, the fluctuating velocities are significantly different between the two fluids. The values of TKE are smaller for xanthan because the high viscous forces contrast the turbulence, as compared to water and glycerin. The fields of TKE relative to the lowest value of power input are reported in **Appendix B**.

Like for the previous comparison, the average EDR can be calculated with **Eq. (2-48)**. The results are reported in **Tab. 4-6**.

Tab. 4-6 Calculation of ε with $V = 2.99$ L, volume of the fluid in the vessel.

Fluid	$PV^{-1} / \text{W m}^{-3}$	$\varepsilon / \text{m}^2 \text{s}^{-3}$
water	98	0.098
$\rho = 997.66 \text{ kg m}^{-3}$	195	0.195
glycerin	100	0.087
$\rho = 1150 \text{ kg m}^{-3}$	200	0.174
xanthan	100	0.100
$\rho = 998.37 \text{ kg m}^{-3}$	200	0.200

These values are calculated by using the density of the fluids: the differences between the values obtained for the three fluids are comparable and no substantial discrepancy is remarked. However, the averaged EDR is an approximate value, from which is not possible to have information on the local intensity of this quantity in the stirred vessel.

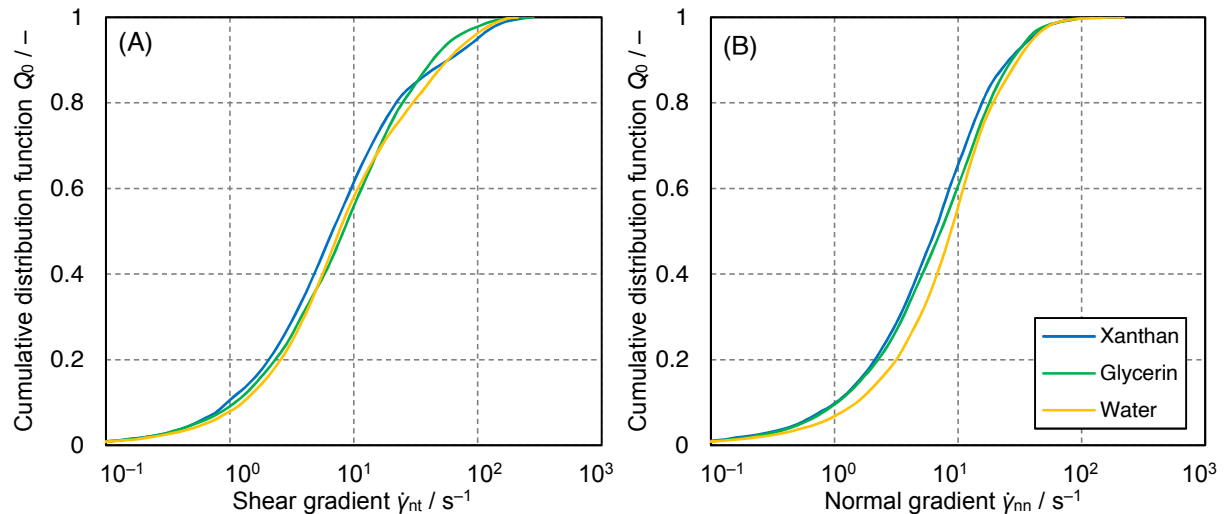


Fig. 4-16 Influence of rheology for PROPRing- $h/d=0.33$ at $PV^{-1} = 98 \text{ W m}^{-3}$: (A) shear gradient, (B) normal gradient.

The shear produced in the three fluids is found very similar in range and distribution, see **Fig. 4-16 (A)**. Considering the similarity between the values of the average EDR calculated for water, glycerin and xanthan, this result for the shear gradient seems to be confirmed. However, it has to be considered that for this comparison the values of average EDR are used, which are not able to provide local information inside the vessel. A little difference is visible for the normal gradient, **Fig. 4-16 (B)**, which shows slightly higher values for water, in the middle range. This suggests that the decrease of the viscosity produces a higher turbulence which exerts a higher normal stress on the particles (compression and elongation forces in the fluid). However, the differences generally are small when comparing both types of gradients, the shear and the normal gradient.

4.2.3 Influence of Impeller Geometry on the Fluid Dynamics in Stirred Vessel

In this subsection, the nine stirrers used in this experimental work are compared. The comparison is done for water, glycerin and xanthan, by considering only one data point of power input equal to 100 W m^{-3} , except for PROPRing- $h/d=0.33$, which is measured in water at a value of power input $PV^{-1} = 98 \text{ W m}^{-3}$. For each fluid, the data are taken with the approach 2DA. To have a better comprehension of the results, the analysis is done separately for each fluid, starting from water, followed by glycerin and xanthan. In this comparison, the interpretation of the results makes use of the plot types presented so far. Hence, in order to have a better visualisation, the impellers are collected in three main groups: two propellers, three pitched blade turbines (PBT) and the bionic loop impeller with the three wave ribbon impellers (WRI).

All the data points used for these comparison are summarized, with the other operating parameters, in **Tab. 3-9**.

Water

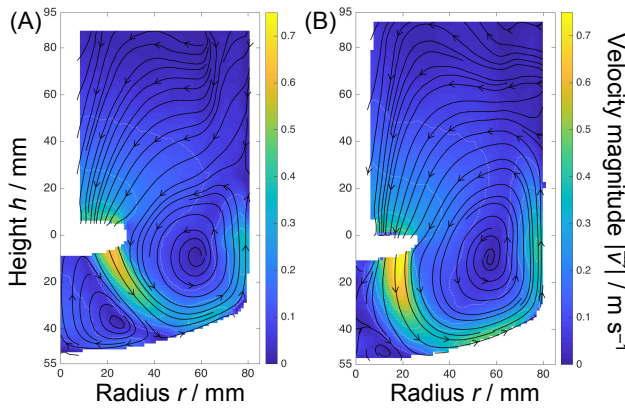


Fig. 4-17 Flow fields in water: (A) PROPRing- $h/d=0.33$, (B) PROP- $h/d=0.33$.

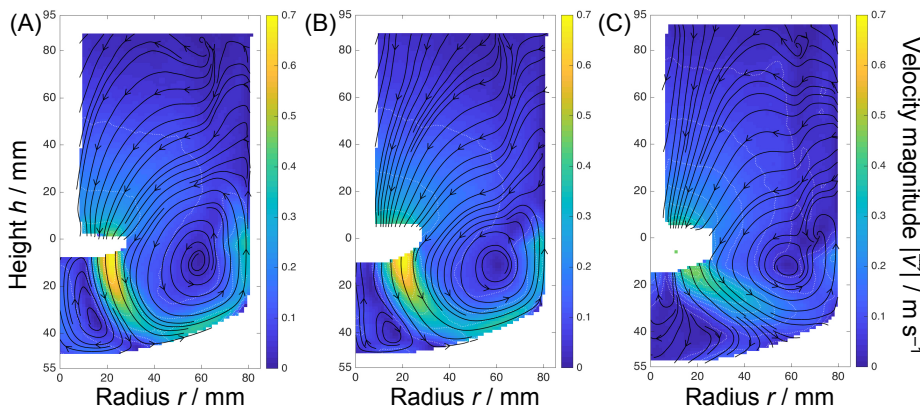


Fig. 4-18 Flow fields in water: (A) PBT-6x22.5°, (B) PBT-6x45°, (C) PBT-6x90°.

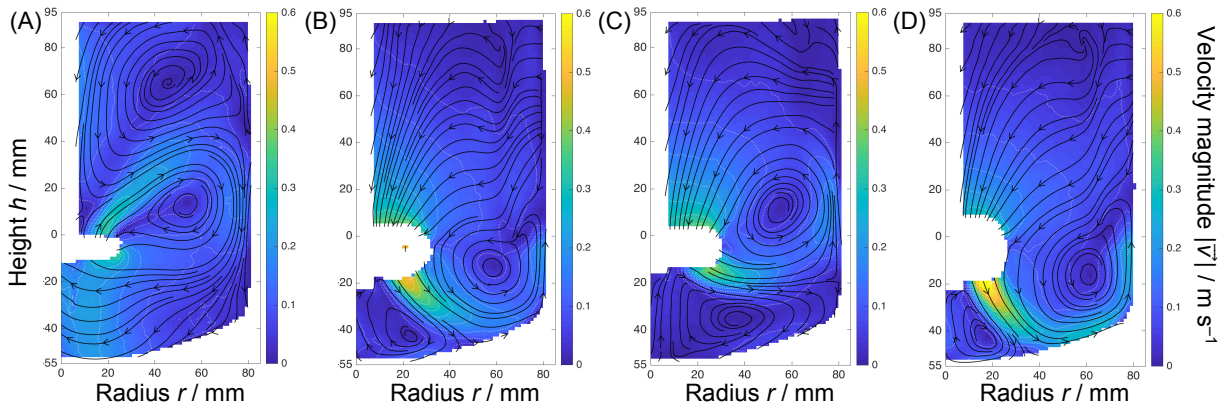


Fig. 4-19 Flow fields in water: (A) BiLoop, (B) WRI- $d/D=0.4$ -41.4°, (C) WRI- $d/D=0.4$ -28.8°, (D) WRI- $d/D=0.33$ -51.2°.

PROPRing- $h/d=0.33$ and PROP- $h/d=0.33$

The normal propeller PROP- $h/d=0.33$ pumps the fluid downward and develops a pure axial flow, which is characterized by a unique circulation loop, see **Fig. 4-17** (B). The addition of the ring to the propeller reduces the axial behaviour of the flow, pumping the water in a more diagonal way and producing two circulation loops, see **Fig. 4-17** (A). The power numbers of the two impellers are similar: for PROPRing- $h/d=0.33$ it is $Ne = 0.39$ and for PROP- $h/d=0.33$ a little bit smaller with $Ne = 0.34$. However, the differences between the flows developed by those two impellers are significant. At the same power input, PROP- $h/d=0.33$ rotates at

$N = 780 \text{ min}^{-1}$, with a tip speed $u_{\text{tip}} = 2.141 \text{ m s}^{-1}$, while PROPRing- $h/d=0.33$ rotates at a lower frequency $N = 706 \text{ rpm}$ and a tip speed $u_{\text{tip}} = 1.997 \text{ m s}^{-1}$. In the plot of the CDF of the normalized velocity, **Fig. 4-20 (A)**, this difference can be slightly detected. The difference in the intensity of the velocity, however, is not substantial. What changes is the fluctuating velocities, that produce a higher TKE for the axial PROP- $h/d=0.33$, as compared to PROPRing- $h/d=0.33$.

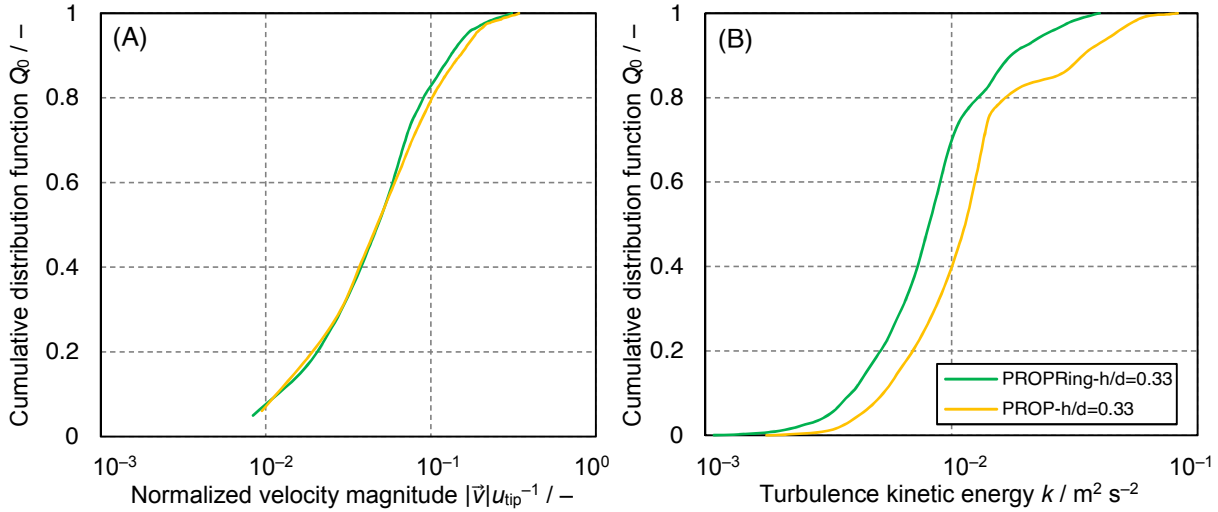


Fig. 4-20 CDFs for PROPRing- $h/d=0.33$ and PROP- $h/d=0.33$, water: (A) normalized velocity, (B) TKE.

PBT-6x22.5°, PBT-6x45° and PBT-6x90°

The pitched blade turbines produce an axial flow, as observed in **Fig. 4-18**. It is found that with the increase of the blade angle, the axial behaviour becomes less pronounced, since the high velocity region moves upwards, producing a smaller swirl in proximity of the impeller. Since axial stirrers have generally low power number Ne , to provide the fluid with the desired power input, it is necessary that these impellers rotate at a higher rotational frequency N , as explained by

$$P = \rho N^3 d^5 \cdot Ne \quad (2-52)$$

A study conducted by C. Y. Ge et al. (2014) on the flow field generated by pitched blade turbines, by using CFD simulations and PIV measurements, affirmed that an increase of the blade angle corresponds to an increase of the power number. This result is also presented in the study of Kumaresan and Joshi (2006) and was one more time confirmed by the measurements that were conducted in this experimental work. The pitched blade turbine affects the flow characteristics in a very significant way (Ranade and Joshi, 1989).

The results of these studies are again confirmed by what is found in this analysis. The power numbers Ne of PBT-6x22.5°, PBT-6x45° and PBT-6x90° are 0.55, 1.79 and 4.00, respectively. The power number clearly increases with the increase of the blade angle.

With the normalization of the velocity, the CDFs of PBT-6x45° and PBT-6x90° are very similar, while for PBT-6x22.5° it is significantly smaller, see **Fig. 4-21 (A)**.

Concerning the TKE, the trend is not univocal: In the range of low TKE, these values are more common in PBT-6x90°, less probable in PBT-6x45°, see **Fig. 4-21 (B)**. High values of TKE, although very few, are found with PBT-6x90°. In general, PBT-6x45° has the highest TKE among the three turbines.

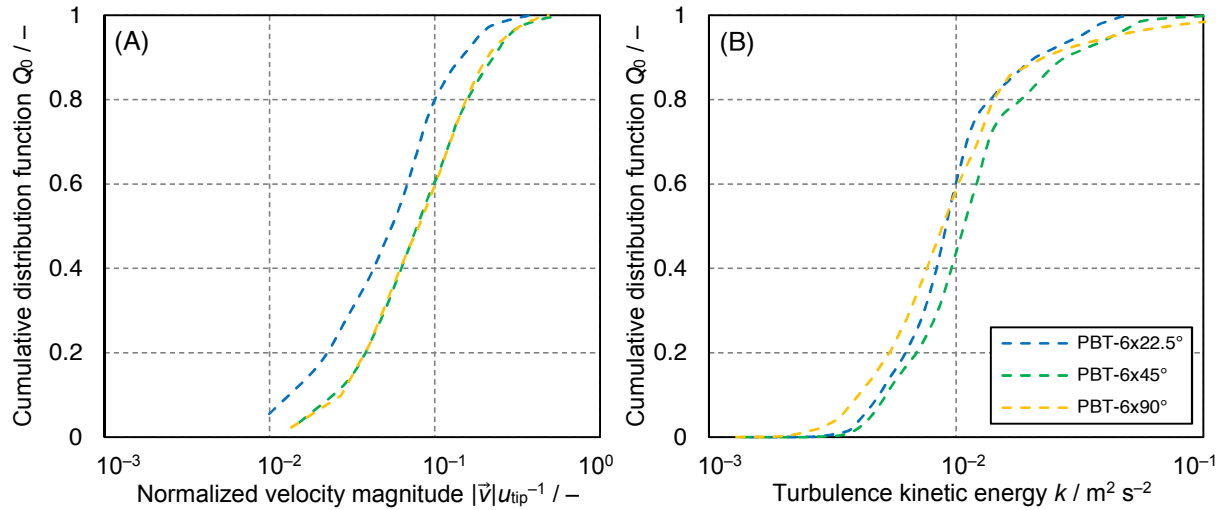


Fig. 4-21 CDFs for PBT-6x22.5°, PBT-6x45° and PBT-6x90°, water: (A) normalized velocity, (B) TKE.

These observations concerning the TKE can be better understood with the support of the TKE fields, see **Fig. 4-22**. For PBT-6x90°, it is found that there is only a small region of high intensities, while for PBT-6x45° the field shows a wider region of higher intensities. This result is coherent with what is observed with the CDFs. The TKE fields of the other two groups of impellers are reported in **Appendix B**.

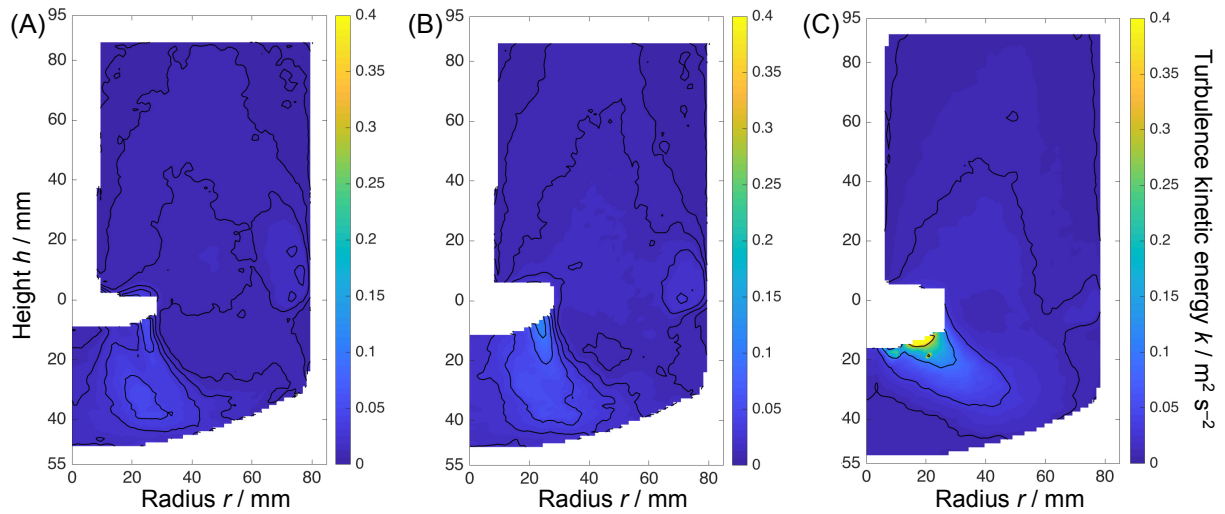


Fig. 4-22 TKE fields in water: (A) PBT-6x22.5°, (B) PBT-6x45°, (C) PBT-6x90°.

BiLoop, WRI-d/D=0.4-41.4°, WRI-d/D=0.4-28.8°, WRI-d/D=0.33-51.2°

The BiLoop impeller shows a particular flow field, characterized with one swirl on the side of the impeller and another one on the upper part of the vessel, see **Fig. 4-19** (A). Furthermore, the fluid is pumped upward, which confers to this impeller the distinctiveness of flow pattern among all the investigated impellers.

Among the WRIs, **Fig. 4-19** (B, C, D), the two impellers that show a similar behavior are WRI-d/D=0.4-41.4° and WRI-d/D=0.33-51.2°, producing an axial flow. The flow generated by WRI-d/D=0.4-28.8° has clearly a more radial feature. The WRIs with $d/D = 0.4$ show a more pronounced axial feature with the increase of the angle, which corresponds to an increase of h/d . The axial behaviour of the three WRIs is more characteristic of WRI-d/D=0.33-51.2°, followed by WRI-d/D=0.4-41.4° and WRI-d/D=0.4-28.8°.

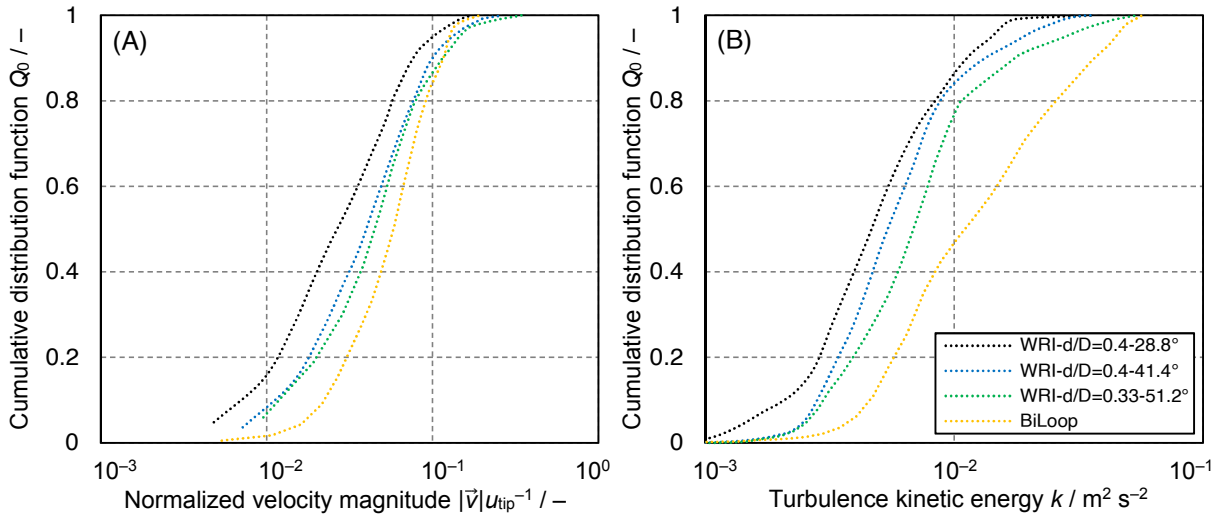


Fig. 4-23 CDFs for BiLoop, WRI- $d/D=0.4-41.4^\circ$, WRI- $d/D=0.4-28.8^\circ$ and WRI- $d/D=0.33-51.2^\circ$, water: (A) normalized velocity, (B) TKE.

The BiLoop impeller shows higher velocities and higher TKE values, see **Fig. 4-23**. The TKE rises very fast, because of the two big swirls in the first half of the vessel. Concerning the WRIs, an increase of the axial behaviour is found to be related to an increase in the velocities and in the TKE values.

The individual observations for every group can be reviewed all together, with the CDFs of normalized velocity and KED, see **Fig. 4-24**.

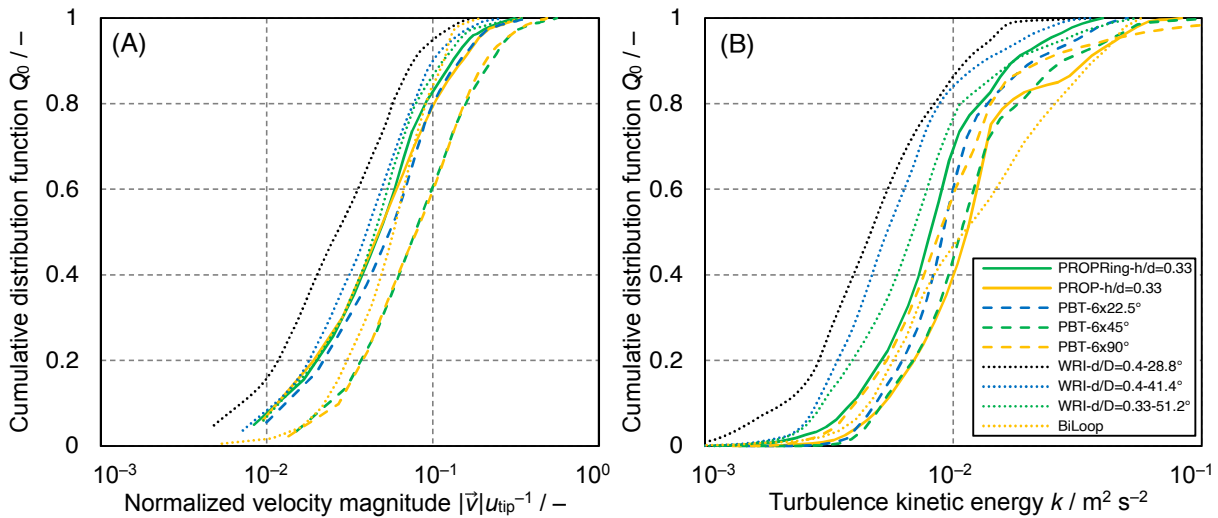


Fig. 4-24 CDFs for all nine impellers, water: (A) normalized velocity, (B) TKE.

BiLoop results with the highest TKE values among all the impellers, with PROP- $h/d=0.33$ and PBT-6x45°. The lowest values of TKE are for the three WRIs. PROPRing- $h/d=0.33$, PBT-6x90° and PBT-6x22.5° place in between.

Glycerin

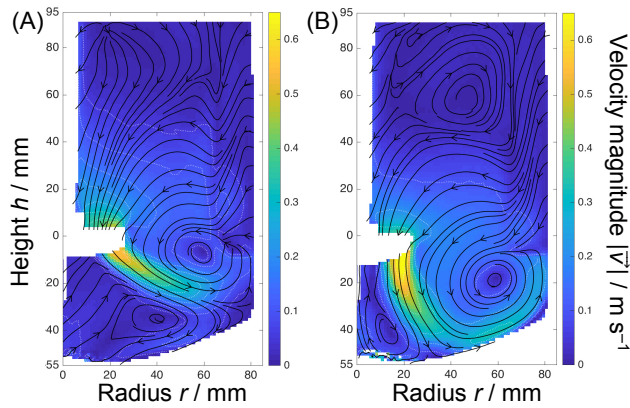


Fig. 4-25 Flow fields in glycerin: (A) PROPRing- $h/d=0.33$, (B) PROP- $h/d=0.33$.

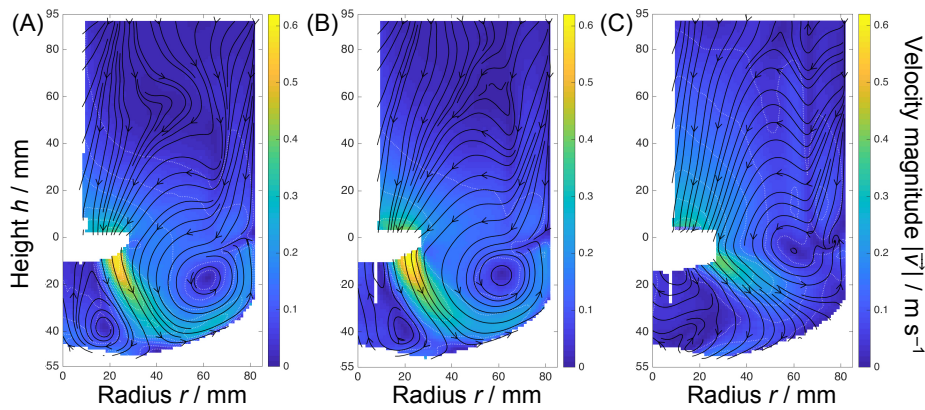


Fig. 4-26 Flow fields in glycerin: (A) PBT-6x22.5°, (B) PBT-6x45°, (C) PBT-6x90°.

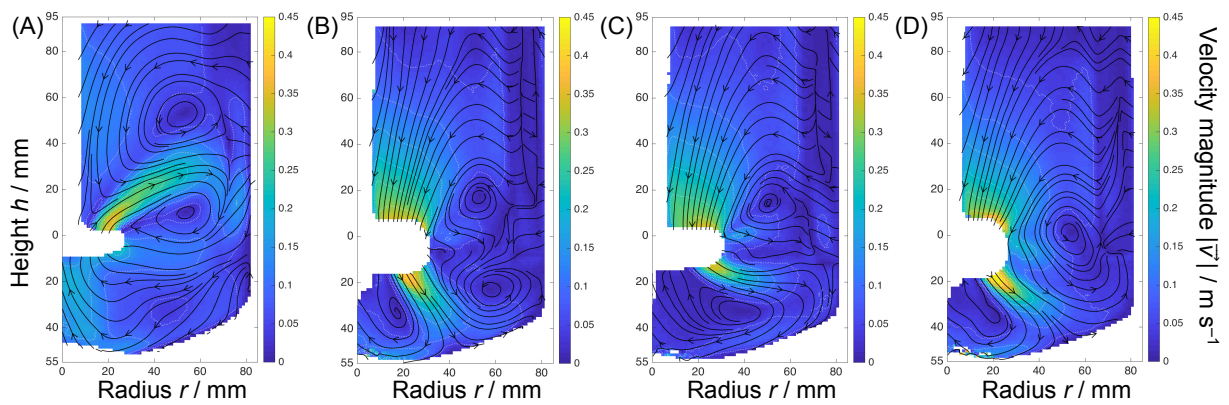


Fig. 4-27 Flow fields in glycerin: (A) BiLoop, (B) WRI- $d/D=0.4-41.4^\circ$, (C) WRI- $d/D=0.4-28.8^\circ$, (D) WRI- $d/D=0.33-51.2^\circ$.

PROPRing- $h/d=0.33$ and PROP- $h/d=0.33$

The PROP- $h/d=0.33$ still shows an axial behavior, although an additional swirl on the side top of the vessel is formed, see **Fig. 4-25** (B). The ring of PROPRing- $h/d=0.33$ causes, also in this case, a radial feature of the flow pattern.

PBT-6x22.5°, PBT-6x45° and PBT-6x90°

For the PBTs, the fluid is pumped downward with a more diagonal direction as the blade angle increases, see **Fig. 4-26**.

The results of the studies of C. Y. Ge et al. (2014) and Kumaresan and Joshi (2006), mentioned in the comparison of the impellers in the previous section, find a demonstration also here. The power number of a PBT increases with the increase of the angle of the blade, which lessens progressively the axial flow. In **Tab. 4-7**, the power numbers of the three PBTs measured for water and glycerin are summarized.

Tab. 4-7 Power numbers of the PBTs, measured for water and glycerin.

Pitched Blade Turbine	$\alpha / ^\circ$	Power number $Ne / -$	
		Water	Glycerin
PBT-6x22.5°	22.5	0.55	0.62
PBT-6x45°	45.0	1.79	1.48
PBT-6x90°	90.0	4.00	3.80

BiLoop, WRI- $d/D=0.4$ -41.4°, WRI- $d/D=0.4$ -28.8° and WRI- $d/D=0.33$ -51.2°

The flow fields developed in glycerin show a bigger complexity in the pattern, especially for the BiLoop and the wave ribbon impellers, see **Fig. 4-27**. Among this group, WRI- $d/D=0.33$ -51.2° has the most similar effect to the case with water, as compared to the others. In general, the velocity above the impeller increases, but the direction of the flow remains the same. With WRI- $d/D=0.4$ -41.4° there is the formation of three swirls close to the impeller, of which two are quite symmetrical to each other. In general, it is observed that an increase in the angle of the wave is correlated to a more axial flow.

The WRIs may be seen, in an approximative way, as stirrers with twisted blades. With regards to blade twist, it was found by Kumaresan and Joshi (2006) that the presence of this characteristic in the impeller shape causes a decrease of the power number. This may justify the low power number of WRIs and propellers.

For the WRIs, it is found that an increase of the angle of the wave corresponds to the increase of the power number, see **Tab. 4-8**.

Tab. 4-8 Power numbers of the wave ribbon impellers, measured for water and glycerin.

Wave Ribbon Impeller	$\alpha / ^\circ$	Power number $Ne / -$	
		Water	Glycerin
WIR- $d/D=0.4$ -28.8°	28.8	0.20	0.25
WIR- $d/D=0.4$ -41.4°	41.4	0.33	0.39
WIR- $d/D=0.33$ -51.2°	51.2	0.63	0.66

The representation of the distribution of TKE of the nine impellers in **Fig. 4-28**, shows that the range of generated TKE is around $10^{-4} - 10^{-1} \text{ m}^2 \text{ s}^{-2}$. Only for PBT-6x45° and PBT-6x90° this upper limit is reached.

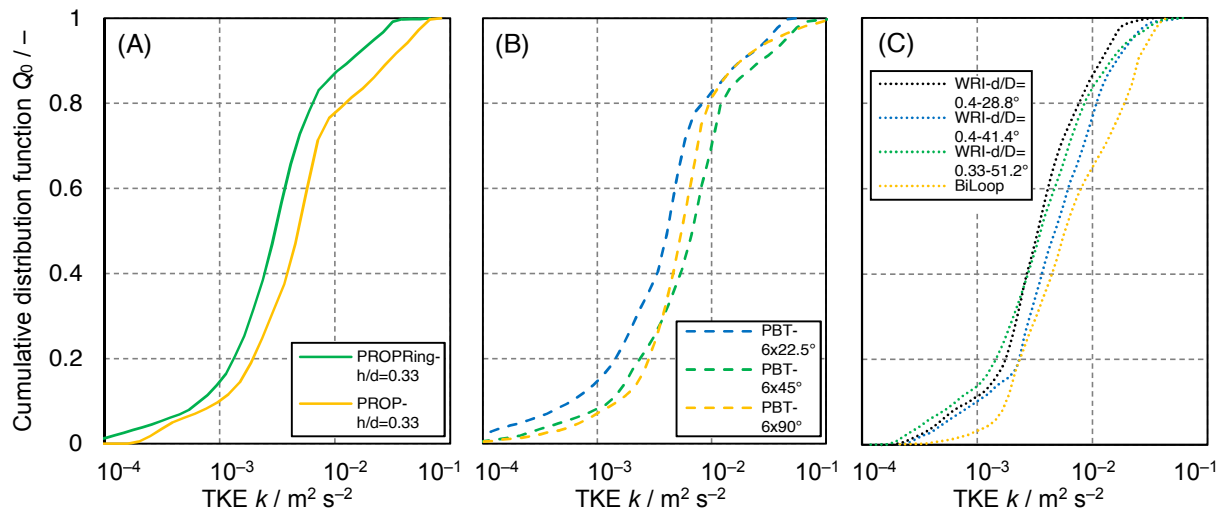


Fig. 4-28 CDFs of TKE for all nine impellers, glycerin: (A) PROPRing- $h/d=0.33$ and PROP- $h/d=0.33$, (B) PBT-6x22.5°, PBT-6x45° and PBT-6x90°, (C) BiLoop, WRI- $d/D=0.4$ -41.4°, WRI- $d/D=0.4$ -28.8° and WRI- $d/D=0.33$ -51.2°.

The range of TKE values calculated for the case of water, considering this comparison based on the same value of power input, is higher and it goes from $10^{-3} - 10^{-1} \text{ m}^2 \text{ s}^{-2}$.

Xanthan

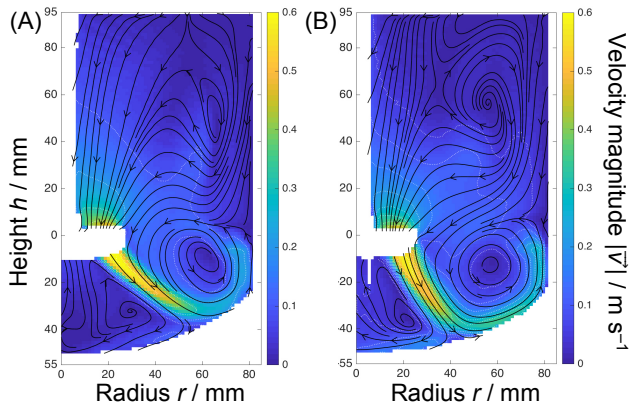


Fig. 4-29 Flow fields in xanthan: (A) PROPRing- $h/d=0.33$, (B) PROP- $h/d=0.33$.

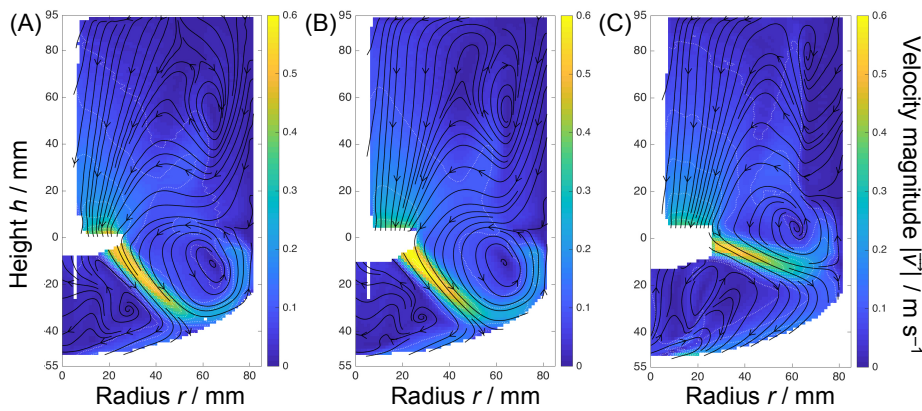


Fig. 4-30 Flow fields in xanthan: (A) PBT-6x22.5°, (B) PBT-6x45°, (C) PBT-6x90°.

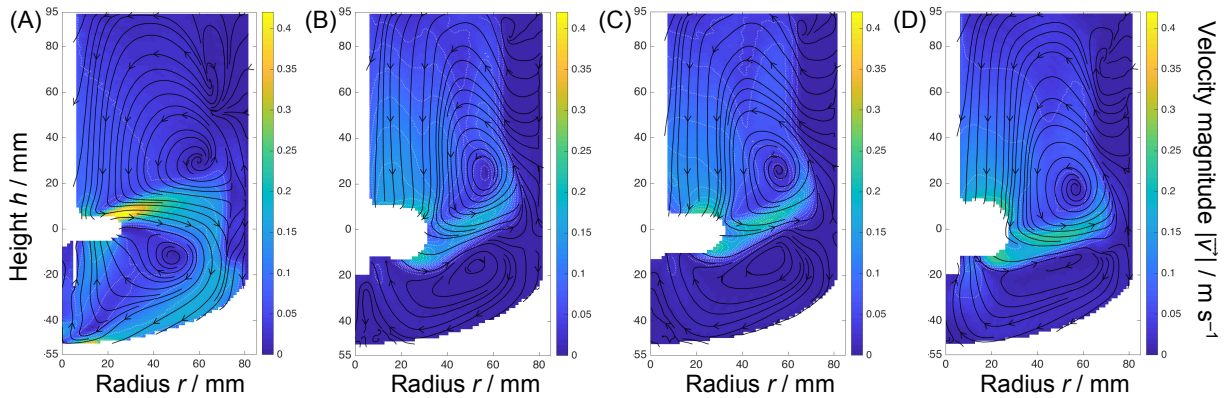


Fig. 4-31 Flow fields in xanthan: (A) BiLoop, (B) WRI- $d/D=0.4-41.4^\circ$, (C) WRI- $d/D=0.4-28.8^\circ$, (D) WRI- $d/D=0.33-51.2^\circ$.

PROPRing- $h/d=0.33$ and PROP- $h/d=0.33$

The PROP- $h/d=0.33$, with the increase of the viscosity of the fluid, loses its pure axial behavior: a small swirl on the top is formed and the circulation path is smaller, as compared to the water case, **Fig. 4-29 (B)**. The ring of PROPRing- $h/d=0.33$ still confers a more radial feature to this impeller, **Fig. 4-29 (A)**.

PBT-6x22.5°, PBT-6x45° and PBT-6x90°

In xanthan, the direction of the fluid pumped by the three PBTs is more diagonal, tending to an almost radial flow with the increase of the blade angle, see **Fig. 4-30**.

In a study conducted by Bakker et al. (1996) on the flow pattern of a PBT in different flow regimes, they concluded that this type of impeller pumps the fluid radially, instead of axially, in laminar conditions.

BiLoop, WRI-d/D=0.4-41.4°, WRI-d/D=0.4-28.8°, WRI-d/D=0.33-51.2°

The WRIs develop two circulation loops, like radial impellers. The high velocities are located above and beside the impeller. BiLoop pumps the liquid upward, but the flow tends more to the sides, see **Fig. 4-31**.

The dramatic change of the flow from axial to radial, when considering water and xanthan, is clearly depending on the fluid rheology.

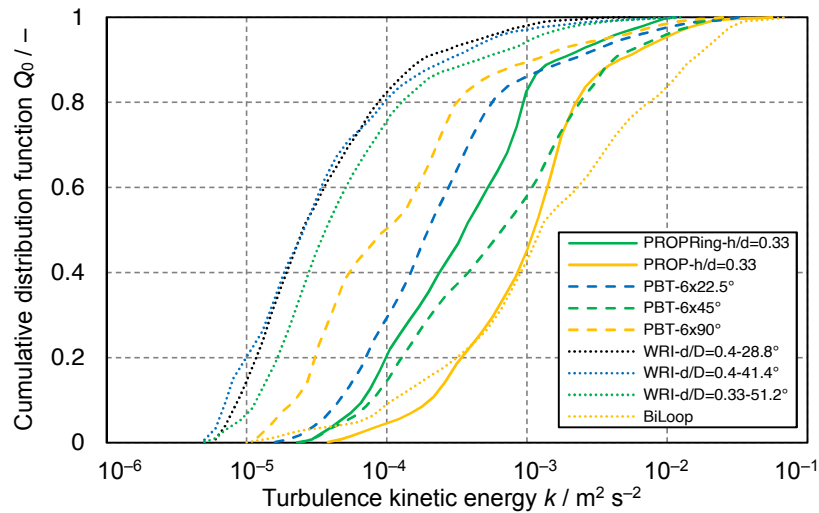


Fig. 4-32 CDFs of TKE for all nine impellers, xanthan.

With the higher viscosity, at the same constant power input, the impeller produces a lower turbulence. The CDF of the TKE in **Fig. 4-32** shows a range of values around $10^{-6} - 10^{-1} \text{ m}^2 \text{ s}^{-2}$.

With xanthan, the differences between the impellers in the distribution of TKE become more significant. The TKE generated by the WRIs are the lowest, also thanks to their radial character, which is shown with much less intensity by PBT-6x90° as well. The BiLoop, PROP-h/d=0.33 and PBT-6x45° are the ones that generate the highest TKE. The PROPRing-h/d=0.33, despite the limiting element represented by the ring, produces higher intensities of TKE as compared to PBT-6x22.5°.

4.2.4 Interpretation of the Particle Stress Induced by Various Impeller Geometry

In the chemical processes that make use of stirred tanks involving a suspension of particles, such as solid suspensions or cells and cells agglomerates, the mechanical agitation plays a critical role in the particle stress, especially when the fluid flows in turbulent regime. The energy provided to the impeller blades causes the generation of large eddies, which

progressively transform in smaller eddies and transfer turbulent kinetic energy, until the viscous forces become dominant and the remaining energy dissipates into thermal heat. The fluctuating velocities of the fluid generates mechanical stress on the suspended material.

The energy dissipation rate is a crucial parameter for the micromixing, because it determines the minimum ultimate size of the eddies, that coincides with the Kolmogorov microscale. As discussed in **Section 2.5**, the relation between the size of the eddies and the size of the particles is determinant on the particle stress, especially in the form of shear.

However, in a turbulent flow the properties are local, so it is the EDR, of which calculation or direct measurement are complex. To overcome this problem, it is possible to use other parameters to study and correlate the particle stress. Among these, there are the average EDR $\bar{\epsilon}$, that can be calculated with **Eq. (2-48)**, and the maximum EDR ϵ_{\max} , that can be estimated by considering the majority of dissipation occurring in the impeller region. This approach was followed by Bliatsiou (2018b) to study the effect of impeller geometry on the particle stress.

The study of Bliatsiou is also projected to find valuable new geometries that can produce lower shear stress. The impellers employed in the study include already known impellers, like the propeller and the PBTs, and new ones, such as PROPRing- $h/d=0.33$, the BiLoop and the WRIs. The experiments conducted in this study concern the measurement, by means of an endoscope, of the particle size (silicone oil dispersed in water) reached at the steady state, with the different impellers. The system consists of a dispersion of silicone oil in water. In general, high shear stress produces the breakage of the particles, resulting in smaller particle sizes.

This study is here used to make a comparison and a validation of the results obtained in this experimental work, in particular for the measurements done in water. Generally, high intensities of shear can suggest a higher particle stress. The approach chosen by Bliatsiou makes use of the Sauter mean diameter, that is the diameter corresponding to the particle with the same ratio volume/surface area as the whole ensemble.

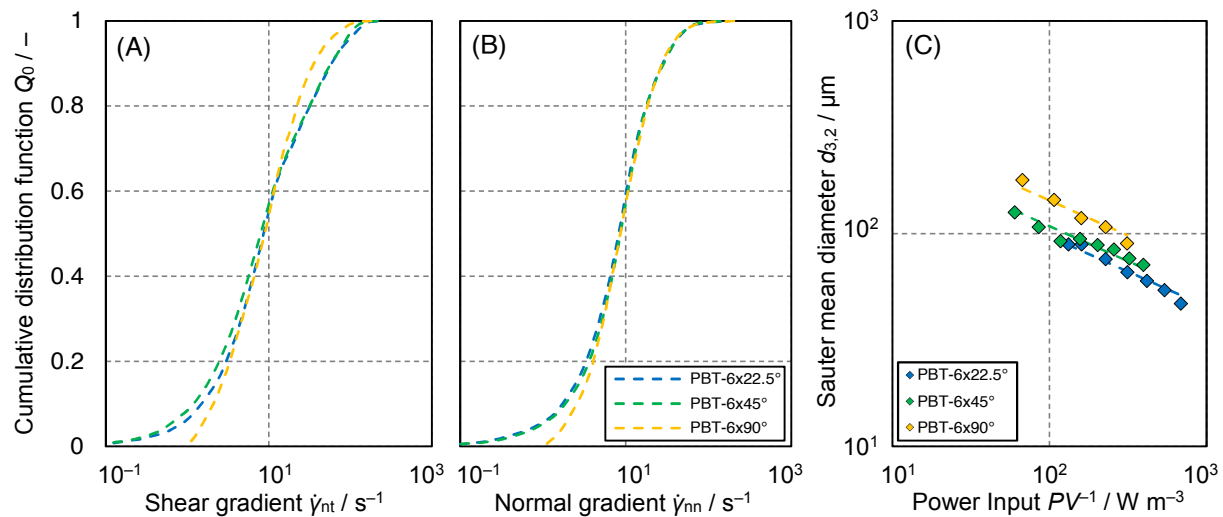


Fig. 4-33 Particle stress with PBT-6x22.5°, PBT-6x45° and PBT-6x90°: (A) shear gradient, (B) normal gradient, (C) power input and corresponding particle size.

In the CDF of the shear gradient, PBT-6x22.5° is found to produce higher shear as compared to PBT-6x45°, **Fig. 4-33** (A). PBT-6x90° produces less shear as compared to the other PBTs

of lower blade angle. On the other hand, the distribution of normal gradients shows a great similarity among the three PBTs for higher values, see **Fig. 4-33**.

The results of the study show that at the same value of $\bar{\epsilon}$, PBT-6x22.5° produces smaller particles, that means that the particle stress generated by this impeller is higher, see **Fig. 4-33** (C). The comparison between the distributions of normal and shear gradients suggests that the particle stress that causes the smaller size of the particles is mainly due to the shear mechanism.

In both results, the differences between PBT-6x22.5° and PBT-6x45° are however small. It is observed that an increase in the blade angle is related to a higher diameter of the particles, hence to a lower particle stress. With the increase of the blade angle, the power number increases and the flow becomes more radial. On the other hand, the impellers that develop the axial flow generate more particle stress.

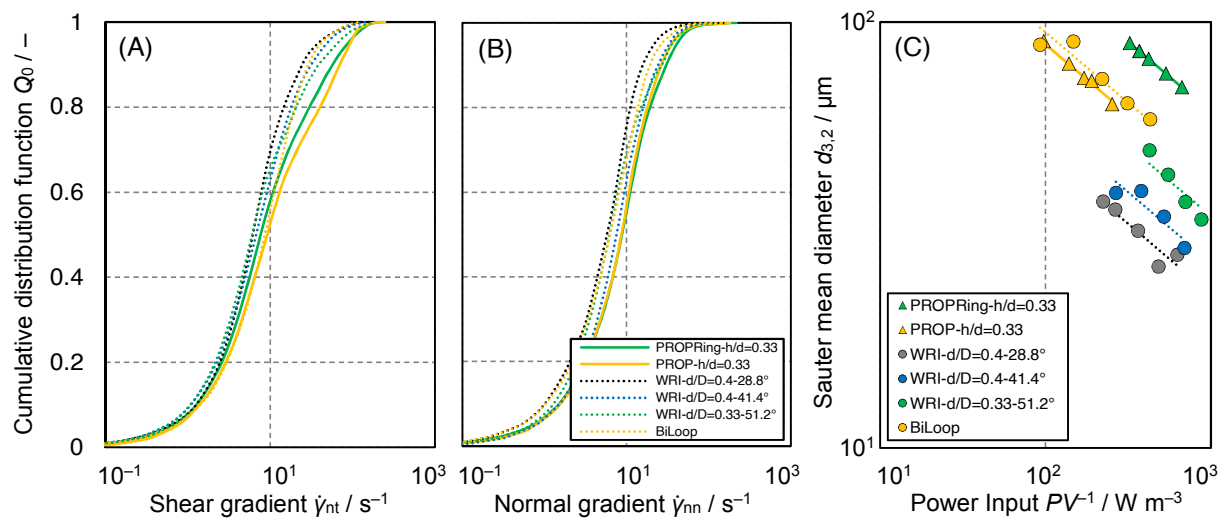


Fig. 4-34 Particle stress with PROPRing- $h/d=0.33$ and PROP- $h/d=0.33$, BiLoop, WRI- $d/D=0.4-41.4^\circ$, WRI- $d/D=0.4-28.8^\circ$, WRI- $d/D=0.33-51.2^\circ$: (A) shear gradient, (B) normal gradient, (C) power input and corresponding particle size.

The PROP- $h/d=0.33$ produces higher shear as compared to PROPRing- $h/d=0.33$ and BiLoop, see **Fig. 4-34** (A). This information is coherent with what is observed in **Fig. 4-34** (C).

But in this case, the comparison between the two results is not totally successful. Considering the WRIs, they produce the smallest particles, meaning that they produce a very high particle stress. The angle of the wave seems to be the parameter that affects the intensity of the particle stress: a smaller angle produces particles of smaller size.

This result is not found in the CDF of the shear gradient and normal gradient, see **Fig. 4-34**: here, the WRIs result even in lower shear values. The reason to explain this incongruity is not clear so far: the particle stress may be due to very high values of shear, localized on the surface of the WRIs. In general, in the region of the blades a particle feels the highest values of shear, because when the particle is attached to the blade, its relative velocity with respect to the blade is equal to 0, and when it moves along just a very tiny distance away from the impeller, it is subjected to the highest velocity, given from the blades to the fluid. If the explanation to the differences observed in **Fig. 4-34** is given by the very high shear on the blades of the WRIs, it may be that these values are not seen with the PIV analysis, because of the spatial resolution and because of the geometrical mask that, added on the impeller area, may cover the perimeter, discarding these values from the calculation. These assumptions

require the comparison with, e.g. CFD simulations, which can provide more detailed information at the proximity of the wave.

The WRIs, producing the smallest particle size, are thought to be indicated for processes that deal with dispersion. A study of Moucha et al. (2003) concluded that the impellers with power number Ne higher than 1 ensure a better mass transfer performance, while the ones with power number smaller than the unity, produce higher dispersion mixing intensities. Hence, the results of that study confirms what is observed for the WRIs. BiLoop produces particles of bigger size, which means that this impeller produces lower stress as compared to the other impellers. This up-pumping impeller produces small values of shear gradients, as shown in the CDF of **Fig. 4-34** (A). Mandenius (2016) explains that to reduce the shear damage on mammalian cells, it is convenient to use low shear, up-pumping impellers, especially with wide blade hydrofoils. Hence, the low stress observed in the case of BiLoop may depend on the up-pumping mode of this impeller.

Particle stress is a topic of great interest in mixing and its investigation may give valuable outcomes that can be used to better carry out those processes that deal with a suspended phase, like in the biotechnological processes. Choosing the best operating conditions and the proper equipment design, including the impeller, is determinant for the success of the process. In biotechnology, the use of various microorganisms, cells, and enzymes makes the definition of a general rule for the systems quite unrealistic. The nature of the particles or aggregates, the rheological properties of the suspension, the presence or not of a gaseous phase are parameters that deeply influence the character of the system. The particle stress is still a wide and complex topic that needs to be investigated.

The results of the PIV measurements show a good coherence with the results that are available in literature and that have been presented so far. However, this study is conducted with new impeller types, hence the amount of comparable results is scarce. This is an additional reason to continue the investigation on these impellers with the CFD simulations. From the vector field calculated with the PIV analysis, it is possible to obtain other valuable results. Wille et al. (2001) suggest the determination of the gradients of velocity in the macroscopic flow field: G_x and G_y are defined as the sum of the absolute gradients for every velocity component x , y , z along one direction, x and y respectively, see **Section 2.3**. The gradient that is perpendicular to the direction of the flow is the shear gradient, while if it is parallel is the elongational (normal) gradient.

The gradients represented in **Fig. 4-35** are for the operating condition with PROP- $h/d=0.33$ in water at 100 W m^{-3} , with the 3DA approach.

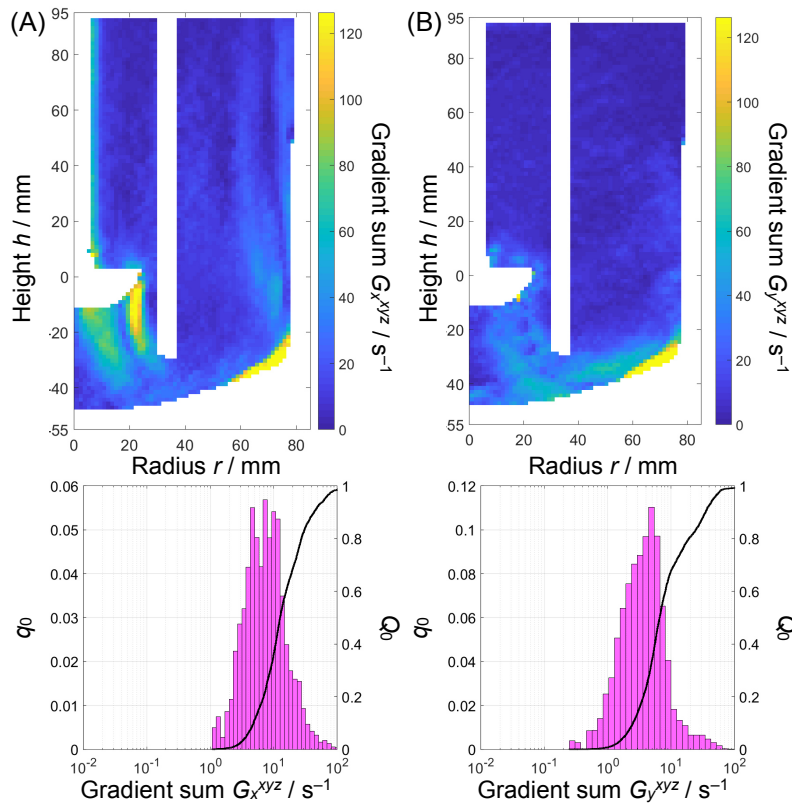


Fig. 4-35 Directed velocity gradients for PROP- $h/d=0.33$, water at $PV^{-1} = 100 \text{ W m}^{-3}$, 3DA approach: (A) scalar field and histogram with CDF of G_x , (B) scalar field and histogram with CDF of G_y .

Furthermore, vorticity can be calculated from the velocity gradient tensor, as described in **Section 2.3**. In **Fig. 4-36** the intensity of the vorticity indicates the rotational direction: a positive vorticity corresponds to a counterclockwise rotation, whereas a negative value corresponds to a clockwise rotation. This representation shows the critical areas in the vessel, that are located in the torispherical bottom where the vorticity causes a change of the flow. The fluid in these areas exerts higher values of shear.

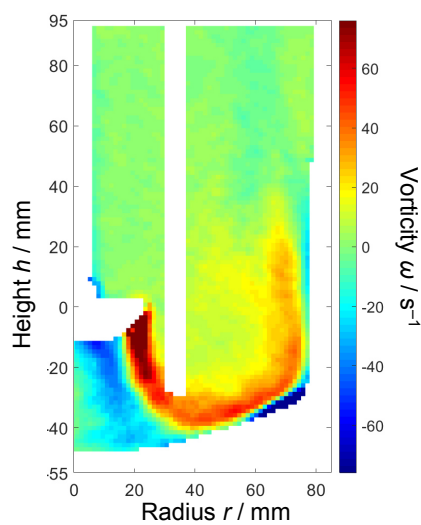


Fig. 4-36 Vorticity field for PROP- $h/d=0.33$, water at $PV^{-1} = 100 \text{ W m}^{-3}$, 3DA approach.

Chapter 5

Conclusions and Outlook

5.1 Improvement of Measuring with PIV

From the velocity vector field calculated with particle image velocimetry it is possible to obtain several results and representations of the dynamics of the fluid, as presented in **Chapter 4**. The different quantities are calculated with the partial derivatives of the velocity components with respect to one of the directions x and y .

The velocity gradients, located in the diagonal of the velocity gradient tensor, are the divergence terms. When the derivative of v_x with respect to x is positive, it means that the fluid stretches along the x direction, otherwise it compresses and in this case the gradient is called convergence. Actually, the use of these terms is not proper for the investigated fluids, since these are incompressible. The velocity gradients are considered as the acceleration or deceleration of the fluid along the two directions. A condensed color diagram that can describe both the components of divergence is reported in **Fig. 5-1 (A)**. Every point of color in the diagram has to be interpreted as a point having coordinates E_{xx} and E_{yy} , located in the square. The interpretation of this plot is not immediate, thus the view of the matching flow field can support in the comprehension, see **Fig. 5-1 (B)**. Below the impeller, the dark region indicates that the fluid is accelerating along the x direction and decelerating along y , then it decelerates along x and accelerates along y in the adjacent yellow area. If the analogous region in the flow field is considered, it is proved that the velocity in the x direction first increases and then decreases when the fluid particles approach the center of the swirl. Along the y direction, starting from the tip of the blades, the velocity increases and then decreases.

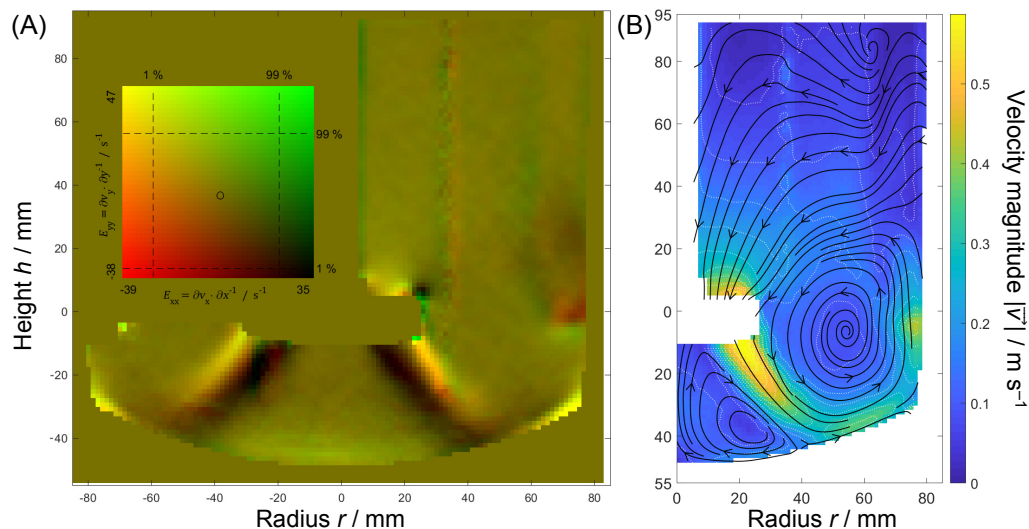


Fig. 5-1 Two-dimensional color diagram representing the divergence with the corresponding flow field, both calculated with 3DA in water with PROPRing- $h/d=0.33$ at a constant power input $PV^{-1} = 100 \text{ W m}^{-3}$: (A) divergence, (B) flow field.

In this experimental work both, 2D-PIV and 3D-PIV, were employed. However, most of the results presented in **Chapter 4** were obtained by using the two-dimensional approach, because of the requirement of more storage space and longer measuring time that go along

with the other type of analysis. In presenting the results, the two approaches were compared in terms of flow field and TKE. What was concluded is that the 3D-PIV gives a more truthful representation of the reality, as opposed to 2D-PIV, which on the other hand is not able to see the additional velocities that cross the laser sheet.

Stereoscopic PIV

The employment of two cameras for the stereoscopic PIV allows the reconstruction of the velocity vector with its three components, thanks to the perspective distortion of the displacement vector that is observed from two different directions (Raffel et al., 2007).

The third component of the velocity, v_z , can be represented with a surface plot, that shows the intensity of the velocity across the laser sheet. In **Fig. 5-2**, the velocity is normalized with the tip speed and it is calculated from the three-dimensional measurement done with PROPRing- $h/d=0.33$ in water at a constant power input $PV^{-1} = 100 \text{ W m}^{-3}$.

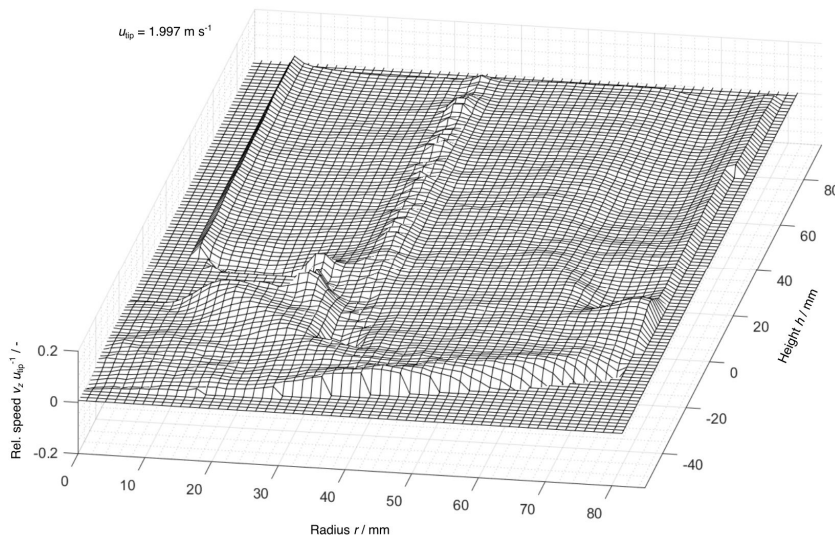


Fig. 5-2 Surface plot of the third component of the velocity vector normalized with the tip speed, PROPRing- $h/d=0.33$ in water at a constant power input $PV^{-1} = 100 \text{ W m}^{-3}$.

With the stereoscopic PIV, the velocity gradient tensor contains the information regarding the first two columns, but the third one is impossible to evaluate, because the velocity vector is calculated only in one plane.

Multiplane PIV

Multiplane PIV is an extension of the stereoscopic PIV. The addition of a parallel plane at which the three components of the velocity vector are calculated, allows to make the derivative with respect to z , hence, to calculate the complete velocity gradient tensor. The system consists of two laser sheets that illuminate the flow seeding particles with orthogonally linearly polarized light, see **Fig. 5-3**. A system of beam-splitter cubes (7) and mirrors (6) orient the laser reflected by the particles to two pairs of high resolution cameras (1, 2, 3, 4), of which angular configuration is corrected with Scheimpflug adapters. (Raffel et al., 2007)

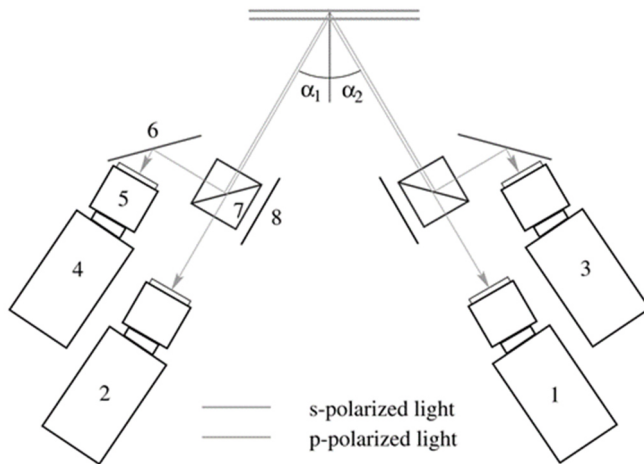


Fig. 5-3 Schematic representation of multiplane stereo-PIV (Raffel et al., 2007).

Tomographic PIV

Tomographic particle image velocimetry (Tomo-PIV) is a technique that, differently from the above-mentioned ones, uses a laser to illuminate a part of volume of the fluid. This technique is able to capture instantaneous three-dimensional flow fields located in complex turbulent structures. The position of multiple cameras from different views on the examined flow allows to get several volume images that are successively processed with a 3D correlation technique on volume elements, called voxels, see **Fig. 5-4** (A).

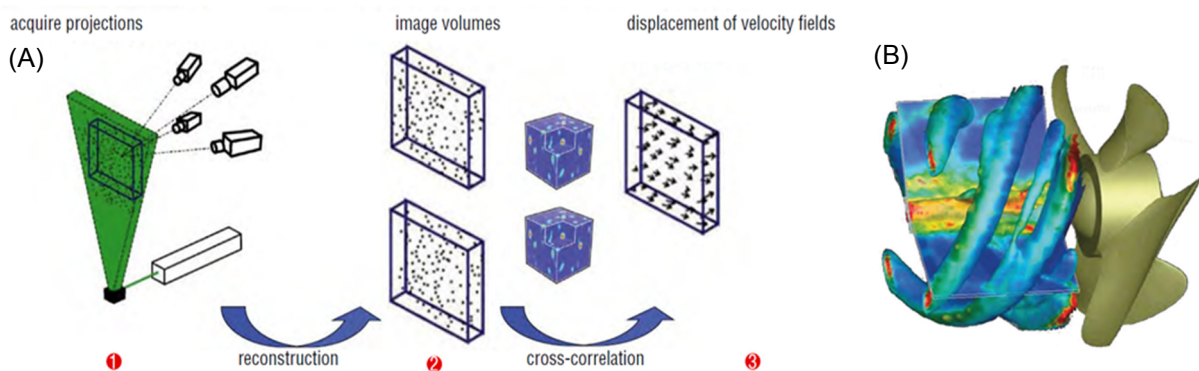


Fig. 5-4 Tomographic PIV: (A) working principle of Tomo-PIV, (B) three-dimensional flow field induced by a propeller (Scarano, 2013).

The use of this technique on stirred vessels could provide a comprehensive three-dimensional representation of the turbulence in the fluid, in particular in the impeller region, see **Fig. 5-4** (B).

5.2 Comparison with CFD

The PIV setup used in this work has two intrinsic limitations for the results that can be obtained with the measurements. Firstly, the spatial resolution of the PIV analysis is found to be unable to detect the smallest turbulent eddies, which are in the Kolmogorov microscale. Furthermore, the mechanisms of stress that occur at the surface of the impeller blades are discarded from the calculation, due to the inability of calculating the velocity vectors in the perimeter of the non-transparent blades.

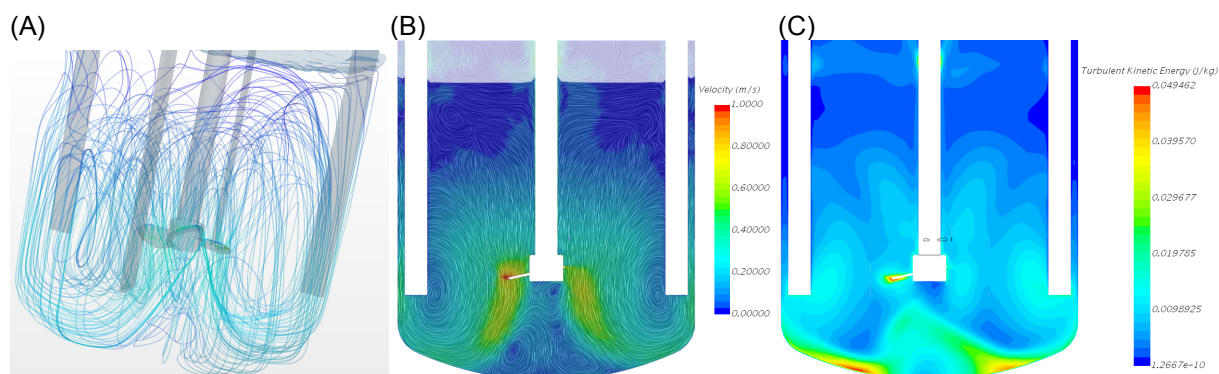


Fig. 5-5 Exemplary output of a CFD simulation for PROP- $h/d=0.33$: (A) streamlines, (B) velocity vector field, (C) turbulence kinetic energy.

CFD is a valid tool to predict the flow fields in stirred vessels, and its application allows to determine the distribution of the average velocity field, turbulent kinetic energy and energy dissipation rate, see **Fig. 5-5**. Some CFD models for the determination of the turbulent flow are based on the Reynolds averaged Navier-Stokes equations. The experimental validations of CFD simulations often make use of PIV, (Sheng et al., 1998).

5.3 Future Perspectives

The use of metallic equipment inside the reactor, such as impeller and baffles, introduces the exclusion in the analysis of a fundamental part of the laser sheet, the one in the impeller region.

A suggestion to overcome this problem finds the solution in the employment of equipment made of PMMA (acrylic glass). This transparent material allows the view of the particles in the region between the impeller blades, see **Fig. 5-6**.



Fig. 5-6 Rushton turbine and baffles made of PMMA.

References

- Amanullah, A., Buckland, B.C., Nienow, A.W., 2004. Mixing in the Fermentation and Cell Culture Industries, in: *Handbook of Industrial Mixing: Science and Practice*. pp. 1071–1170. <https://doi.org/10.1002/0471451452.ch18>
- ANSYS Training Manual, ©2009 ANSYS.
- Arevalo-Villena, M., Briones-Perez, A., Corbo, M.R., Sinigaglia, M., Bevilacqua, A., 2017. Biotechnological application of yeasts in food science: Starter cultures, probiotics and enzyme production. *J. Appl. Microbiol.* 123, 1360–1372. <https://doi.org/10.1111/jam.13548>
- Armenante, P.M., Mazzarotta, B., Chang, G.M., 1999. Power consumption in stirred tanks provided with multiple pitched-blade turbines. *Ind. Eng. Chem. Res.* <https://doi.org/10.1021/ie980692o>
- Aubin, J., Le Sauze, N., Bertrand, J., Fletcher, D.F., Xuereb, C., 2004. PIV measurements of flow in an aerated tank stirred by a down- and an up-pumping axial flow impeller. *Exp. Therm. Fluid Sci.* 28, 447–456. <https://doi.org/10.1016/j.expthermflusci.2001.12.001>
- Aubin, J., Mavros, P., Fletcher, D.F., Bertrand, J., Xuereb, C., 2001. Effect of axial agitator configuration (up-pumping, down-pumping, reverse rotation) on flow patterns generated in stirred vessels. *Chem. Eng. Res. Des.* 79, 845–856. <https://doi.org/10.1205/02638760152721046>
- Aubin, J., Xuereb, C., 2006. Design of multiple impeller stirred tanks for the mixing of highly viscous fluids using CFD. *Chem. Eng. Sci.* 61, 2913–2920. <https://doi.org/10.1016/j.ces.2005.10.075>
- Baeshen, N.A., Baeshen, M.N., Sheikh, A., Bora, R.S., Ahmed, M.M.M., Ramadan, H.A.I., Saini, K.S., Redwan, E.M., 2014. Cell factories for insulin production.
- Bakker, A., Meyers, K.J., Ward, R.W., Lee, C.K., 1996. The laminar and turbulent flow pattern of a pitched blade turbine. *Trans. IChemE*.
- Bamforth, C.W., 2007. *Food, Fermentation and Micro-organisms*, Food, Fermentation and Micro-organisms. <https://doi.org/10.1002/9780470995273>
- Bird, R.B., Stewart, W.E., Lightfoot, E.N., 2002. *Transport phenomena*, 2nd ed. John Wiley & Sons, Inc.
- Bliatsiou, C., Pommerehne, K., Waldherr, P., Tesche, S., Böhm, L., Krull, R., Kraume, M., 2018a. Rheological characteristics of filamentous cultivation broths and suitable model systems (Poster), in: *Himmelfahrtstagung*.
- Bliatsiou, C., Malik, A., Böhm, L., Kraume, M., 2018b. Investigation of the effect of the impeller geometry on particle stress in stirred tanks. *Ind. Eng. Chem. Res.*, not published yet
- Brooks, G.F., Carroll, K.C., Butel, J.S., Morse, S.A., Mietzner, T.A., 2013. *Jawetz, Melnick, & Adelberg's Medical Microbiology*, 26th ed. McGraw-Hill. <https://doi.org/10.1017/CBO9781107415324.004>
- Brown, D.A.R., Jones, P.N., Middleton, J.C., 2004. Experimental methods - part A: Measuring tools and techniques for mixing and flow visualization studies, in: *Paul, E.L.*

- Atiemo-Obeng, V.A., Kresta, S.M. (Eds.), Handbook of Industrial Mixing: Science and Practice. John Wiley & Sons, Inc., pp. 145–202. <https://doi.org/10.1002/0471451452.ch18>
- Burd, J.F., Usategui-Gomez, M., 1973. A colorimetric assay for serum lactate dehydrogenase. Clin. Chim. Acta. [https://doi.org/10.1016/0009-8981\(73\)90174-5](https://doi.org/10.1016/0009-8981(73)90174-5)
- Cairns, T.C., Nai, C., Meyer, V., 2018. How a fungus shapes biotechnology: 100 years of *Aspergillus niger* research. Fungal Biol. Biotechnol. <https://doi.org/10.1186/s40694-018-0054-5>
- Calluaud, D., David, L., Pineau, G., Texier, A., Larinier, M., 2011. Turbulence kinetic energy dissipation rate estimation from PIV velocity fields : Application to the study of the flow in vertical slot fishways . 34th IAHR World Congr. - Balanc. Uncertainty, 33rd Hydrol. Water Resour. Symp. 10th Hydraul. Conf. 26 June - 1 July 2011, Brisbane, Aust. 2768–2775.
- Cherry, R.S., Papoutsakis, E.T., 1988. Physical mechanisms of cell damage in microcarrier cell culture bioreactors. Biotechnol. Bioeng. <https://doi.org/10.1002/bit.260320808>
- Chudacek, M.W., 1985. Impeller Power Numbers and Impeller Flow Numbers in Profiled Bottom Tanks. Ind. Eng. Chem. Process Des. Dev. <https://doi.org/10.1021/i200030a056>
- Cinar, A., Parcilekar, S.J., Undey, C., Birol, G., 2003. Batch Fermentation: Modeling, Monitoring, and Control. <https://doi.org/10.1007/978-1-59745-523-7>
- Cooper, G.M., 2000. The Cell: a Molecular Approach, 2nd ed. <https://doi.org/10.1109/VPPC.2008.4677655>
- D.L.Nelson, M.M.Cox, 2010. I principi di biochimica di Lehninger.
- Daub, A., Böhm, M., Delueg, S., Mühlmann, M., Schneider, G., Büchs, J., 2014. Characterization of hydromechanical stress in aerated stirred tanks up to 40 m3 scale by measurement of maximum stable drop size. J. Biol. Eng. 8. <https://doi.org/10.1186/1754-1611-8-17>
- Deen, N.G., Hjertager, B.H., 2002. Particle image velocimetry measurements in an aerated stirred tank. Chem. Eng. Commun. 189, 1208–1221. <https://doi.org/10.1080/00986440213881>
- Deen, N.G., Solberg, T., 2000. Comparison of PIV and LDA Measurement Methods Applied to the Gas-Liquid Flow in a Bubble Column. 10th Int. Symp. Appl. Laser Tech. to Fluid Mech 1–12.
- Delafosse, A., Collignon, M.-L., Marc, A., Toye, D., Olmos, E., 2015. Revisiting the determination of hydromechanical stresses encountered by microcarriers in stem cell culture bioreactors, in: BMC Proceedings - 24th European Society for Animal Cell Technology (ESACT) Meeting. p. P41. <https://doi.org/10.1186/1753-6561-9-S9-P41>
- Delafosse, A., Collignon, M.L., Crine, M., Toye, D., 2011. Estimation of the turbulent kinetic energy dissipation rate from 2D-PIV measurements in a vessel stirred by an axial Mixel TTP impeller. Chem. Eng. Sci. 66, 1728–1737. <https://doi.org/10.1016/j.ces.2011.01.011>
- Doran, P.M., 2012. Bioprocess Engineering Principles. <https://doi.org/10.1016/B978-0-12-220855-3.X5000-7>
- Doran, P.M., 1995. Bioprocess Engineering Principles. Elsevier Science & Technology Books.

- Gavrilescu, M., Roman, R. V., Efimov, V., 1993. The volumetric oxygen mass transfer coefficient in antibiotic biosynthesis liquids. *Acta Biotechnol.* <https://doi.org/10.1002/abio.370130114>
- Ge, C., Wang, J., Gu, X., Feng, L., 2014. Chemical Engineering Research and Design Reply to Comments on “CFD simulation and PIV measurement of the flow field generated by modified pitched blade turbine impellers” by Ge et al. [Chem. Eng. Res. Des. (2013)], <http://dx.doi.org/10.1016/j.cher.2014.03.003>, Chem. Eng. Res. Des. 92, 992–993. <https://doi.org/10.1016/j.cherd.2014.03.003>
- Ge, C.Y., Wang, J.J., Gu, X.P., Feng, L.F., 2014. CFD simulation and PIV measurement of the flow field generated by modified pitched blade turbine impellers. *Chem. Eng. Res. Des.* 92, 1027–1036. <https://doi.org/10.1016/j.cherd.2013.08.024>
- Gouesbet, G., Gréhan, G., 2015. Laser-based optical measurement techniques of discrete particles: A review. *Int. J. Multiph. Flow.* <https://doi.org/10.1016/j.ijmultiphaseflow.2014.07.001>
- Hadad, T., Liberzon, A., Bernhaim, A., Gurka, R., 2011. Characteristics of seeding particles for PIV/PTV analysis. *APS Meet. Abstr.*
- Haimes, R., Kenwright, D., 1999. On the velocity gradient tensor and fluid feature extraction. *Proc. AIAA 14th Comput. Fluid Dyn. Conf.* 3288–3297. <https://doi.org/10.1.1.30.3918>
- Hemrajani, R., Tattersson, G., 2004. Mechanically Stirred Vessels, in: Paul, E.L., Atiemo-Obeng, V.A., Kresta, S.M. (Eds.), *Handbook of Industrial Mixing: Science and Practice*. John Wiley & Sons, Inc., pp. 345–390. <https://doi.org/10.1002/0471451452.ch6>
- Henzler, H.J., Schäfer, E.E., 1987. Viskose und elastische Eigenschaften von Fermentationslösungen. *Chemie Ing. Tech.* 59, 940–944. <https://doi.org/10.1002/cite.330591209>
- Hohl, L., Panckow, R.P., Schulz, J.M., Jurtz, N., Böhm, L., Kraume, M., 2018. Description of Disperse Multiphase Processes: Quo Vadis? *Chemie Ing. Tech.* 1–19. <https://doi.org/10.1002/cite.201800079>
- Holmes, D.B., Voncken, R.M., Dekker, J.A., 1964. Fluid flow in turbine-stirred, baffled tanks-I. Circulation time. *Chem. Eng. Sci.* 19, 201–208. [https://doi.org/10.1016/0009-2509\(64\)85030-2](https://doi.org/10.1016/0009-2509(64)85030-2)
- Idalia, V.-M.N., Bernardo, F., 2017. *Escherichia coli* as a Model Organism and Its Application in Biotechnology. *Escherichia coli - Recent Adv. Physiol. Pathog. Biotechnol. Appl.* <https://doi.org/10.5772/67306>
- Jones, W., Launder, B., 1972. The Prediction of Laminarization with a Two-Equation Model of Turbulence. *Int. J. Heat Mass Transf.* 15, 301–304.
- KamepaiQ, 2018, Камера Ай-Кью, <https://www.cameraiq.ru/catalog/series/shaimpfliug-adapter>, accessed 09/2018.
- Karathia, H., Vilaprinyo, E., Sorribas, A., Alves, R., 2011. *Saccharomyces cerevisiae* as a model organism: A comparative study. *PLoS One.* <https://doi.org/10.1371/journal.pone.0016015>
- Kolmogorov, A.N., 1991a. The Local Structure of Turbulence in Incompressible Viscous Fluid for Very Large Reynolds Numbers. *Proc. R. Soc. A Math. Phys. Eng. Sci.* 434, 9–13. <https://doi.org/10.1098/rspa.1991.0075>

- Kolmogorov, A.N., 1991b. Dissipation of Energy in the Locally Isotropic Turbulence. *Proc. R. Soc. A Math. Phys. Eng. Sci.* 434, 15–17. <https://doi.org/10.1098/rspa.1991.0076>
- Kolmogorov, A.N., 1968. Local Structure of Turbulence in an Incompressible Viscous Fluid at Very High Reynolds Numbers. *Sov. Phys. Uspekhi* 10, 200–303.
- Krämer, B., 2018, Measurement of the optimal concentration of flow seeding particles at Verfahrenstechnik, TU Berlin, laboratory results not published.
- Kumaresan, T., Joshi, J.B., 2006. Effect of impeller design on the flow pattern and mixing in stirred tanks. *Chem. Eng. J.* 115, 173–193. <https://doi.org/10.1016/j.cej.2005.10.002>
- Kuzmichew, A., Tsybulski, L., 2008. Evaporators with induction heating and their applications. *Prz. Elektrotechniczny* 84, 32–35. <https://doi.org/10.5772/32009>
- La Fontaine, R., 1996. Particle image velocimetry applied to a stirred vessel. *Exp. Therm. Fluid Sci.* 12, 256–264. [https://doi.org/10.1016/0894-1777\(95\)00096-8](https://doi.org/10.1016/0894-1777(95)00096-8)
- Lagier, J.C., Edouard, S., Pagnier, I., Mediannikov, O., Drancourt, M., Raoult, D., 2015. Current and past strategies for bacterial culture in clinical microbiology. *Clin. Microbiol. Rev.* <https://doi.org/10.1128/CMR.00110-14>
- Lemoine, F., Wolff, M., Lebouche, M., 1996. Simultaneous concentration and velocity measurements using combined laser-induced fluorescence and laser Doppler velocimetry: Application to turbulent transport. *Exp. Fluids* 20, 319–327. <https://doi.org/10.1007/BF00191013>
- Li, Z., Bao, Y., Gao, Z., 2011. PIV experiments and large eddy simulations of single-loop flow fields in Rushton turbine stirred tanks. *Chem. Eng. Sci.* 66, 1219–1231. <https://doi.org/10.1016/j.ces.2010.12.024>
- Lim, J.S., Kim, J.H., Kim, C., Kim, S.W., 2002. Morphological and rheological properties of culture broth of *Cephalosporium acremonium* M25. *Korea-Australia Rheol. J.* 14, 11–16.
- Liu, X., Bao, Y., Li, Z., Gao, Z., Smith, J.M., 2008. Particle image velocimetry study of turbulence characteristics in a vessel agitated by a dual Rushton impeller. *Chinese J. Chem. Eng.* 16, 700–708.
- MacWilliams, M.P., Laio, M.-K., 2006. Luria Broth (LB) and Luria Agar (LA) Media and Their Uses Protocol. *Am. Soc. Microbiol.* 2016–2019.
- Mandenius, C.-F., 2016. Bioreactors: Design, Operation and Novel Applications. <https://doi.org/10.1002/9783527683369>
- McManamey, W., 1980. A circulation model for batch mixing in agitated, baffled vessels. *Chem. Eng. Res. Des.*
- Metzner, A.B., Otto, R.E., 1957. Agitation of non-Newtonian fluids. *AIChE J.* 3, 3–10. <https://doi.org/10.1002/aic.690030103>
- Moucha, T., Linek, V., Prokopová, E., 2003. Gas hold-up, mixing time and gas-liquid volumetric mass transfer coefficient of various multiple-impeller configurations: Rushton turbine, pitched blade and techmix impeller and their combinations. *Chem. Eng. Sci.* 58, 1839–1846. [https://doi.org/10.1016/S0009-2509\(02\)00682-6](https://doi.org/10.1016/S0009-2509(02)00682-6)
- Nere, N.K., Patwardhan, A.W., Joshi, J.B., 2003. Liquid-phase mixing in stirred vessels: Turbulent flow regime. *Ind. Eng. Chem. Res.* 42, 2661–2698. <https://doi.org/10.1021/ie0206397>

- Nielsen, J., 2013. Production of biopharmaceutical proteins by yeast. *Bioengineered*. <https://doi.org/10.4161/bioe.22856>
- Nienow, A.W., 1997. On impeller circulation and mixing effectiveness in the turbulent flow regime. *Chem. Eng. Sci.* 52, 2557–2565. [https://doi.org/10.1016/S0009-2509\(97\)00072-9](https://doi.org/10.1016/S0009-2509(97)00072-9)
- Ofner, B., 2011. Phase Doppler Anemometry (PDA), in: *Optical Measurements*. pp. 139–152. <https://doi.org/10.1016/B978-075067123-1/50025-9>
- Oh, S.K.W., Nienow, A.W., Al-Rubeai, M., Emery, A.N., 1992. Further studies of the culture of mouse hybridomas in an agitated bioreactor with and without continuous sparging. *J. Biotechnol.* 22, 245–270. [https://doi.org/10.1016/0168-1656\(92\)90144-X](https://doi.org/10.1016/0168-1656(92)90144-X)
- Pan, C., Min, J., Liu, X., Gao, Z., 2008. Investigation of Fluid Flow in a Dual Rushton Impeller Stirred Tank Using Particle Image Velocimetry. *Chinese J. Chem. Eng.* 16, 693–699. [https://doi.org/10.1016/S1004-9541\(08\)60142-1](https://doi.org/10.1016/S1004-9541(08)60142-1)
- Pandey, A., Larroche, C., Soccol, C.R., Dussap, C.-G., 2008. Advances in fermentation technology, in: *Bioreactors: Functions in Fermentation Processes*. pp. 172–201.
- Paul, E.L., Midler, M., Sun, Y., 2004. Mixing in the Fine Chemicals and Pharmaceutical Industries, *Handbook of Industrial Mixing: Science and Practice*. <https://doi.org/10.1002/0471451452.ch17>
- Prakash, O., Shouche, Y., Jangid, K., Kostka, J.E., 2013. Microbial cultivation and the role of microbial resource centers in the omics era. *Appl. Microbiol. Biotechnol.* 97, 51–62. <https://doi.org/10.1007/s00253-012-4533-y>
- Raffel, M., Willert, C.E., Wereley, S.T., Kompenhans, J., 2007. *Particle Image Velocimetry: a Practical Guide*, 2nd ed. Springer. <https://doi.org/10.1057/9780230509306>
- Ramírez-Muñoz, J., Guadarrama-Pérez, R., Márquez-Baños, V.E., 2017. A direct calculation method of the Metzner-Otto constant by using computational fluid dynamics. *Chem. Eng. Sci.* 174, 347–353. <https://doi.org/10.1016/j.ces.2017.09.023>
- Ranade, V. V., Joshi, J.B., 1989. Flow Generated by Pitched Blade Turbines I: Measurements Using Laser Doppler Anemometer. *Chem. Eng. Commun.* 81, 197–224. <https://doi.org/10.1080/00986448908940539>
- Raven, J.A., Giordano, M., 2014. Algae. *Curr. Biol.* 24, R590–R595. <https://doi.org/10.1016/j.cub.2014.05.039>
- Roche, B., 2013. Sales of biologics to show robust growth through to 2013. *Discovery*. <https://doi.org/10.1038/nrd3040>
- Ruggiero, M.A., Gordon, D.P., Orrell, T.M., Bailly, N., Bourgoin, T., Brusca, R.C., Cavalier-Smith, T., Guiry, M.D., Kirk, P.M., 2015. A higher level classification of all living organisms. *PLoS One* 10, 1–60. <https://doi.org/10.1371/journal.pone.0119248>
- Saarenrinne, P., Piirto, M., 2000. Turbulent kinetic energy dissipation rate estimation from PIV velocity vector fields. *Exp. Fluids* 29. <https://doi.org/10.1007/s003480070032>
- Sagaut, P., 2006. *Large Eddy Simulation for incompressible flows: an introduction*. Springer. <https://doi.org/10.1088/1468-5248/2/1/705>
- Sagaut, P., Lee, Y.-T., 2002. *Large Eddy Simulation for Incompressible Flows: An Introduction*. *Scientific Computation Series. Appl. Mech. Rev.* 55, B115.

<https://doi.org/10.1115/1.1508154>

Scarano, F., 2013. Tomographic PIV: Principles and practice. *Meas. Sci. Technol.* 24. <https://doi.org/10.1088/0957-0233/24/1/012001>

Sheng, J., Meng, H., Fox, R.O., 2000. A large eddy piv method for turbulence dissipation rate estimation. *Chem. Eng. Sci.* 55, 4423–4434. [https://doi.org/10.1016/S0009-2509\(00\)00039-7](https://doi.org/10.1016/S0009-2509(00)00039-7)

Skelland, A.H.P., 1967. *Non-Newtonian Flow and Heat Transfer*.

Smith, J.J., Lilly, M.D., Fox, R.I., 1990. The effect of agitation on the morphology and penicillin production of *Penicillium chrysogenum*. *Biotechnol. Bioeng.* <https://doi.org/10.1002/bit.260351009>

Spier, M.R., Vandenberghe, L.P. de S., Medeiros, A.B.P., Soccol, C.R., 2012. Application of different types of bioreactor in bioprocesses.

Stewart, G.G., 2016. Industrial uses of yeast – brewing and distilling. *New Food - Brew. Suppl.* <https://doi.org/http://dx.doi.org/10.1016/j.amepre.2007.02.044>

Verma, A., Rastogi, S., Agrahari, S., Singh, A., 2011. Biotechnology in the realm of history. *J. Pharm. Bioallied Sci.* 3, 321. <https://doi.org/10.4103/0975-7406.84430>

Wille, M., Langer, G., Werner, U., 2001. The influence of macroscopic elongational flow on dispersion processes in agitated tanks. *Chem. Eng. Technol.* 24, 119–127. [https://doi.org/10.1002/1521-4125\(200102\)24:2<119::AID-CEAT119>3.0.CO;2-G](https://doi.org/10.1002/1521-4125(200102)24:2<119::AID-CEAT119>3.0.CO;2-G)

Wollny, S., 2010. Experimentelle und numerische Untersuchungen zur Partikelbeanspruchung in gerührten (Bio-) Reaktoren 194.

Xu, D., Chen, J., 2013. Accurate estimate of turbulent dissipation rate using PIV data. *Exp. Therm. Fluid Sci.* 44, 662–672. <https://doi.org/10.1016/j.expthermflusci.2012.09.006>

Yang, H., Liu, J., Wen, X., Lu, C., 2015. Molecular mechanism of photosystem I assembly in oxygenic organisms. *Biochim. Biophys. Acta* 1847, 838–848. <https://doi.org/10.1016/j.bbabbio.2014.12.011>

Zhu, H., Nienow, A.W., Bujalski, W., Simmons, M.J.H., 2009. Mixing studies in a model aerated bioreactor equipped with an up- or a down-pumping “Elephant Ear” agitator: Power, hold-up and aerated flow field measurements. *Chem. Eng. Res. Des.* 87, 307–317. <https://doi.org/10.1016/j.cherd.2008.08.013>

Appendix

Appendix A

Pre-experimental Establishment of Measuring Technique

This part of the appendix contains the velocity profiles of PROPRing- $h/d=0.33$ and the flow fields of PROP- $h/d=0.33$, WRI- $d/D=0.4-28.8^\circ$ and WRI- $d/D=0.33-51.2^\circ$ calculated with the approaches 2DA and 3DA.

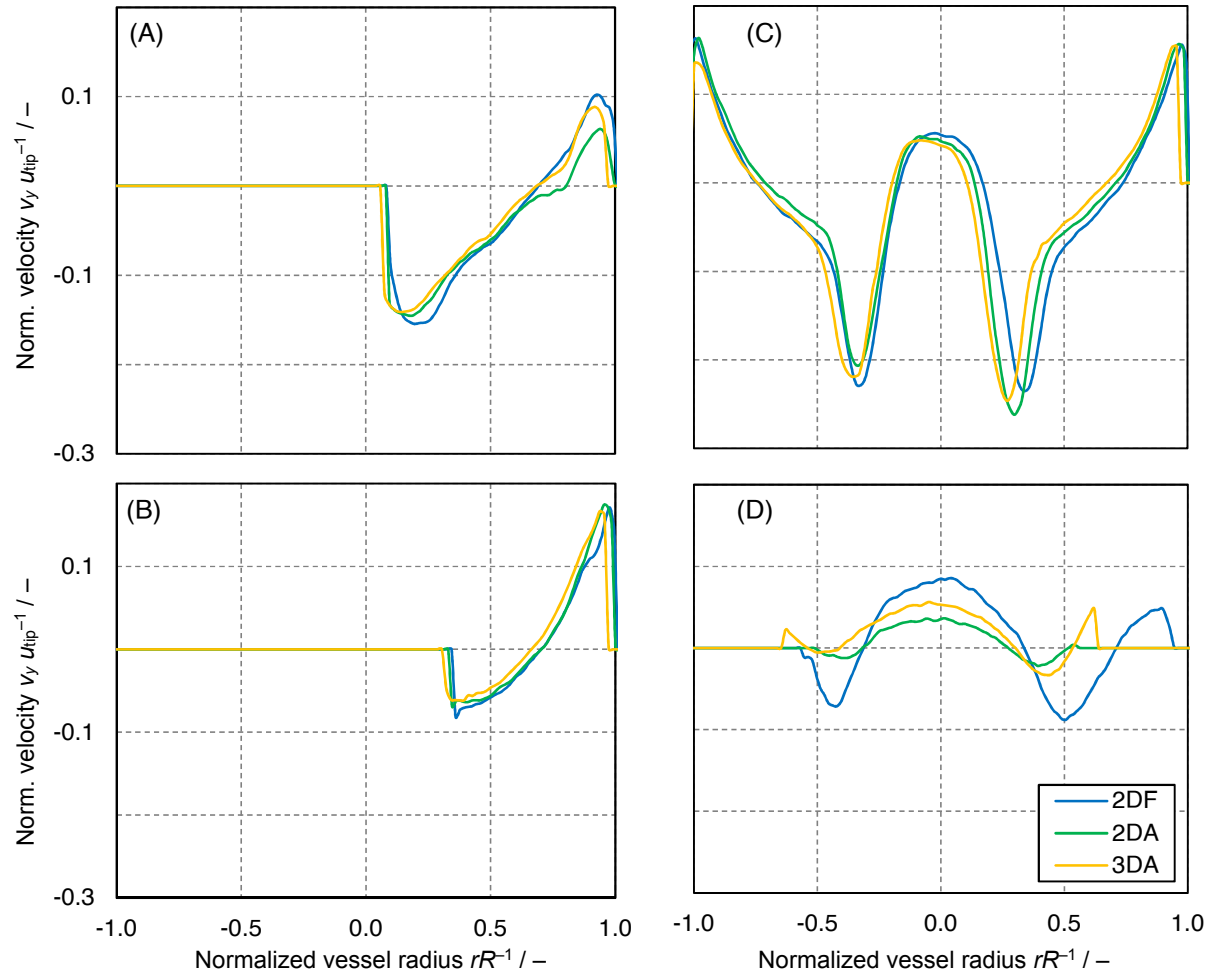


Fig. A-1 Horizontal profiles of normalized velocity along y direction, PROPRing- $h/d=0.33$: (A) position 4, (B) position 5, (C) position 6, (D) position 7.

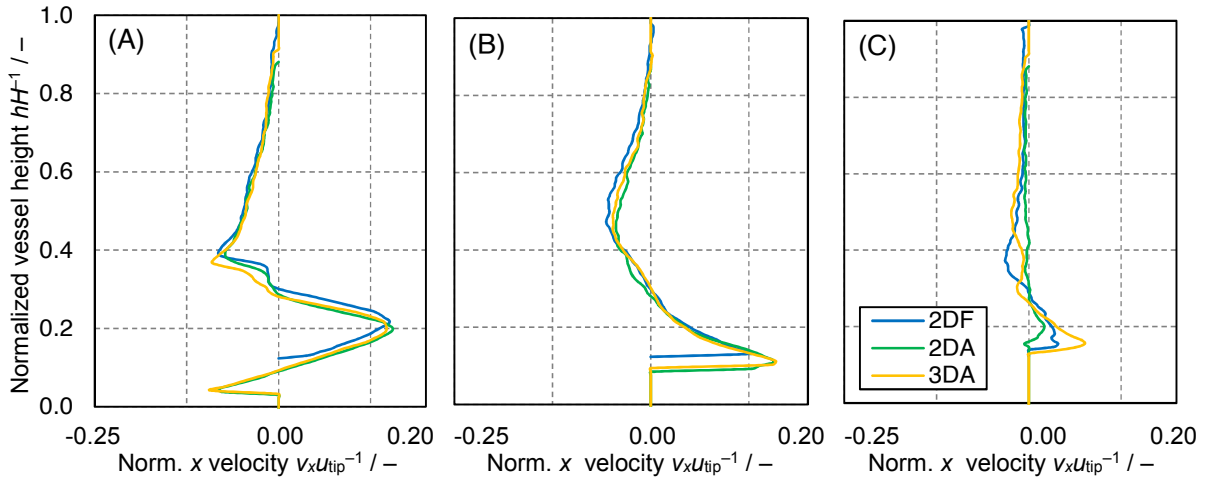


Fig. A-2 Vertical profiles of normalized velocity along x direction, PROPRing- $h/d=0.33$: (A) position 1, (B) position 2, (C) position 3.

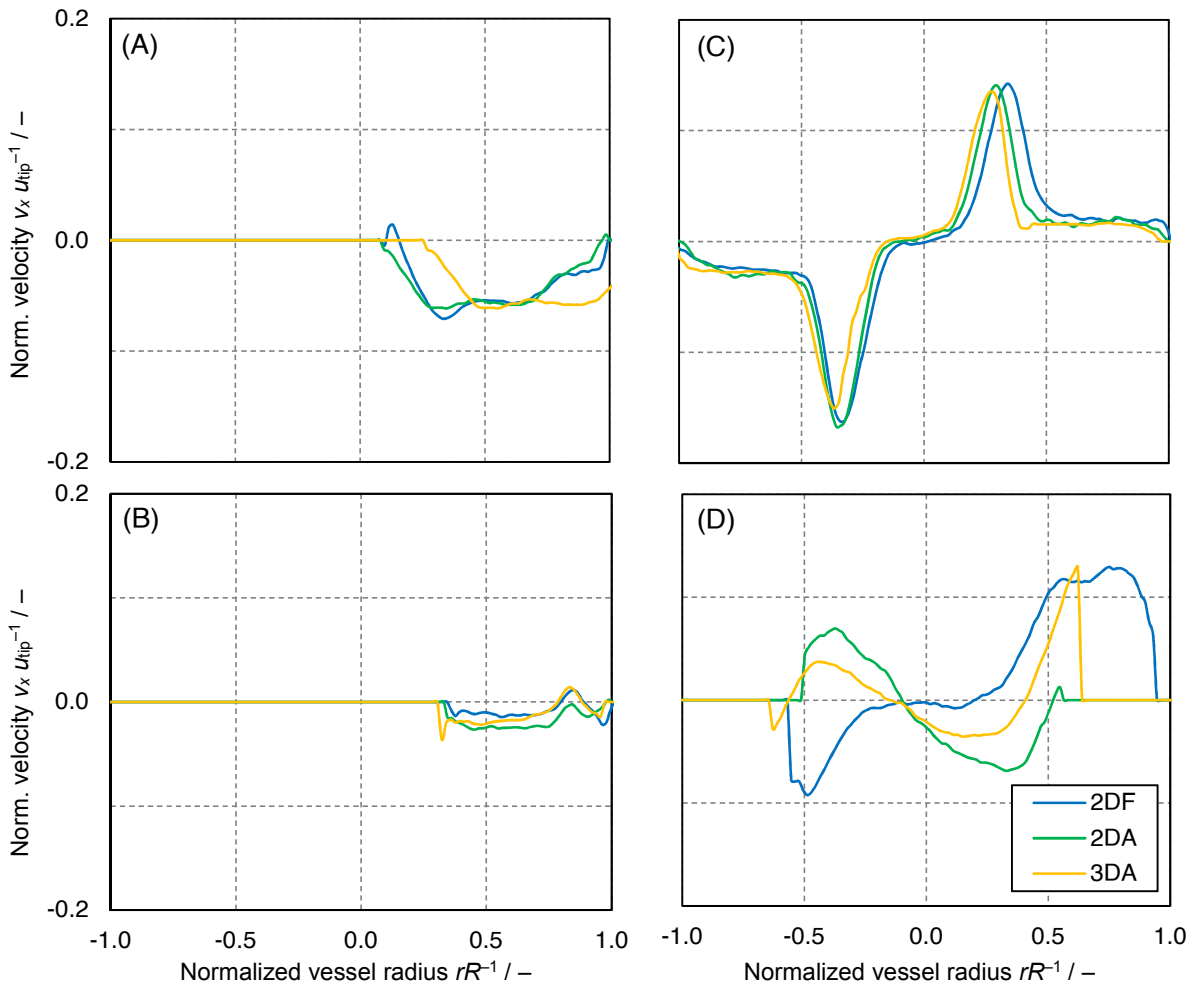


Fig. A-3 Horizontal profiles of normalized velocity along x direction, PROPRing- $h/d=0.33$: (A) position 4, (B) position 5, (C) position 6, (D) position 7.

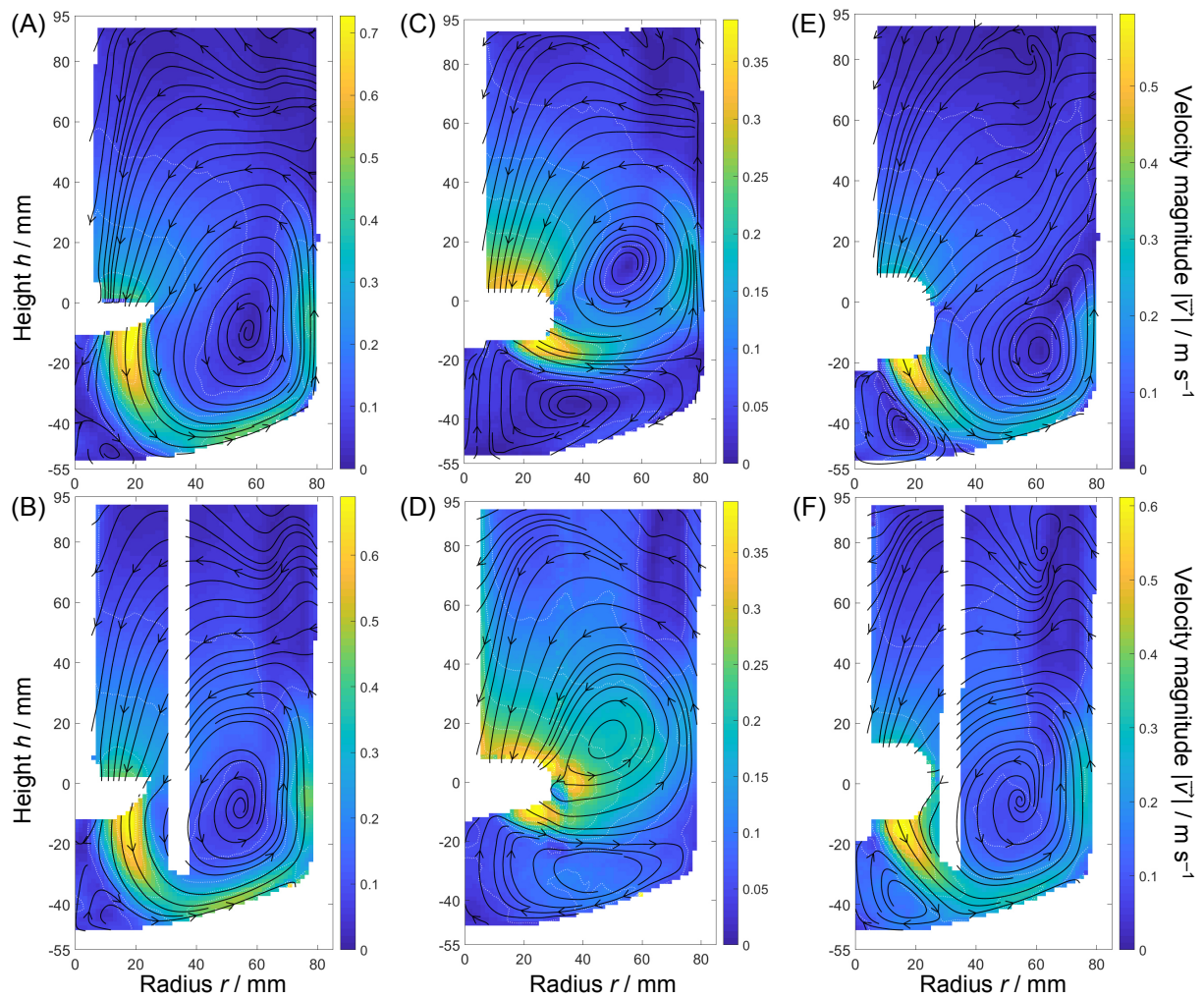


Fig. A-4 Flow fields observed with the approaches 2DA and 3DA: (A) PROP- $h/d=0.33$, 2DA, (B) PROP- $h/d=0.33$, 3DA, (C) WRI- $d/D=0.4-28.8^\circ$, 2DA, (D) WRI- $d/D=0.4-28.8^\circ$, 3DA, (E) WRI- $d/D=0.33-51.2^\circ$, 2DA, (F) WRI- $d/D=0.33-51.2^\circ$, 3DA.

Appendix B

This part of the appendix reports the additional results obtained in the systematic investigation.

Influence of power input

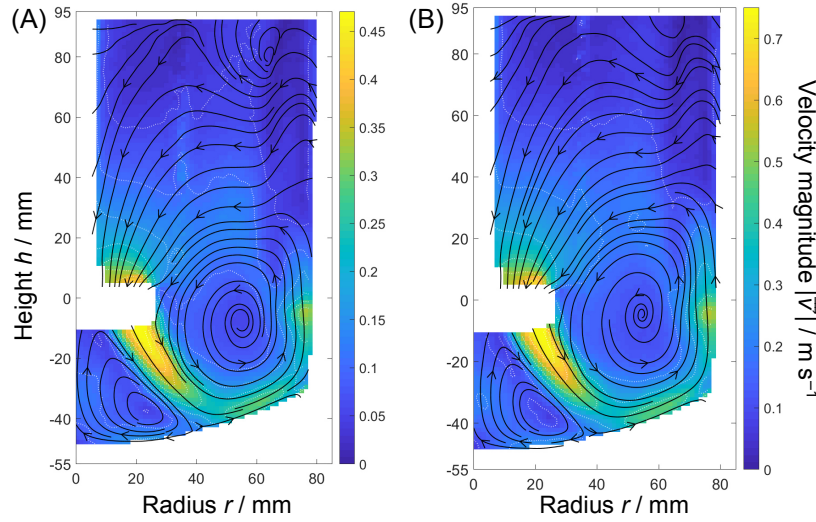


Fig. B-1 Flow field observed with PROPRing- $h/d=0.33$ in water with approach 3DA, with increasing power input: (A) $PV^{-1} = 49 \text{ W m}^{-3}$, (B) $PV^{-1} = 195 \text{ W m}^{-3}$.

Influence of rheology

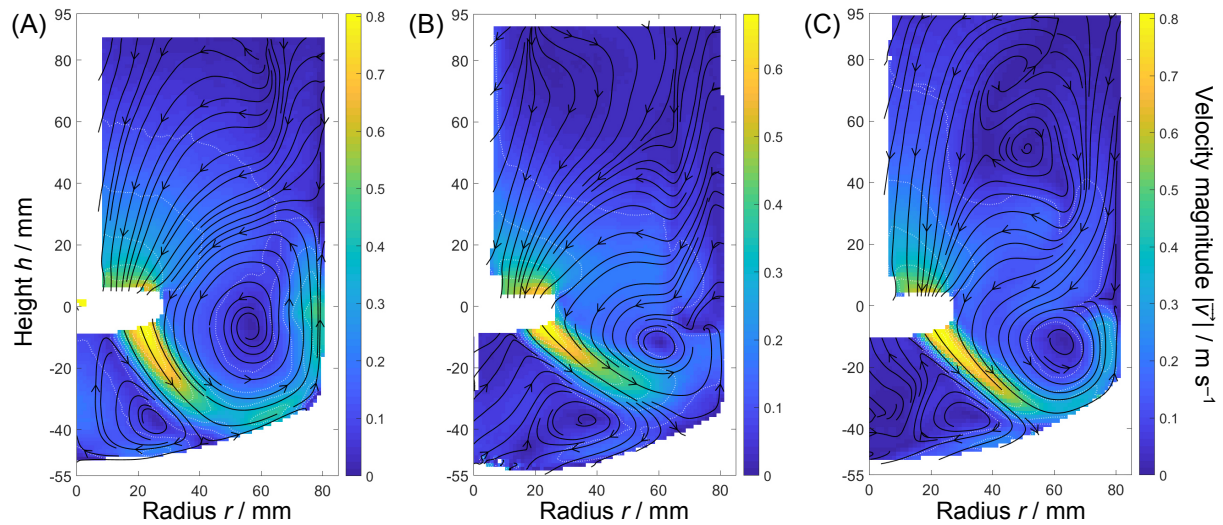


Fig. B-2 Influence of rheology on the flow patterns developed with PROPRing- $h/d=0.33$, for $PV^{-1} = 200 \text{ W m}^{-3}$: (A) water, (B) glycerin, (C) xanthan.

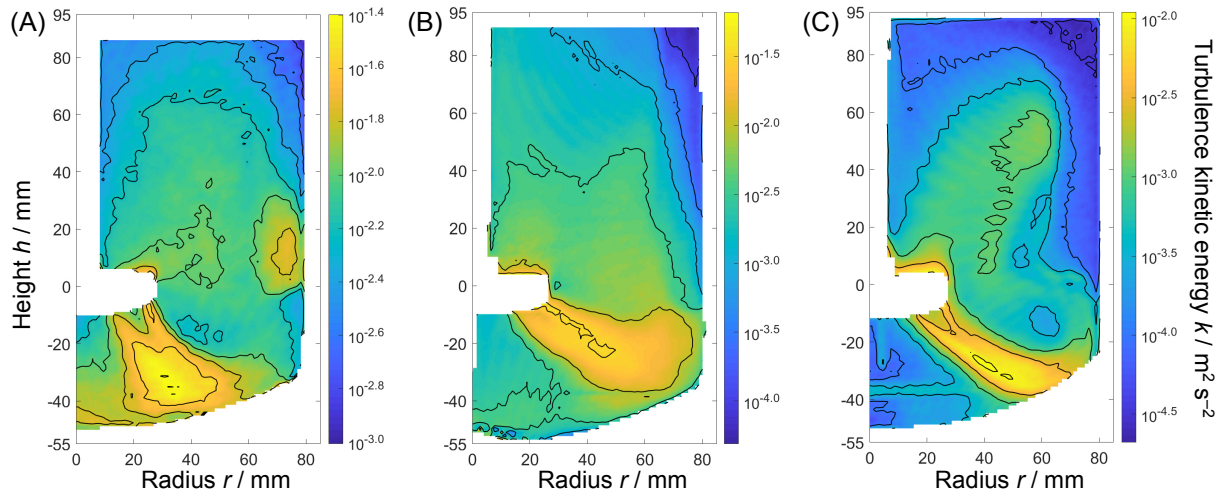


Fig. B-3 Influence of rheology on TKE field developed with PROPRing- $h/d=0.33$, for $PV^{-1} = 100 \text{ W m}^{-3}$: (A) water, (B) glycerin, (C) xanthan.

Influence of geometry

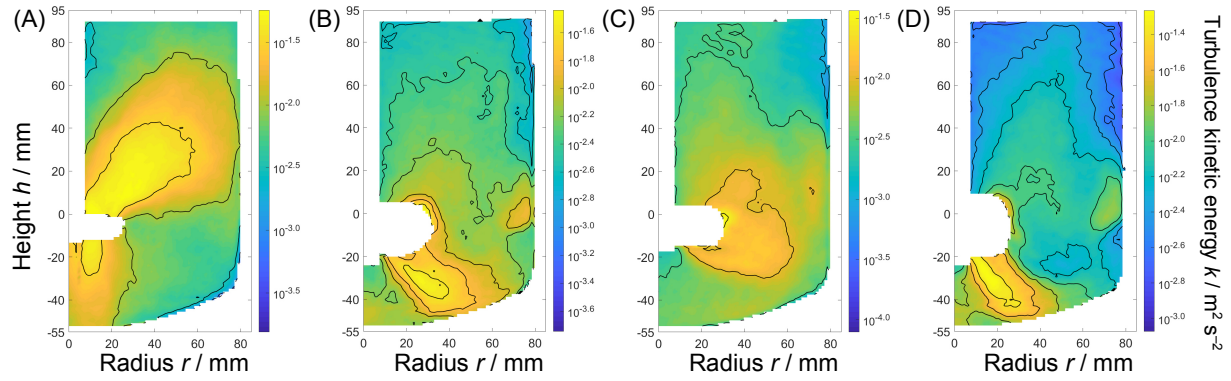


Fig. B-4 TKE fields in water: (A) BiLoop, (B) WRI- $d/D=0.4-41.4^\circ$, (C) WRI- $d/D=0.4-28.8^\circ$, (D) WRI- $d/D=0.33-51.2^\circ$

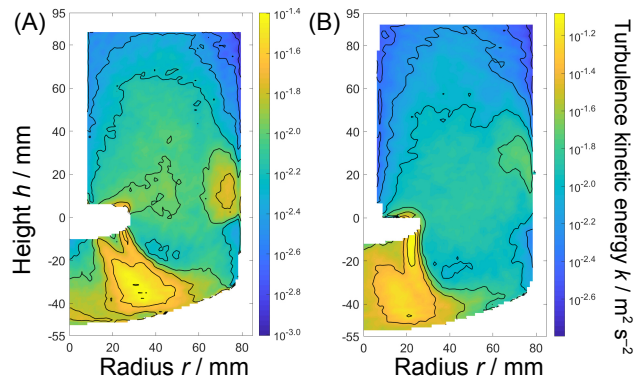


Fig. B-5 TKE fields in water: (A) PROPRing- $h/d=0.33$, (B) PROP- $h/d=0.33$.